The Development of Two-Phase Xenon Dark Matter Detectors

John Kwong

Abstract

The nature of dark matter remains one of the great unsolved mysteries of modern physics. The existence of dark matter has been inferred from its gravitational interactions and is strongly supported on theoretical grounds. A primary candidate for the dark matter is the Weakly Interacting Massive Particle (WIMP), which may be an undiscovered particle from the supersymmetric sector. This dissertation describes the research and development in two-phase liquid xenon dark matter detector technology and the results from the full-scale detector XENON10. Two-phase liquid xenon detectors use position sensitivity and simultaneous measurement of light and charge to remove background electron recoil events. The development of this technology has been rapid – the work in this dissertation began in the summer of 2003 when the potential of this technology had yet to be determined, and in early 2008 the XENON10 collaboration published the then world-best upper limit on the spin-independent WIMP-nucleon cross section. The first measurement of the charge based discrimination performance at low energies was achieved in a prototype in early 2005. This prototype also determined the performance of discrimination via scintillation pulse shape. Although pulse shape discrimination was shown to be far weaker than that from charge yield, the combined use of the two methods demonstrated a discrimination power beyond that achieved by either method alone. Alternative detector technologies were also explored. Electron multiplication on wire grids was demonstrated in a two-phase prototype and its discrimination power potential is shown to be near that of the typical electroluminescence charge-readout technique. This could allow for the removal of some or all of the photo-multipliers in the detector, which would greatly reduce radioactive backgrounds. The use

of a wavelength shifter was tested in an attempt to improve light collection and was shown to impede charge collection. The magnitude of fluctuations in recombination in electron recoils, which are an important component in charge resolution, was also measured. The final chapter describes the XENON10 detector, its operation at the Gran Sasso National Laboratory, the analysis of the data, and the results of the WIMP search.

Acknowledgements

First and foremost, I would like to thank my advisor, Professor Tom Shutt for providing such incredible scientific insight, encouragement and support throughout the past six years. I would also like to thank Professor Elena Aprile for being so welcoming during my time at Nevis and the other leaders of XENON10, in particular Rick Gaitskell, Karl Giboni, Laura Baudis, Richard Gaitskell, Jose Lopes, Dan McKinsey, and Uwe Oberlack. My work would also not be possible without the help Alexander Bolozdynya, Pawel Majewski, Masaki Yamashita, Pawel Brusov, Kirk McDonald, and Changguo Lu. I would also like to thank Cristiano Galbiati for reviewing my thesis.

I would also like to express special thanks to my fellow flannel-wearing labmate Eric Dahl for helping me maintain my sanity during the endless hours in lab. I wish him success in Chicago and many long nights listening to Wesley Willis and William Hung in lab.

I would also like to express thanks to my numerous colleagues: Alfredo Ferella, Kaixuan Ni, Guillaume Plante, Maria Elena, Angel Manzur, Louis Kastens, Peter Sorensen, Luiz de Viveiros, Simon Fiorucci, Joerg Orboeck, Ana Conceição, Sean Bryan, Jon Leong, Adam Bradley, Annika Peter, Justin Kinney, Nathan Shaman, Jeremy Mock, Sander Zanderbergen, Mike Usowicz, and Sashank Karri.

I am also grateful to my friends back home – Katrina Pagonis, Nick Pagonis, Loretta Tse, Jia Yuan Li, and Michael Wong – for constantly hassling me to finish this thesis. I would especially like to thank you, my darling, for always believing in me and being there for me whenever I needed you. You are the best (and you know it) and I will never forget your artistic renderings of WIMPs.

Finally, I would like thank my family for all their love and support.

Contents

List of Figures

xv

xxvii

List of Tables

Chapter 1

Dark Matter

1.1 Introduction

Most of the matter in the universe is dark and its nature is unknown. Revealing the nature of dark matter will have enormous implications for our fundamental understanding of the universe. The existence of dark matter was first inferred through its gravitational effects on normal matter and with the advent of precision cosmology, its contribution to the total mass-energy has been pinpointed. This chapter reviews some of the basic evidence and proposed explanations for dark matter.

1.2 Evidence for Dark Matter

Much of the early evidence for dark matter was from observations of the motion of gravitationally bound bodies at the galaxy and cluster level. Recently, evidence has come from more sophisticated techniques such as measurements of the CMB anisotropies, gravitational lensing by galaxy clusters, primordial elemental abundances, and redshift surveys of large-scale structure. Furthermore, these measurements strongly suggest that much of the matter is non-relativistic (cold) and non-baryonic.

1.2.1 Evidence at the Galactic Level

The rotational curves of spiral galaxies provide one of the clearest indications of dark matter. The velocity is determined by measuring the Doppler redshift of atomic transition lines and the common 21 cm line (HI) from neutral hydrogen clouds. The velocity is expected to drop off based on the luminous mass but has been well observed to level off with distance from the galactic center. Assuming that Newtonian dynamics is correct at long distances, the circular velocity at a radius r is

$$v(r) = \sqrt{\frac{GM(r)}{r}}, \tag{1.1}$$

where $M(r)$ is the total mass contained in r. The mass is $M(r) = 4\pi \int \rho(r) r^2 \, dr$. For $v(r)$ to be constant, we must have $M(r) \propto r$ or, equivalently, $\rho(r) \propto r^{-2}$.

Persic et al probed the general mass structure properties of spirals by using the rotation curves of about 1100 spiral galaxies with brightness over a range of 6 magnitudes and distance out to 2 optical radii. Galaxies of different sizes are compared by scaling to the optical radius R_{opt} which is the radius that contains 83% of the light. It has been shown that all spiral rotation curves can be represented by a "universal rotation curve," which depends only on the luminosity. Figure 1.1 shows the fit of the universal rotation curve to galaxies divided up into 11 luminosity bins. Here, we see that the rotational curves rise sharply at $R/R_{opt} < 1$ and then level off. This study also found that as the luminosity is decreased, the discrepancy increases between luminous matter and matter based on the rotation curve.

The presence of dark matter can also be seen in elliptical galaxies. Elliptical galaxies generally lack neutral hydrogen which is ubiquitous and extensive in spirals, but instead have hot x-ray emitting (thermal bremsstrahlung) gas in hydrostatic equilibrium that provides a means of measuring the dark matter distribution. Dark matter comprises a significant but not dominate portion of the total mass within the half-light radius r_e and increase in dominance at larger radii. An excellent summary on dark matter in elliptical galaxies is given by [76].
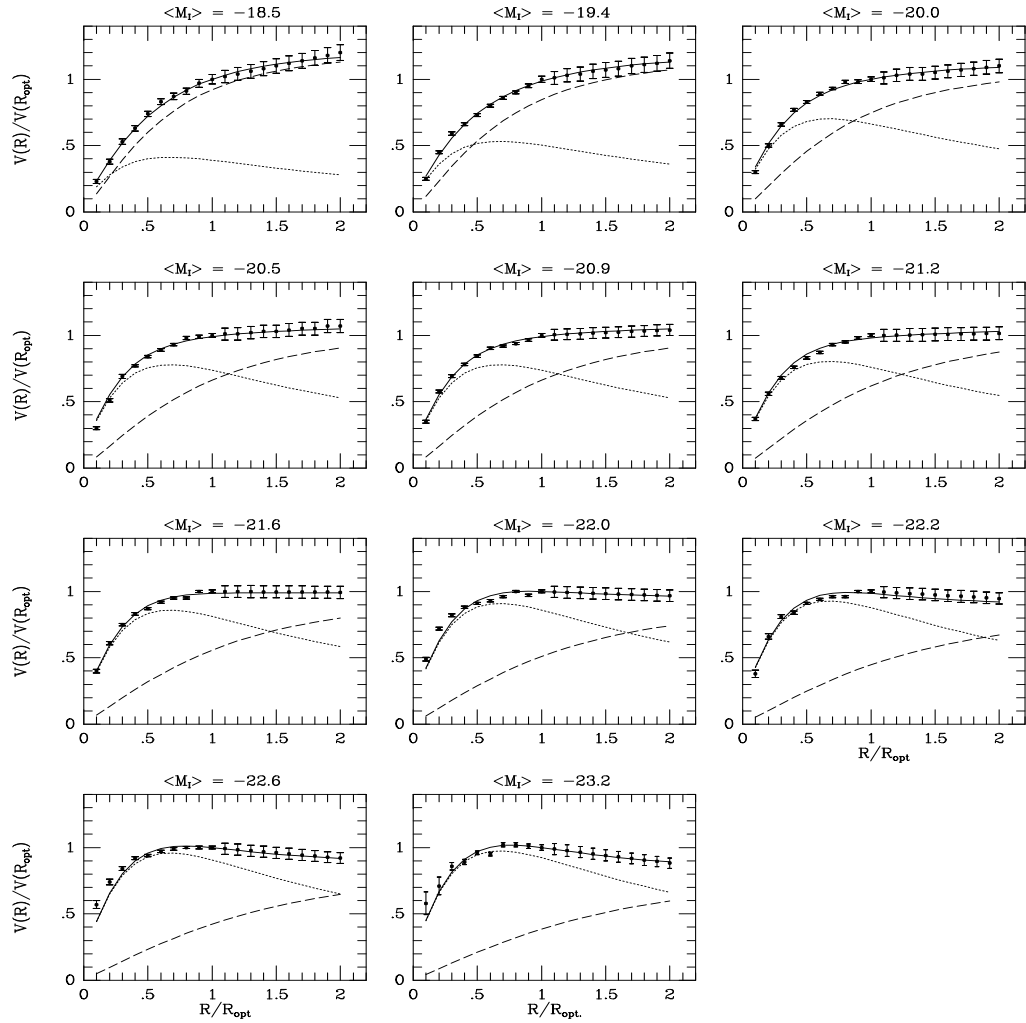
Figure 1.1: Average rotation curves and universal rotation curve fits to groups of galaxies divided into 11 luminosity bins. Each bin contains 50 to 100 galaxies. The dotted and dashed lines indicate the contribution of the disc and the dark halo, respectively. The solid line is the quadrature sum of these two contributions. This plot shows that the velocity is roughly constant between 1–2 R_{opt}. The optical radius R_{opt} is the radius that contains 83% of the light. These plots are from [1].

1.2.2   Evidence at the Extra-Galactic Level

Dark matter has been also observed in the space between galaxies of groups ($\lesssim$50 galaxies) and clusters ($\gtrsim$50). The dark matter content can be measured by virial methods, x-ray and gravitational lensing. The virial theorem allows the mass to be determined based on the velocities of galaxies. Quite simply, the virial theorem states that the average kinetic energy is equal to minus one-half times the average gravitational potential energy. In 1933, Zwicky measured the velocity dispersion of galaxies in the Coma cluster and found that objects in the periphery of the Coma cluster orbited faster than that expected from the mass as inferred by its luminosity [77]. With this discovery, Zwicky is usually credited as the first person to provide evidence for dark matter. Girardi et al has also applied the virial theorem on a sample of about 100 galaxy clusters from various surveys [78]. The masses calculated with the virial theorem agree well with the values determined by x-ray measurements. The determination of mass by x-rays from intergalactic gas is similar to methods used for elliptical galaxies. Many such studies have been performed [79, 80].

Dark matter has also been observed in galaxy clusters via gravitational lensing, which has the advantage of not requiring assumptions on the internal dynamics, unlike the previously described methods. There are several classes of lensing. In strong gravitational lensing, the effect is very visible resulting in arcs and multiple images of the background object. Such cases are few and difficult to analyze due to the high non-linearity of the effect. In weak lensing, the distortions (ellipticity vectors and brightness) are much more minute and can only be detected by analyzing a large number of sources. Gravitational lensing measurements have confirmed the results of virial and x-ray analyses [81]. An overview of weak lensing can be found in [82, 83].

Data from the Sloan Digital Sky Survey (SDSS) has been used to probe the halo mass profile of isolated galaxies. This study showed halo profiles agreeing with that of dark matter models and contradicting those of MOND [84]. A flat rotation curve (which corresponds to a density distribution of $\rho \propto r^{-2}$) agrees with MOND while a falling velocity dispersion ($\rho \propto r^{-3}$) is predicted by galactic simulations of dark matter halos. The key to distinguishing

between halo profiles is to measure the velocities of objects at very large radii ($<$100 kpc). Tracers such as neutral hydrogen (HI) and x-ray emissions from diffuse hot gases in isolated elliptical galaxies indicate the presence of dark matter halos but neither indicators extend far enough to distinguish halo profiles. Strong gravitational lensing also provides a probe of only the inner regions. Weak gravitational lensing has also failed to distinguish between models. Observation of the motion of satellites (smaller galaxies) of galaxies provide an excellent probe of the dark matter distribution at large radii but statistics had been limited until SDSS. In this study, about 3,000 satellites with absolute blue magnitudes extending down to $M_B = -14$ were found. The velocity dispersion of these satellites were found to decrease with distance from the primary. This was the first direct observational confirmation of density decline which agrees with all cosmological models. Furthermore, the results contradict alternative theories such as Modified Newtonian dynamics (MOND).

1.2.3 Evidence at the Cosmological Level

Cold non-baryonic dark matter is a key component to our best models of the universe. In these models, dark matter is needed to explain the anisotropies and polarization in the cosmic microwave background (CMB) and the formation of large scale structures. Also, some dark matter is needed to explain the abundance of primordial elements generated by Big Bang nucleosynthesis (BBN). Experimental confirmation of these models support the idea that most of dark matter in the universe is cold and non-baryonic.

Cosmic Microwave Background

The CMB was first proposed by Robert Dicke in 1946 and was first detected by Penzias and Wilson in 1964 [85]. Its detection gave much support for the Big Bang Theory. About 379,000 years after the beginning of the universe when the temperature had dropped to about 3000 K, the electrons combined with the protons to form hydrogen. At this point, the photons decoupled from matter as they were no longer energetic enough to ionize hydrogen. The temperature of the photons continued to decrease as the universe expanded. These are
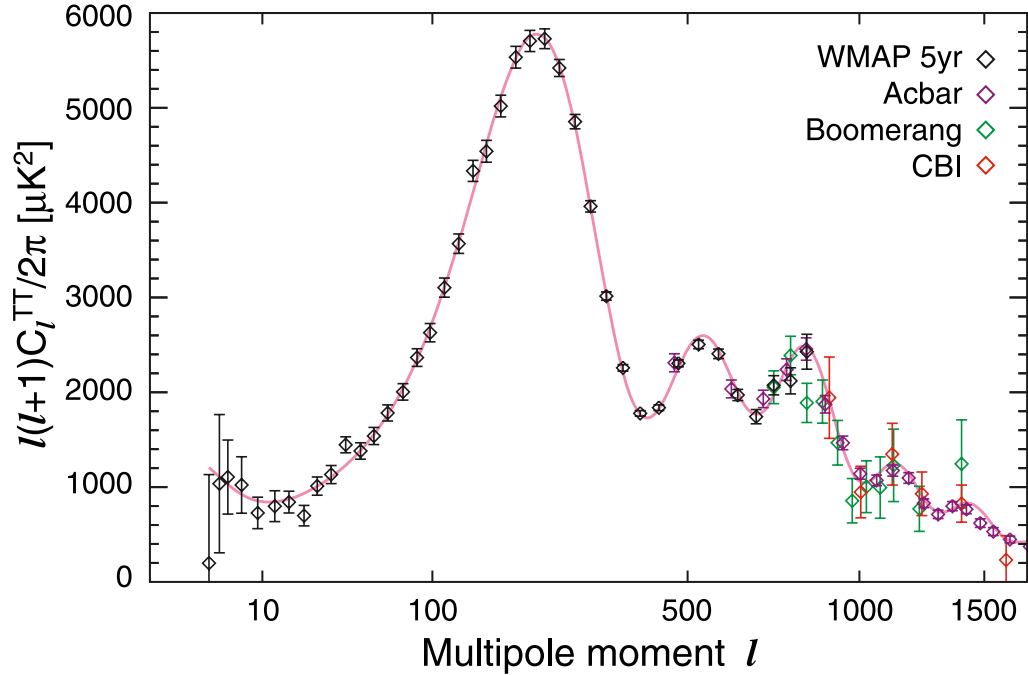
Figure 1.2: The power spectrum of the cosmic microwave background radiation anisotropies from the first five years of the Wilkinson Microwave Anisotropy Probe (WMAP) data with the best fit spectrum from the ΛCDM/WMAP chain as indicated by the red line. Also shown are recent results from ACBAR, Boomerang, and CBI. Figure taken from [2].

the CMB photons. The CMB spectrum almost perfectly follows the theoretical curve of a T = 2.725 K black body and is isotropic up to roughly 1 part in 100,000. The CMB essentially gives a snapshot of the structure of the early universe, and dark matter, if present, would be apparent in the CMB as it affects the evolution of this structure.

There are several sources of anisotropies [86]. The CMB is maximally blue shifted in one direction and maximally redshifted in the opposite direction. This dipole anisotropy, which is roughly 1 part in 1000, is due to the movement of our frame of reference relative to the CMB rest frame. The other sources of anisotropies can be divided into two categories. The primary anisotropies are due to processes occurring until the time of recombination and the secondary fluctuations are due to phenomena occurring since then. Some basic mechanisms for the primary anisotropies are acoustic oscillations and diffusion damping (also known as collisional dissipation or Silk damping). The acoustic oscillations are due to

two opposing effects in the photon-baryon plasma. The baryons accumulate by gravitational force while the pressure in the photons pushes the gas apart. This results in oscillations which give the characteristic peak structure of the CMB. Diffusion damping occurred during recombination as the mean free path of photons increased. The photons diffused from hot regions to cooler ones while dragging along protons and electrons. This reduces smaller scale anisotropies. Some secondary anisotropy contributions include the Sachs-Wolfe effect which causes the wavelength of photons to be shifted by changing gravitational potentials and the Sunyaev-Zel'dovich effect, which is essentially a reverse Compton interaction where high energy electrons transfer energy to CMB photons.

The anisotropies were first measured by the Far Infrared Absolute Spectrophotometer (FIRAS) on the COBE satellite [87]. The Wilkinson Microwave Anisotropy Probe (WMAP), launched into space in 2001, provides the most accurate measurement of the CMB [2]. Other prominent experiments include the balloon-borne BOOMERanG [88] and MAXIMA [89] and ground-based ACBAR [90] and DASI [91]. The Planck telescope, launching in April 2009, will improve upon the results of WMAP [92].

The angular power spectrum is obtained by decomposing the map into spherical harmonics, while taking into consideration various distortions such as emissions from galaxies. Figure 1.2 shows the power spectrum of the cosmic microwave background radiation temperature as measured by WMAP and other detectors. The size and location of the peaks provide valuable information on cosmological parameters, such as the curvature and matter/energy composition of the universe. WMAP provides a very precise composition of the universe: $\Omega_\Lambda = 0.742 \pm 0.030$ (dark energy), $\Omega_c h^2 = 0.1099 \pm 0.0062$ (cold dark matter) and $\Omega_b h^2 = 0.02273 \pm 0.00624\%$ (baryonic) [93]. For $h = 0.719$, $\Omega_c = 0.213$ and $\Omega_b = 0.0440$.

Big Bang Nucleosynthesis

The theory of Big Bang nucleosynthesis, which was first proposed by Alpher and Gamov [94], describes the formation of light elements during the very hot phase of the universe. Matching the observed abundances of these elements to the predicted values constrains
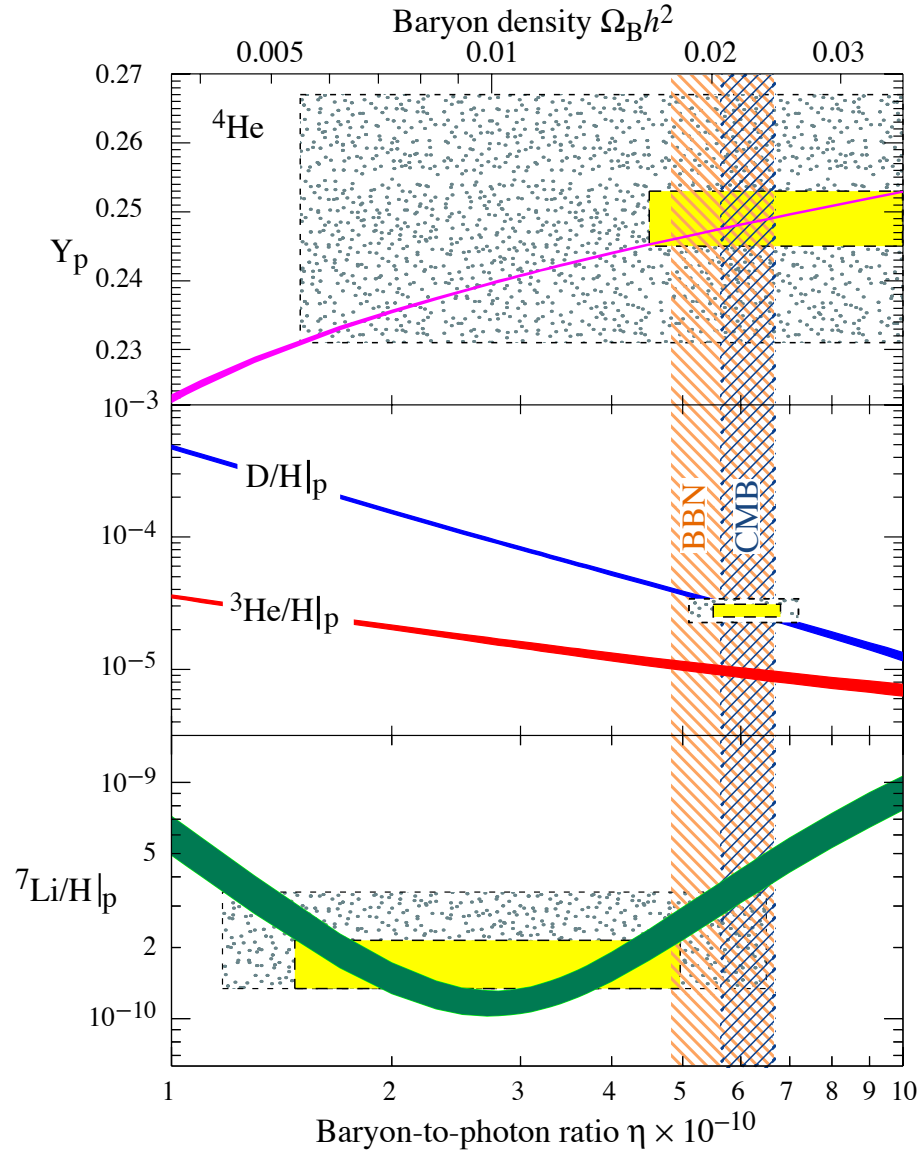
Figure 1.3: The abundances of ^{4}He, D, ^{3}He and ^{7}Li relative to H as a function of the baryon/photon fraction (η) or the reduced baryon density ($\Omega_B h^2$). The blue lines indicate the 1-σ predicted values. The hatched areas are values determined by measuring various primitive astronomical sources. Figure taken from [3].

the relative abundance of baryons in the universe (Ω_b), which can be compared to the independently determined values from the CMB anisotropy measurements.

BBN began three minutes after the Big Bang when the universe was cool enough for protons and neutrons to form and combine into atoms, and ended about seventeen minutes later. BBN predicts the primordial abundances to be roughly 75% H (hydrogen comprising 75% of the baryon mass, not 75% of the atoms), 25% ^{4}He, 0.01% D (^{2}H) and 10^{-10} ^{7}Li [3]. No elements beyond beryllium are created because of the absence of stable nuclei with 5 or 8 nucleons (no nucleosynthesis via p^{4}He, n^{4}He or ^{4}He^{4}He reactions). Figure 1.3 shows the measured and predicted abundances of ^{4}He, D, ^{3}He and ^{7}Li relative to H as a function of the photon/baryon fraction (η) and the reduced baryon density ($\Omega_B h^2$). The evolution of the chemical abundances follow simple thermodynamics with consideration for the expansion of the universe. As the temperature decreased, the rate of conversion between protons and neutrons dropped faster than the Hubble expansion rate which resulted in a "freeze-out" of a non-equilibrium population. The freeze-out locked in a baryon population of 7 protons for every 1 neutron, which explains the observation of ^{4}He comprising 25% of the mass – out of every 16 nucleons (2 neutrons and 14 protons), four of them combine to form ^{4}He and thus make up 1/4 of the mass. This percentage is not strongly dependent on the initial conditions. BBN (or some other explanation) is needed to explain the amount of ^{4}He because the observed amount is far larger than what could have been generated by stellar nucleosynthesis. The primordial abundance of ^{4}He is inferred from H II regions within dwarf galaxies [95].

Unlike ^{4}He, deuterium is not very stable and is easy to destroy. Two deuterium atoms can fuse into a ^{4}He which is more stable. Not all of the deuterium is destroyed during BBN because of cooling. Its primordial abundance depends strongly on the baryon density as this dictates how much is destroyed. Since no post Big Bang processes are known to create deuterium and it is easily destroyed, most measured values can be seen as lower limits. Measurements of distant quasars provide the best estimate of its primordial abundance [96, 97]. The abundance of ^{3}He is difficult to measure in extra-galactic sources because

its emission spectrum is more or less the same as ^{4}He. Thus its proportion is deduced only from sources within our solar system and H II regions in our galaxy. Due to the difficulty in measuring its abundance and the uncertainty in stellar contribution [98], ^{3}He is not used as a probe. The amount of ^{7}Li can be deduced by probing the outermost layers of old stars where much less stellar nucleosynthesis has occurred and thus have a mixture that resembles the primordial fluid [99]. The predicted and measured ^{7}Li abundances are the same order of magnitude. The lack of a better agreement is more likely due to our incomplete understanding of stellar physics rather than of BBN.

Figure 1.3 shows the constraints by observed abundances that set a bound in the baryon fractional density. The concordance gives the baryon content as $0.017 \geq \Omega_B h^2 \geq 0.024$ (95% CL) [3] (or $0.033 \geq \Omega_B \geq 0.046$ for $h = 0.719$). Also shown in Figure 1.3 is the bound independently determined by WMAP measurements which remarkably agrees with the bounds set by BBN.

Large Scale Structure

The observed large-scale structure of the universe supports the existence of cold dark matter. The matter density distribution which is imprinted in the CMB should also be apparent in the current distribution of galaxies. The distribution has been determined by extensive redshift surveys such as the 2dF Galaxy Redshift Survey (2dFGRS) and Sloan Digital Sky Survey (SDSS). Figure 1.4 shows the reconstructed position of galaxies from the SDSS data. Over a million galaxies have been cataloged by these studies. The organization of structures beyond the size of super cluster was not well known until the discovery of structures such as the "Great Wall" by Geller and Huchra [100]. It is believed that the structures evolved from the "bottom up" – that is, smaller structures such as galaxies formed first, then clusters and super clusters. This hypothesis is supported by the age of stars and by the existence of currently forming super clusters. As simulations have shown, a universe with only baryons cannot lead to the structure we see today [101]. The baryons were too strongly coupled to the photons until recombination which is too late to grow these
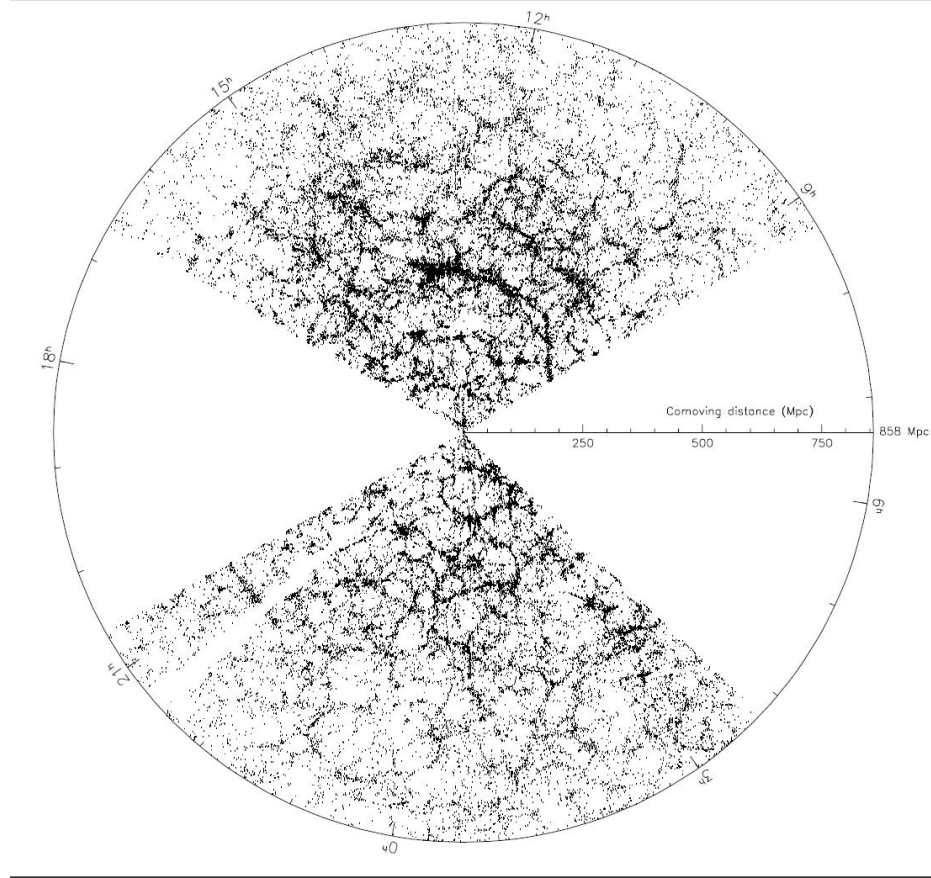
Figure 1.4: Redshift map of Sloan Digital Sky Survey data which exhibits the bubble and filament-like structures. Figure taken from [4].

structures. Non-baryonic cold dark matter allows structures to begin forming sooner as they are decoupled from the photons. A universe with hot dark matter would not have started galaxy formation soon enough and would have created structures that are too large [102]. Detailed analysis of the redshift survey data has yielded matter densities in accordance to that determined by WMAP. Analysis of the 2dFGRS data gives $\Omega_m = 0.26 \pm 0.05$ and $\Omega_b = 0.044 \pm 0.016$ assuming $h = 0.07$ based on a sample of 221,000 galaxies [103]. SDSS gives values in agreement [104]. Combining redshift survey data with WMAP results in significant improvements in cosmological parameters [105, 106, 107].

As shown in this section, we have discovered much evidence dark matter at various scales. The more sophisticated measurements at the cosmological scale strongly and independently

suggest that most of the dark matter is cold, non-baryonic and comprises about a quarter of the mass/energy of the universe. Most impressive is that observations of BBN, CMB and large scale structure formation are probes of the universe at vastly different times – the universe at several minutes, 379,000 years, and billions of years, respectively. In the next section, we review the dark matter candidates and alternative explanations.

1.3   Solutions to the Dark Matter Mystery

1.3.1   Baryonic Dark Matter

As discussed in the previous section, most of the matter in the universe is dark and non-baryonic. However, not all of the baryonic matter has been accounted for. The amount of luminous mass in the universe is $\Omega_{lum} \sim 0.005$ while $\Omega_b = 0.04$. A proposed candidate for baryonic dark matter is neutral hydrogen which is seen in intergalactic clouds at high redshifts ($z > 1$). If the density of this gas is low enough, these clouds might not have collapsed yet to produce stars. Neutral hydrogen is detected by observing the Lyman-α forest (the absorption spectra of high-z quasar emissions). Measurements give only a lower bound of $\Omega_b h^2 \geq 0.018$ due to various systematics [108]. The Lyman-α forest disappears at $z < 1$ – the dark baryons must have taken some other form. The most popular form has been the massive compact halo objects (MACHO), which includes dim objects such as brown dwarfs, black holes, white dwarfs, and neutron stars. These objects are detected indirectly through gravitational microlensing. Such searches involve monitoring numerous stars for a brief increase in light intensity when a MACHO crosses the direct line of sight between the observer and the star. Several microlensing searches for these objects have so far found too few incidents to account for all of the missing mass [109, 110]. In fact, MACHOs comprise at most 25% of the baryonic dark matter.

1.3.2 Non-Baryonic Dark Matter

Neutrino

Although neutrinos are stable and massive [111, 112], they are not good candidates for dark matter. As previously stated, even small amounts of neutrinos over dampen the small scale fluctuations in the CMB power spectrum. This happens because the neutrinos travel at such a high speeds that they smooth out any fluctuations in the matter density until they are cooled down by expansion. Also, it is difficult to see how neutrinos could populate the dark galactic halos [113]. WMAP and SDSS data have constrained neutrinos to comprise no more than 12% of dark matter [105].

Axions

The missing mass problem might be evidence of particles from extensions to the Standard Model. One such particle is the axion which is a low-mass neutral pseudoscalar particle that was first postulated by the Peccei-Quinn theory as a solution to the problem of strong CP violation in QCD [114, 115, 116]. Experiments and astrophysical arguments limit the mass to between 1×10^{-6} and 1×10^{-3} eV [117, 118, 119]. A summary of past and present searches can be found in [120]. Since axions are chargeless and have small cross sections for strong and weak interactions, they rarely interact with ordinary matter. Given their low mass, decay modes are unlikely which allows for the existence of a large non-thermal and cold relic population that "froze out" shortly after the Big Bang. A discussion on relic populations is given in the next section in the context of weakly interacting massive particles.

Axions couple to photons according to

$$\mathcal{L} = -\frac{1}{4} g_{a\gamma} F_{\mu\nu} \tilde{F}^{\mu\nu} \, a = g_{a\gamma} \boldsymbol{E} \cdot \boldsymbol{B} \, a \qquad (1.2)$$

where F is the electromagnetic field-strength tensor, $\boldsymbol{E}$ and $\boldsymbol{B}$ are the electric and magnetic fields, g is the axion-photon coupling strength, and a is the axion field. Several current experiments exploit this coupling and have a realistic chance for detection if they exist.

One such experiment is the Axion Dark Matter Experiment (ADMX) which exploits the conversion of axions into photons in sensitive microwave cavities [121, 122]. The expected signature of the axion signal is a peak of excess power at a frequency of $f = mc^2/h$, where m is the mass of the axion, c is the speed of light, and h is the Planck constant. Since the axion mass is unknown, the microwave resonator cavity must be tunable. This experiment has excluded a local dark matter halo of KSVZ axions of mass 1.9–3.3×10^{-6} eV with greater than 90% confidence [123].

If axions are real, we expect the sun to be a detectable source of axions. Solar axions are produced when x-rays scatter off electrons and protons in the presence of a strong electric field and are expected to have a broad energy spectrum with an average energy of 4.2 keV [124]. The CERN Axion Solar Telescope (CAST) searches for these axions with a detector that exploits the reverse Primakoff effect whereby a strong transverse 9.0 T magnetic field converts the solar axions back into x-rays of the same energy as the parent axion. Their first run has set a 95% CL for the axion mass at $m \leq 2 \times 10^{-2}$ eV [125].

The PVLAS experiment fires polarized light through a long vacuum region with a 5.5 T magnetic field and searches for anomalous rotations of polarization [126]. According to the theory, the vacuum becomes birefringent – photons with polarization aligned with the magnetic field are delayed as they are preferentially transformed into axions which travel slower than the speed of light. The PVLAS collaboration initially claimed detection of an irregular rotation corresponding an axion mass of 1–1.5 meV, but retracted their results upon obtaining a null result after upgrades [127]. Note that detection of axions in CAST and PVLAS does not give the axion background density.

Weakly Interacting Massive Particles

Another cold, stable, non-baryonic dark matter candidate is the weakly interacting massive particle (WIMP) which participates in only weak and gravitational interactions and has a mass of at least several tens of GeV (otherwise they would have already been observed in colliders). No known particle has these characteristics. Supersymmetry predicts the
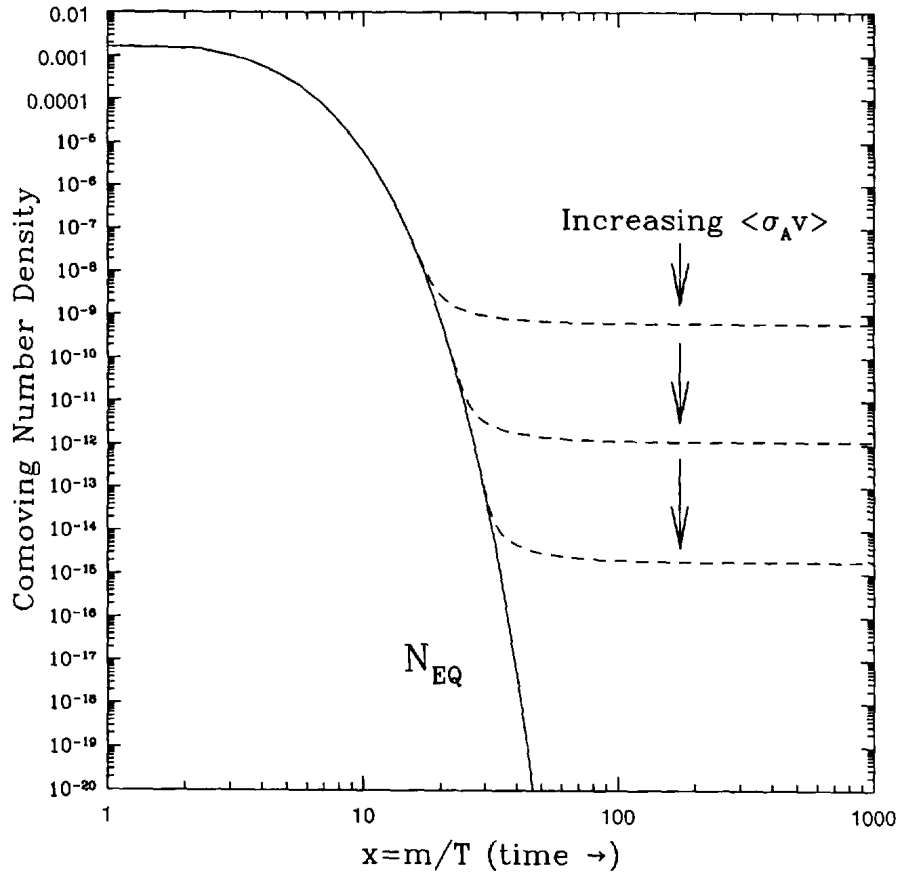
Figure 1.5: Comoving WIMP density as a function of time. The equilibrium density (solid line) and actual abundances (dashed lines) for various annihilation rates are shown. Figure taken from [5].

existence of WIMP-like particles [5]. In this framework, every standard particle has a corresponding "superpartner", with all quantum numbers being identical except for spin which differs by 1/2. The supersymmetric partners of the Z-boson, photon and neutral Higgs have the same quantum numbers and thus can mix to form the "neutralinos." In many models, the lightest of the four neutralinos is the lightest supersymmetric particle (LSP), and if R-parity is conserved, this particle is a possible stable relic of the Big Bang. Its mass is not well constrained. Theorists favor a mass ranging from several GeVs to a few hundred TeVs. The LEP accelerator has set a $\sim$40 GeV lower limit [121]. To preserve unitarity, an upper limit of 3.2 TeV has been suggested [128].

If the WIMP (which we refer to as χ) exists and is stable, a cosmological relic of WIMPs could have been produced during the Big Bang [129, 130]. At $T > M_\chi$, the χ's would have existed in thermal equilibrium, decaying to lighter particles and vice versa. After $T < M_\chi$, the χ's annihilate ($\chi\bar{\chi} \to l\bar{l}$, assuming that χ is a Majorana particle) and drop rapidly in abundance. When the annihilation rate drops below expansion, the population "freezes out," leaving behind the present population. This idea has been used to constrain the mass of the heavy neutrino [131].

The relic abundance can be approximated by assuming an energy independent WIMP-annihilation cross section. This calculation and a more rigorous one are described in [5]. The number density of χ at thermal equilibrium is

$$n_\chi^{eq} = \frac{g}{(2\pi)^3} \int f(\mathbf{p}) \, d^3\mathbf{p}, \qquad (1.3)$$

where g is the number of internal degrees of freedom of the particle and $f(\mathbf{p})$ is the Fermi-Dirac or Bose-Einstein distribution. At $T \gg m_\chi$, $n_\chi^{eq} \propto T^3$ while at $T \ll m_\chi$, $n_\chi^{eq} \approx g(m_\chi T/2\pi)^{3/2} \exp(-m_\chi/T)$ – the WIMP abundance drops exponentially at a rate of $\Gamma \langle \sigma_A v \rangle n_\chi$ where $\langle \sigma_A v \rangle$ is the thermally averaged total annihilation cross section multiplied by the relative velocity. Freeze-out occurs when $\Gamma < H$, where H is the Hubble constant. At this point the density of WIMPs is too low in density for annihilation to continue. The Boltzmann equation describing the evolution of the WIMP density is

$$\frac{dn_\chi}{dt} + 3Hn_\chi = -\langle \sigma_A v \rangle \left[(n_\chi)^2 - (n_\chi^{eq})^2 \right]. \qquad (1.4)$$

The second term on the left hand side represents the effects of expansion. The first and second terms account for the annihilation and creation of WIMPs, respectively. This equation applies for Dirac and Majorana particles. The Hubble expansion term is negligible at earlier times (and the density follows the thermal equilibrium abundance) and dominates at later times. The freeze out temperature is provided by $\Gamma(T_f) = H(T_f)$ which gives $T_f \approx m_\chi/20$. The Hubble expansion rate falls with temperature as $H(T) = 1.66 g_*^{1/2} T^2/m_{Pl}$ where $m_{Pl} = 1.22 \times 10^{19}$ GeV and g_* is roughly equal to the number of bosonic relativistic degrees of freedom plus 7/8 times the number of fermionic relativistic degrees of freedom.

The χ mass density as a fraction of the critical density, Ω_χ, can be calculated as a function of the annihilation rate. Note that the entropy per unit comoving volume $s = 0.4g_*T^3$ is constant and thus n_χ/s is constant as well. This gives

$$
\begin{aligned}
(n_\chi/s)_0 &= (n_\chi/s)_f \tag{1.5} \\
&= \frac{H(T_f)}{\langle\sigma_A v\rangle s(T_f)} \tag{1.6} \\
&= \frac{1.66}{0.4}\frac{1}{g_*^{1/2}T_f m_{Pl}\langle\sigma_A v\rangle} \tag{1.7} \\
&\approx 100\frac{1}{g_*^{1/2}m_\chi m_{Pl}\langle\sigma_A v\rangle}, \tag{1.8}
\end{aligned}
$$

where the subscripts 0 and f denote values for today and at freeze-out, respectively. The entropy density today is $s_0 \approx 4000$ cm^{-3} and the critical density is $\rho_c \approx 10^{-5}\,h^2$ GeV cm^{-3}. The mass density of WIMPs is

$$
\begin{aligned}
\Omega_\chi h^2 &= \frac{m_\chi n_\chi}{\rho_c} \tag{1.9} \\
&\approx 3\times10^{-27}\frac{\text{cm}^3\,\text{s}^{-1}}{\langle\sigma_A v\rangle}, \tag{1.10}
\end{aligned}
$$

which is independent of m_χ. As expected, the mass density is inversely proportional to the annihilation cross section. Figure 1.5 shows the equilibrium density and comoving abundances as a function of inverse temperature for various annihilation cross sections.

We have derived the relic density that a stable particle should have if it exists. The annihilation cross section of a new particle interacting at the weak scale can be estimated as $\langle\sigma_A v\rangle \sim \alpha^2(100\text{ GeV})^{-2} \sim 10^{-25}$ cm^3 s^{-2} where $\alpha \sim 10^{-2}$. This value is close to that projected by cosmological arguments which strongly suggests that if a stable particle associated with the electro-weak scale interactions exists then it is likely to be *the* dark matter particle. This coincidence has provided strong motivation for finding WIMPs. The rich and diverse community of experimental searches is described in the next chapter.

1.3.3 Modified Gravity

Modified Newtonian dynamics (MOND) was first proposed by Mordehai Milgrom in 1981 as an explanation to the galaxy rotation problem [132]. Milgrom proposed a modification

of Newton's second law of motion: at very small accelerations ($a < 1.2 \times 10^{-10}$ m s^{-2}), the gravitation force is proportional to a^2 and not a and thus the velocity falls off with r^{-1} instead of r^{-2}. This gives a flat velocity curve far from the center. However, it has been shown that 80% of the mass in galaxy clusters is unaccounted for in a MOND framework [133] and as previously stated, observations of satellites orbiting about isolated galaxies from SDSS give a halo profile that contradicts that predicted by MOND [84]. Also, MOND is not a relativistic formulation of gravity so gravitational waves, gravitational lensing, cosmological expansion and other standard phenomena derived from general relativity are notably absent. In response to these deficiencies, Bekenstein proposed a relativistic theory called Tensor-Vector-Scalar (TeVeS) that reduces to MOND in the Newtonian regime [134]. This theory also appears to produce gravitational lensing. Improved measurements of the third acoustic peak of the CMB anisotropies places severe restrictions on these theories [135] in strong favor of the cold dark matter model. Also, these theories do not offer an adequate explanation for the gravitational lensing observations of colliding galaxy clusters where the dark matter separates from the normal matter. The hot gases of the two clusters interact electromagnetically and slow down while the stars and dark matter passed through. Two such examples are the Bullet cluster (1E 0657-56) [136] and the MACS J0025.4-1222 [137].

Chapter 2

Dark Matter Searches

2.1 Introduction

The great importance of detecting WIMPs has given birth to many experimental searches. Thus far, no uncontested experimental evidence for WIMPs has emerged. These experiments can be divided into three categories: indirect detection, direct detection and high energy collider searches. This chapter gives an overview of the searches.

2.2 Indirect Detection Experiments

Indirect detection experiments search for the decay products of WIMP-pair annihilations. Since a pair annihilation requires two WIMP particles, the rate scales with n^2 and thus it is best to examine potential wells such as the Earth and Sun, where they can accumulate through inelastic collisions. Since WIMPs are slow moving, they decay into products with an energy of M_χ and if they are massive enough, they may annihilate into gauge bosons and charged Higgs. We can not directly observe these particles but we can potentially detect their decay products. For the decay products to be observable, they must be stable and be distinguishable from background. Four candidates meet these requirements: gamma rays, neutrinos, anti-protons and positrons.

2.2.1 Gamma Ray Experiments

WIMP annihilations generate gamma rays via $\chi\chi \to \gamma\gamma$ and $\chi\chi \to \gamma Z$ with energies of M_χ and $M_\chi(1 - M_Z^2/4M_\chi^2)$, respectively and since the WIMPs are slow moving, these gammas are mono-energetic. As WIMPs, by definition, do not couple directly to photons, the Feynman diagrams for these two annihilation channels include loops (see Figure 2.1) and thus are suppressed. In general, the photon flux from WIMP annihilation is

$$\phi(E, \Delta\Omega) \sim \frac{\sigma v}{M_\chi^2} \times \int_{l.o.s} \int_{\Delta\Omega} \rho^2(s)\, ds\, d\Omega \qquad (2.1)$$

where σ is the WIMP annihilation cross section, v is the relative speed of two interacting WIMPs in the center of mass frame, ρ is the mass density, and M_χ is the mass of the WIMP. The integral expression integrates the WIMP density over the line of sight and solid angle. The density of the dark halo generally takes the form of

$$\rho(r) = \frac{\rho_c}{(r/a)^\gamma (1 + (r/a)^\alpha)^{(\beta-\gamma)/\alpha}}, \qquad (2.2)$$

where r is the distance from the center of the galaxy, a is a model dependent radius of the galactic core, and ρ_c is a constant that normalizes the dark matter density to that of the local density (0.3–0.5 GeV cm^{-3}) [138]. The parameters, α, β, and γ depend on the model and have ranges of 1–2, 2–3 and 0–1.5, respectively [138]. The optimal source is nearby, has a large concentration of WIMPs, and has a low background. The galactic center has an enhancement due to the higher density of WIMPs but also has a larger background. The galactic halo, on the other hand, has a lower background but also has a lower signal due to the lower WIMP density.

Space telescopes allow for the direct detection of these high energy gamma rays. These detectors typically consist of an anti-coincidence shield, a layer of high-Z material, a spark chamber or silicon particle tracker, and a NaI or CsI scintillation calorimeter (see Figure 2.2). Gammas are detected by watching for pair conversions to electrons and positions. Reconstructing the energies and tracks of the charged particles gives the gamma energy and direction. The anti-coincidence shield for removing charged particle background is
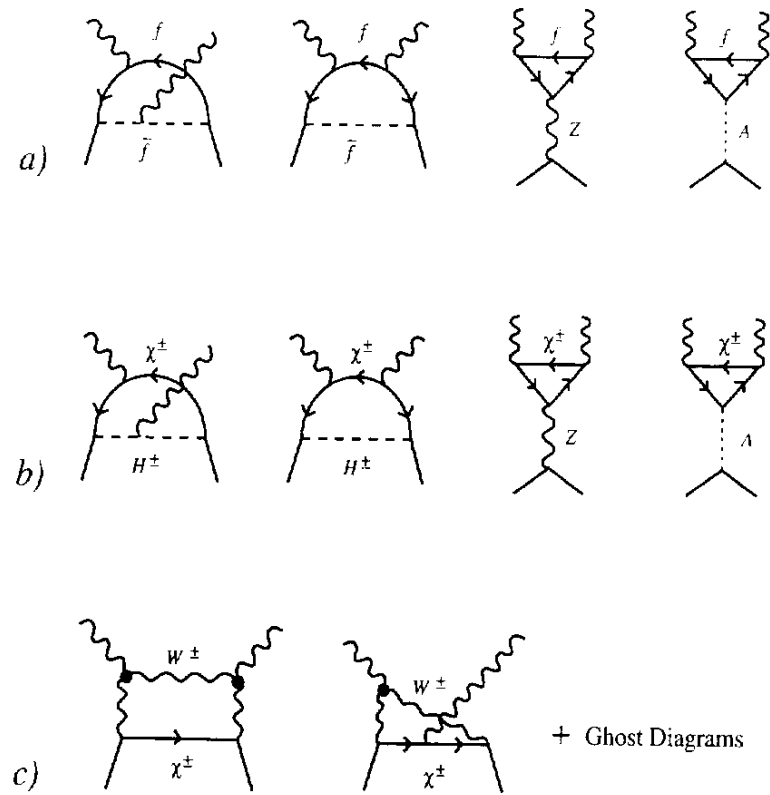
Figure 2.1: Feynman diagram of neutralino annihilations into photons: (a) fermion-sfermion loops, (b) charged Higgs-chargino loops, and (c) chargino-W-boson loops. This diagram is from [5].

charged-particle
anticoincidence
shield

γ ray

pair-
conversion
foils

particle-
tracking
detectors

e+   e-

calorimeter
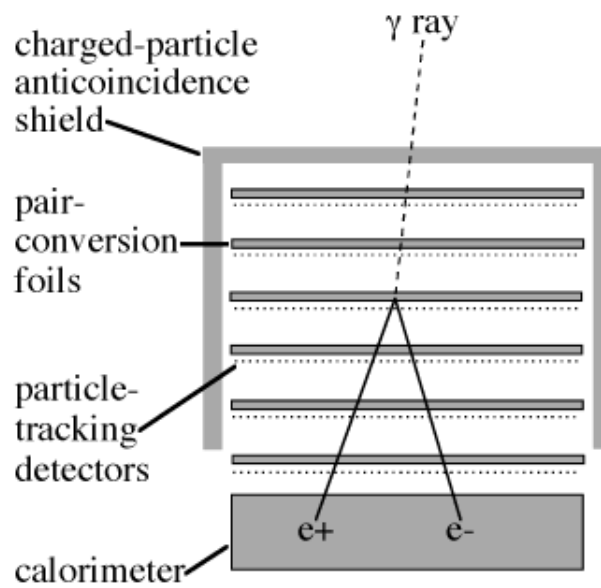
Figure 2.2: Diagram of the gamma-ray telescope measurement technique used in EGRET and LAT. The gammas convert into an electron and positron in the tungsten strips. Their positions are sensed by the strip detector and their energies are measured by an NaI or CsI calorimeter. Surrounding the detector is a high efficiency anti-coincidence shield. This diagram is from [6].

usually a scintillator coated dome surrounding the rest of the detector. This background has an intensity that is $\sim 10^5$ greater than that of the gamma-rays. An overview of the potential of observing these gamma rays for dark matter can be found in [139].

The Energetic Gamma-Ray Experiment Telescope (EGRET) was one of four gamma ray detectors on the Compton Gamma Ray Observatory (CGRO), which ran from 1991 to 2000. This detector had a 0.5 sr field of view, an energy range from 20 MeV to 30 GeV and an energy resolution of 10%. EGRET measured the diffuse emission from the Galactic plane discovering that at energies above ~ 1 GeV, the flux was $\sim 60\%$ higher than the predicted value [140], an excess which suggests the presence of WIMP annihilation [141, 142]. From the spectral shape of the excess gamma-rays, the WIMP mass is estimated to be between 50 and 100 GeV. Others have claimed that the dark matter interpretation is ruled out by anti-proton fluxes [143] and that this observation is due an inaccurate estimation of the sensitivity at around 1 GeV [144]. This issue may be resolved with the Large Area Telescope (LAT) aboard the Gamma-ray Large Area Space Telescope (GLAST) [145], which was launched into orbit in June 2008. GLAST will observe a larger energy range (20 MeV to 300 GeV), greater field of view (20% of the sky), and larger collection area (8000 cm^2 versus EGRET's 1500 cm^2) with a resolution of several arcminutes for the highest energy photons and about 3 degrees for 100 MeV gammas. The large energy range will provide some overlap with ground based detectors.

While restrictions on the size and flux will always limit the maximum energy that space telescopes can observe, ground-based experiments do not have such limitations. These experiments have been observing the night sky for Cerenkov light emitted by gamma rays interacting with the upper atmosphere. These bursts of light have a duration of 3–4 ns and a wavelength of 300–400 nm, and typically cover an area of land with a radius on the order of 100 m. These detectors, called Imaging Atmospheric Cerenkov Telescopes (IACTs), have an energy range of 100 GeV to several TeVs and usually examine a region at ~ 10 km high where the showers reaches their maximum intensity. The telescopes typically consist of a large number of mirrors pointing toward a camera consisting of many PMTs.
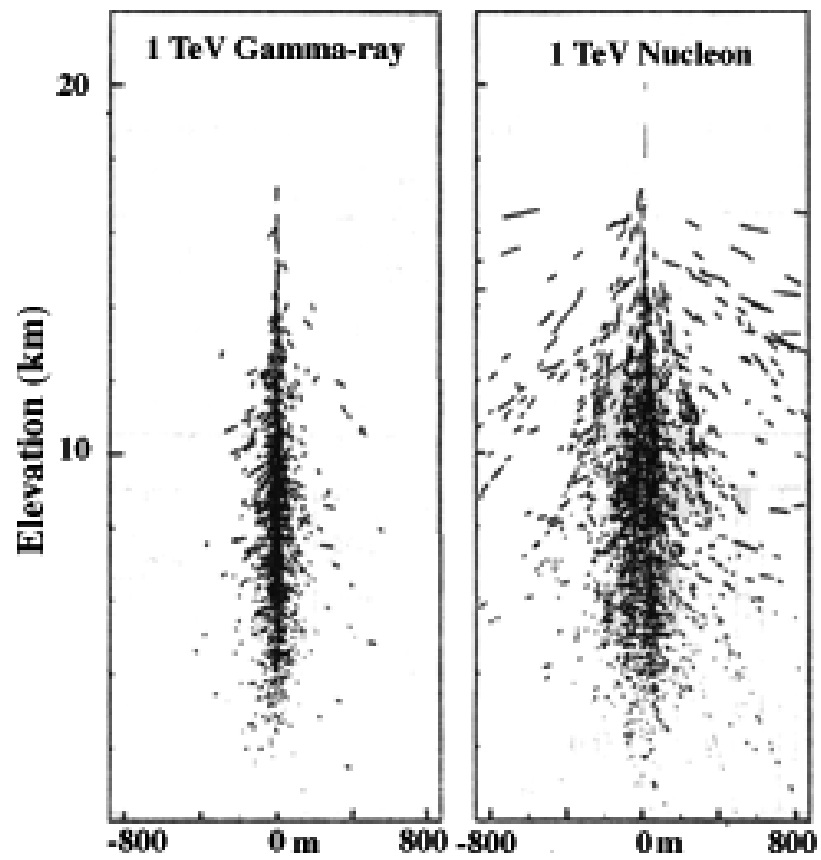
Figure 2.3: Comparison between gamma (left) and cosmic ray (right) induced showers, the latter of which tends to be broader, less smooth and occur closer to the surface of the earth.
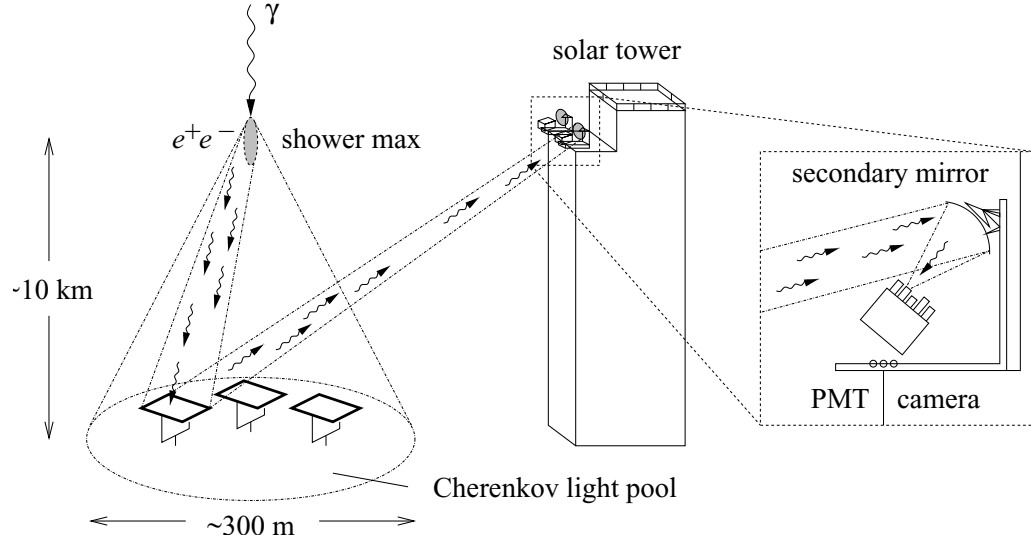
Figure 2.4: Schematic of how CELESTE and STACEE employ the mirrors of former solar power plants to collect Cerenkov light.

Distinguishing smoother, more symmetric gamma-ray showers from boarder, more uneven hadronic showers is crucial to increasing sensitivity as the rate of $\sim$1 TeV gammas is so low. Figure 2.3 compares the two different types of showers. This technique was pioneered by the Whipple 10m telescope [146, 147]. HEGRA, located at the Canary Island of La Palma, was the first to use multiple telescopes for stereoscopic shower reconstruction, which provides better energy resolution and discrimination of background [148]. Some currently running experiments including VERITAS [149], CANGAROO [150], MAGIC [151, 152], and HESS [153] have measured nearby dark matter dominated sources such as the spheroidal galaxy DARCO and set flux upper limits. These experiments have not yet reached the sensitivity to exclude dark matter but have placed limits on enhancement factors.

Two experiments, CELESTE and STACEE, employ heliostats (tracking mirrors) of defunct solar power plants to collect Cerenkov light. The CELESTE experiment uses a former solar power plant in the French Pyrenees [154]. The 53 mirrors, which have a total surface area of $\sim$2900 m^2, reflect light to a single PMT in the collection tower. From 2001 to 2003, CELESTE observed the Andromeda Galaxy (M31), which is the nearest and largest galaxy (10^{12} M$_\odot$) in the Local Group. The experiment had a sensitivity that was one or

two orders of magnitude too low for observing the predicted flux. Gamma detection of spiral galaxies such as M31 are difficult to interpret in terms of dark matter annihilations because of the presence of non-thermal processes, cosmic ray acceleration, and other poorly understood physical mechanisms. Bad weather prevented CELESTE from observing the Draco spheroidal galaxy, which is a better source as it is nearby and dominated by dark matter. This source was observed by the STACEE experiment which used the mirrors of the National Solar Thermal Test Facility (NSTTF) in Albuquerque, New Mexico [155, 156]. No excess in the gamma-ray signal was observed from Draco.

The Milagro experiment uses a large 5000 m^2 pool of water as a target for gamma ray induced showers. PMTs in the water detect the Cerenkov light emitted by the secondaries of the air shower. Milagro has a wide view but a low efficiency for background rejection. This detector has observed the sun for neutralino annihilations, finding no statistically significant signal [157].

2.2.2 Neutrino Experiments

WIMP annihilations can release neutrinos. Since neutrinos interact so rarely with normal matter, very massive natural structures such as the ocean and polar ice caps are needed. Muon neutrinos interact with target via W-boson exchange generating muons, which generates Cerenkov light. Electron neutrinos are not seen because resulting electrons are quickly absorbed before reaching detectors. Tau neutrinos are not detected because the tau generation is suppressed by its high mass. The neutrino interaction cross section is proportional to E_ν and the range of the muon is proportional to E_μ so there is an E_ν^2 enhancement, thus favoring detectors with high energy ranges. A continuous spectrum (rather than a line) is expected as neutrinos are produced not only through $\chi\chi \to \nu\bar{\nu}$ but also via $\chi\chi \to f\bar{f}$, where f may decay into a neutrino or hadronize and decay into a neutrino if it is a quark. Neutrinos from the sun can also have their energy shifted as they escape. These detectors must also be able to reject atmospheric neutrinos which have a flux that is 10^6 greater than that of the upward muons.

Some experiments which have searched for these neutrinos include Baksan [158], Super-Kamiokande [67], MACRO [159], and AMANDA [160]. None of these experiments have observed excess neutrinos but they have set flux upper limits. Larger experiments are being constructed. The ANTARES detector consists of 900 downward facing PMTs attached onto 12 strings at a depth of about 2500 m in the waters of the French Mediterranean coast near Toulon [161]. Light scatters less in water than in ice but has more background light from sources such as bioluminescent organisms and radioactive salts. The successor to the AMANDA detector is IceCube, which is similar to ANTARES but uses the ice of the South Pole [162]. When completed, IceCube will be the largest neutrino detector with 4800 PMTs covering a fiducial volume of 1 km^3. The PMTs are suspended in the fiducial volume by 1.5 mile long strings. IceCube views events arriving from below which filters out the otherwise overwhelming muon rate. Due to the low angle of the sun at the South Pole, the ability to separate solar neutrinos from background is weak. The IceCube experiment is likely to exclude portions of supersymmetric space that have yet to be omitted by direct searches.

There may also be an amplification of WIMP annihilations in the Galactic center which can be observed as an enhancement in the neutrino flux as shown by Gondolo and Silk [7]. Dark matter halos are expected to have a steep central cusp with a density profile following $\rho \propto r^{-\gamma}$. Semi-analytical calculations find $\gamma \sim$ 1–2 and simulations give $\gamma = 0.3$–1.5. The presence of a large black hole of mass $\sim 2 \times 10^6 M_\odot$ at the galactic center would lead to a large "spike" in the annihilation products in the surrounding region. The evidence for the existence of such a super massive black hole is overwhelming with observations of nearby objects and gives a density profile, $\rho \propto r^{-\gamma}$, with $\gamma \geq 3/2$. Observation of the annihilation products in this spike can help us determine the type of halo core, as a central cusp would result in a magnification in annihilation. Observations favor a softened core density which lead to only a small enhancement in annihilation rates. If the halo has a central cusp, as expected from simulations, the enhancement can be five orders of magnitude or more. An upper limit to the muon flux can impose an upper bound on γ or indicate that the neutralinos are not the dark matter particle annihilating there. Future experiments in the Northern
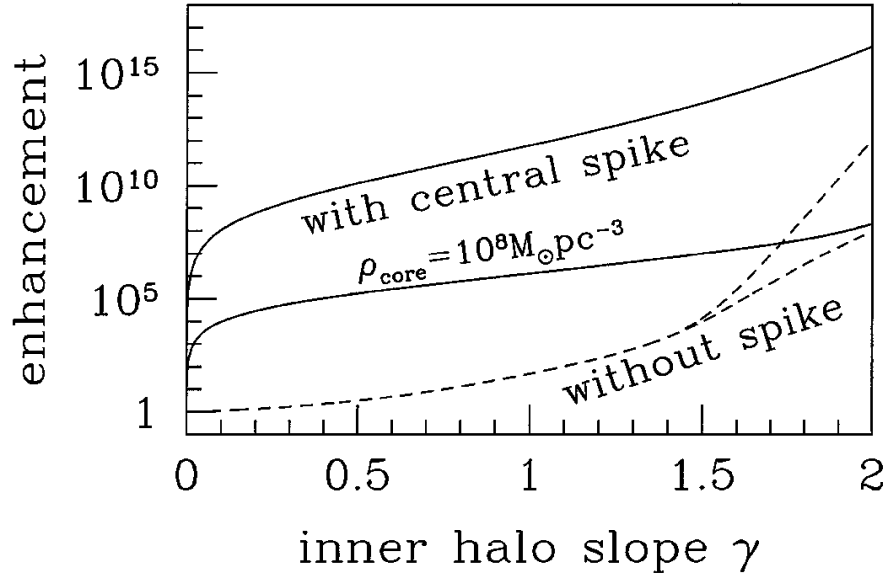
Figure 2.5: Enhancement in WIMP annihilations in the Galactic center versus γ for different types of cores [7].

Hemisphere, which can see upward moving neutrinos from galactic center, will improve the bound. Figure 2.5 is a plot of the enhancement as a function of γ. Figure 2.6 shows the expected flux of neutrino-induced muons from the galactic center with and without the black hole. Future flux limits will further exclude portions of the supersymmetric space. Others claim that the spike is not present or is severely weakened when additional important processes are included which have been neglected in the study by Gondolo and Silk [163].

2.2.3 Cosmic Anti-Matter Experiments

Normal matter from WIMP decays are not seen given the large background of cosmic ray protons and electrons. However, their antimatter decay products may be observable because of the lower anti-matter background. For kinematic reasons, the background flux of low energy antiprotons is suppressed. The idea of searching for excess antiprotons in cosmic rays as a sign of dark matter was first proposed in the 1980s [164, 165]. The background of secondary antiprotons from cosmic ray spallation of the interstellar medium has an energy spectrum that peaks at $\sim$2 GeV (see Figure 2.7). WIMP annihilations should provide a
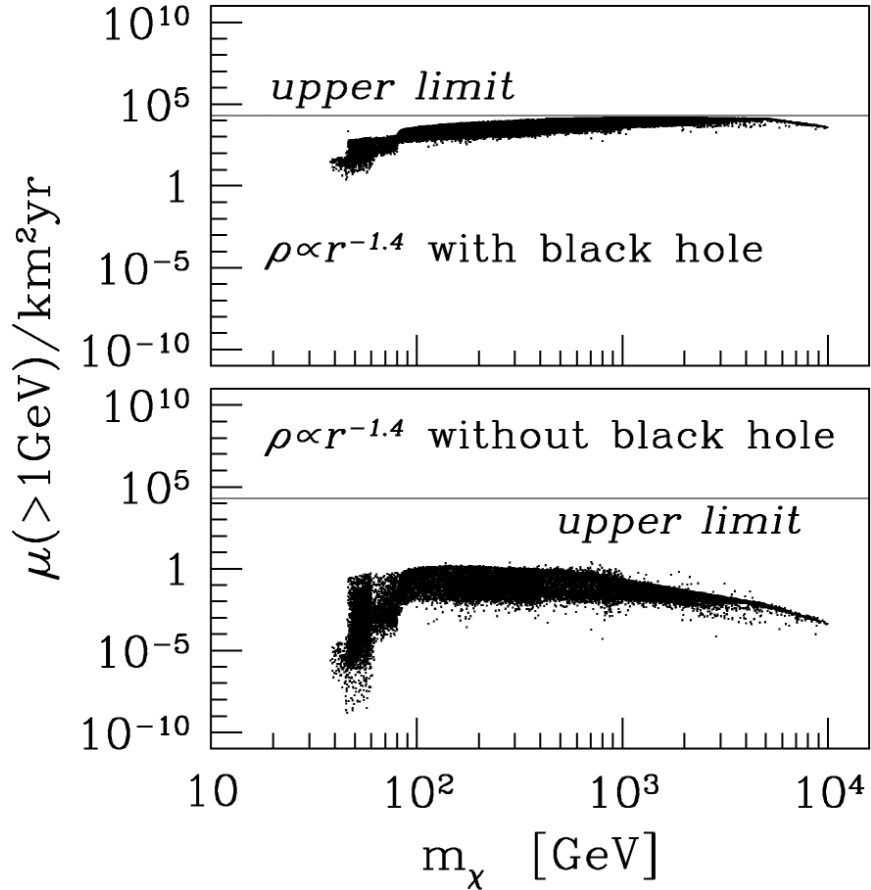
Figure 2.6: Expected flux (dots) of neutrino induced muons in a neutrino telescope from neutralino annihilations with and without a central black hole [7]. The current upper limit is indicated by the horizontal line.

continuum of antiprotons below 1 GeV. Measurement of antiprotons require satellite or balloon-borne experiments. One such experiment is the Balloon-borne Experiment with a Superconducting Spectrometer (BESS) which measured the antiproton spectrum with a drift chamber in a 1 T magnetic field and scintillation counter. This was the first experiment to establish the generic 2 GeV peak. Since the spectrum could be entirely attributed to cosmic ray spallation, the experiment provided no insight into WIMP annihilations. PAMELA (Payload for Antimatter Matter Exploration and Light-nuclei Astrophysics), a satellite-borne charged cosmic ray detector [166], has recent released preliminary results of anti-proton measurements which agree with BESS and other previous experiments [10].

Given the uncertainties in production and propagation of secondary antiprotons, it is uncertain whether these measurements will further constrain WIMP models [8].

In the 1990s, it was proposed that if the WIMPs are heavier than $W^\pm$ and Z^0 bosons and have a significant annihilation branch into $W^\pm$ and Z^0 pairs, then the branches ($W^+ \rightarrow e^+ + \nu_e$ and $Z_0 \rightarrow e^+ + e^-$ should provide a very distinct feature in the cosmic-ray position spectrum (as seen in Figure 2.8) [9]. These positrons have an energy of roughly half of the neutralino mass. The predicted peaks may be washed out by boosting in the case of $m_\chi \gg m_{W,Z}$ or by energy loss as the positrons travel across the galaxy. The gauge bosons also decay into quarks and pions, which consequently decay to produce positrons. These positrons form another peak at $M_\chi/20$.

PAMELA has recently published preliminary results of its measurement of the cosmic ray positron fraction up to 100 GeV [10]. This measurement contained much higher statistics and probed higher energies than any previous measurement. Figure 2.9 compares PAMELA's measurement with a calculation for secondary production of positrons during the propagation of cosmic ray nuclei. The observed rise may indicate annihilation of dark matter in the galactic halo or production of positrons by near-by pulsars [167].

Some indirect detection experiment may exclude portions of supersymmetric space not yet excluded by other experiments but unless astrophysical backgrounds are fully understood there will always be some uncertainty. In direct detection experiments, there is no ambiguity once backgrounds and other detector systematics are sufficiently suppressed or understood. However, even if dark matter is found first in direct detection experiments or colliders, these indirect detection experiments are still needed to probe the halo distribution.

2.3 Direct Detection Experiments

The race for direct detection of the WIMP began in the 1980s with the first experiments using conventional high purity germanium and silicon detectors at liquid nitrogen temperatures. In the next decade, NaI scintillation detectors gained favor as they have some background discrimination capabilities based on the scintillation pulse shape. DAMA is the
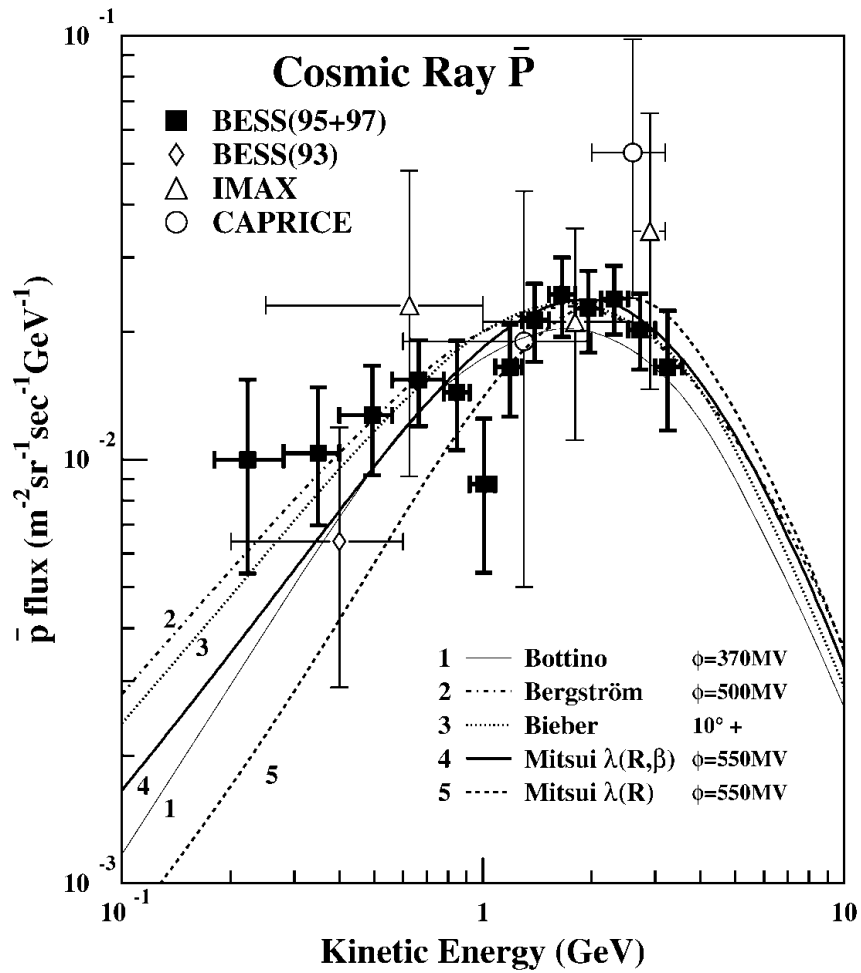
Figure 2.7: Antiproton measurements by BESS and other experiments. The curves represent recent calculations of the secondary antiproton spectra for the solar minimum period [8].
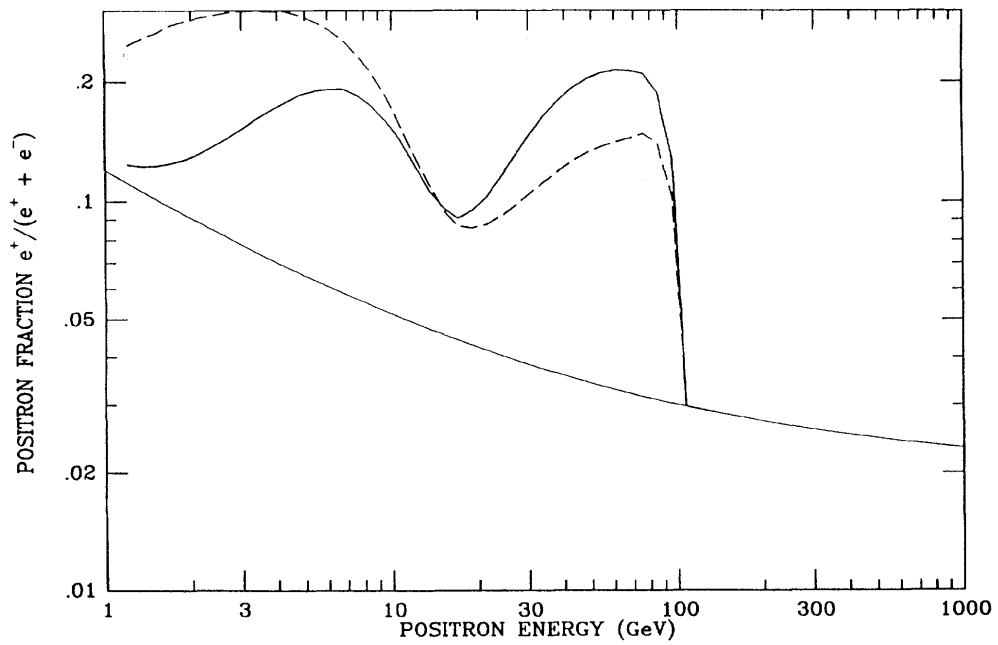
Figure 2.8: Differential positron flux divided by sum of differential electron and positron fluxes for 120 GeV neutralinos. The solid curve represents a model with constant positron confinement time. The dashed line presents the model with a positron confinement time that decreases with energy [9].
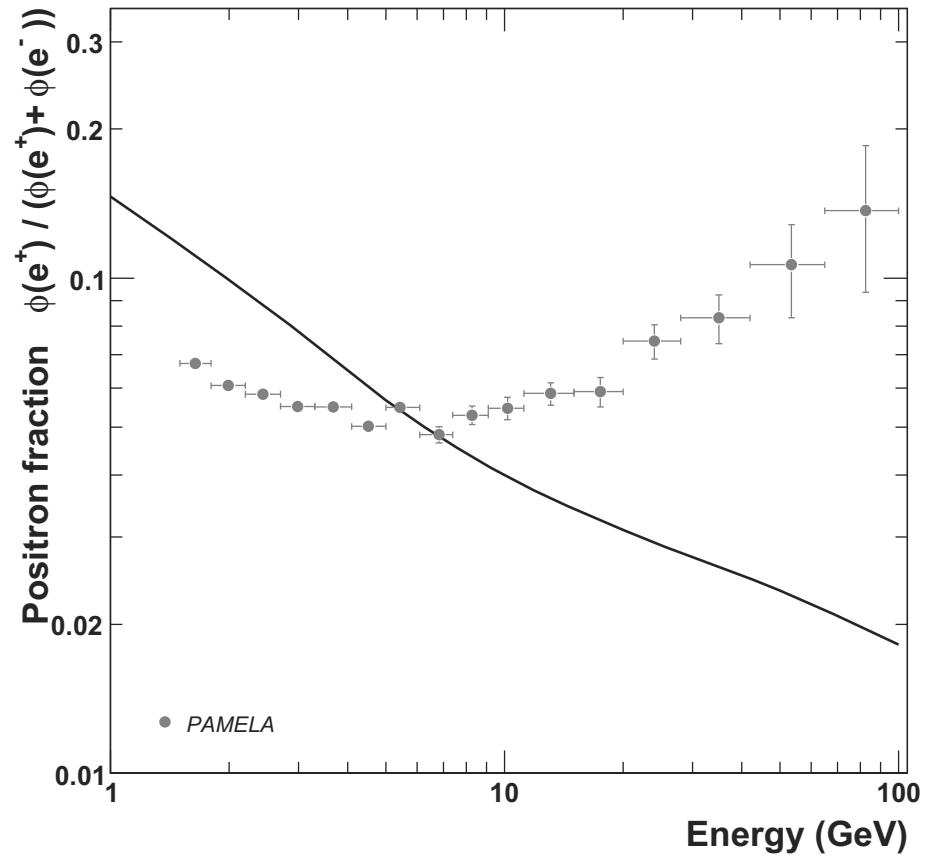
Figure 2.9: Positron fraction as measured by PAMELA and theoretical prediction (black line) for pure secondary production of positrons during the production of cosmic-rays in the galaxy. Plot taken from [10].

PHONONS

CUORE, CREST I

CRESST
ROSEBUD

CDMS,
EDELWEISS

SCINTILLATION

CLEAN, DAMA, DEAP,
NAIAD, XMASS, ZEPLIN I

XENON, ZEPLIN II,
LUX, WARP, ArDM

IONIZATION

ANAIS, COSME,
DRIFT
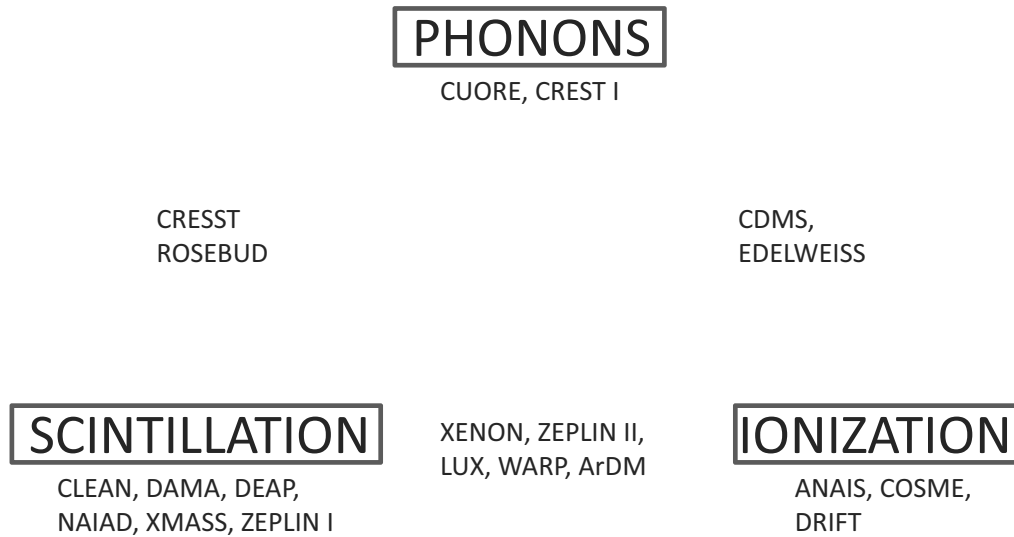
Figure 2.10: Chart of direct detection searches categorized by measurement technique.

only group to have claimed detection of the WIMP. They have observed an annual modulation using their 100 kg NaI detector [168]. However, many other experiments have since contradicted these results. Also seen in the 1990s was the rise of sub-kelvin superconducting semiconductor detectors which have excellent event-by-event discrimination through direct measurement of phonons and ionization. By the mid-2000s, the same principle was demonstrated in two-phase xenon and argon detectors, which have gained attention because of their scalability. Also being developed are single-phase liquid neon and liquid argon detectors with very powerful pulse shape discrimination. A comprehensive list of direct detection experiments can be found in [169]. Figure 2.10 is a chart of the direct detection searches categorized by measurement technique. In this section, we first give an overview of the signal generation in such detectors and then provide a brief overview of past and current experiments.

2.3.1 Physics of Direct Detection

Here, we give a brief summary of the calculation of the WIMP signal in direct detection experiments. A more complete overview can be found in [170].

Interaction Rate

The WIMP-nucleon cross section upper limit is calculated by comparing the observed rate upper limit to that expected from the theoretical calculations. The expected differential event rate can be written as

$$\frac{dR}{dE} = R_0 \, S(E) \, F^2(E) \, I, \tag{2.3}$$

where R_0 is the total event rate; $S(E)$ is the spectral function that includes the effects of orbital velocity of the earth, detection efficiency for nuclear recoils, and instrumental limitations; F is the form factor correction; and I is the factor related to the type of spin interaction. The rest of this section is describes these terms.

The differential dark matter particle density is

$$dn = \frac{n_0}{k} \, f(\mathbf{v}, \mathbf{v}_E) \, d^3\mathbf{v}, \tag{2.4}$$

where k is a normalization constant, n_0 is the mean dark matter density, $\mathbf{v}$ is the velocity of the dark matter particle onto the target, and $\mathbf{v}_E$ is the velocity of the earth relative to the dark matter halo. The normalization constant, k, is defined as

$$k = \int_0^{2\pi} d\phi \int_{-1}^{+1} d(\cos\theta) \int_0^{v_{esc}} f(\mathbf{v}, \mathbf{v}_E) \, v^2 \, dv, \tag{2.5}$$

where v_{esc} is the escape velocity of the WIMP in the halo. The dark matter velocity distribution is usually taken to be Maxwellian:

$$f(\mathbf{v}, \mathbf{v}_E) = \exp\left(-\frac{(\mathbf{v} - \mathbf{v}_E)^2}{v_0^2}\right). \tag{2.6}$$

For $v_{esc} = \infty$, $k = k_0 = (\pi \, v_0^2)^{3/2}$ and with a truncation at $|\mathbf{v} + \mathbf{v}_E| = v_{esc}$,

$$k = k_1 = k_0 \left[\text{erf}\left(\frac{v_{esc}}{v_0}\right) - \frac{2}{\sqrt{\pi}} \frac{v_{esc}}{v_0} e^{-v_{esc}^2/v_0^2}\right]. \tag{2.7}$$

The event rate per unit mass of WIMPs traveling with velocity v onto a target of atomic mass A and nucleus cross section of σ is

$$dR = \frac{N_0}{A} \, \sigma \, v \, dn, \tag{2.8}$$

where N_0 is the Avogadro's number (6.022×10^{23}) and dn is the differential particle density defined in Equation 2.4. The total event rate is

$$R = \frac{N_0}{A} \sigma_0 \int v \, dn \equiv \frac{N_0}{A} \sigma_0 \, n_0 \, \langle v \rangle, \tag{2.9}$$

where σ_0 is the zero-momentum cross section. The total event rate per unit mass for $\mathbf{v}_E = 0$ and $v_{esc} = \infty$ is defined as

$$R_0 = \frac{2}{\sqrt{\pi}} \frac{N_0}{A} \frac{\rho_\chi}{M_\chi} \sigma_0 \, v_0, \tag{2.10}$$

where ρ_χ is the halo dark matter density for which we will use a nominal value of 0.3 GeV c^{-2} cm^{-3}. By substituting R_0 into Equation 2.9, we obtain

$$R = R_0 \frac{\sqrt{\pi}}{2} \frac{\langle v \rangle}{v_0} \tag{2.11}$$

$$= R_0 \frac{k_0}{k} \frac{1}{2\pi v_0^4} \int v f(\mathbf{v}, \mathbf{v}_E) d^3 v, \tag{2.12}$$

and define the differential form as

$$dR = R_0 \frac{k_0}{k} \frac{1}{2\pi v_0^4} v \, f(\mathbf{v}, \mathbf{v_E}) \, d^3 v. \tag{2.13}$$

R_0 can be written in units of kg^{-1} d^{-1} or "tru." With $\rho_\chi = 0.3$ GeV c^{-2} cm^{-3} and $v_0 = 230$ km s^{-2}, we obtain

$$R_0 = \frac{377}{M_\chi M_T} \left(\frac{\sigma_0}{1 \text{ pb}} \right) \left(\frac{\rho_\chi}{0.3 \text{ GeV } c^{-2} \text{ cm}^{-3}} \right) \left(\frac{v_0}{230 \text{ km s}^{-1}} \right), \tag{2.14}$$

where M_T and M_χ are in units of GeV c^{-2} and $M_T = 0.932 \, A$.

The recoil energy of the target nucleus hit by a dark matter particle of energy $E = \frac{1}{2} M_E v^2$ and scattering at an angle of θ is

$$E_R = E \, r \, (1 - \cos \theta)/2, \tag{2.15}$$

where $r = 4 M_\chi M_T / (M_\chi + M_T)^2$ Assuming isotropic scattering (the recoils are uniform in E_R between 0 and Er), we obtain

$$\frac{dR}{dE_R} = \int_{E_{min}}^{E_{max}} \frac{1}{Er} dR(E) \tag{2.16}$$

$$= \int_{v_{min}}^{v_{max}} \left(\frac{v_0}{v} \right)^2 dR(v), \tag{2.17}$$

where the E_{min} (E_{max}) is the smallest (largest) energy that can give the recoil energy E_R; $E_0 = \frac{1}{2} M_\chi v_0^2 = (v_0/v)^2 E$; and v_{min} (v_{max}) is the velocity corresponding to the energy E_{min} (E_{max}). Substituting in Equation 2.13, we obtain

$$\frac{dR}{dE_R} = \frac{R_0}{E_0 r} \frac{k_0}{k} \frac{1}{2\pi v_0^2} \int_{v_{min}}^{v_{max}} \frac{1}{v} f(\mathbf{v}, \mathbf{v_E}) d^3 v. \tag{2.18}$$

Integrating v from 0 to ∞ for $v_E = 0$ gives the unmodified nuclear recoil spectrum

$$\frac{dR(v_E = 0, \infty)}{dE_R} = \frac{R_0}{E_0 r} e^{-E_R/E_0 r}, \tag{2.19}$$

which shows that the dark matter recoil spectrum is a falling exponential. This explains the importance of having sensitivity at low energies. For other cases of v_E and v_{esc}, the differential recoil spectrums are

$$\frac{dR(0, v_{esc})}{dE_R} = \frac{k_0}{k_1} \frac{R_0}{E_0 r} \left(e^{-E_R/E_0 r} - e^{-v_{esc}^2/v_0^2} \right) \tag{2.20}$$

$$= \frac{k_0}{k_1} \left(\frac{dR(0, \infty)}{dE_R} - \frac{R_0}{E_0 r} e^{-v_{esc}^2/v_0^2} \right); \tag{2.21}$$

$$\frac{dR(v_E, \infty)}{dE_R} = \frac{R_0}{E_0 r} \frac{\sqrt{\pi}}{4} \frac{v_0}{v_E} \left[\text{erf}\left(\frac{v_{min} + v_E}{v_0} \right) - \text{erf}\left(\frac{v_{min} - v_E}{v_0} \right) \right]; \tag{2.22}$$

$$\frac{dR(v_E, v_{esc})}{dE_R} = \frac{k_0}{k_1} \left[\frac{dR(v_E, \infty)}{dE_R} - \frac{R_0}{E_0 r} e^{-v_{esc}^2/v_0^2} \right]. \tag{2.23}$$

The spectrum $dR(v_E, \infty)/dE_R$ can be approximated as

$$\frac{dR(v_E, \infty)}{dE_R} = c_1 \frac{R_0}{E_0 r} e^{-c_2 E_R/E_0 r}, \tag{2.24}$$

where c_1 and c_2 are fitting constants of order unity. The integral of Equation 2.24 gives the relation between the two constants. For most purposes, the average values of $c_1 = 0.751$ and $c_2 = 0.561$ can be used. The integrated rate of the recoil energy range between E_1 and E_2 is

$$R(E_1, E_2) = R_0 \frac{c_1}{c_2} \left[e^{-c_2 E_1/E_0 r} - e^{-c_2 E_2/E_0 r} \right]. \tag{2.25}$$

Form Factor Correction

At higher momentum transfers ($q = \sqrt{2 M_T E_R}$), the de Broglie wavelength (h/q) becomes comparable to the size of the nucleus and the cross section begins to drop. The nuclear
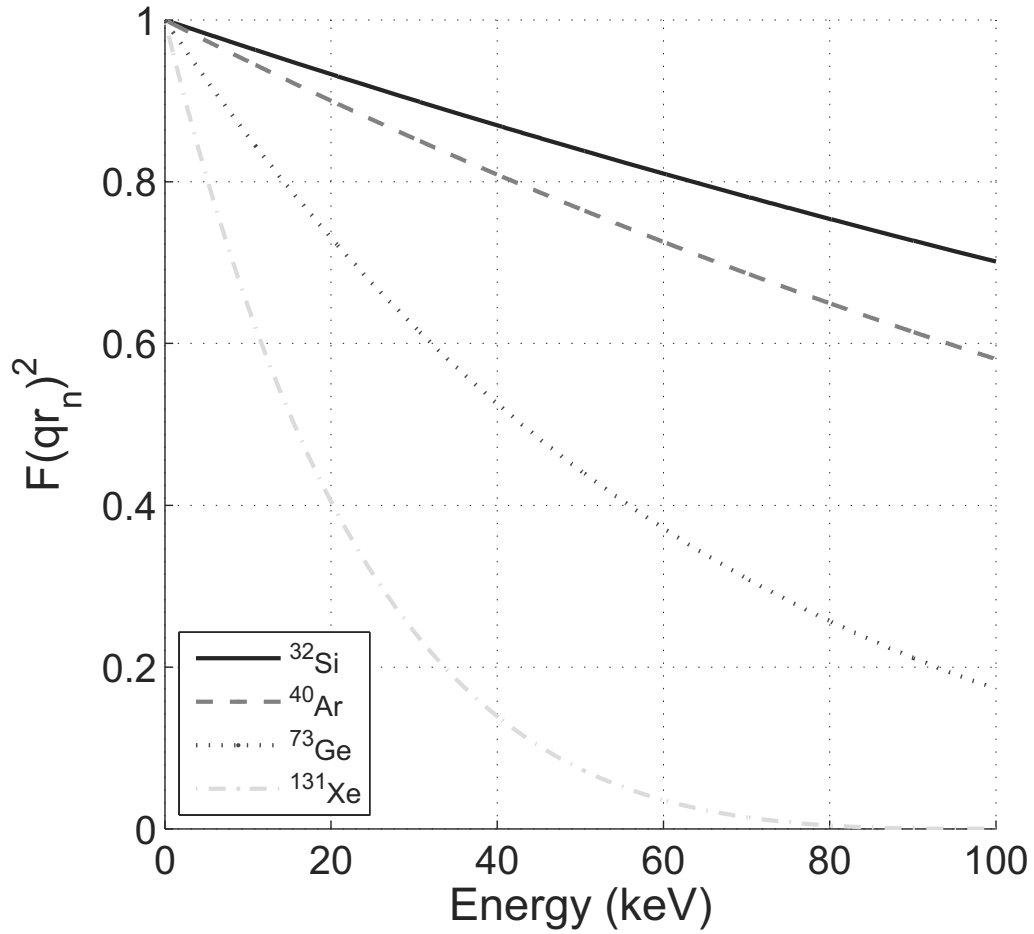
Figure 2.11: Spin-independent nuclear form factor versus recoil energy (Equation 2.33, $s = 1$, and $r_n = \sqrt{(5/3)(0.89A^{1/3} + 0.3)^2 - 5s^2}$) for various targets. The low form factor for xenon is the reason why xenon detectors must have a low energy threshold.

form factor correction, $F(q)$, is included to account for this effect. It is a function of the dimensionless quantity $qr_n/\hbar$, where r_n is the nuclear radius. With $M_T = 0.932\,A$, we have

$$q(\text{MeV}c^{-1}) = [2 \times 0.932(\text{GeV}c^{-2})A\,E_R(\text{keV})]^{1/2}, \tag{2.26}$$

and with $\hbar = 197.3$ MeV fm and $r_n = a_n A^{1/3} + b_n$, we obtain

$$qr_n(\text{dimensionless}) = 6.92 \times 10^{-3}A^{1/2}E_R^{1/2}(a_n A^{1/3} + b_n), \tag{2.27}$$

where E_R is in units of keV and a_n and b_n are in units of fm. The cross section can be separated into two parts as

$$\sigma(qr_n) = \sigma_0 F^2(qr_n), \tag{2.28}$$

where σ_0 is the zero-momentum cross section that contains information on the particular interaction, and F is the form factor containing the momentum transfer dependence. The form factor is, in the first Born approximation, the Fourier transform of the density of scatterer centers, ρ:

$$
\begin{aligned}
F(q) &= \int \rho(r) e^{i\mathbf{q}\cdot\mathbf{r}} d^3 r \tag{2.29} \\
&= \frac{4\pi}{q} \int_0^\infty r \sin(qr)\rho(r)dr. \tag{2.30}
\end{aligned}
$$

Assuming a thin shell density distribution gives

$$F(qr_n) = j_0(qr_n) = \frac{\sin(qr_n)}{qr_n}, \tag{2.31}$$

where j_0 is the spherical Bessel function of index 0. For a solid sphere,

$$F(qr_n) = \frac{3j_1(qr_n)}{qr_n} = 3\left(\frac{\sin(qr_n)}{(qr_n)^3} - \frac{\cos(qr_n)}{(qr_n)^2}\right). \tag{2.32}$$

For a more exact calculation of the form factor in the spin-independent case, we use a scatterer distribution that mirrors the charge distribution that is determined by electron and muon scattering. These distributions have a uniform distribution with a drop to zero over a "skin" thickness. One such distribution gives

$$F(qr_n) = 3\frac{j_1(qr_n)}{qr_n} e^{-(qs)^2/2} \tag{2.33}$$

where s is the skin thickness [171]. Figure 2.11 shows the spin-independent form factor (Equation 2.33) for various targets as a function of recoil energy.

In detailed calculations that include contributions from all nucleons, the form factor for the spin-dependent case has three parts representing the proton, neutron and interference terms or three terms representing the isoscalar $(p + n)$, isovector $(p - n)$ and interference terms. In the latter form, $F(qr_n)^2 = S(q)/S(0)$ where

$$S(q) = a_0^2 S_{00}(q) + a_1^2 S_{11}(q) + a_0 a_1 S_{01}(q), \tag{2.34}$$
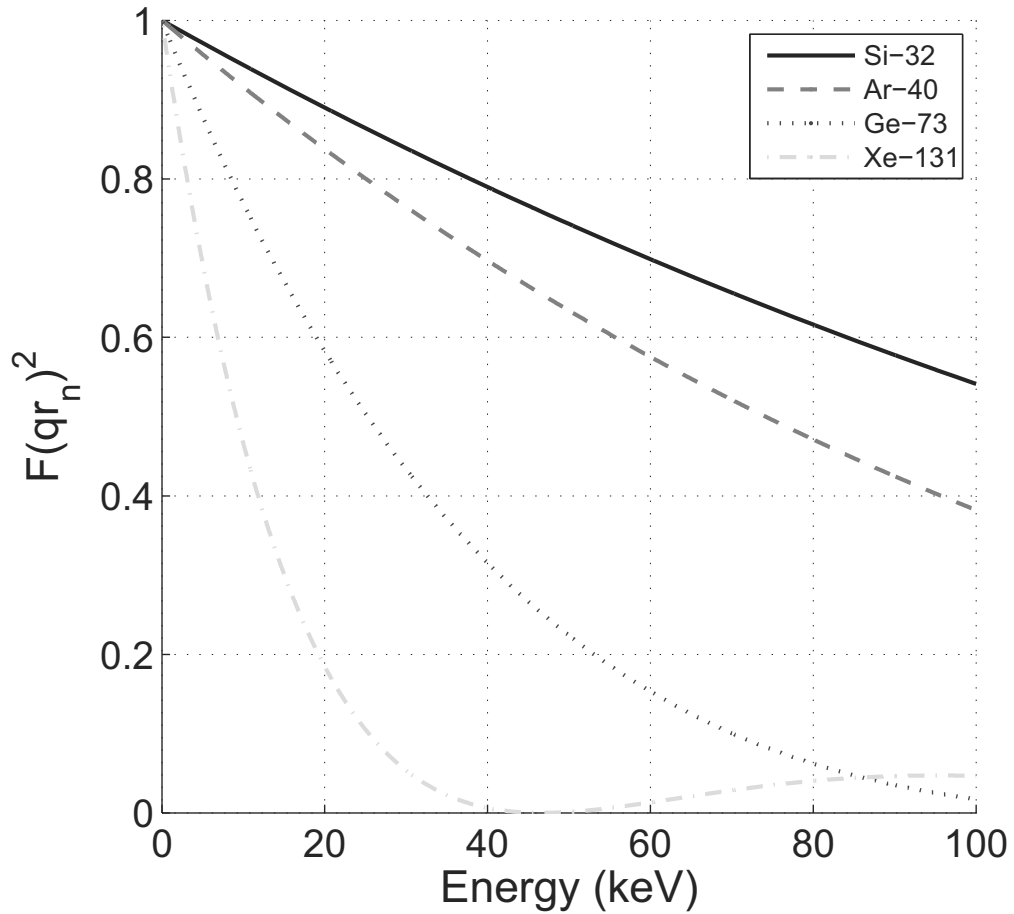
Figure 2.12: Spin-dependent nuclear form factor (thin-shell approximation; Equation 2.31) versus recoil energy for various targets.

and a_0 and a_1 are the isoscalar and isovector coefficients, respectively, related to the WIMP-nucleon spin factors. The spin-dependent form factor (as seen in Figure 2.12) can be estimated with the thin shell approximation (Equation 2.31). We see that the form factors of spin-dependent and spin-independent interactions drops significantly with energy, which are additional reasons why having sensitivity to low energy recoils is so important.

Another component in the differential rate (Equation 2.3) is the spin component. The total zero-momentum WIMP-nucleus cross section can be written as

$$\sigma_0 = 4\, G_F^2\, \mu_N^2\, C, \tag{2.35}$$

where G_F is the Fermi coupling constant, $\mu_N = M_T M_\chi/(M_T + M_\chi)$, and C is an en-

hancement factor that is different for spin-dependent (C_{SD}) and spin-independent (C_{SI}) interactions. For the spin-dependent interactions only unpaired nucleons contribute to the scattering amplitude, thus only nuclei with an odd number of protons and/or odd number of neutrons can have a spin-dependent cross-section. In the spin-dependent case,

$$C_{SD} = \frac{8}{\pi}\Lambda^2 J(J+1),\tag{2.36}$$

where

$$\Lambda = \frac{1}{J}[a_p\langle S_p\rangle + a_n\langle S_n\rangle],\tag{2.37}$$

with a_p and a_n as the WIMP-proton and WIMP-neutron effective couplings, respectively, $\langle S_n\rangle$ and $\langle S_p\rangle$ as the neutron and proton spin expectation values of the nucleus, and J as the total nuclear spin. More details can be found in [5]. In the spin-independent case,

$$C_{SI} = \frac{1}{\pi G_F^2}[Zf_p + (A-Z)f_n]^2,\tag{2.38}$$

where f_p and f_n are the effective WIMP-proton and WIMP-neutron couplings, respectively. For Majorana WIMPs, $f_p \sim f_n$ and

$$C_{SI} = \frac{1}{\pi G_F^2}(Af_p)^2.\tag{2.39}$$

This equation shows that the spin-independent cross sections follows A^2.

Annual Modulation

The motion of the Earth around the Sun induces an annual modulation in the WIMP signal. The velocity of the Earth is

$$v_E \approx v_s + v_e \sin\delta\cos(2\pi(t-t_0)),\tag{2.40}$$

where $v_s \approx 230$ km s^{-1} is the velocity of the Sun (disc rotation), $v_e \approx 30$ km s^{-1} is the rotational velocity of the Earth, $\delta = 30.7^o$ is the angle between the solar system axis and velocity vector of the Sun, and t_0 is June 2nd when the Earth's speed is maximum [172]. Figure 2.13 is a plot of the average, June and December differential rates assuming
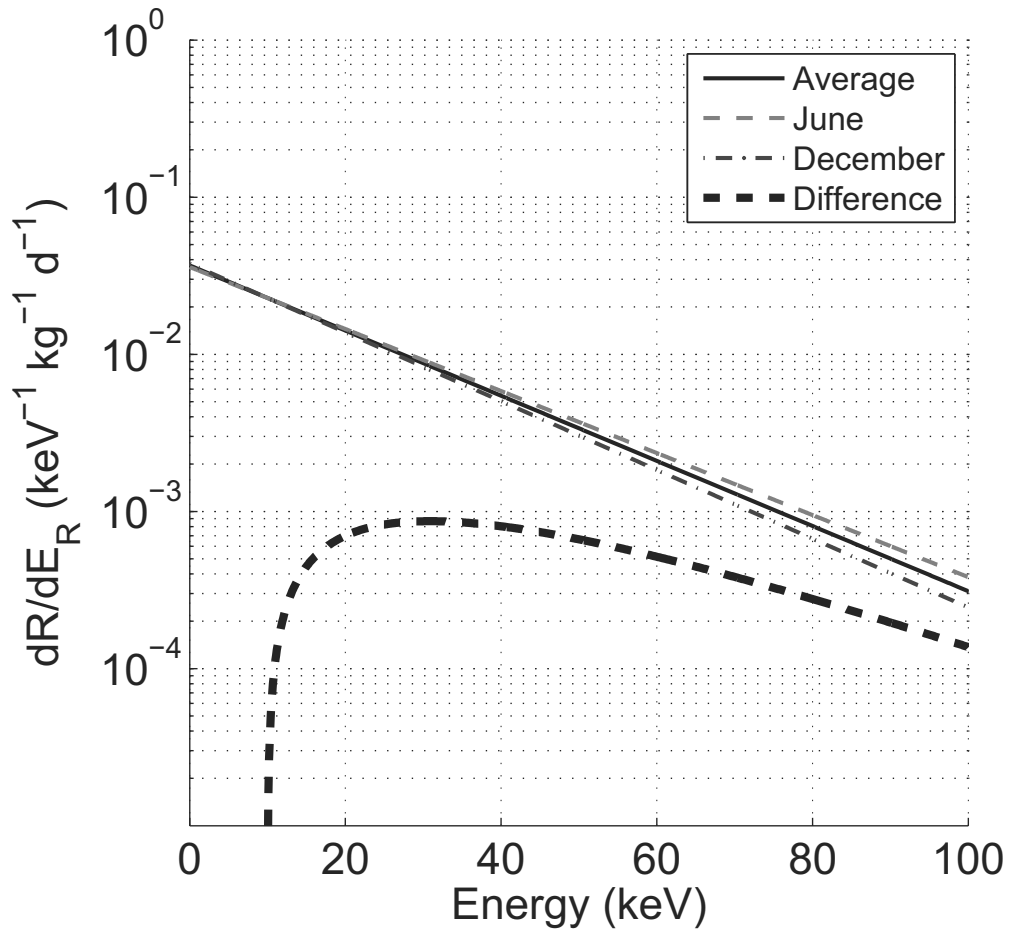
Figure 2.13: The average, June, and December differential rates. Also included is the difference between June (maximum) and December (minimum) rates. This assumes $\sigma_0 = 10^{-5}$ pb, $M_\chi = 100$ GeV c^{-2}, $v_0 = 230$ km s^{-1}, $v_s = 230$ km s^{-1}, $v_E = 30$ km s^{-1}, and $v_{esc} = 600$ km s^{-1}.

$\sigma_0 = 10^{-5}$ pb, $M_\chi = 100$ GeV c^{-2}, $v_0 = 230$ km s^{-1}, $v_s = 230$ km s^{-1}, $v_E = 30$ km s^{-1}, and $v_{esc} = 600$ km s^{-1}. Also included in this plot is the difference between the June (maximum) and December (minimum) rates.

2.3.2 Ionization Detectors

The absence of radioimpurities, low energy threshold ($\sim$1 keV), high energy resolution (1 keV) are some reasons why germanium is a good target material for dark matter detectors. The first Ge detectors were simply those built in the 1980s for detecting neutrinoless double

beta decay of ^{76}Ge. These first generation detectors helped eliminate Dirac neutrinos and cosmions [173] as possible dark matter candidates but were limited by electronics noise and the lack of background discrimination capability. Next generation ionization detectors use parts with less radioimpurities and separate modules for anti-coincidence background vetoing. Cosmogenically produced tritium is a concern because its 18.6 keV end-point results in background spanning the entire expected measurable WIMP spectrum. ^{68}Ge is another radioisotope that is cosmogenically generated from ^{70}Ge. This problem can be partially alleviated by moving the detector underground or by using enriched high purity germanium (HPGe). The IGEX and H/M are two experiments which employ enriched ^{76}Ge for double-beta decay and WIMP detection [174]. IGEX-2002 has generated the best exclusion plot among detectors of this class [175]. The Heidelberg Dark Matter Search (HDMS) detector, running at Gran Sasso, consists of two ^{73}Ge enriched HPGe detectors, a p-type crystal surrounded by a well-type Ge crystal. The presence of ^{73}Ge is needed to probe the spin-dependent WIMP-nucleon cross section. This experiment has measured a dark matter limit with a final setup [176]. GEDEON plans to use an array of twenty-eight 2 kg crystals to reach a background rate of 10^{-3} dru below 100 keV with the expectation of exploring the annual modulation [177]. The GENIUS-TF is currently operating several detectors at Gran Sasso using natural abundance Ge detectors with a total mass of 10 kg [178]. The detector sits directly in liquid nitrogen, which serves as both a cooling medium and as a shield against external radioactivity. GERDA will first use the HPGe crystals previous used in H/M and IGEX and have a total mass of 15 kg and then move on to 20 kg of new modules. The detector will use water and liquid argon for shielding with the liquid argon also serving as a cooling medium [179]. The MAJORANA experiment will use two-hundred HPGe detectors with a total mass of 500 kg Ge, isotopically enriched to 86% in ^{73}Ge [180].

2-4 keV

2-5 keV
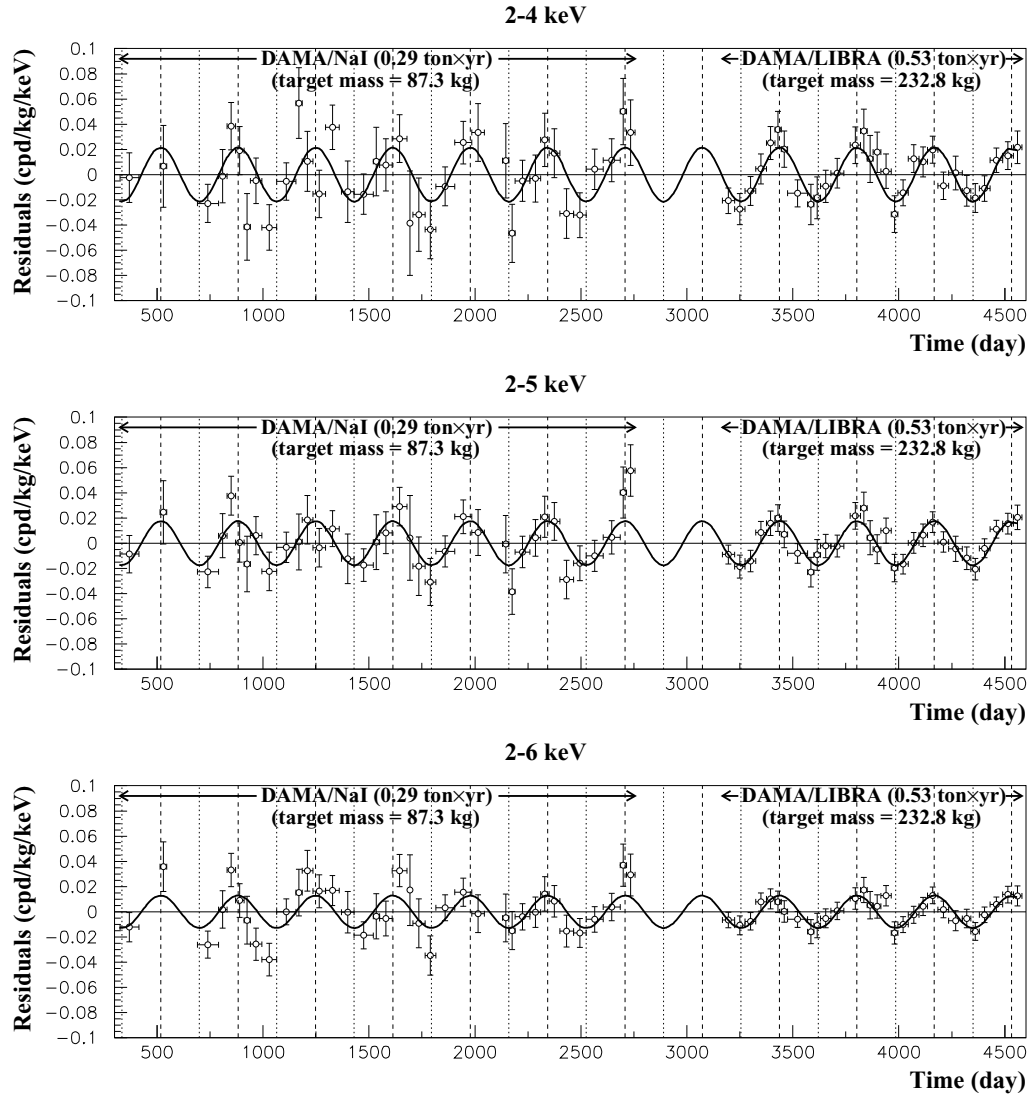
2-6 keV

Figure 2.14: Model independent residual rate of single hit events in the energy ranges 2–4, 2–5, and 2–6 keV as a function of time over a 12 year period. Both the 0.29 ton-year DAMA/NaI and 0.53 ton-year DAMA/LIBRA data are included. The curves represent the cosinusoidal functions expected for a WIMP signal with the modulation amplitudes obtained by best fit. Plot taken from [11].

2.3.3 Solid Scintillation Detectors

In the mid-1990s, the performance of solid scintillation detectors eventually surpassed that of the Ge and Si detectors. Although these detectors have high gamma backgrounds, they are able to acquire greater sensitivity with pulse shape discrimination. Some of the early experiments include detectors built by BPRS [181], DAMA [181], ELEGANTS [182], Boulby DM collaboration [183]. These detectors generally have excellent long term stability allowing for the search of the annual modulation in the signal. The first direct detection experiment to report a positive annual modulation signal was DAMA/NaI in 1997 with a 3364 kg-day exposure in the winter and a 1185 kg-day exposure over the summer, using a detector consisting of nine 9.7 kg NaI detectors at Gran Sasso [184]. The results of additional exposures with this detector were also published again showing the annual modulation [168]. The DAMA collaboration recently published results from their DAMA/LIBRA (Large sodium Iodide Bulk for RAre processes) detector which consist of twenty-five 9.7 kg radiopure NaI modules [185, 11]. DAMA/LIBRA collected an exposure of 0.53 ton-year over four annual cycles which clearly displayed again the annual modulation in the single-hit residual rate. Figure 2.14 shows the residual rate in various energy bins of the DAMA/NaI and DAMA/LIBRA data as a function of time. Their observations, however, contradict the null results of many other experiments.

2.3.4 MilliKelvin Cryogenic Detectors

Motivated by the need for greater background discrimination power, the community explored cryogenic detectors that exploit the relative quenching in scintillation and charge signals of electron and nuclear recoils. These detectors usually run at millikelvin temperatures (using helium dilution refrigerators) and measure the energy through the collection of phonons. Since the efficiencies of phonon generation in electron and nuclear recoils are the same, the phonon channel provides direct calorimetry for both types of recoil. Super conducting elements sitting near phase transition provide extremely sensitive measurements of phonons.
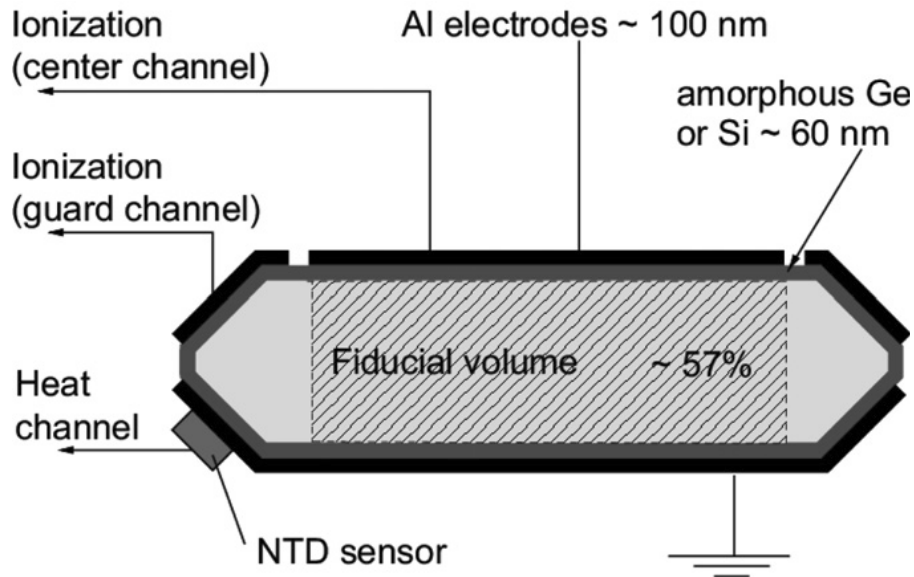
Figure 2.15: A schematic of the EDELWEISS-I detector.

EDELWIESS and CDMS are two experiments that measure phonons and ionization for discrimination in germanium crystals at millikelvin temperatures. The ionization yield for nuclear recoils is about four times lower than that for electron recoils. EDELWEISS-I has been operating in the Laboratoire Souterrain de Modane (LSM), which provides 4800 m.w.e. of rock shielding [186]. For temperature measurements, the detectors use neutron-transmutation-doped-germanium (NTD-Ge) thermometric sensors. The detectors also have aluminum electrodes for establishing the charge collecting field. See Figure 2.15 for a diagram of the detector. To select events in the center where the fields are more uniform, a cut is applied which requires that >75% of the charge signal be seen by the middle electrode. More details on the detector can be found in [187]. This detector achieved a rejection efficiency of >99.9% while maintaining a 90% acceptance for nuclear recoils down to an energy of 15 keV. An exposure of 62 kg-days was accumulated with three 320 g modules over 3 years and a cross section limit was published [186]. The collaboration is currently testing the twenty-eight 320 g Ge modules of their next generation detector called EDELWEISS-II. With a new cryostat, they hope to include up to 100 detectors and gain a two orders of magnitude improvement in sensitivity over EDELWEISS-I [188].

CDMS developed their first detectors in the 1990s, which ran in the Stanford Underground Facility. The later detectors, which have been running in the Soudan Underground Laboratory of of Minnesota, have consistently given the best cross section upper limits. CDMS uses Si and Ge detectors which have >99.99% background discrimination efficiency above 10 keV in the detector's bulk region. During the initial operation of their 160 g Ge detector, CDMS-I, many events were observed to have incomplete charge collection and, as a result, resembled nuclear recoils. These events were determined to be occurring near the surface and were minimized by adding new ionization contacts [189]. A limit was published in 2000 with data from Si and Ge detectors [190]. Then in 2004, the collaboration published the first results of CDMS-II running in the Soudan Underground Laboratory, which collected a net Ge exposure of 19.4 kg-day and set what was the lowest exclusion limit at the time [191]. Their newest limit was set from a 121.3 kg-day exposure which observed no events in nineteen 250 g Ge and eleven 100 g Si modules [14]. The data gave the same minimum WIMP-nucleon spin-independent cross section as that of XENON10 (which set the lowest upper-limit at time of publication) and provides the best sensitivity for masses above 42 GeV (see Figure 2.24.) They have proposed 27 kg Ge experiment called SuperCDMS which is significantly larger than CDMS-II [192].

CRESST-I consisted of several 262 g sapphire crystals, each with a tungsten superconducting phase transition (SPT) thermometer [193]. A first series of runs in 1999 revealed a much higher than expected background. The background did not appear to be due to radioactivity as it was time dependent and not Poissonian. The source of the background was eventually identified as cracks in the sapphire crystal. The cracks formed due to the tremendous amount of force applied at the small contacts. The problem was remediated by replacing the sapphire contacts with plastic ones. Using the crystal with the lowest energy threshold and a second one to eliminate coincidence events, 140 hours of data was collected to set a cross section limit [193].

CRESST-II at Gran Sasso National Laboratory takes a different approach by measuring scintillation and phonons in Ca_2WO_4 [194]. Ca_2WO_4 was chosen because of its relatively

high light yield and lack of degradation in light yield for events near the edge. The difference between the scintillation output of nuclear and electron recoils provides the discrimination. Similar to the measurement in CRESST-I, the phonons are measured with the tungsten SPT thermometers. The light is measured with a separate silicon wafer containing another SPT thermometer. To increase the collection efficiency of phonons created by photons, there are additional aluminum phonon collectors. To further increase the light collection, a 99% reflective polymeric multilayered foil surrounds the crystal. The group has taken 20.5 kg-days of data with two Ca_2WO_4 300 g prototypes to set a WIMP-nucleon cross section limit [194].

2.3.5 Liquid Noble Element Detectors

Detectors using liquid neon, argon or xenon can be practically enlarged to the 1-ton scale unlike competing technologies such as cryogenic semiconductors. Furthermore, liquid noble elements are relatively inexpensive, easily purified, require relatively simple cryogenics, have high scintillation and charge yields, allow for background discrimination and can provide self-shielding. Also, liquid neon and xenon do not have problematic long-lived radioactive isotopes. On the other hand, argon has a large background from ^{39}Ar which beta decays with an endpoint energy of 565 keV and half-life of 269 years and is generated by cosmic ray interactions via ^{40}Ar(n, 2n)^{39}Ar. Its presence in commercial argon results in a background rate of $\sim$1 Bq/kg. Liquid argon detectors must rely on the highly efficient pulse shape discrimination to overcome this background. Xenon has ^{85}Kr which beta decays with a half-life of 10.76 years but can be removed with distillation or chromatography.

Here, we describe the two basic forms of these detectors – single- and two-phase.

Single Phase Detectors

Single phase detectors measure only the scintillation light, which can provide background discrimination if the detector is sensitive to the photon arrival times. The scintillation pulse of nuclear recoils tend to have a larger fraction of the light at the head of the pulse

Table 2.1: Scintillation constants of liquid neon, argon and xenon [71, 22, 72].

element	τ_1	τ_2	$(\frac{I_1}{I_3})_{ER}$	$(\frac{I_1}{I_3})_{NR}$
Ne	18.2 ns	14.9 μs	0.10	0.66
Ar	4.0 ns	1.59 μs	0.3	3
Xe	2.2 ns	27 ns	0.05	1.6
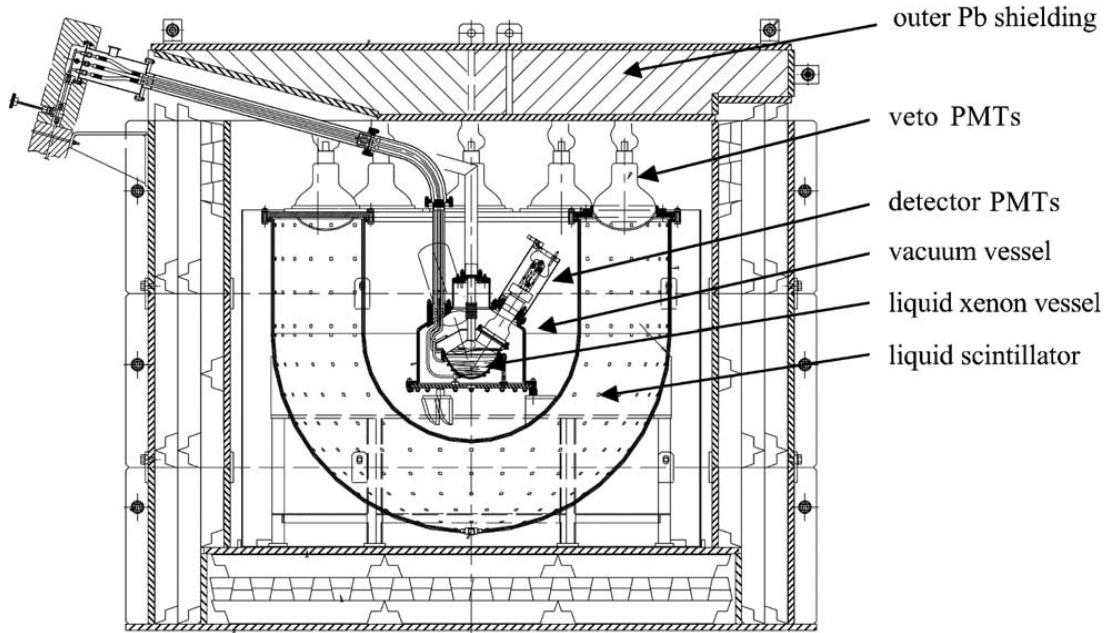
Figure 2.16: The Zeplin-I detector surrounded by veto and shield [12].

as nuclear recoils tend to generate a greater portion of excimers in the singlet state which decays more quickly than the triplet states. Table 2.1 shows the scintillation parameters of liquid neon, argon and xenon. The pulse shape is usually quantified by the tail fall-time or by the fraction of pulse integral in the head of pulse. Pulse shape discrimination is very powerful in liquid neon and argon because of the great disparity between the singlet and triplet times. Our measurement of the pulse shape discrimination in liquid xenon is described in Section 5.3. See Section 3.4 for more details on the principle of pulse shape discrimination.

In the 1990s, the DAMA group engaged in basic R&D relevant to single phase liquid xenon detectors. Before taking dark matter data, the DAMA group measured two key char-

acteristics of liquid xenon: the scintillation efficiency of nuclear recoils relative to electron recoils and the pulse shape of the two types of recoils. In 1996, DAMA collected dark matter data with a three PMT detector containing 6.5 kg of ^{85}Kr-free xenon enriched in ^{129}Xe to 99.5%. The detector collected a 1763.2 kg-day exposure and set a cross section limit similar to that set by their NaI detector. Pulse shape discrimination was employed to remove some of the background [195].

A similar detector called ZEPLIN-I was built by the UK Dark Matter Group. It had a fiducial mass of 3.2 kg and collected scintillation with three PMTs. Figure 2.16 is a diagram of the detector, shield and liquid scintillator veto. The long volume of liquid xenon between each of the PMTs and the active volume allowed for the rejection of background events from the PMTs by demanding that the signal be present in multiple PMTs. The pulse shape parameter τ_m was the time interval between 5% and 90% of the maximum amplitude in the tail. Figure 2.17 shows the spectrum of τ_m for electron recoils of 7–10 keV. Figure 2.18 shows the τ_m spectrums from data containing both types of recoils at various energy ranges. Data of only nuclear recoils was not taken. The detector collected 293 kg-days of data in the 2300 m.w.e. deep UK Boulby mine and set a 90% confidence limit for spin-independent cross section with a minimum at 1.1×10^{-6} pb [12].

Another single-phase liquid xenon experiment is XMASS, which hopes to construct a multi-ton spherical detector for detecting solar neutrinos, neutrinoless double beta decay (^{136}Xe $\rightarrow$ ^{136}Ba $+$ 2e$^-$) and WIMPs [196]. It will rely on self-shielding to remove background. A large number of PMTs point toward the center which allows for the vertex reconstruction that is required to remove multiple scatters and edge events. The group has built a smaller cube-shaped 100 kg (3 kg fiducial volume) prototype with 54 PMTs (9 on each face) demonstrating self-shielding and achieving a light collection of 0.6 photoelectrons/keV [196]. The group has also built a distillation system that has reduced ^{85}Kr levels in xenon from about 3 ppb to 3.3 ppt [197]. In 2007, XMASS received funding for a 800 kg (100 kg fiducial volume) detector [198, 199]. They have started construction for this detector which is expected to be completed within two to three years. This detector
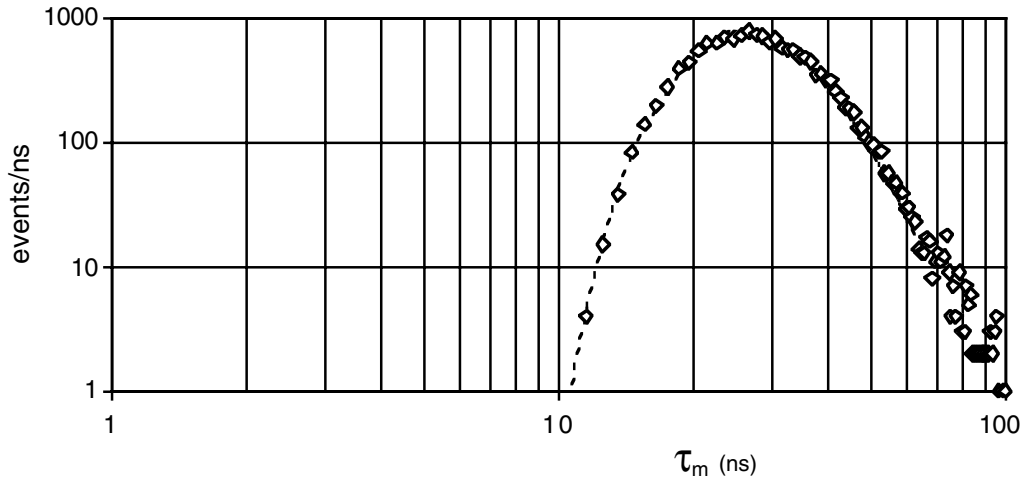
Figure 2.17: The distribution of τ_m from gamma rays between 7–10 keV as measured by the ZEPLIN-I detector [12].

will have 812 hexagonal face PMTs in a pentakis dodecahedron configuration and sit in a 10 meter high and 10 meter diameter water shield with several PMTs for muon rejection.

The DEAP/CLEAN collaboration is working on several detectors with liquid neon and liquid argon. They have measured the scintillation parameters for liquid neon [72] and argon [200] in small prototypes and have constructed DEAP-I, a 7 kg liquid argon module with two PMTs that is currently running at SNOLAB [201]. They plan to construct a 3600 kg liquid argon module in 2009 [202].

Two-Phase Liquid Noble Element Experiments

Two-phase liquid noble element time projection chamber detectors measure both scintillation and ionization to discriminate against background gammas. An excellent summary of two-phase detectors is given by [37]. Figure 2.19 shows the operation of the two-phase detector. A particle collides with the target and generates excitations and ionization. Immediate de-excitation and recombination releases the "primary" scintillation. With an electric field established by biased mesh electrodes, a portion of the electrons are prevented from recombining and are drifted away from the event site. The electrons are pulled out of the liquid into the gas where they excite the xenon gas, releasing a second burst of light known
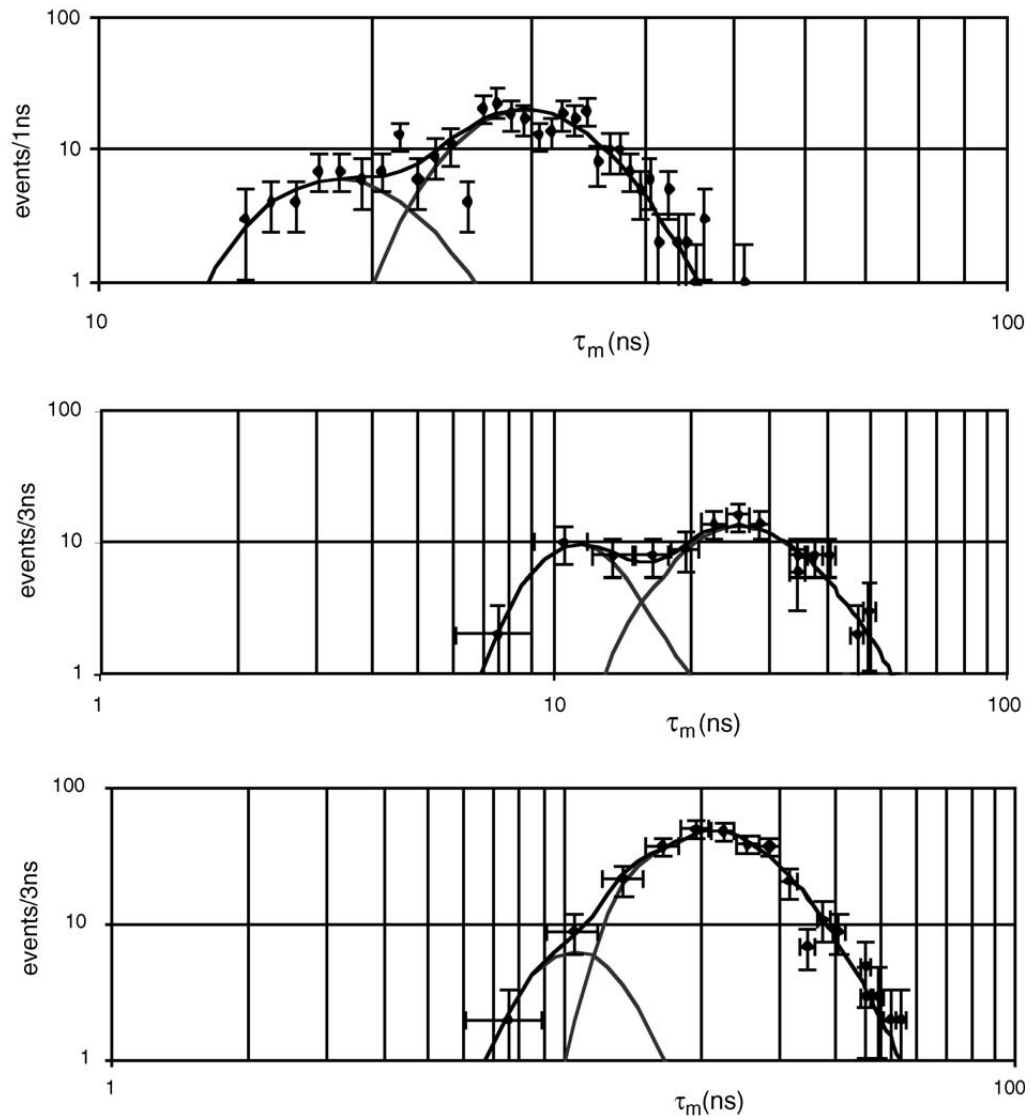
Figure 2.18: Neutron calibration results of the ZEPLIN-I detector showing that $\tau_{NR} < \tau_{ER}$. Top: AmBe events in energy range 20–30 keV. Center: ambient neutrons and ^{60}Co gammas in the energy range 3–7 keV. Bottom: AmBe events in energy range 3–8 keV [12].
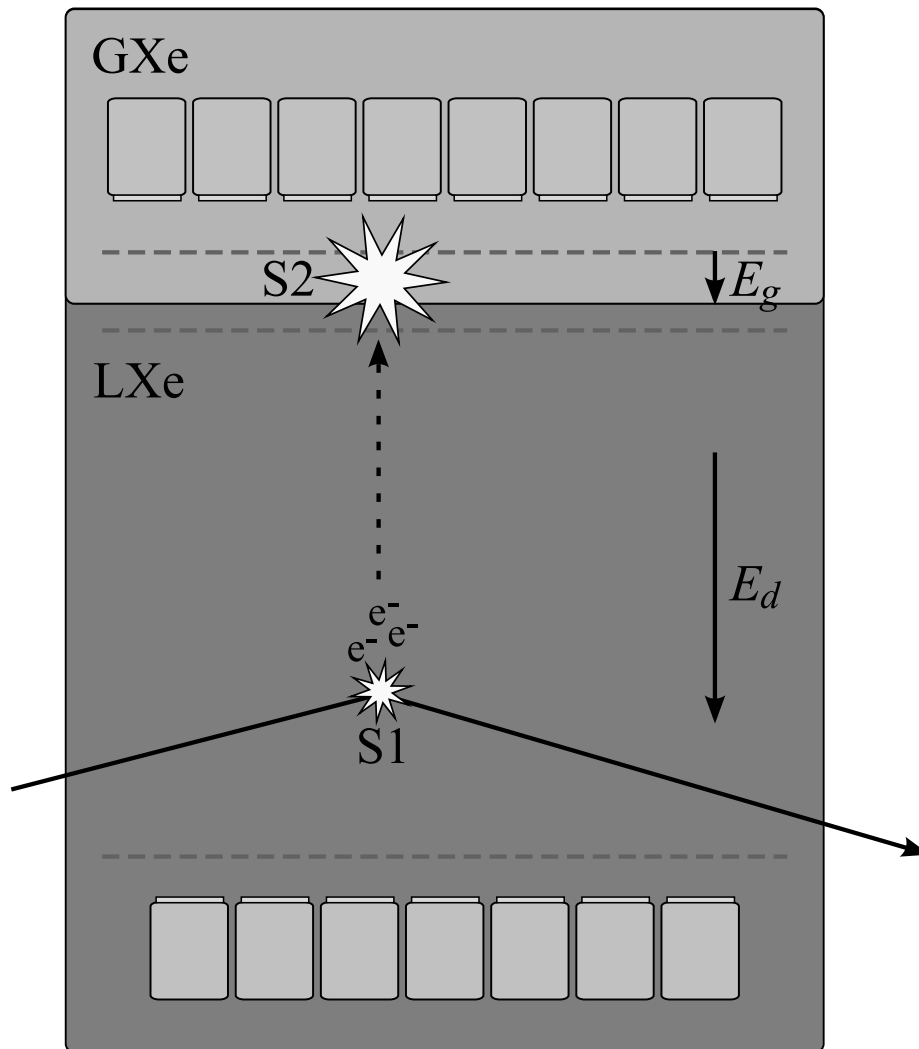
Figure 2.19: Diagram of a two-phase detector with two PMT arrays. A particle interaction emits light and electrons. The electrons are pulled out of the liquid where they excite the gas and emit a burst of light. The light is usually detected by PMTs.

as the proportional or secondary scintillation. The fraction of electrons that are pulled out of the liquid depends on the electric field (see Section 3.5.3). Typically several tens of photons are generated per electron (see Section 3.5.4 for more details). This powerful technique has the ability to sense single electrons (an alternative method of directly measuring charge avalanches is described in Section 5.5). Both the primary and proportional light are measured by PMTs or similar devices. Typically, there is an array of PMTs in the liquid below the active volume and another array above in the gas. The PMTs in the liquid have a much greater collection efficiency for primary light than those in the gas because most of the photons stay in the liquid due to a mismatch in the refractive indices [42]. A multiple-PMT array in the gas allows for x–y position reconstruction. Typically, the primary and proportional scintillation signals are referred to as "S1" and "S2", respectively, and the size of these signals as $S1$ and $S2$, respectively. The basis of charge-based discrimination (as with pulse shape discrimination) lies in the linear energy transfer (LET) – the fraction of charge recombination is positively correlated with the LET. This manifests as a lower ionization to scintillation ratio for nuclear recoils: $(S2/S1)_{ER} > (S2/S1)_{NR}$, where ER and NR stand for electron and nuclear recoils, respectively. In two-phase liquid argon detectors, both recombination and pulse shape discrimination are employed, with most of the discrimination power deriving from the latter principle. (Section 5.3 demonstrates the use of both principles simultaneously in LXe detectors.)

There are two two-phase experiments using argon. WARP has been running a small 2.3 liter (1.87 liter sensitive) module in the Gran Sasso National Laboratory . The detector has seven $2''$ PMTs in the gas and three mesh electrodes. The drift volume is surrounded by a high performance diffuse reflector coated with tetra-phenyl-butadiene (TPB), a wavelength shifter for converting the 128 nm photons to about 440 nm. Increasing the wavelength boosts the primary light signal by raising the detector reflectance and PMT quantum efficiency. Figure 2.20 shows $\log(S2/S1)$ versus recoil energy with the single-hit nuclear recoils highlighted. Cross section limits were published based on an 96.5 kg-day exposure [203]. Their results indicated that the two discrimination methods are independent, which is nec-
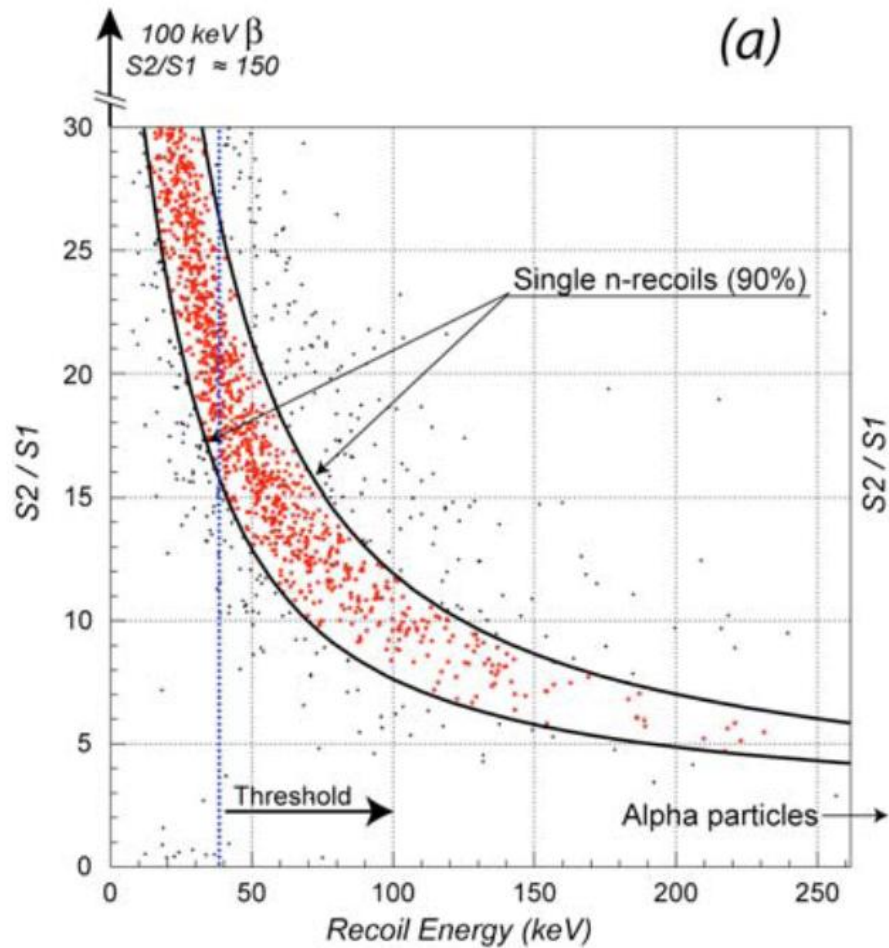
Figure 2.20: Plot of $\log(S2/S1)$ versus recoil energy in WARP with the single scatters bounded by the two black lines.

essary for the discrimination efficiencies to compound. They are currently building a 140 kg module surrounded by an argon anti-coincidence shield. To further reduce background they have sought argon with lower concentrations of ^{39}Ar. Instead of pursuing centrifugation, which is likely to be prohibitively expensive, they have looked for underground sources that have been shielded from cosmic rays. One such source contains an ^{39}Ar concentration that is 5% that of normal argon [204].

The other two-phase liquid argon detector is the 1 ton detector by ArDM which is currently under construction. The ArDM detector is similar to WARP except that the top PMT array is replaced with a GEM charge readout system (see Section 5.5.2) to reduce
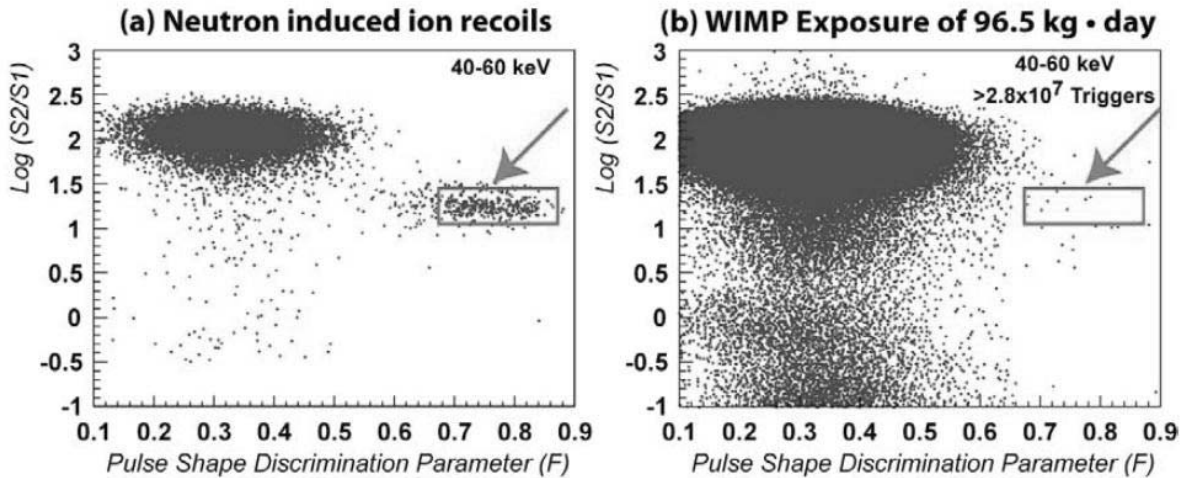
Figure 2.21: Plot of $\log(S2/S1)$ versus prompt/total between 40 and 60 keV, of the AmBe (gamma and neutron) and WIMP search data from WARP. The acceptance window is represented by the red box. Eight events were observed in the acceptance window but only five events remain in the single-hit window.

background [205, 206]. They have measured a gain of up to 10^4 with a two-stage GEM structure in pure argon at 87 K.

There have been several two-phase liquid xenon dark matter detectors. XENON10 at Gran Sasso National Laboratory was the first such detector to publish a limit – this detector and its results are be discussed in Chapter 6. The ZEPLIN collaboration has published cross section limits for two two-phase liquid xenon detectors. In 2007, the collaboration published spin-independent [207] and spin-dependent [62] cross section limits for the 31 kg (7 kg fiducial volume) ZEPLIN-II detector at the Boulby Mine. Their next detector, ZEPLIN-III published limits about a year later. This 6.5 kg fiducial volume detector achieved better results than ZEPLIN-II as it had a PMT array in the liquid (as opposed in the gas) which gave a significantly higher light collection and lower energy threshold [208]. Their first run of 847 kg-days exposure set a spin-independent cross section limit with a minimum of 7.7×10^{-8}pb at the WIMP mass of 55 GeV [15]. This data was also used to set a spin-dependent WIMP-neutron cross section limit with minimum of 1.8×10^{-2} pb at 55 GeV [16]. Both limits improved upon the results of XENON10 for masses above ~100 GeV. Liquid xenon detectors are unable to set competitive WIMP-proton limits because of the

lack of isotopes with unpaired protons. There are currently two 100 kg scale detectors that are likely to publish new limits within a year. The XENON collaboration is working on XENON100 which has a total mass of 170 kg and 65 kg in fiducial volume and is running in the cryostat and shield that previously housed XENON10 [209]. The LUX collaboration is working on 300 kg module with 100 kg fiducial volume which will run in the Homestake mine [210].

2.3.6 Gaseous Detectors

The DRIFT collaboration has been developing the low pressure Negative Ion Time Projection Chamber (NITPC) for WIMP detection. One goal of these detectors is to deduce the directionality of the WIMP "wind" by reconstructing the ion tracks. The detectors employ large time projection chambers with multi-wire readouts. The tracks are reconstructed by signal size and arrival times of the ionization. For this approach, gas is needed to generate ionization clouds large enough for their shapes to be probed. The target medium is $\sim$40 torr carbon disulfide (CS_2), which is a electronegative gas that replaces electrons as the charge carrier and consequently lowers the loss of track information due to diffusion. Good discrimination on the order of 10^6 is achieved between nuclear and electron recoils as they have drastically different track lengths. Figure 2.22 shows the wire signals for alpha and neutron events. In this figure, the number of ion pairs (NIPs) collected by each wire and track lengths (RDs) are given for each event, showing that the ionization density (total NIP/RD) is larger for the nuclear recoil event. The sulphur nucleus has a small spin-independent cross section and thus needs to be compensated by increasing the total target mass. The collaboration has finished constructing and testing DRIFT-I, a 1 m^3 module [211], and is working on DRIFT-II which runs with a higher drift field to decrease the effects of diffusion [212].
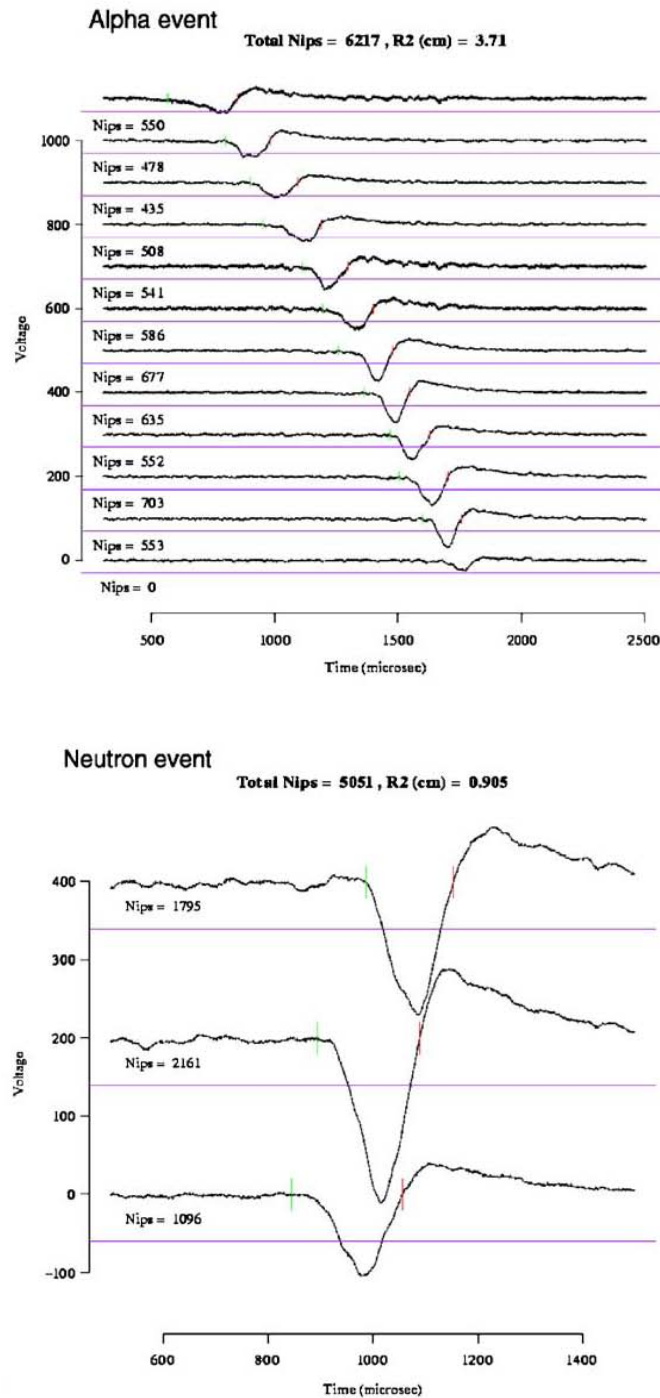
Figure 2.22: DRIFT-I wire signals of alpha (top) and neutron (below) events. The number of ion pairs (NIPs) collected for is indicated for each wire and is proportional to the energy collected by the wire. The "RD" is the 2D track length. The ionization density (total NIP/RD) is larger for nuclear recoil event.
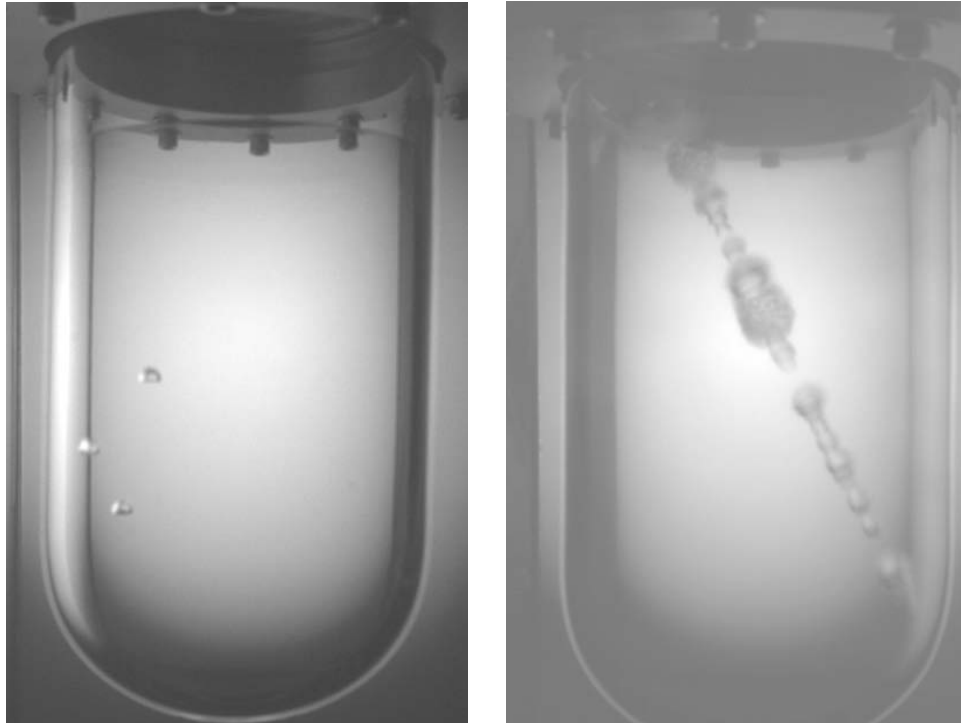
Figure 2.23: The tracks of a neutron triple scatter (left) and muon (right) in a COUPP prototype.

2.3.7   Superheated Liquid Bubble Detectors

The invention of the bubble chamber in the 1950s by Donald Glaser lead to the discovery of many particles [213]. The application of this concept for cold dark matter detection was first proposed in the 1990s [214] and has been implemented in the search for dark matter. These detectors employ superheated fluids in which bubbles form upon energy deposition of sufficient concentration. Several materials have been used which allow nuclear recoils (and other interactions of similar LET) to form bubbles. In additional to having very high discrimination efficiencies ($>10^9$), these detectors are cheap, scalable, and require fairly simple equipment. One of the disadvantages is the presence of alpha-emitting contaminants and the spontaneous formation of bubbles by impurities and surface defects. The bubbles are usually detected with microphones and their positions can be reconstructed with CCD cameras. There are two basic approaches. The superheated droplets detectors (SDDs)

have micro-droplets ($\sim$10 μm) suspended in a matrix. The other approach employs bulk superheated fluids. The former technique helps to avoid problems with the spontaneous formation of bubbles at the edges. This technique, however, is limited by which targets can be used because of the need to avoid de-emulsification. These experiments are limited to targets such as C_2ClF_5, which are good for spin-dependent searches due to the presence of fluorine but are not good for spin-independent searches. CF_3I and CF_3Br are good for both searches but cannot be used well in SSDs. They have to be used in bulk superheated fluid detectors which generally have problems with surface defects but allow for easily interchanging of target material.

PICASSO and SIMPLE are two SDD experiments. SIMPLE has published a spin-dependent cross section limit comparable to other detectors despite its relatively low 0.42 kg-day exposure with C_2ClF_5 [215]. SIMPLE has also explored the use of CF_3I but has yet to achieve long term stability. PICASSO has published spin-dependent cross section limits with a 2 kg-day exposure using C_4F_{10} [65] and is currently working on thirty-five 4.5 liter modules each with a mass of 2.6 kg [216].

The Chicagoland Observatory for Underground Particle Physics (COUPP) experiment uses a bulk superheated fluid. To lessen the problem of surface defects, smooth quartz vials are used with a lining of buffer fluid. The wetting of the surface can be improved by slow vapor deposition, and the trapped bubbles in the surface defects can be outgassed. With a set of targets of different spin-dependent and spin-independent sensitivities (for example, C_3F_8 or C_4F_{10}, which have higher spin-dependent couplings than CF_3I), they can make more precise measurements of the coupling constants [217]. Figure 2.23 shows the tracks of neutrons and muon events in a COUPP prototype. COUPP has collected a 250 kg-day exposure with 1.5 kg CF_3I module running underground in Fermilab which was able to improve spin-dependent WIMP-proton cross section limits even with little attention paid to alpha-recoil backgrounds from U/Th in quartz and radon from air, rubber seals, and welds [66]. This detector demonstrated a background leakage of $\sim10^{10}$ at $\sim$10 keV recoil energy which is unmatched by any other WIMP detector; for comparison, CDMS has a
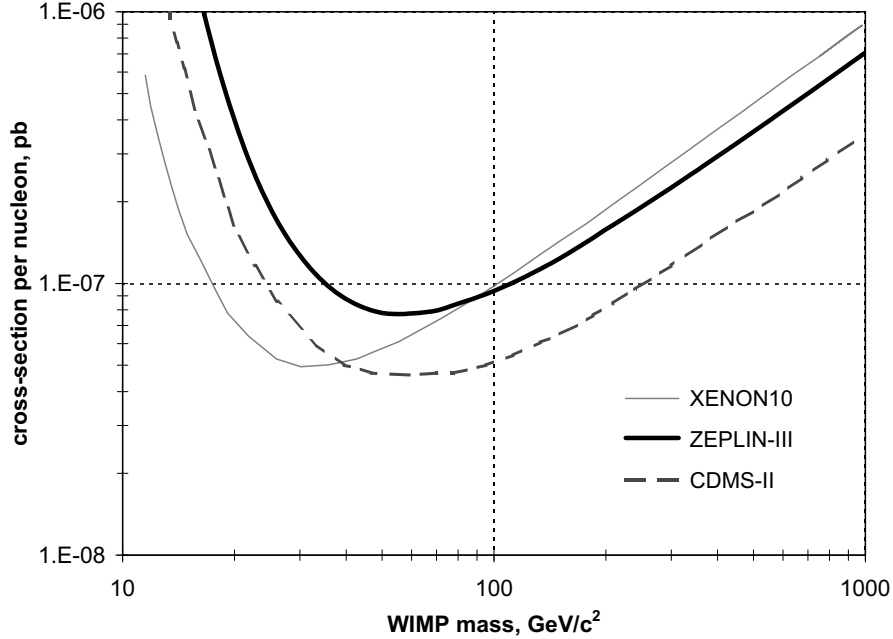
Figure 2.24: 90% confidence upper limit to the WIMP-nucleon elastic scattering cross sections set by the top three experiments: XENON10 [13], CDMS-II [14] and ZEPLIN-III [15]. Figure taken from [15].

rejection factor of 10^{-4}–10^{-5}. COUPP is currently constructing a $\sim$50 kg detector.

Figure 2.24 shows the spin-independent cross section upper limit set by XENON, CDMS and ZEPLIN-III. Figure 2.25 shows the upper limits on pure WIMP-neutron and WIMP-proton cross sections set by many experiments. Two-phase liquid xenon detectors (XENON and LUX) are in a position to continue leading the field in setting spin-independent and WIMP-neutron limits as they do not have any technical roadblocks against further expansion. Furthermore, as they scaled up, they will also be taking increasing advantage of self-shielding. Unlike single-phase liquid xenon detectors, two-phase detectors can efficiently remove multiple scatter neutron events. Argon experiments must find argon with low intrinsic background to be competitive. CDMS has consistently generated top results but the expansion to SuperCDMS would be expensive (>$30 million). Gaseous detectors like DRIFT are unlikely to set new limits due to their low mass. The droplet detectors have enormous potential due to their nearly infinite background rejection efficiency, low instru-
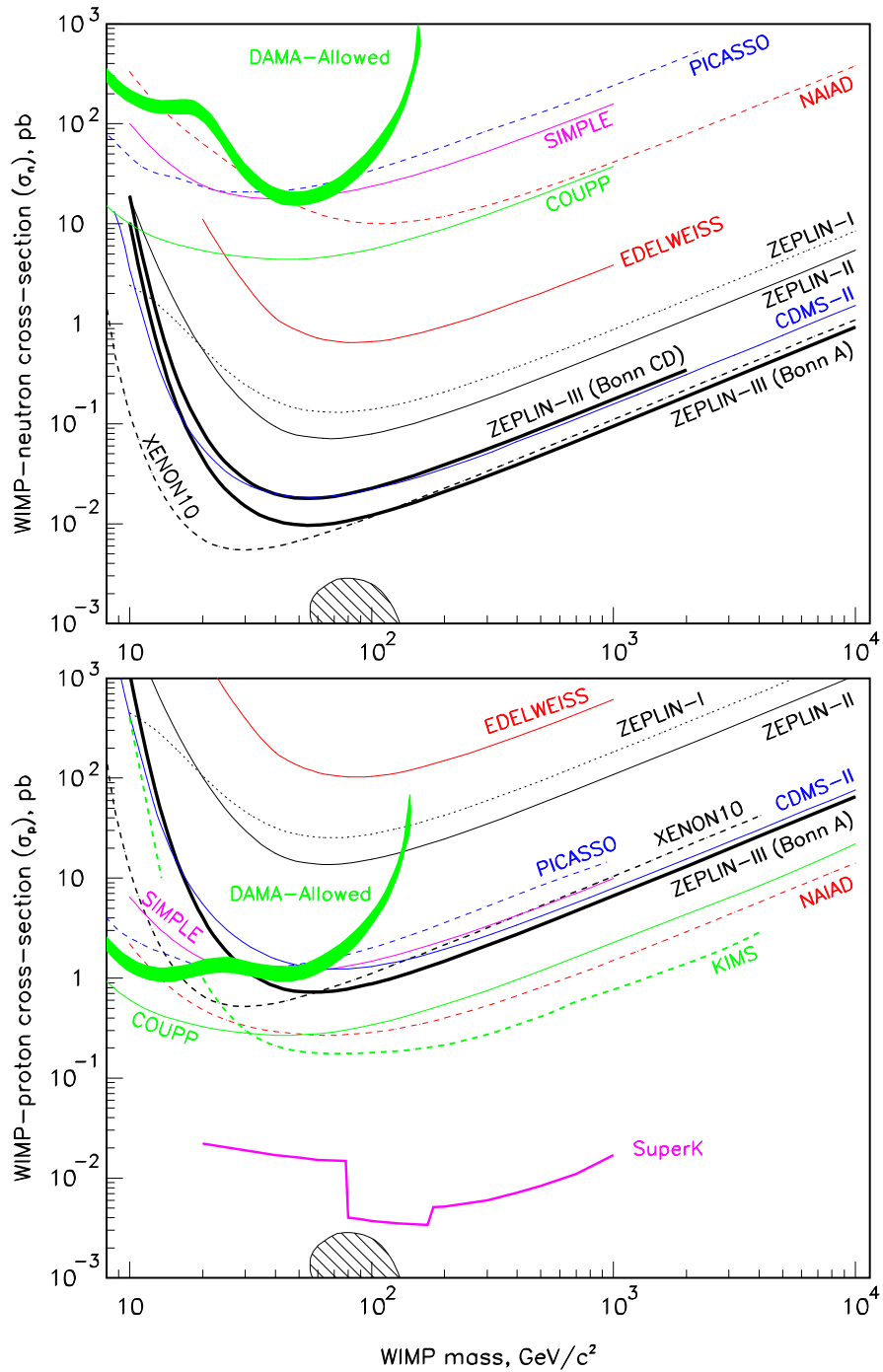
Figure 2.25: Upper limits to pure WIMP-neutron (top) and WIMP-proton (bottom) spin-dependent cross sections set by many experiments: ZEPLIN-I, ZEPLIN-II, XENON10, CDMS-II, COUPP, EDELWEISS, KIMS, NAIAD, PICASSO and SIMPLE. See [16] for references. The hatched area is the top of the 95% probability region for neutralinos in the Constrained Minimal Supersymmetric Standard Model (CMSSM) [17]. Figure taken from [16].

mental complexity and very low cost. With the elimination of alpha-emitting contaminants, COUPP may see an improvement in sensitivity of up to six orders of magnitude, excluding much SUSY space.

2.4 High Energy Collider Searches

The discovery of the neutralino could be one of the major discoveries at the Large Hadron Collider (LHC) at CERN [218, 219]. The 14 TeV proton collider is expected to provide enough energy for such particles if they exist. These particles are likely to escape undetected and be identified with a missing mass signature. The future International Linear Collider (ILC) will also be able to search for neutralinos via 1 TeV electron-positron collisions [220]. Due to a reported price tag of about $7 billion [221], this accelerator may never be constructed. It must be noted that even if the neutralino is discovered in a collider, indirect and direct detection experiments will still be needed to show the existence of a neutralino halo.

Chapter 3

Xenon

3.1 Introduction

Xenon is a colorless and odorless noble gas of atomic number 54 that exists in trace amounts in the atmosphere. This noble gas was discovered on July 12, 1898 by Sir William Ramsay and Morris Travers, who named it after the Greek word $\xi \epsilon \nu o \nu$, meaning foreign or strange. Since its discovery, many practical uses of xenon have been found in medicine, lighting, propulsion and particle detection. Major research on the application of liquid xenon in multi-wire ionization chambers were performed in the 1960s. Throughout the next two decades, measurements were done on key values such as the Fano factors, scintillation yields, and decays times. A detailed history of xenon detectors can be found in [222]. In this section, we give a brief overview of some of the applications of xenon, its general physical and chemical properties, and specific properties related to its application in particle detectors.

3.2 Applications of Xenon

Xenon has been used since the late 1970s as a propellant in ion thrusters of spacecrafts because of its low ionization potential per atomic weight [223]. In these devices, xenon ions are first created by bombarding xenon with a stream of electrons and then accelerated by an
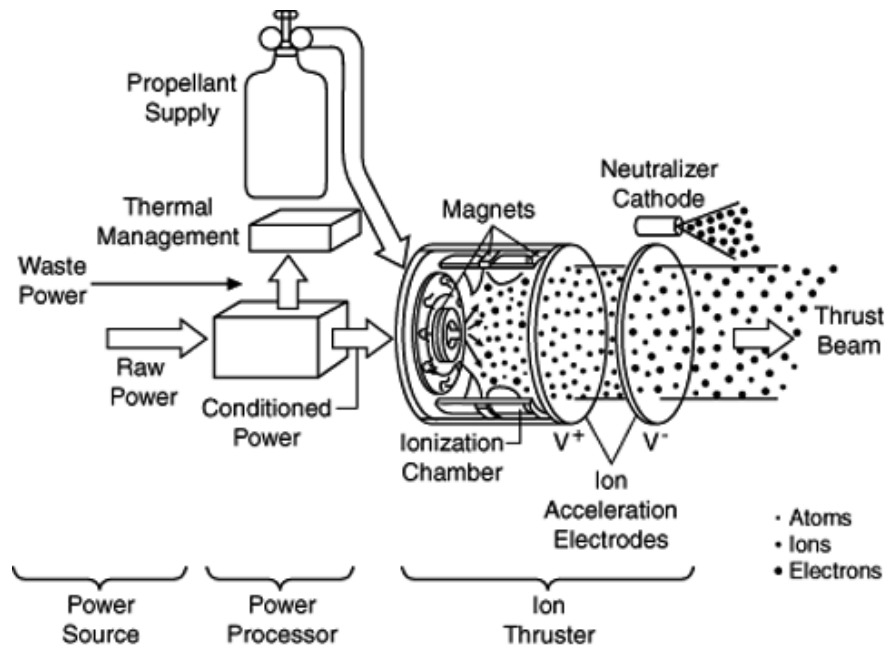
Figure 3.1: Diagram of an ion propulsion system. Xenon is typically used as the propellant because of its low ionization potential per atomic weight.

electric field. The electrons are kept in the ionization region by a magnetic field (See Figure 3.1). These thruster require ∼10 kW of power and generate a thrust of several hundred mN.

Xenon gas is an excellent light source. It has been used in flash lamps because of its fast response and also in movie projector lamps because their emission spectrum resembles natural light more than that of typical light bulbs. Xenon-neon mixtures are used in plasma television screens.

Xenon serves multiple purposes in medicine. The anesthetic effects of xenon on mice were first published in 1946 [224]. Soon afterward, its anesthetic effects were tested in humans [225] but widespread use has only recently been seriously considered [226]. It has many properties of an ideal anesthetic: high insolubility in human tissue enabling faster induction and emergence than other inhaled anesthetics, low toxicity, and absence of teratogenicity. Furthermore, the use of xenon has been motivated by environmental concerns as it does not destroy the ozone layer like common anesthetics. Although expensive, the use of xenon
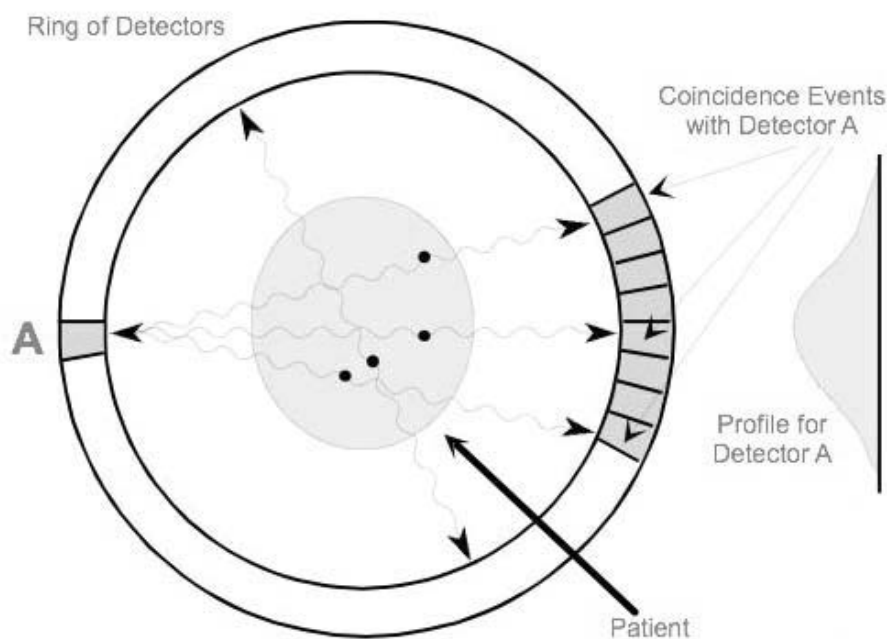
Figure 3.2: Position emission tomography. Liquid xenon detectors on the periphery detect the gammas emitted from position-electron annihilations.

can be cost effective if recycled in a closed environment.

Xenon is also used in medical imaging both as a source and as a detector medium. A key feature of xenon is its rapid clearance from the body, which importantly limits the dosage to the patient. One such diagnostic inhalant is ^{133}Xe which has a half-life of 5.25 days and is produced in the fission of ^{235}U. Only the 80.9 keV gamma ($\Gamma = 38.0\%$) is used for imaging. ^{133}Xe has been used to successfully monitor blood flow [227]. ^{129}Xe has been used in magnetic resonance imaging (MRI). By hyperpolarizing ^{129}Xe, the nuclear magnetic resonance signal is greatly enhanced. Hyperpolarization of ^{129}Xe to four or five orders of magnitude above the Boltzmann polarization can be achieved by having the xenon undergo spin exchange with evaporated rubidium that has been polarized with circularly polarized light [228]. In the gas phase, the ^{129}Xe has a relaxation time of several hours [229] while in blood, the polarization lasts for only several seconds [230]. Liquid xenon has been considered as a target in positron emission tomography (PET), which is a medical imaging technique whereby the patient is injected with a positron-emitting tracer isotope. The two

Table 3.1: General properties of noble elements.

Property	He	Ne	Ar	Kr	Xe
Symbol	He	Ne	Ar	Kr	Xe
Atomic Number	2	10	18	36	54
Atomic Radius (pm)	31	38	71	88	108
Gas Density at 1 atm, 298 K (g/l)	0.16	0.82	1.63	3.43	5.40
Liquid Density at 1 atm, $T_{boiling}$(g/cm^3)	0.12	1.21	1.40	2.41	2.94
Boiling Temperature at 1 atm (K)	4.22	27.07	87.30	119.93	165.03
Melting Temperature at 1 atm (K)	-	24.56	83.80	115.79	161.4
Critical Temperature (K)	5.19	44.4	150.8	209.4	289.7
Critical Pressure (atm)	2.24	27.2	48.1	54.3	57.6
Critical Density (g/cm^3)	0.0696	0.482	0.544	0.91	1.10
Triple Point Temperature (K)	N/A	24.56	83.81	115.78	161.41
Triple Point Pressure (atm)	N/A	0.424	0.68	0.722	0.805
Dielectric Constant of Liquid	1.049	1.188	1.51	1.66	1.95

collinear 511 keV gamma rays from positron-electron annihilations are detected by a ring of modules containing PMTs and electrodes in LXe (as seen in Figure 3.2) [231, 232]. The annihilation positions are reconstructed by time-of-flight information.

3.3 General Properties

Xenon is found in the atmosphere at concentration of 0.09 ppm and can be extracted by fractional distillation, requiring 220 watt-hours of energy per gas liter. The melting and boiling points of xenon at 1 atm are 161.4 K and 165.0 K, respectively, and as for all noble elements (except helium, which does not freeze at 1 atm), the temperatures are close. Figure 3.3 shows the phase diagram of xenon and Figure 3.4 shows the vapor pressure as a function of temperature. Of all the noble elements, xenon in liquid form has the second highest density at about 3.0 g cm^{-3} (radon has a density of 4.4 g cm^{-3}). Figure 3.5 is a plot of the liquid xenon density versus temperature. Solid xenon has a density of 3.64 g cm^{-3}. As with all noble elements, xenon undergoes very few chemical reactions. Some examples of synthetic xenon compounds are PtF_6Xe, XeF_2, XeF_4, and XeF_6. Some basic properties of xenon and other noble elements are given in Table 3.1.

There are nine stable naturally occurring isotopes: ^{124}Xe, ^{126}Xe, ^{128}Xe, ^{129}Xe, ^{130}Xe,
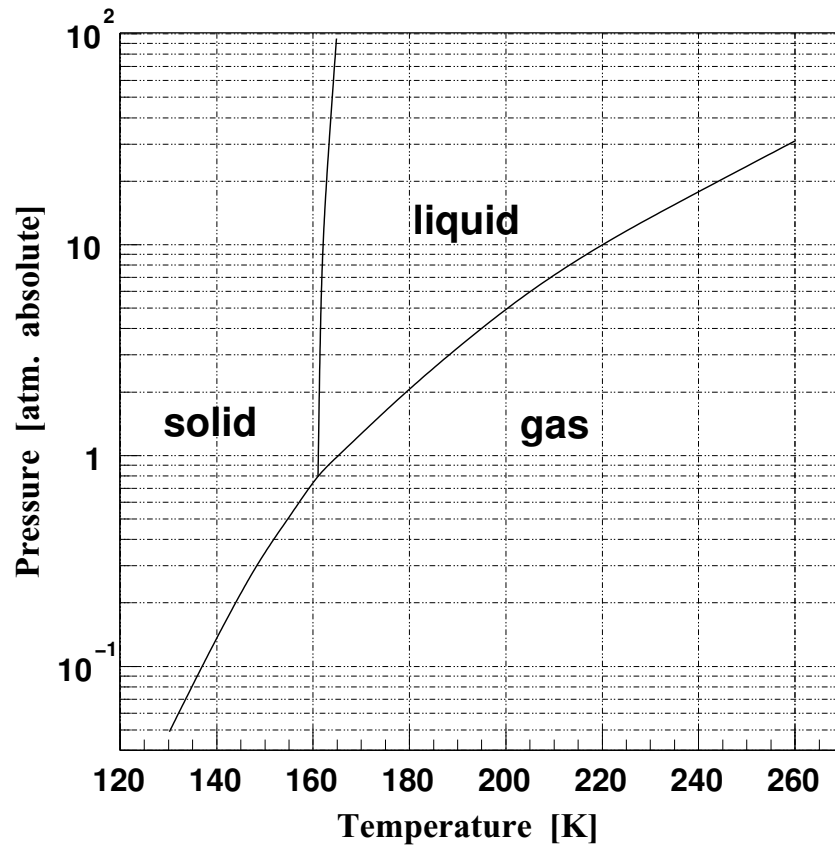
Figure 3.3: Phase diagram of xenon.

[131]Xe, [132]Xe, [134]Xe, and [136]Xe. Only tin has more stable isotopes. The properties of these isotopes are summarized in Table 3.2. [124]Xe, [134]Xe and [136]Xe are expected to double beta decay but have not been observed to do so. The Enriched Xenon Observatory (EXO) aims to detect the neutrino-less double beta decay of [136]Xe, which would prove that neutrinos are massive Majorana particles [233]. Over 40 isotopes have been created and studied. [131m]Xe, ^{133}Xe, [133m]Xe, and [135]Xe result from fission of [235]U and [239]Pu making them indicators of nuclear explosions. [135]Xe, with its large cross section to thermal neutrons (2.65×10^6 barns), is responsible for the "xenon poisoning" seen in reactors whereby [135]Xe captures the neutrons (and transforms into stable [136]Xe) that would otherwise initiate fission. This isotope is generated by the decay of [135]I, a common fission product. Under normal operations, the reaction rate is set such that [135]Xe is burned and maintained at an equilibrium
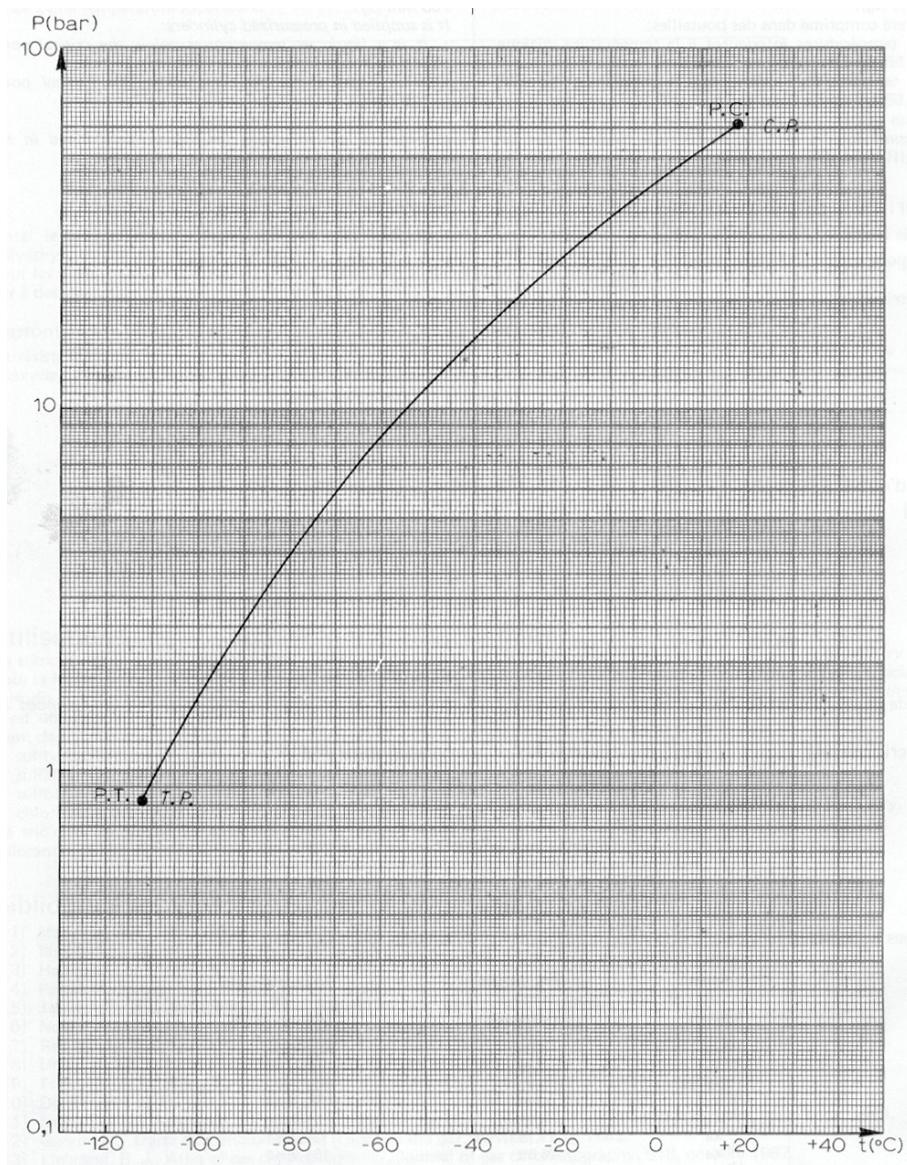
Figure 3.4: The vapor pressure of xenon as a function of temperature.
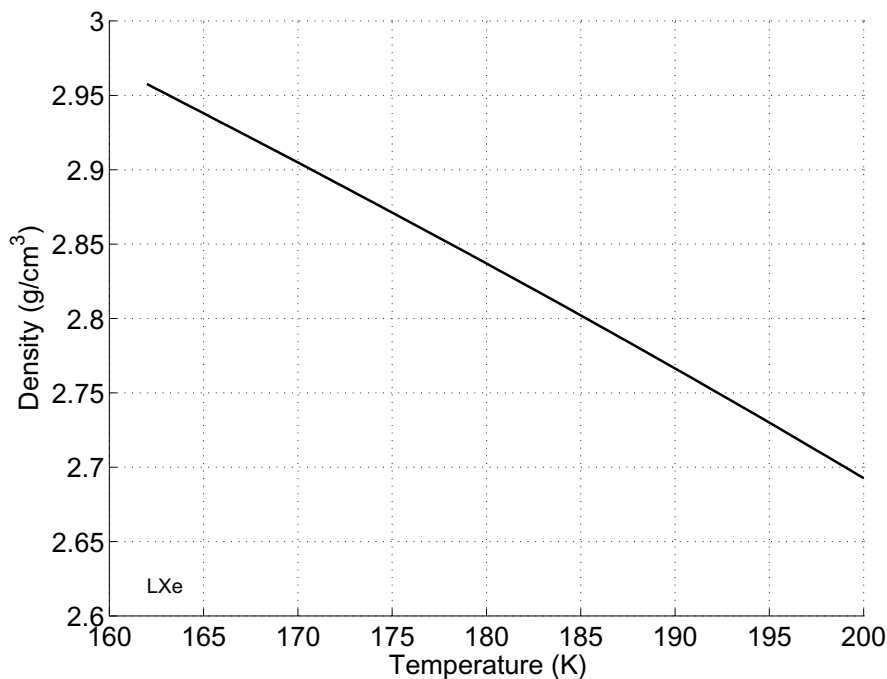
Figure 3.5: The density of liquid xenon as a function of temperature.

concentration. A failure to recognize the presence of ^{135}Xe caused the Chernobyl disaster [234].

Although, xenon has no long-lived isotopes, it does contain ^{85}Kr, which is a beta emitter. Fortunately, ^{85}Kr can be removed to negligible levels by distillation [197] or chromatography [235].

3.4   Basic Particle Interactions with Xenon

An important characteristic of the target material is its efficiency in transforming radiation energy into measurable quanta (e.g., phonons, photons, and electrons). The type of interaction depends on the particle's charge, mass, and momentum. Light charged particles such as electrons and alphas interact electromagnetically producing tracks of atomic excitations and ionizations. Charged particles can also generate bremsstrahlung and/or Cerenkov radiation but neither of these processes occur in our energy range of interest (<100 keV).

Table 3.2: Properties of naturally occurring xenon isotopes.

Isotope	Atomic Mass (m_a/u)	Natural Abundance (%)	Nuclear Spin (I)	Magnetic Moment (μ/μ_N)
^{124}Xe	123.9058942	0.09	0	0
^{126}Xe	125.904281	0.09	0	0
^{128}Xe	127.9035312	1.92	0	0
^{129}Xe	128.9047801	26.44	1/2	-0.777977
^{130}Xe	129.9035094	4.08	0	0
^{131}Xe	130.905072	21.18	3/2	0.691861
^{132}Xe	131.904144	26.89	0	0
^{134}Xe	133.905395	10.44	0	0
^{136}Xe	135.907214	8.87	0	0

Chargeless particles like gammas and neutrons do not directly generate bulk excitation and ionization directly but do so by generating recoiling electrons or nuclei, respectively. A recoiling heavy nucleus not only generates atomic excitations and ionizations but also atomic motion. This results in an apparent suppression (or "quenching") of scintillation and ionization with respect to electron recoils of the same energy. It is important to point out that discrimination in two-phase xenon detectors do not rely on this suppression as both the scintillation and ionization channels are equally suppressed. Both photons and electrons can travel long distances in xenon that is free of impurities.

This section describes the basic interactions of various particles with xenon, the processes concerning the intermediate products and the transport properties of the induced ionization and scintillation.

Gamma Ray Interactions

Gamma rays eject an electron through photoelectric absorption, Compton scattering or pair production (if the energy of the gamma exceeds twice the rest mass of the electron). The cross section of these three processes are proportional to $Z^4/E_\gamma^{7/2}$, Z/E_γ, and $Z^2 \ln(2E_\gamma)$, respectively. Photoelectric absorption results in the complete absorption of a photon, generating an electron with energy equal to that of the photon minus the ionization energy. In Compton scattering, only a fraction of the photon energy is spent in ejecting the electron
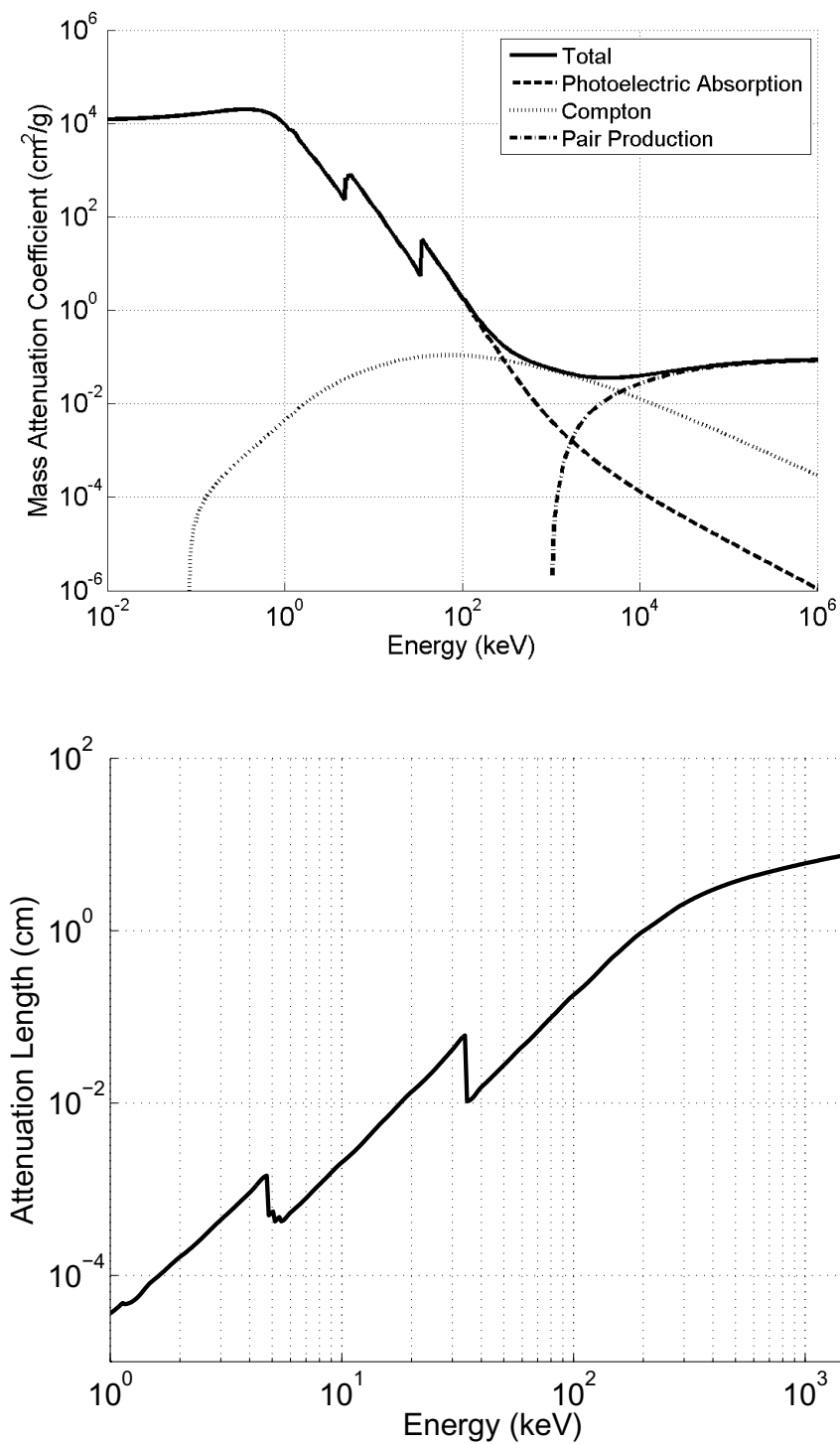
Figure 3.6: The mass attenuation coefficient (top) for photons on xenon and the total attenuation length (bottom) of gammas in liquid xenon as a function of energy [18].

and that energy is related to the scattering angle by

$$\frac{1}{E_f} - \frac{1}{E_0} = \frac{1}{m_e c^2}(1 - \cos\theta).\qquad(3.1)$$

Pair production is only possible for gammas with energy $E_\gamma \geq 2m_e = 1.02$ MeV, the rest mass of two electrons. Photoelectric absorption is the dominant interaction of lower energy photons. Figure 3.6 shows the mass attenuation coefficient for the three different types of gamma interactions and the total attenuation length of gammas in liquid xenon as a function of energy. The structures at ~5 keV and ~30 keV represent the L-shell and K-shell absorption edges. The abrupt drops in the mean free path at edges are due to the energy of the gamma being sufficient to eject electrons of an additional shell. The vacancy is filled with an other shell electron which releases an x-ray or Auger electron. These plots show the effectiveness of LXe for self-shielding. The attenuation length of 1 MeV gammas is ~6 cm in LXe.

Neutron Interactions

Neutrons interact primarily with nuclei since, as chargeless particles, they can not interact with the surrounding electrons. Neutrons can either scatter off of or be absorbed by nuclei. In elastic scattering, the total kinetic energy remains the same. A neutron recoiling off a nucleus of atomic weight A will lose an average energy of $2EA/(A+1)^2$. This expression explains the effectiveness of hydrogen-rich materials (such as water and plastic) as neutron moderators. In the case of inelastic scattering, some of the energy can be channeled into exciting the nucleus. The excited nucleus eventually relaxes and radiates. A neutron can also be absorbed by nucleus. In general, the addition of a neutron can lead to a rearrangement of the nuclear structure and an eventual emission of gammas, neutrons, protons, deuterons or alphas. Fission fragmentation can also occur. Collisions yielding protons, deuterons, multiple neutrons and other larger fragments are negligible until $E > 1$–10 MeV. Some nuclear excited states are very brief such as ^{125m}Xe, which decays with a half-life of 57 s and emits a 253 keV gamma. ^{125m}Xe can be produced by absorption of thermal neutrons, $(^{124}\text{Xe}(n,\gamma)^{125m}\text{Xe})$. ^{131m}Xe, which is produced by inelastic scattering of ^{131}Xe,

has a half-life of 11.8 days and emits 163.9 keV gammas upon relaxation. Its long half-life makes it a useful source for uniformly probing all regions of the detector [236].

Recoiling Particles in Liquid Xenon

In this section, we give a general overview of the interactions of recoiling particles in liquid xenon and the interactions of resulting products.

Energetic particles slow down as they deposit energy into the detector medium. They can lose energy electronically through the creation of atomic excitations and ionization or by generating atomic motion (phonons). Alphas and electrons (from gamma interactions and beta decays) lose energy almost entirely through the former process whereas a recoiling xenon atom (from a neutron or WIMP collision) will lose energy primarily through the latter.

The electronic energy deposition creates scintillation by the following processes:

1) De-excitation

$$\mathrm{Xe^* + Xe} \quad \rightarrow \quad \mathrm{Xe_2^*} \tag{3.2}$$

$$\mathrm{Xe_2^*} \quad \rightarrow \quad \mathrm{2Xe} + h\nu \tag{3.3}$$

2) Recombination

$$\mathrm{Xe^+ + Xe} \quad \rightarrow \quad \mathrm{Xe_2^+} \tag{3.4}$$

$$\mathrm{Xe_2^+} + e^- \quad \rightarrow \quad \mathrm{Xe^{**} + Xe} \tag{3.5}$$

$$\mathrm{Xe^{**}} \quad \rightarrow \quad \mathrm{Xe^*} + heat \tag{3.6}$$

$$\mathrm{Xe^* + Xe} \quad \rightarrow \quad \mathrm{Xe_2^*} \tag{3.7}$$

$$\mathrm{Xe_2^*} \quad \rightarrow \quad \mathrm{2Xe} + h\nu \tag{3.8}$$

The scintillation of all noble elements is believed to follow this mechanism. Importantly, this scintillation mechanism results in the generation of photons that do not ionize the xenon. In the presence of an electric field, some of the electrons are prevented from recombining which results in less scintillation. The recombination scintillation mechanism results in an
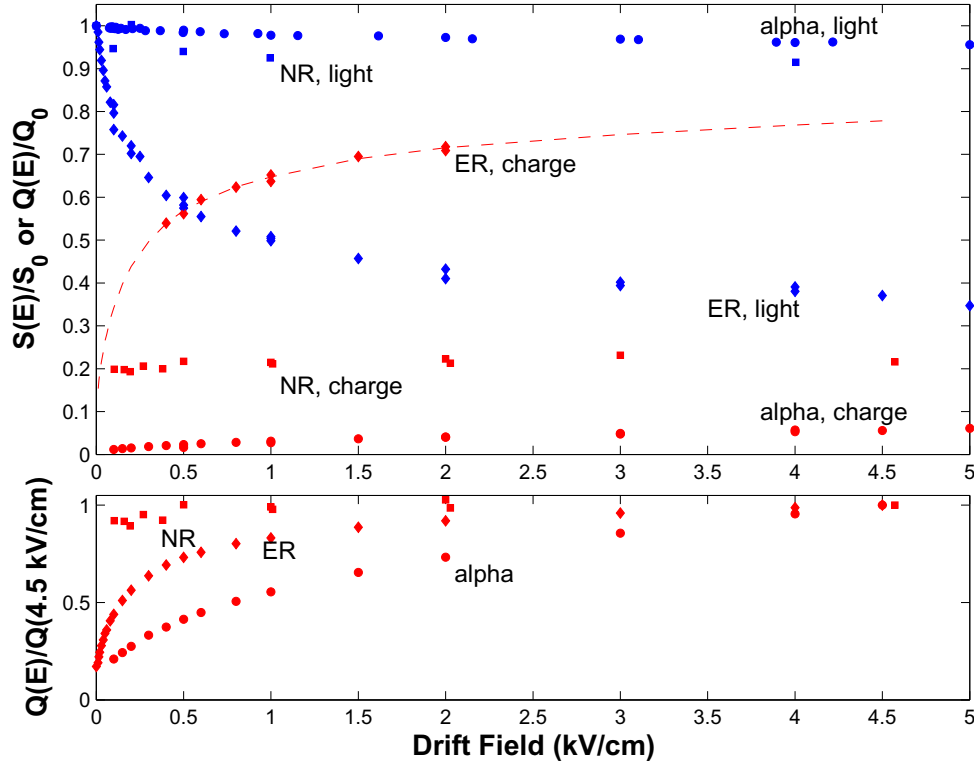
Figure 3.7: Above – light and charge yield of 122 keV gammas, 56 keV nuclear recoils, 5.3 MeV alphas relative to that of the maximum value as a function of electric field. Below – same ionization data but plotted as a fraction of the 4.5 kV/cm value. These measurements were performed by the Case and Columbia groups [19].

observable one-to-one anticorrelation between the average electron and photon yields across electric fields. The anticorrelation is also seen at a single electric field as the fraction of recombination fluctuates from event to event. This fluctuation leads to a observed variance in the charge signal that greatly exceeds that expected from Poisson statistics (Fano factor > 1). More details on recombination fluctuations and our measurements of its values for 122 keV gammas at different electric fields is given in Section 5.6. Note that the total number of electrons and photons do not change with electric field.

Electrons, alphas and Xe atoms propagate through liquid xenon in different ways manifesting as different charge and light yields. The top graph of Figure 3.7 shows the light and charge yield as a function of field for 122 keV gammas, 56 keV nuclear recoils, 5.3 MeV
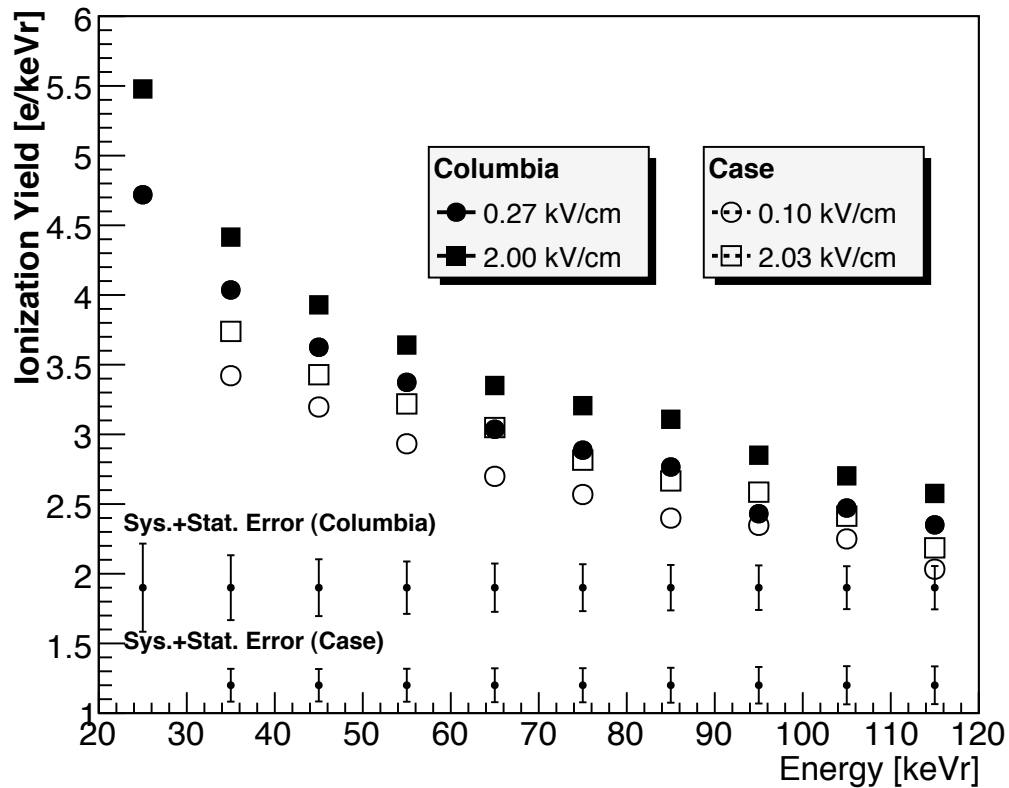
Figure 3.8: The energy dependence of nuclear recoils as measured by Columbia and Case [19].

alphas relative to their respective maximum values as measured by the Case and Columbia groups [19]. The bottom graph of Figure 3.7 shows the ionization yield relative to their respective values at 4.5 kV/cm. As expected the charge yield increases with field. Figure 3.9 shows the electronic stopping power of electron, alpha, and Xe recoils as a function of energy as given by ESTAR, ASTAR [18] and SRIM [20]. Also included is the total energy lost to electronic excitation per unit path length for Xe recoils, which differs from the electronic stopping power in that it includes energy lost via electronic stopping of secondary recoils. The decrease in Xe recoil stopping power at lower energies is responsible for the rise in ionization yield (see Figure 3.8, which shows measurement by the Case group and our collaborators at Columbia [19]). The stopping power of Xe nuclei at 56 keV (including the daughter recoils) is higher than that of 5.3 MeV alphas. Presumably this would translate
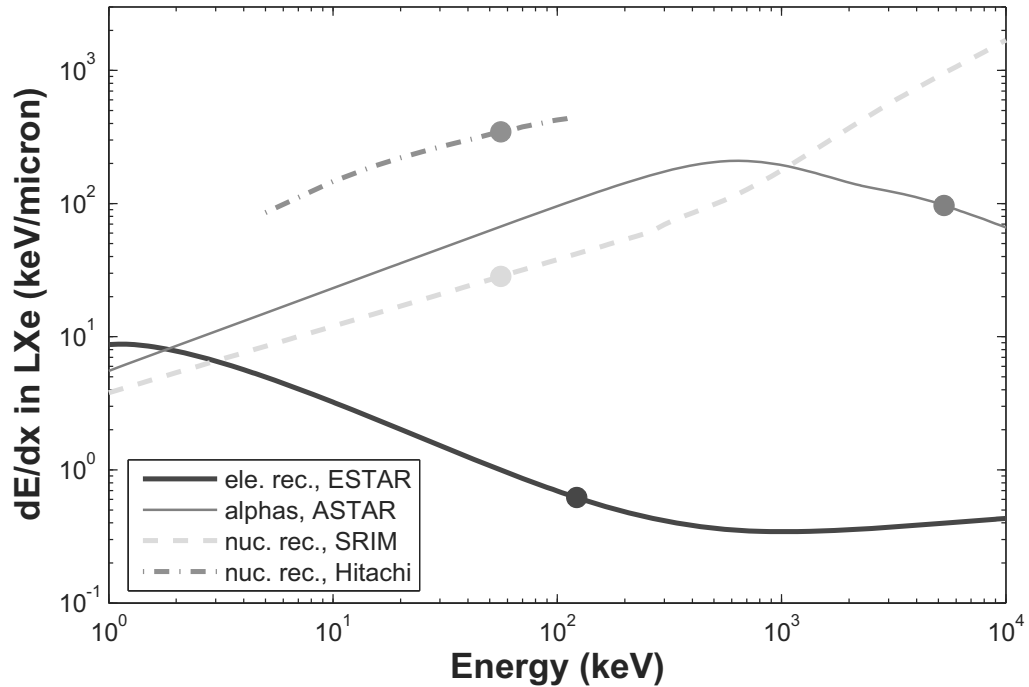
Figure 3.9: The electronic stopping power of electron, alpha and Xe atom recoils [18, 20, 21]. The Hitachi result includes the energy lost via stopping of secondary recoils.

into a higher charge density and thus a lower ionization yield for the nuclear recoils. Instead, we observe that the nuclear recoils give the higher ionization yield. This suggests that other aspects such as the track structure also play a role. Alphas are presumed to have straight cylindrical tracks with a dense core and a "penumbra" of delta rays [237]. A nuclear recoil track Monte Carlo was written using cross sections and stopping powers in [238] and is described in [60]. Simulations show that the nuclear recoil tracks have many branches (see Figure 3.10(a)) with much of the energy carried away by these branches, which presumably end in a very sparse track since the stopping power falls with energy. The electron recoil track (see Figure 3.10(b)), in comparison, does not have the branching structure of Xe recoils and are larger with lower ionization density, hence the relatively higher yield and field dependence. Electron recoil tracks were created with PENELOPE, a simulation package for propagating electrons and photons [239].

The scintillation pulses in liquid noble element detectors have been observed to contain
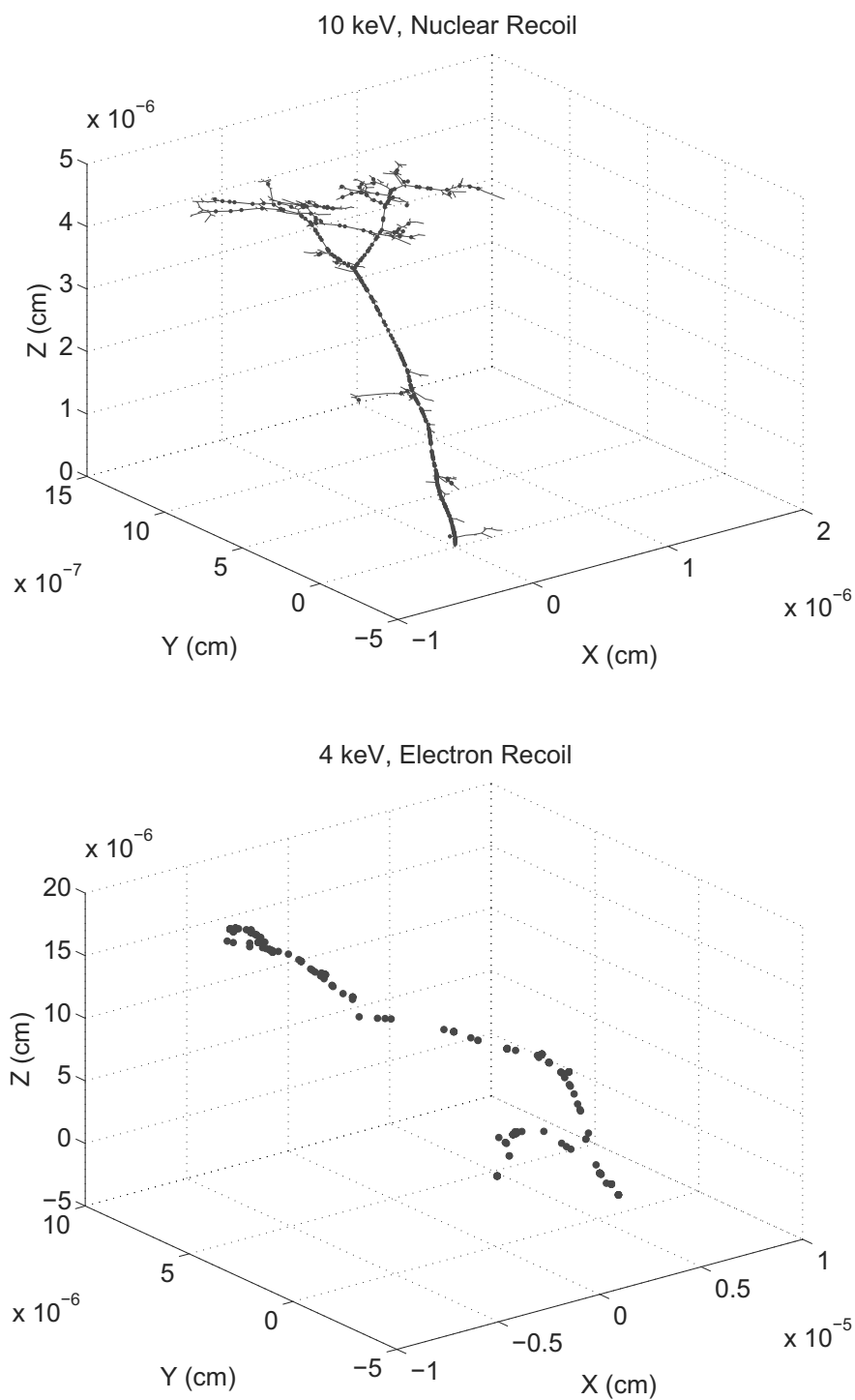
Figure 3.10: Tracks of 10 keV nuclear recoil (top) and 4 keV electron recoil (bottom) in liquid xenon. The ions are indicated by dots.
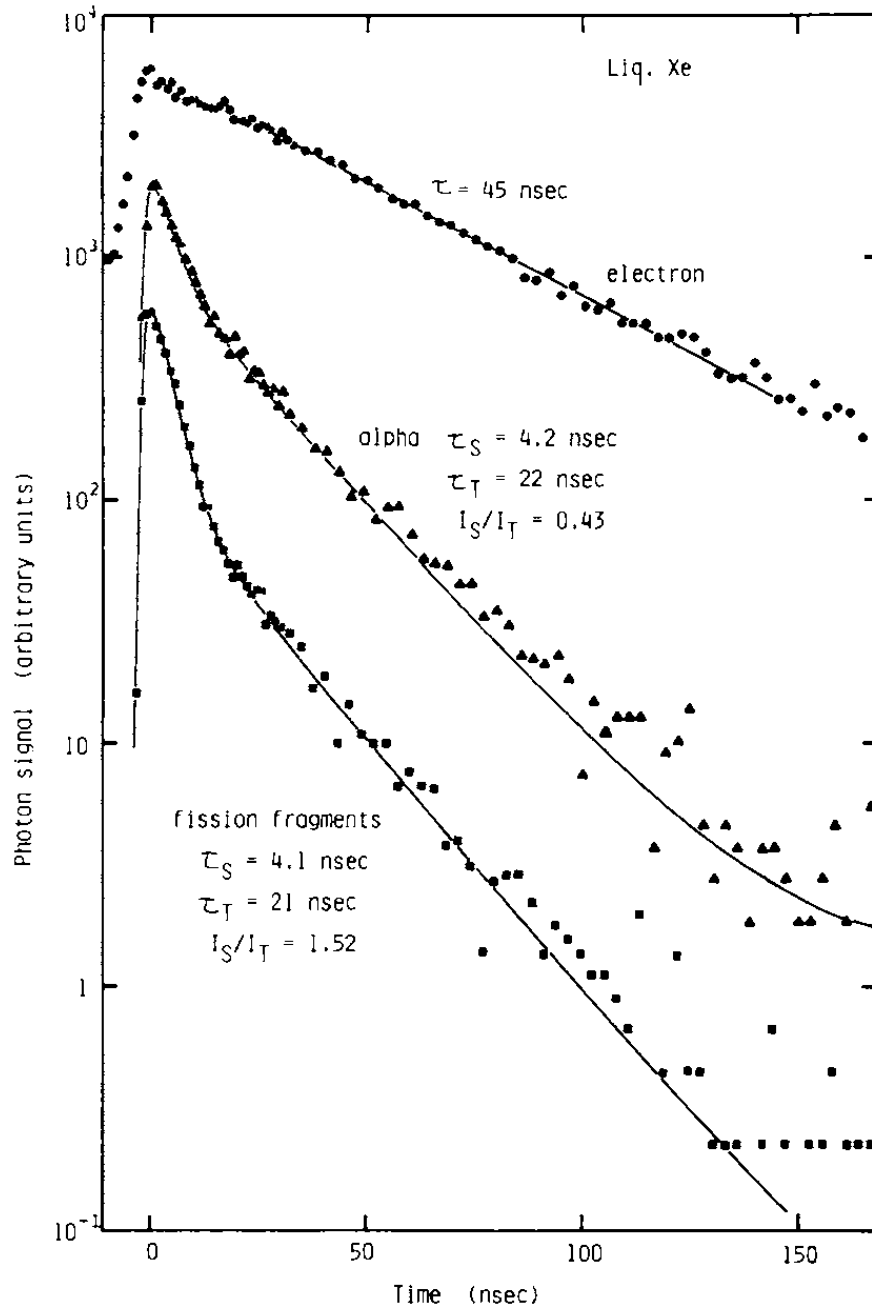
Figure 3.11: The scintillation pulse shape under different particle excitations at zero electric field as measured by Hitachi [22].
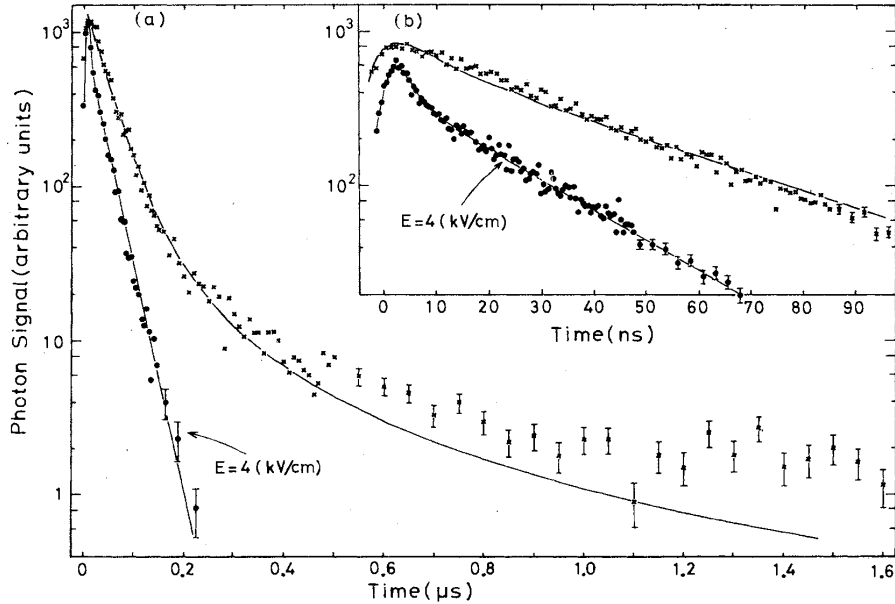
Figure 3.12: The electron recoil scintillation pulse at an electric field of zero and 4.0 kV/cm as measured by Kubota [23].

Table 3.3: Scintillation constants and intensity ratios of various particles in liquid xenon [71, 22].

Particle	τ_1	τ_3	$(\frac{I_1}{I_3})$
Electron (1 MeV, 4 kV/cm)	2.2±0.3 ns	27±1 ns	0.05
Alpha (^{210}Po and ^{252}Cf)	4.3±0.6 ns	22±1.5 ns	0.45±0.07
Fission Fragment (^{252}Cf)	4.3±0.5 ns	21±2 ns	1.6±0.2

two falling exponential components. The excimers, Xe_2^*, can exist in either the singlet or triplet state, which have decay times of 4 and 27 ns, respectively, for xenon. It has been shown that the ratio of singlet to triplet states is positively correlated with the LET [22]. As a result, the nuclear recoils, with higher LET, release light more promptly (see Table 3.3). Figure 3.11 shows the scintillation pulse of electron, alpha and fission fragment interactions at zero electric field. It has also been demonstrated that the decay times are independent of the LET [22]. The scintillation of electron recoils in liquid xenon has a 45 ns fall time tail component at zero field that disappears when an electric field is applied. Figure 3.12 shows the electron recoil light pulse at zero and 4.5 kV/cm electric fields. This field dependence suggests that the tail is due to charge recombination. As this component is not observed

for nuclear recoils (because of the much shorter recombination times), it serves as another mechanism for PSD in xenon. The recombination tail is also not observed for any type of recoil in liquid argon or neon, presumably for the same reason. The conversion of singlets to triplets (which is the lower energy excited state) by free electrons has been proposed as the mechanism behind the positive correlation between LET and I_1/I_3 [240, 22] – the electrons of lower LET events exist unbounded for a longer period and thus have a greater chance for converting states. The conversion of singlets to triplets is unlikely to occur because of the energy difference. This reaction has been observed in the gaseous state [241]. Section 5.3 describes the Case group's study of pulse shape discrimination in a two-phase liquid xenon detector.

As previously mentioned, the Xe recoils deposit most of their energy into atomic motion which is not observed in liquid xenon detectors. The fraction of the total energy deposited in electronic interactions is typically known as the "nuclear quenching" factor. A theory formed by Lindhard [242] describes the appropriation of energy by incident ions into nuclear motion and electronic excitation. The relative scintillation yield at zero electric field between nuclear and electron recoils (usually with respect to 122 keV electron recoils), $\mathcal{L}_{eff}$, is less than that of nuclear quenching as calculated by Lindhard because of two effects: "electronic quenching" and electron loss. As the scintillation decay times do not appear to be dependent on LET, the electronic quenching is presumed to occur before self-trapping, perhaps involving the loss of Xe*. Hitachi proposes a mechanism for electronic quenching [21]:

$$\mathrm{Xe}^* + \mathrm{Xe}^* \rightarrow \mathrm{Xe} + \mathrm{Xe} + e^-. \tag{3.9}$$

One potential photon is lost in this process. A photon is also lost if an electron drifts away instead of recombining. The nuclear quenching (Lindhard) multiplied by electronic quenching factors gives the relative scintillation yield. The relative scintillation is very important as this value sets the recoil energy axis with respect to a gamma calibration line and consequently determines the expected WIMP event rate for a particular cross section.

The nuclear recoil energy based on $S1$ is

$$E_r = E_e/\mathcal{L}_{eff} \cdot S_e/S_r, \tag{3.10}$$

where E_e is the electron recoil energy scaled linearly from gamma peak and S_e and S_r are the electric field dependent scintillation yields relative to that at zero field for electron and nuclear recoils. Many groups have measured $\mathcal{L}_{eff}$ at energies relevant to WIMP searches. These experiments generally measure this value by irradiating a single-phase detector with a mono-energetic bean of neutrons. The recoil energy is constrained by tagging the scattered neutrons at different angles with a secondary liquid scintillation detector. Figure 3.13 shows the $\mathcal{L}_{eff}$ of these measurements including a theoretical prediction. Also included in the plot are the values predicted by Hitachi [21] and that determined by comparing XENON10 data with simulations [30].

3.5 Charge and Light Transport Properties

The electrons and photons that are generated by particle interactions must sometimes travel great distances before they are collected. The manner in which electrons and photons interact with the xenon is important as this affects the quality of the signal. Electrons diffuse as they drift through xenon and can be collected by charge impurities. Photons can also be absorbed by impurities. Due to its scintillation mechanism, the xenon is invisible to its own scintillation and thus the photons can travel far as long as the xenon is clean. In this section, we give a brief survey on the transport properties of electrons and photons in the xenon.

3.5.1 Electron and Ion Mobilities in Xenon

As the electrons drift, they diffuse a distance $\sqrt{4Dt}$ where D is the diffusion constant and t is time. Figure 3.17 shows the energy dependence of the diffusion constants of electrons in liquid xenon and liquid argon [35, 243].
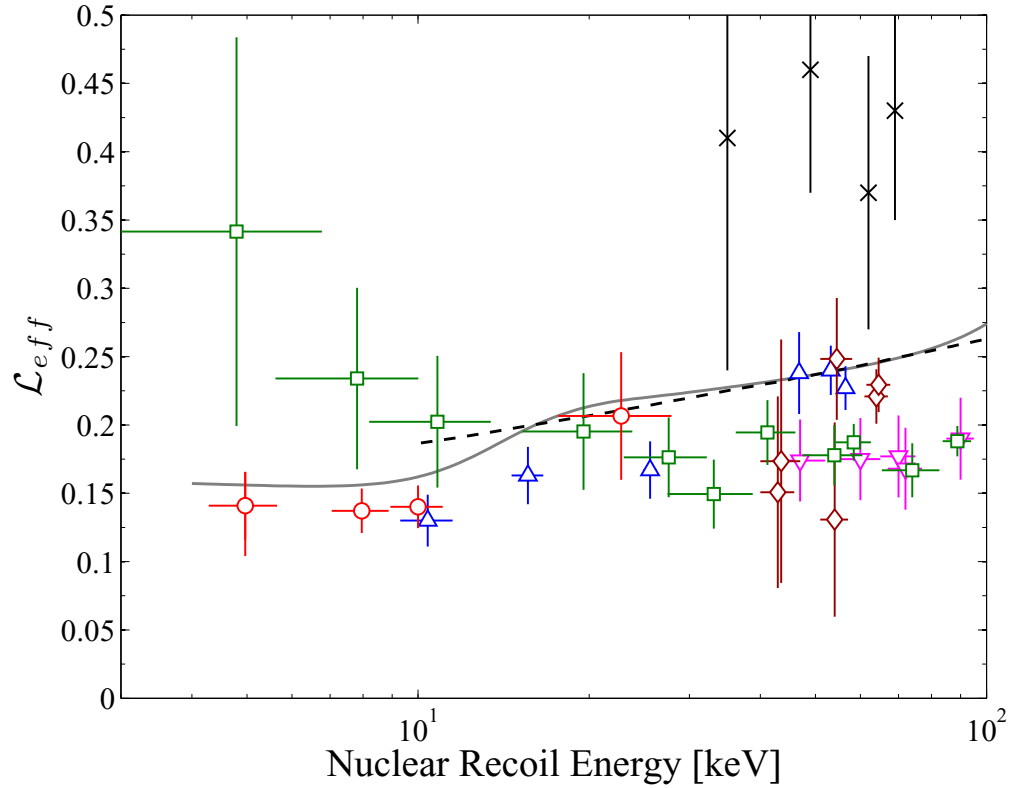
Figure 3.13: The scintillation efficiency of nuclear recoils relative to 122 keV electron recoils. The symbols and corresponding references: red circle – Aprile et al. (2008) [24], blue triangle – Aprile et al. (2005) [25], green square – Chepel et al. [26], brown diamond – Akimov et al. [27], cross – Bernabei et al. [28], pink triangle – Arneodo et al. [29]. The solid line represents the values determined by a best-fit analysis of the XENON10 data [30]. The dash line represents the theoretical prediction by Hitachi [21]. This plot is from [24].
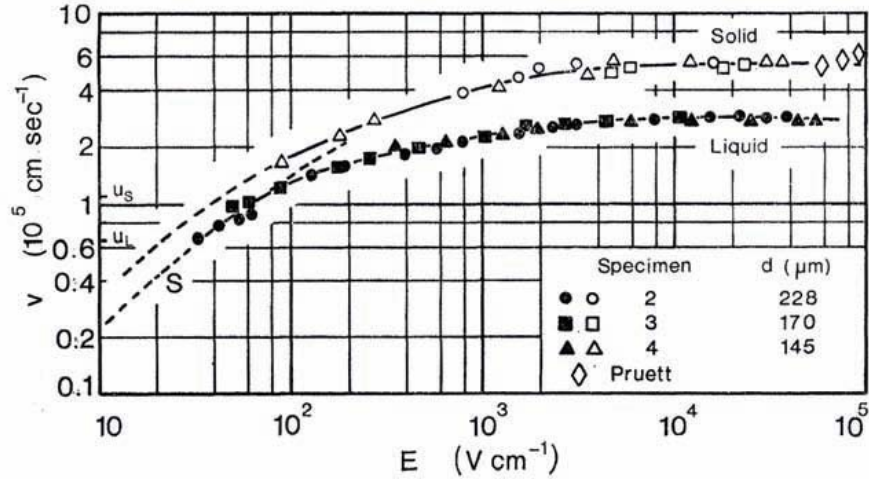
Figure 3.14: The electron velocity in solid xenon at 157 K and liquid xenon at 163 K [31].

In the presence of an electric field, electrons and ions accelerate and achieve stable average drift velocities. The velocity of electrons in liquid and solid xenon increases with field until ~1 kV/cm as seen in Figure 3.14 [31]. For gas, the electron mobility is constant until about E/N = 2×10^{-2} Td (1 Td = 10^{-17} V cm^2) as seen in Figure 3.15. Note that the drift velocity is higher in liquid for the same E/N. Xenon ions and molecular ions (Xe$_2^-$) move much slower than electrons in liquid xenon as they are much heavier. Figure 3.16 is a plot of the mobilities of Xe$^-$ and Xe$_2^-$ in xenon gas as a function of the electric field.

3.5.2 Electron Capture

Impurities in the xenon can capture electrons. This decreases the size of the signal and introduces a position dependence. The latter effect is readily seen in two phase detectors, where the depth of the event determines how much liquid xenon the electrons must pass through before being extracted into the gas. There are three types of attachment processes [222]:

1) Radiative attachment

$$e + AB \rightarrow AB^- + h\nu \tag{3.11}$$
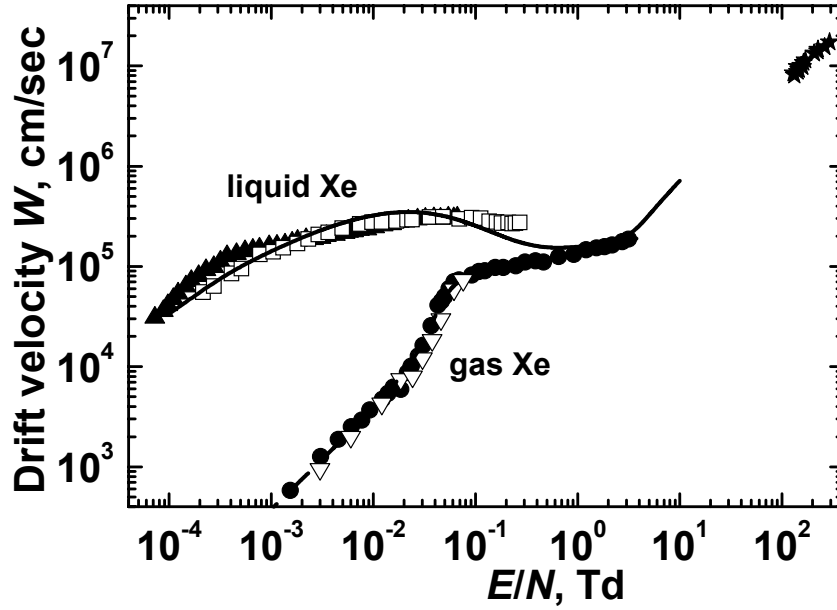
Figure 3.15: The electron velocity in liquid and gas xenon as a function of E/N which is the electric field divided by the density (cm^{-3}) [32]. The points at the upper right corner are for xenon gas. 1 Td = 10^{-17} V cm^2. E/N = 10^{-2} Td, corresponds to 1.4 kV/cm in liquid ($\rho = 3.0$ g/cm^3) and 2.7 V/cm in gas ($\rho = 5.9 \times 10^{-3}$ g/cm^3).

2) Dissociative attachment

$$e + AB \rightarrow A + B^- \tag{3.12}$$

3) Three-body attachment

$$e + AB \quad \rightarrow \quad (AB^-)^* \tag{3.13}$$

$$(AB^-)^* + \text{Xe} \quad \rightarrow \quad AB^- + \text{Xe} \tag{3.14}$$

In the three-body attachment, the Xe atom carries away the binding energy (energy of electron affinity). The typical charge sensitive LXe detector has a uniform drift field volume with a charge collecting cathode. The collected ionization Q can be quantified by the following equation:

$$Q(x) = Q(0) \ e^{-\frac{x}{l_e}} = Q(0) \ e^{-\frac{t}{\tau_e}}, \tag{3.15}$$

where $Q(0)$ is the initial amount of charge, x and t are the drift distance and time, re-
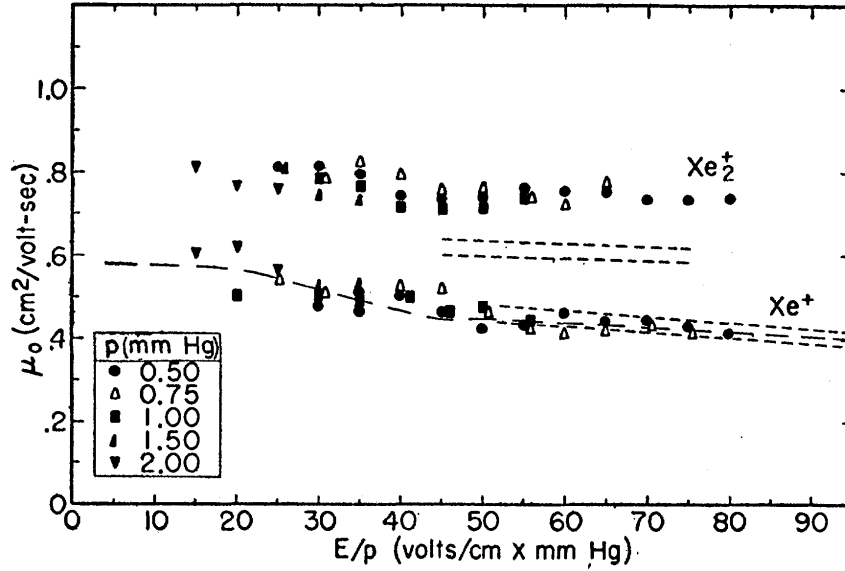
Figure 3.16: Mobilities of Xe^- and Xe_2^- in xenon gas as functions of electric field [33].

spectively, to the collecting electrode, and l_e and τ_e are the electron drift length and drift time fit parameters, respectively, with $l_e = v_e \tau_e$, where v_e is the electron drift velocity. The electron drift length is obtained by fitting the $S2$ of a gamma line to Equation 3.15. The rate of attachment (defined as $k = (\tau_e n_i)^{-1}$ where n_i is the density of impurities) of electrons to SF_6, N_2O, and O_2 as a function of electric field has been measured in LAr and LXe [36] and is shown in Figure 3.18. The attachment rate to SF_6 is much higher than that to N_2O and O_2 at the electric fields measured – at 1 kV/cm, the difference is greater than two orders of magnitude. Between 10^2 to 10^4 V/cm, the attachment rate increases with field for N_2O but decreases for the other two solutes.

One of the early arguments against the development of commercial liquid xenon detectors was the lack of long-term purity. Now, purification can be achieved by passing xenon through various devices. One such product is the Oxisorb$^{\text{TM}}$ purifier [244], which contains a cartridge made of glass or aluminum that absorbs water and molecular oxygen. According to manufacturer specifications, water and oxygen can be cleaned to <30 ppb and <5 ppb, respectively, on input streams of 10 ppm. Xenon can also be purified with metal getters (e.g. Saes MonoTorr$^{\text{TM}}$). Spark purifiers have been applied to both liquid and gas xenon
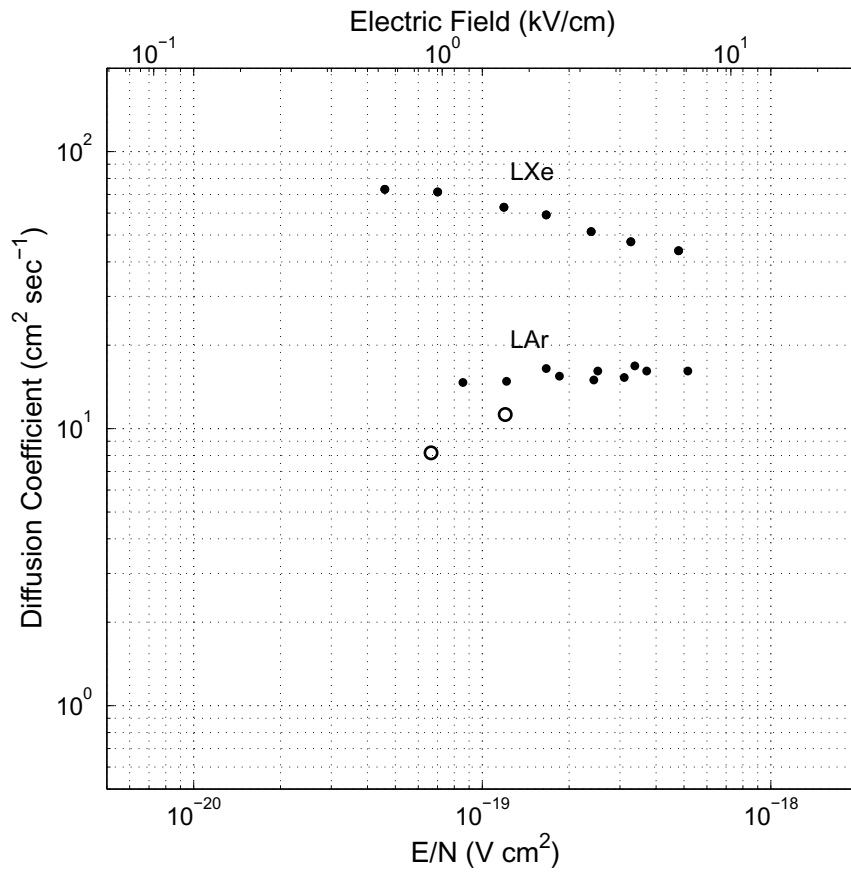
Figure 3.17: Electron diffusion coefficients in liquid xenon and argon versus electric field. The top axis is the electric field for liquid xenon case where $\rho = 3.0$ g/cm^3 [34]. The open circles are measurements by Derenzo [35].
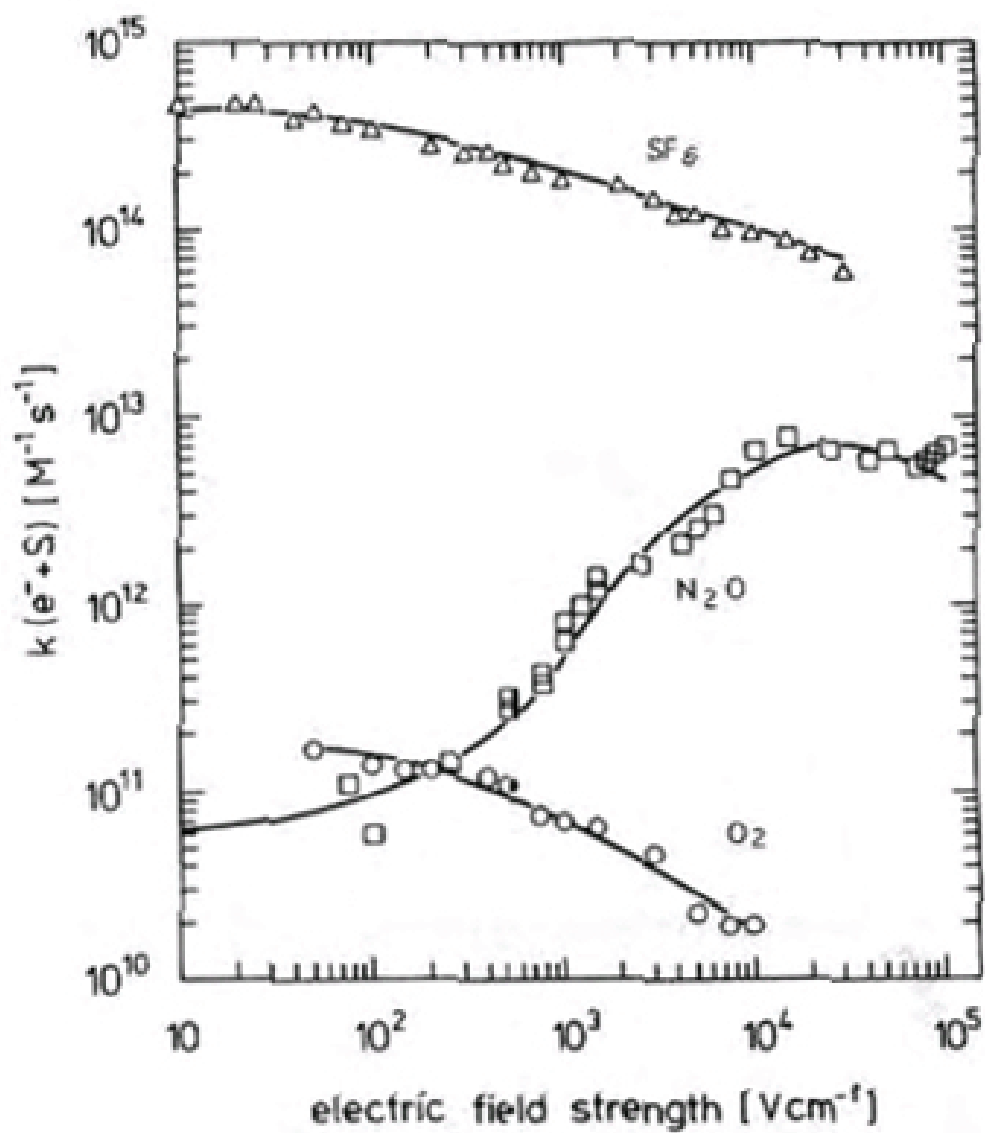
Figure 3.18: The electron attachment rates to SF_6, N_2O, and O_2 in LXe as a function of electric field [36]

[245, 246], achieving drift lengths greater than a meter. This system operates on the same principle as that of the hot metal getters but with greater efficiency. The purifier works by creating sparks between two titanium electrodes, which create titanium dust with chemically clean surfaces that absorb impurities. In fact, it has been shown that the titanium dust can continue cleaning the xenon for years [247]. Purity is further enhanced by the UV light of the sparks, which breaks down complex molecules. Usually, the xenon is first purified with an Oxisorb cartridge and getter before being cleaned with the spark purifier. Spark purifiers have the advantage of being able to clean liquid xenon, allowing for a much higher purification rate. It has been shown that the level of purity achieved with chemical methods (Oxisorb$^{\text{TM}}$, molecular sieve,or metal getter) require 1–2 weeks of purification to reach the same level of purity achieved in 1–2 days with a spark purifier [245].

3.5.3   Transport of Charges Across Gas-Liquid Interface

Liberated electrons can be pulled out of the liquid and into the gas if they acquire enough momentum. The potential energy at the interface can be described by

$$V_1(Z) \;=\; V_0 - eE_1Z + A_1, Z < 0, \tag{3.16}$$

$$V_2(Z) \;=\; -eE_2Z + A_2, Z > 0, \tag{3.17}$$

$$A_{1,2} = \frac{-e^2(\epsilon_1 - \epsilon_2)}{4\epsilon_{1,2}(Z + \beta Z/|Z|)(\epsilon_1 + \epsilon_2)}, \tag{3.18}$$

where V_0 is the ground state energy of the electron in the liquid; ϵ_1 and ϵ_2 are the dielectric constants of the liquid and gas, respectively; β is the thickness of the liquid-gas transition layer; and $Z < 0$ is the liquid phase. Electrons with momentum greater than $\sqrt{2m_e|V_0|}$ can leave the liquid. Figure 3.19 shows the potential energy versus Z for $V_0 < 0$ and $V_0 > 0$. Figure 3.20 shows measurements of the electron extraction efficiencies of argon and xenon in liquid and solid states [38].
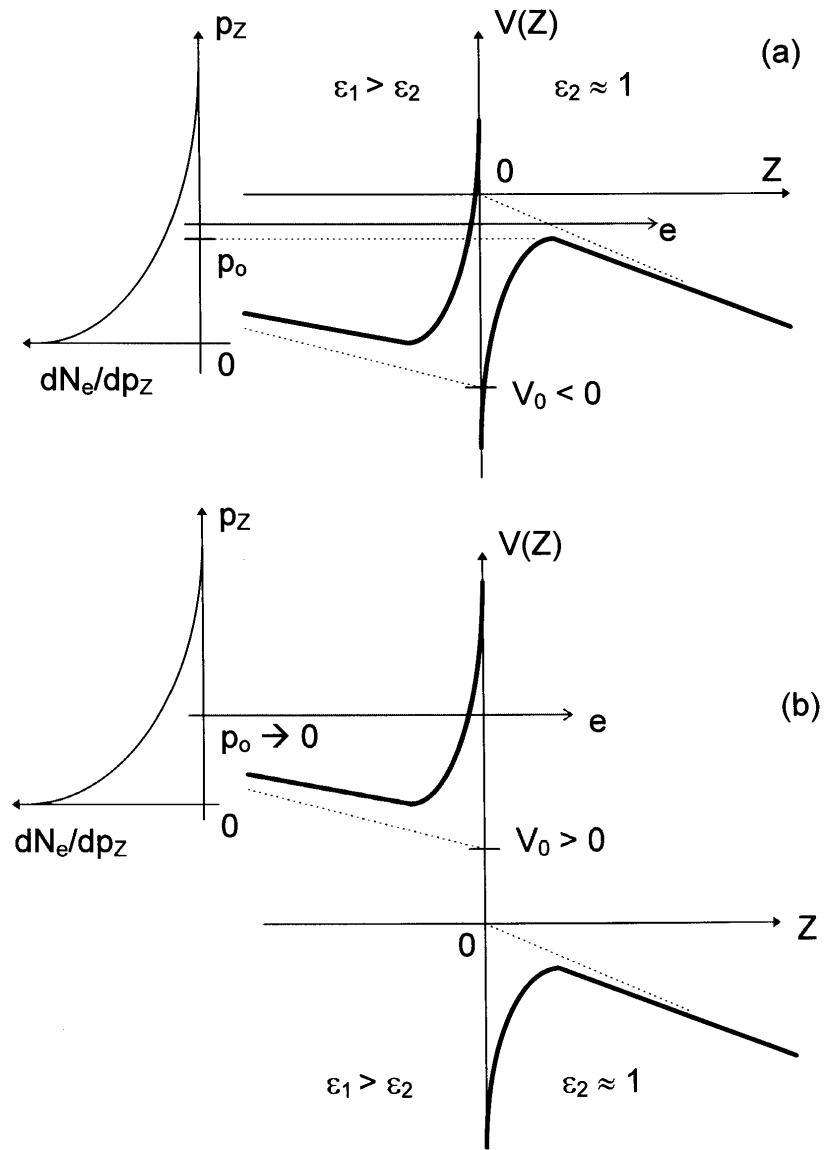
Figure 3.19: The potential energy of free electrons near the liquid/gas interface for a non-polar dielectric with negative (a) and positive (b) energy V_0 of ground state [37].
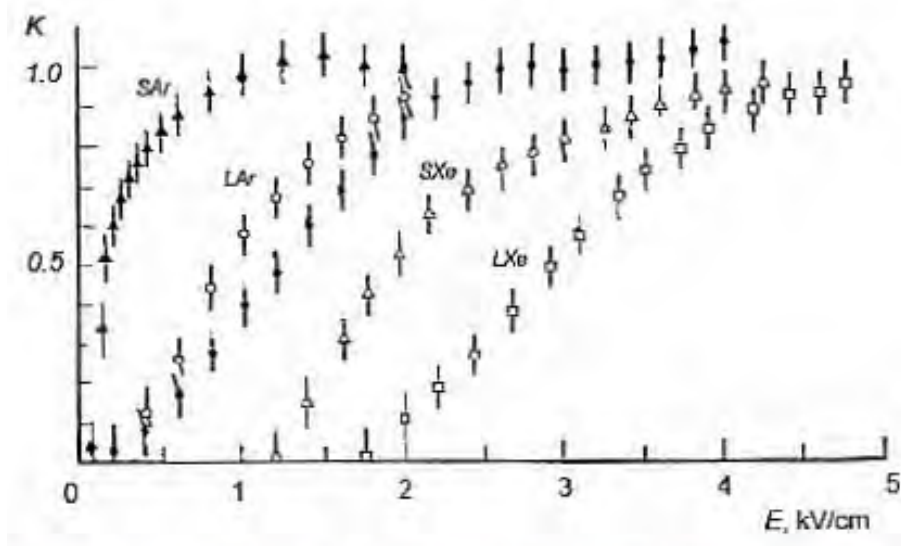
Figure 3.20: The electric field dependence of the liquid-to-gas extraction efficiency of electrons in solid argon (T = 80 K), liquid argon (T = 90 K, closed circles - fast component, open circles - slow component), solid xenon (T = 160 K), and liquid xenon (T = 165 K) [38].

3.5.4 Proportional Scintillation

If electrons acquire sufficient drift velocity, they can excite the xenon gas and release scintillation. The number of proportional light photons created by electrons drifting in noble gases follows the empirical equation

$$dN_{ph} = a \left(\frac{E}{P} - b\right) P \, dx, \tag{3.19}$$

where E [cm/kV] is the electric field; P [bar] is the pressure; dx [cm] is the distance traveled; and a and b are the fitted constants which are 70 photons/keV and 1 kV/cm/bar, respectively, for xenon gas [37].

3.5.5 Scintillation Propagation

Light attenuation can be described by an attenuation length λ_{att}, which consists of two components, the absorption length, λ_{abs}, and the elastic scattering length, λ_{sca}. The relation
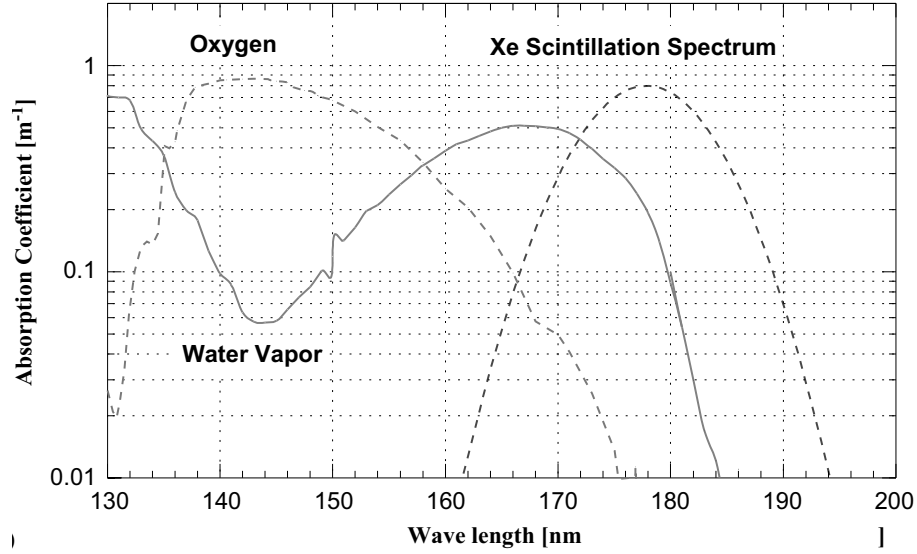
Figure 3.21: Absorption spectrum of 1 ppm of water and oxygen in liquid xenon [39]. Also shown is the Xe scintillation spectrum.

between the interaction lengths is

$$\frac{1}{\lambda_{att}} = \frac{1}{\lambda_{abs}} + \frac{1}{\lambda_{sca}}. \tag{3.20}$$

In scintillation detectors, the λ_{abs} is much more important than the λ_{sca} as elastically scattered light can still be collected. Due to the unique scintillation mechanism of xenon, it is essentially transparent to its own scintillation. Impurities are responsible for light absorption. Two common light absorbing impurities in liquid xenon are water and oxygen. Figure 3.21 shows the absorption spectrum of 1 ppm of water and oxygen overlapped with the emission spectrum of xenon [248, 249]. The absorption length in liquid xenon has been measured to be greater than 100 cm in a 100 liter prototype developed for the MEG experiment [39].

Elastic scattering is dominated by Rayleigh scattering. The Rayleigh scattering length can also affect the final signal size – decreasing this length increases the total travel distance and thus raises the probability of absorption. The inverse of the Rayleigh scattering length is

$$\frac{1}{\lambda_R} = \frac{\omega^4}{6\pi c^4} \left[kT\kappa_T\rho^2 \left(\frac{\partial \epsilon}{\partial \rho} \right)_T^2 + \frac{kT^2}{\rho c_v} \left(\frac{\partial \epsilon}{\partial T} \right)_\rho^2 \right] \tag{3.21}$$
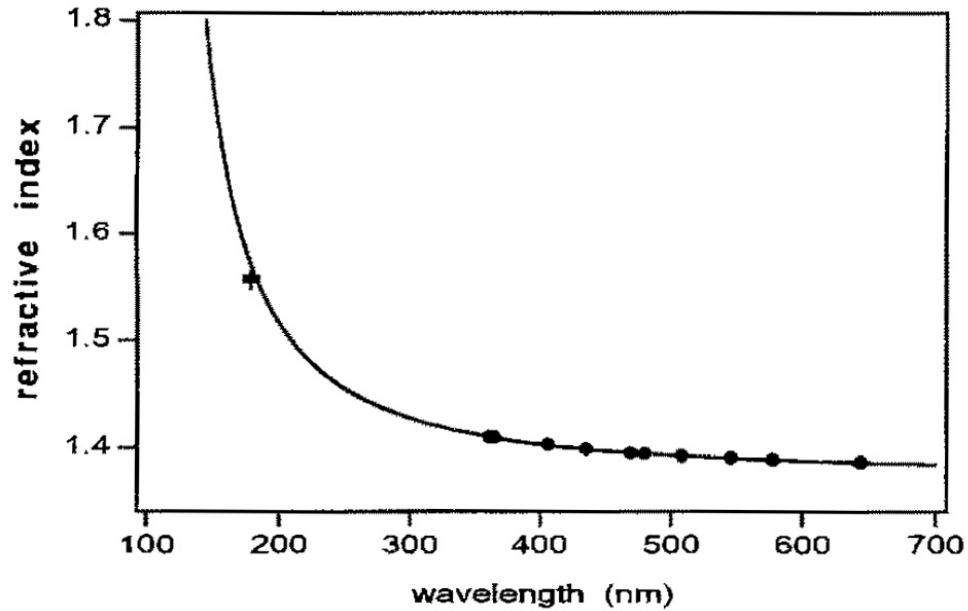
Figure 3.22: The refractive index of liquid xenon at the the triple point versus wavelength [40, 41].

where ω is the angular frequency of the scintillation, c is the speed of light, k is Boltzmann's constant, T is the temperature, ρ is the liquid density, κ_T is the isothermal compressibility, c_v is the heat capacity at constant volume and ϵ is the dielectric constant [250]. The scattering length has been calculated to be 30 cm [251] and measured to be 29 cm [252]. Equation 3.21 also shows how the spatial density fluctuations by temperature gradients can increase the amount of Rayleigh scattering. Note, that Equation 3.21 shows that the $\lambda_R \propto \lambda_{Xe}^4$, where λ_{Xe} is the scintillation wavelength. This means that increasing the wavelength can greatly extend the Rayleigh scattering length. This can be accomplished by coating the walls of the detector volume with a wavelength shifter or by doping the liquid.

As previously stated, most photons generated in the liquid tend to stay there due to the large mismatch in refractive indices of the liquid and gas. The refractive index of xenon gas is $\sim$1. The refractive index of liquid xenon depends on wavelength (Figure 3.22) and density (Figure 3.23). The critical angle of total internal reflection at 170°C is $\arcsin(1.0/1.69) = 36°$.
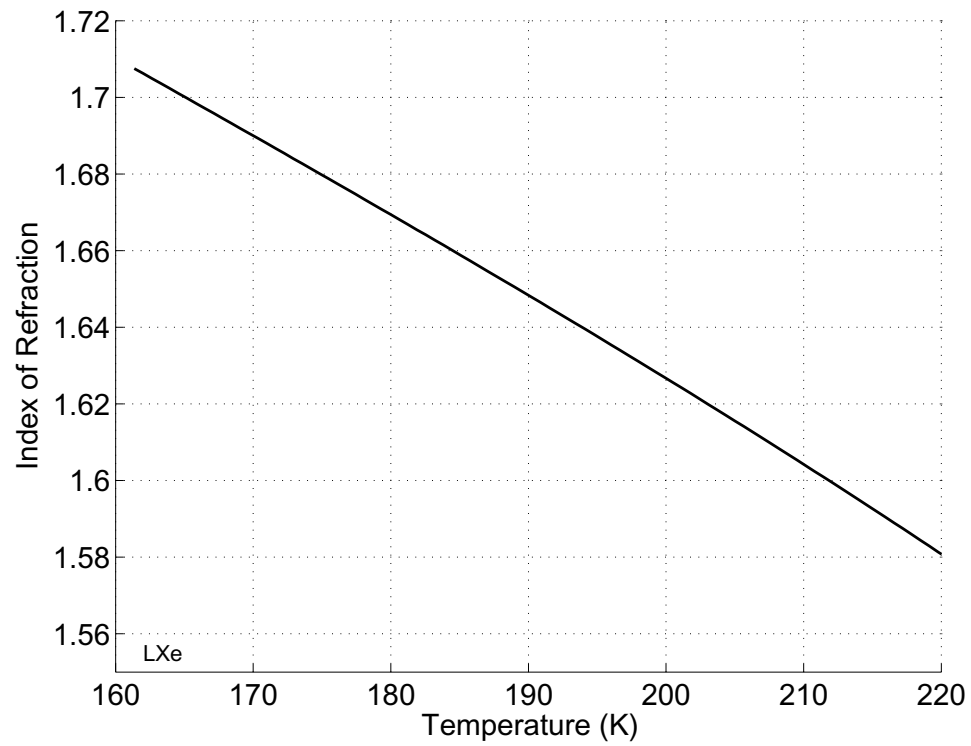
Figure 3.23: The index of refraction of liquid xenon as a function of temperature [42]. The discrepancy between this measurement and that by Barkov et al. [40], shown in Figure 3.22 may be due to a lower attenuation length in the latter measure

Chapter 4

Case Detector

All the research and development described in the next chapter was performed with a cryostat that was constructed and tested at Princeton University in 2003 by Tom Shutt and the author. The cryostat and initial set of detectors were designed by Shutt. Many of the subsequent detectors and supporting structures were designed and constructed by the author.

This section gives a description of the Case cryostat, detectors and other supporting structures.

4.1   Case Cryostat

To obtain robust and consistent light and charge signals from the detector, the cryostat must provide a stable isothermal environment for the liquid xenon. In addition, the cryostat must also be reliable, easy to use and affordable. There are two common sources of cooling power. Cooling with liquid nitrogen is cheap and reliable as there are no moving parts. The detector can be cooled by extending a long rod or "cold-finger" between the liquid nitrogen and detector. The other option is to use a pulse-tube refrigerator (PTR), which is convenient but has a greater chance for mechanical failures (leaks, pump failures, etc.) thus necessitating a separate emergency cooling system. In a cold-finger cryostat, liquid xenon will simply freeze, during an electrical blackout as the heating units shut off. Another
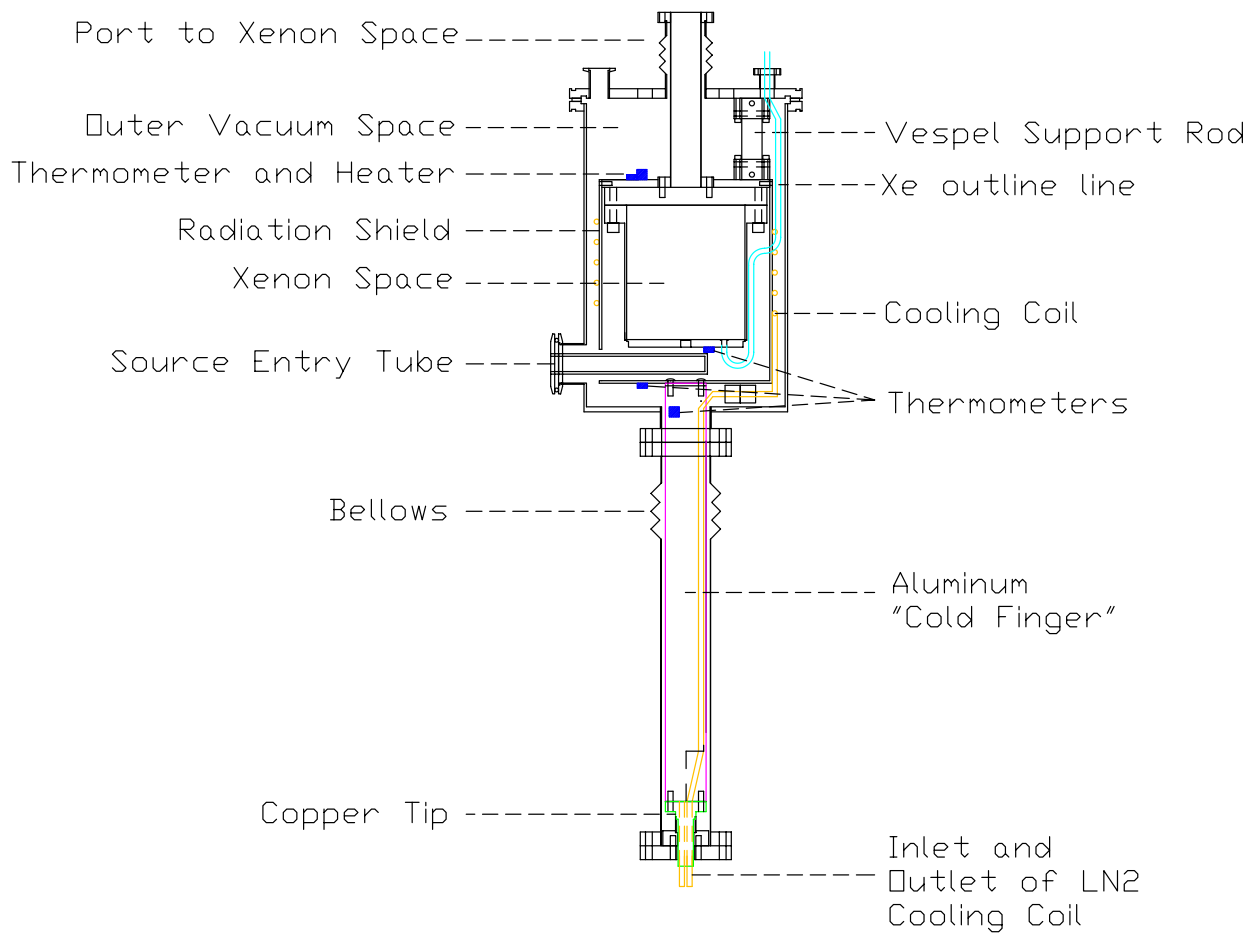
Figure 4.1: Cold-finger cryostat designed by Tom Shutt.

disadvantage of the PTR system is the high upfront equipment cost.

We opted for a vacuum-insulated liquid nitrogen cooled cold-finger cryostat constructed primarily out of commercial parts. Figure 4.1 is a side view of the Case cryostat designed by Tom Shutt. The cryostat has a 22″ long, 2″ diameter aluminum rod as the cold-finger and three concentric cans: the outer chamber can, the radiation shield can and the Xe can. The use of modified commercial parts helps to lower the cost and allows for easier modifications. The outer can is constructed out of stainless steel 10″ ISO-LF parts and provides the vacuum insulation for the detector and aluminum rod. There are three 2-3/4″ Conflat ports with thin-walled tubing (to minimize heat loads) that extend from the Xe can. These three ports are each welded to the outer can with a bellows to eliminate stresses during thermal contractions.

The aluminum radiation shield can is bolted onto the aluminum base plate. The aluminum stick is attached to the bottom of this can, and bolted onto the other end of the stick is a copper tip that comes into direct contact with the liquid nitrogen. To conserve liquid nitrogen when running at higher temperatures, a thermal impedance (i.e. plastic disc) is inserted in between the bottom of the radiation shield and the aluminum stick. A 1/4″ copper tube loop is soldered onto the aluminum can with inputs and outputs at the bottom of the aluminum cold-finger. This loop serves as a conduit for liquid nitrogen, providing the >100 W cooling power needed for the initial cool down.

Attached to the copper piece at the end of the cold-finger is a pouch containing activated carbon (also called activated charcoal). The carbon improves the vacuum by adsorbing residual gas atoms through van der Waals attraction. Activated carbon has an exceptionally high surface area for adsorption – one gram has a surface area of $\sim$500 m^2.

The Xe can is a 316 stainless steel 8″ diameter, 6.6″ long Conflat half-nipple that holds the detector (as seen in Figure 4.2). The tube end is welded shut with a stainless steel plate. The center of this plate is partially bored out to a thickness of 1 mm to provide an entrance "window" for low energy gammas. A 1/4″ stainless steel tube is welded to the bottom of the can and serves as the outlet for the LXe. As the walls of the Xe can are fairly thin
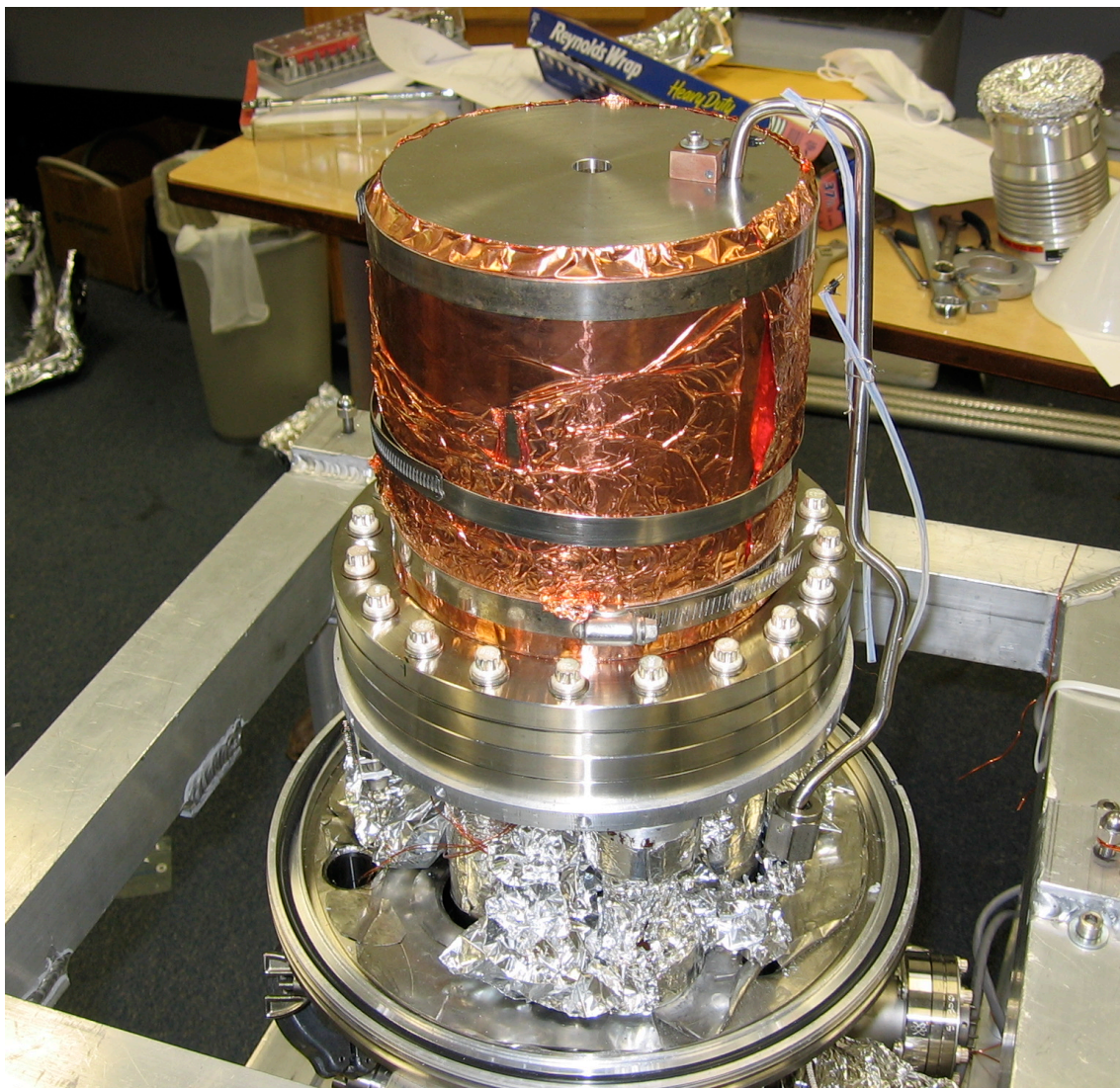
Figure 4.2: Xe can, upside-down. The $1/4''$ stainless steel tube is the liquid xenon outlet tube. The apparent hole at the center of the bottom surface is the entrance "window" for low energy gammas. The copper block next to the tube is an enclosure for the platinum thermistor. Surrounding the walls of the can are many layers of copper foil which increase the temperature uniformity of the chamber.

and made of stainless steel which has low thermal conductivity, the opposite ends of the can are fairly decoupled and lead to non-uniformities in the LXe temperature. To increase the conductivity, several layers of copper foil (k $\sim$ 400 W/m/K) has been tightly wrapped around the walls of the can.

To introduce low energy gammas into the detector region through the window on the Xe can, an aluminum tube passes through openings in the outer vacuum can and radiation shield (as seen in Figure 4.1). This tube allows for the changing of radioactive sources without opening the cryostat.

Three 1″ diameter Vespel rods bolted onto the aluminum base plate and outer vacuum chamber support the weight of the internal structures. Vespel is used instead of metal because of its low thermal conductivity yet high strength. A stable cryostat temperature is maintained by a proportional-integral-derivative (PID) controller that powers a 50 W heater and monitors several platinum thermistors on the Xe can, radiation shield and cold-finger. Thin copper quad-twist cryogenic wires connect the thermometers to the controller. The standard four-wire measurement technique is used to eliminate the distortions from changes in the electric lines. The resistance of the Pt thermocouple is measured by passing a known current through two of the wires and measuring the voltage drop across the thermometer with the other two. There is no voltage drop across any of the voltage sensing wires as there is no current, thus the wire resistance is irrelevant. We observe a LXe temperature stable to within 0.1 K. Both the inner (Xe can) and outer vacuum spaces are monitored with ion gauges while pumping. To cover higher pressures, the inner and outer spaces are monitored with a Convectron (thermocouple) and Baratron (capacitance) gauges, respectively. Figure 4.3(a) and Figure 4.3(b) are plots of the temperature at the bottom of the Xe can and xenon gas pressure, respectively, over 20 days. The temperature rms was 16 mK over the 20 days and 5 mK over the first 5 days.

Care was taken to minimize the various sources of heat leakage. One source of heat is conduction through material which follows

$$P = \frac{kA}{L}\Delta T, \tag{4.1}$$
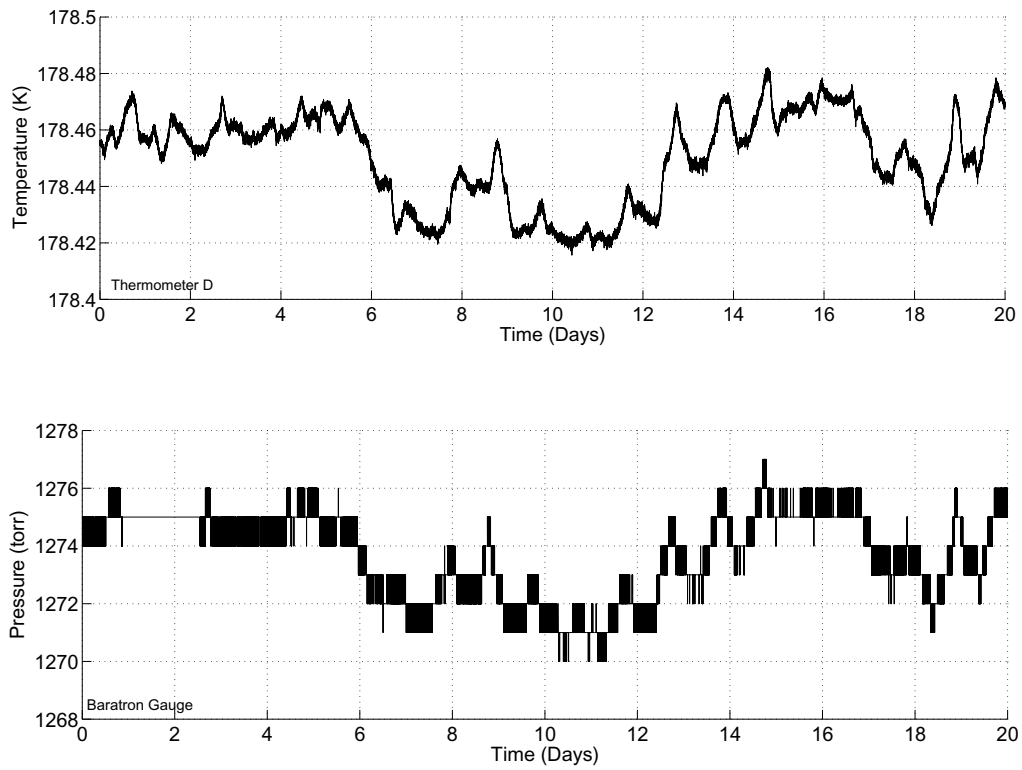
Figure 4.3: The temperature at the bottom of the Xe can (top) and the pressure (bottom) versus time.

Table 4.1: Thermal conductivities common substances are room temperature [73].

Material	Conductivity (W/m K)
Air	0.024
Aluminum	156
Copper	395
Diamond	2000
Gold	298
Polyimide	0.33
Silver	419
Stainless Steel	15
Water	0.59

where k is the thermal conductivity, A is the cross section area, L is the length and ΔT is the temperature difference across the material. Table 4.1 shows the thermal conductivities of various materials at room temperature. The three $1.5''$ stainless steel tubes, three Vespel rods and electrical lines introduce heat loads of about 2 W, 0.56 W, and several tens of mW respectively. The heat load by residual gas is negligible.

Another source of heat is black-body radiation. The total power of black-body radiation on the inner surface follows Stefan-Boltzmann law:

$$P = A\epsilon\sigma(T^4 - T_0^4), \tag{4.2}$$

where A is the inner surface area, ϵ is the emissivity of that surface, $\sigma = 5.67 \times 10^{-8}$ J s^{-1} m^{-2} K^{-4} is the Stephan-Boltzmann constant, T is the temperature of the inner surface and T_0 is the temperature of the surrounding surface. Table 4.2 shows the emissivity of several materials. The emissivity depends on the surface temperature and finish. To reduce the radiative load, ten layers of aluminized mylar (super insulation) cover the sides and bottom of the radiation shield can, the Vespel rods, stainless steel bellows and the top of the aluminum base plate (as seen in Figure 4.4). The aluminized mylar has an emissivity of $\sim$5%. The radiative load without the mylar insulation is about 4.5 W. The ten layers cuts the radiation load by a factor of $\sim$10. This insulation also lowers the heat load by lowering the mean free path of the residual gas particles.

Figure 4.4: The radiation can covered with 10 layer aluminized mylar. The Vespel rods and stainless steel bellows have also been covered with the insulation.

Table 4.2: Table of emissivities of common materials [74].

Material	Temperature	Emissivity
Aluminum, unoxidized	100°C	0.03
Aluminum, oxidized	199°C	0.11
Aluminum, heavily oxidized	93°C	0.20
Carbon, unoxidized	100°C	0.81
Copper, highly polished	38°C	0.02
Copper, black, oxidized	38°C	0.78
Glass, convex D	100°C	0.80
Glass, nonex	100°C	0.82
Iron, oxidized	100 C°C	0.74
Iron, unoxidized	100°C	0.05
Silver, polished	200°C	0.02
Stainless steel 301, polished	24°C	0.27
Stainless steel 301, polished	232°C	0.57
Stainless steel 303, polished	316°C	0.74
Stainless steel 316, polished	24°C	0.28
Stainless steel 316, polished	232°C	0.57

4.2 Gas System

The gas panel directs the flow of gas between the two storage bottles and between the bottles and the detector while purifying the xenon with a metal getter. Figure 4.5 is a photo of the bottles, panel and cryostat. Figure 4.6 is a schematic of the gas system. All components are connected with $1/4''$ stainless steel tubing with Swagelok VCR fittings with metal gasket compression seals. These high performance seals have a maximum leak rate of 4×10^{-9} std cm^3 s^{-1}. A regulator with a constant downstream pressure sits between the gas bottles and the panel. There are several Swagelok bellows valves for defining the flow path. The pressure at several points on the panel are measured with dial pressure gauges. The flow of gas is controlled by a calibrated mass flow controller. Also on the gas panel is a Monotorr getter purifier and gas pump. The panel was constructed inside a cleanroom to limit the entrance of dust. The $1/4''$ tubing was cleaned in an ultrasonic bath with alcohol before installation. Before use, the gas panel and gas bottles were evacuated while baking at 100°C and 200°C, respectively. Before initial use, the entire system was checked with a helium leak detector.
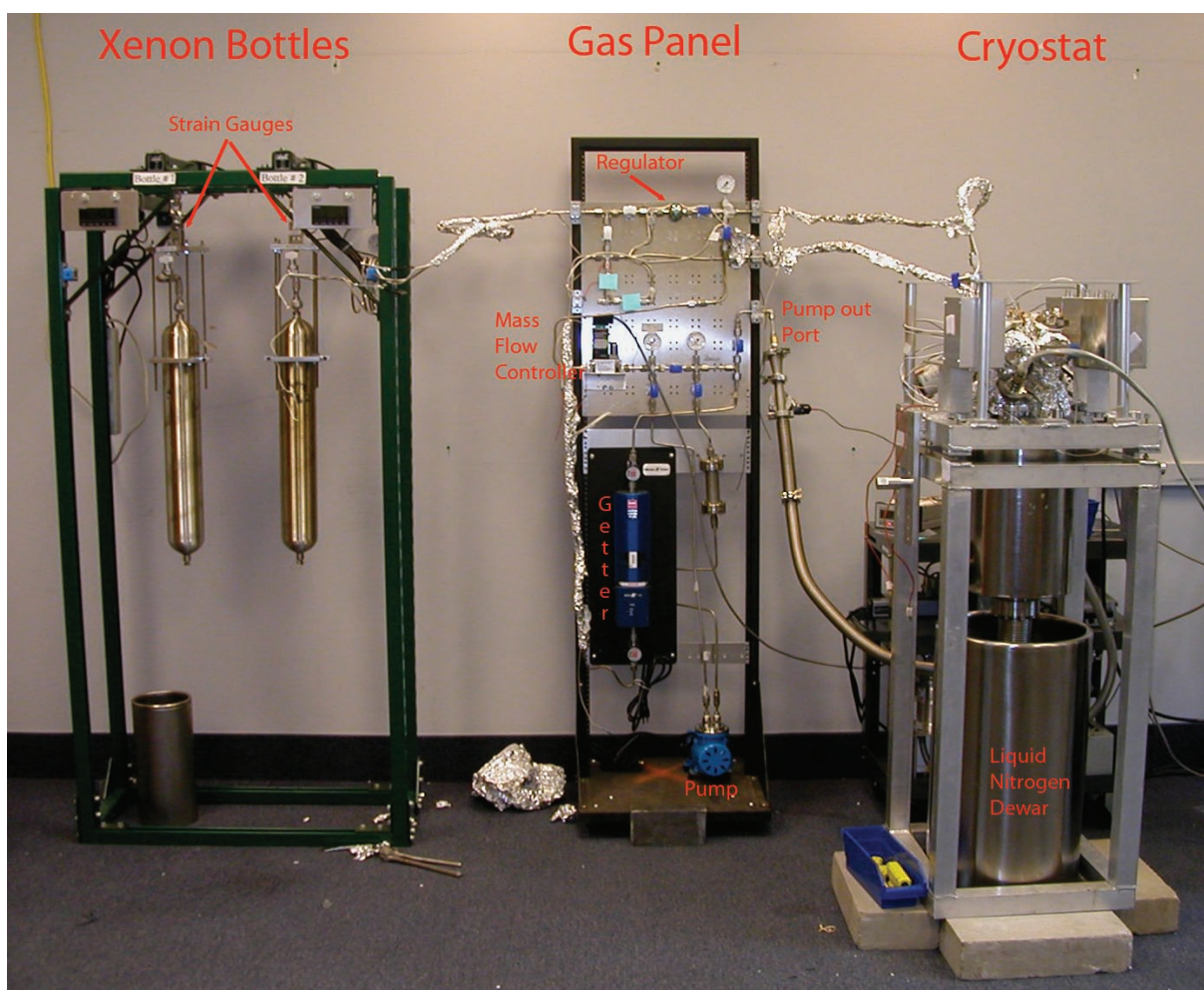
Figure 4.5: Xenon bottles, gas panel and cryostat.
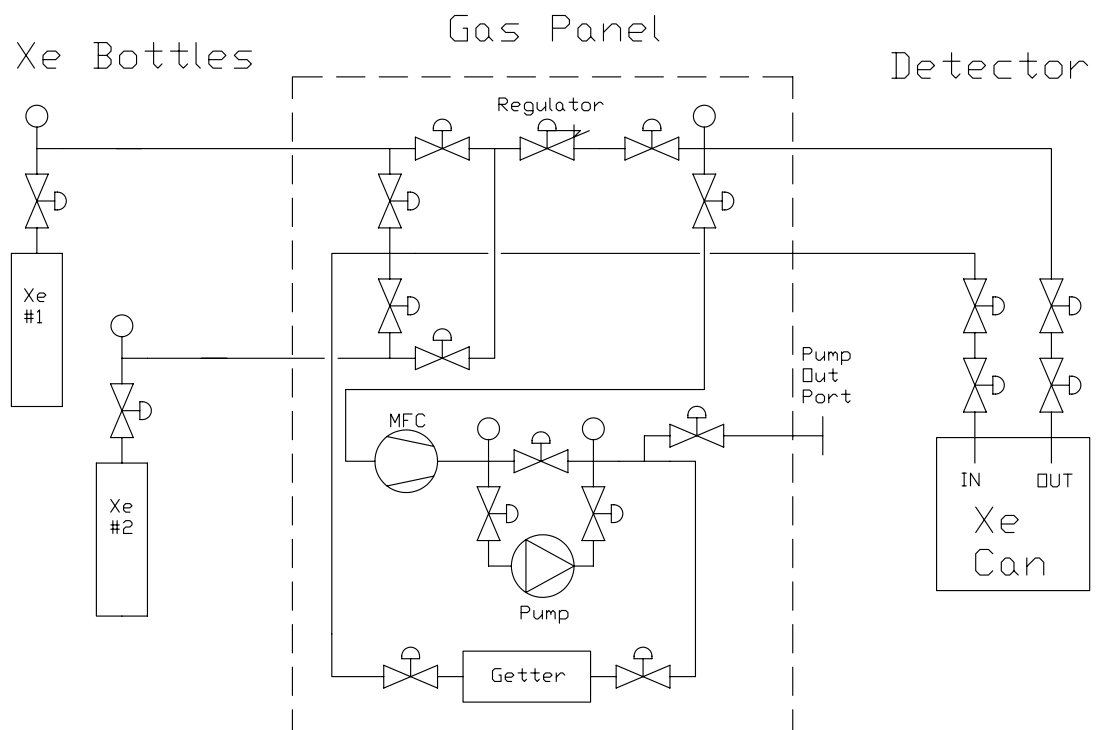
Figure 4.6: Schematic of the gas system.

The gas bottles are stainless steel Swagelok double-ended cylinders with one end welded shut. Welded onto the opposite end of each bottle is a ~130 bar pressure rupture disc. The mass of the bottles are tracked with Ortec strain gauges.

Another way of cleaning the xenon and detector is by repeatedly recuperating all the xenon back into the bottles and then refilling the can. The xenon is extracted by cooling the bottles in liquid nitrogen. The regulator provides a constant 2.5 atm downstream pressure when filling from the storage bottles. Purification by recirculation is accomplished by pulling liquid xenon out of the can up the tube where it evaporates and pushing the xenon gas through the getter and back into the xenon can where it recondenses. The diaphragm gas pump drives the recirculation at a maximum rate of 3.3 liters per minute.

4.3   Detectors

Our primary goal in designing our detectors was to achieve high, uniform and stable light and charge collection. This requires highly reflective parts, a high quantum efficiency PMT placed in the detector volume and overall cleanliness. Details on the specific detectors are described in the next chapter along with their results. In this section, we give an overview of the various components.

4.3.1   Reflectors

Increasing light collection improves the signal resolution and threshold, both of which are key factors in the dark matter sensitivity. Highly reflective materials are placed around fiducial region to increase the photon collection. The primary reflector material used is PTFE (Teflon) which has been shown to have a reflectance to 175 nm photons ranging from 55% [43] to 95% [253]. The results observed in XENON10 suggest >98% PTFE reflectance. This large variation can be explained by two known sources of degradation: exposure to high intensity UV and the presence of light absorbing contaminants [254]. Figure 4.7 shows the reflectance of common reflectors below 220 nm [43]. In Section 5.4, we show the results of our attempt to improve light collection by use of a wavelength shifter and a reflector
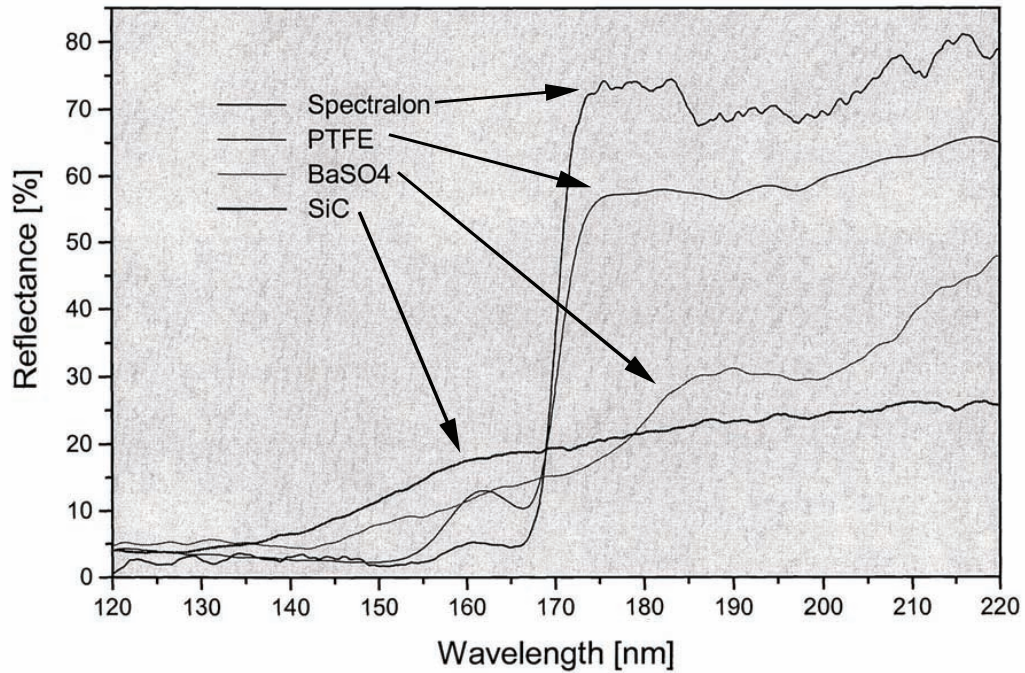
Figure 4.7: Reflectance of some common reflectors below 220 nm [43].

material called Spectralon.

A simplified photon propagation Monte Carlo developed primarily by Tom Shutt was used to project the light collection efficiency and positional variation. Figures 4.8(a) and 4.8(b) are maps of the light collection efficiency of the bottom and top PMTs, respectively, of the Xed1b detector (which is described in greater detail in Section 5.2.1).

4.3.2 Wire Grids

Most of the wire grids used at Case and many of those used for earlier measurements at Columbia were designed and constructed by the author. We opted for wire grids over other forms of electrodes such as electroformed meshes (as used for XENON10) because they could be created in the lab thus affording a higher level of agility and lower cost. No field shaping rings were needed as the active volume geometry was always flat with a height of ~1 cm and a diameter of ~4 cm. Figure 4.10 is the electric field map of a system with two planes and two wire grids. These maps were created by Maxwell 2D to determine the
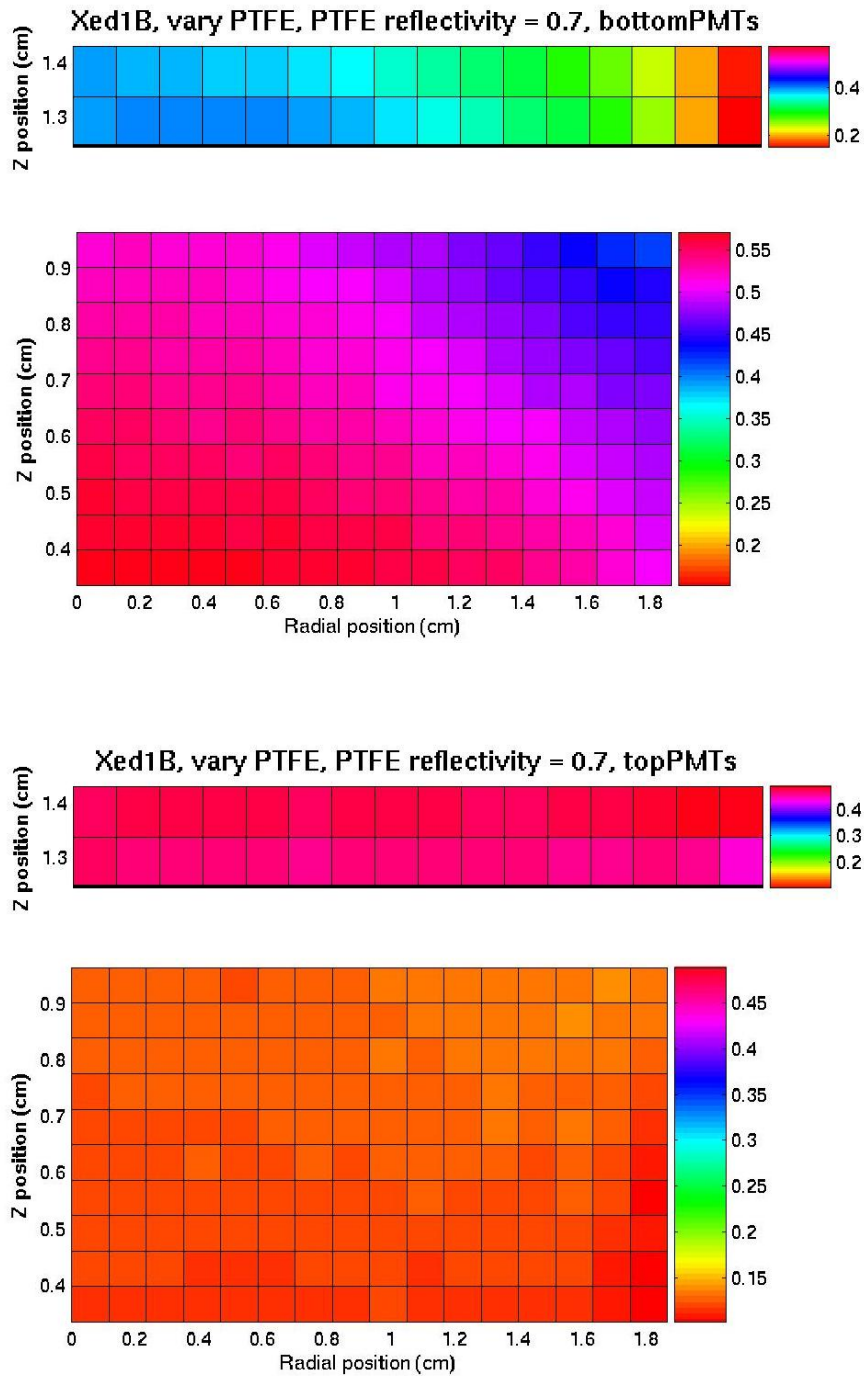
Figure 4.8: Maps of the light collection efficiency of the bottom and top PMTs for light emitting from the active volume ($0.2 \leq z \leq 1.0$ cm) and region between the liquid level and anode grid ($1.2 \leq z \leq 1.4$ cm) where the proportional light is generated.
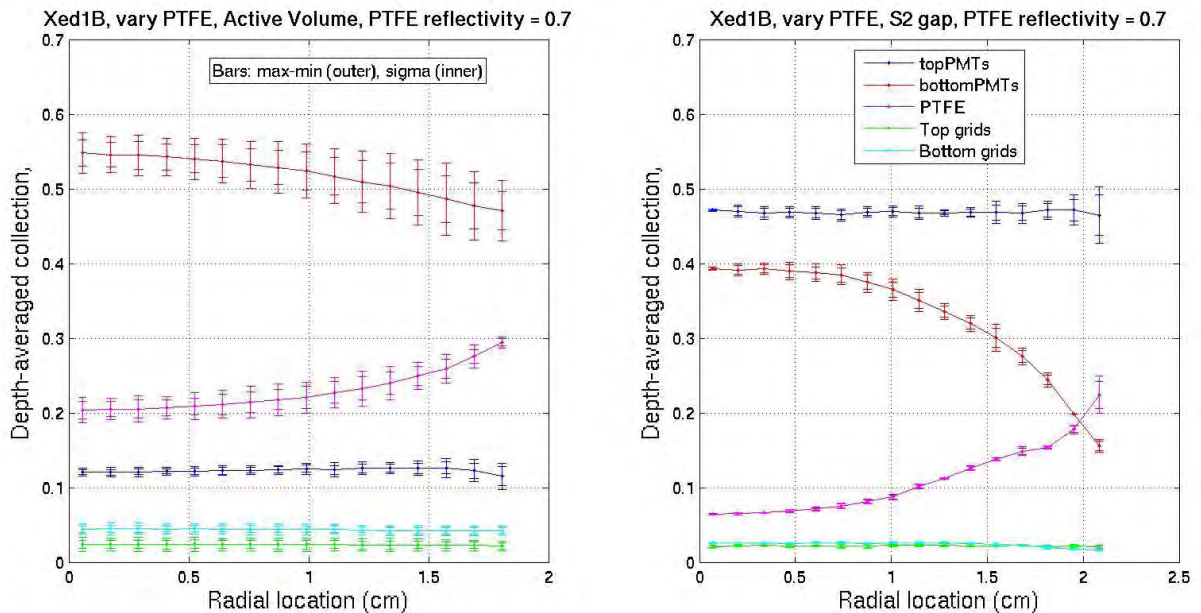
Figure 4.9: Light collection efficiency of various surface as a function of radius.

uniformity of the electric fields. The electric field of the active volume of our detectors were generally uniform to 5%. This high uniformity near the walls is due to the PTFE dielectric constant ($\sim$2) closely matching that of LXe ($\sim$1.9) and to the electrodes radially extending beyond the active volume.

Selection of Wire Grid Materials

All fine wires used for our experiments were purchased from California Fine Wire. In our prototypes, beryllium-copper (BeCu), gold-plated aluminum and tungsten wires were used. The reflectivities are likely to vary greatly with sample as features such as oxide layers and roughness can have a sizable impact (as they do for the emissivity). Because of these uncertainties, it is best to simply minimize the size and number of wires in the liquid. The wires in the liquid had a diameter of 40 μm or less. In the gas, the wire size is less important as most of the primary scintillation is retained in the liquid. To prevent electron multiplication in the gas (except in detector for gas gain measurement) these wires generally had a diameter of 125 μm. A uniform pitch (distance between adjacent wires) of 2 mm was
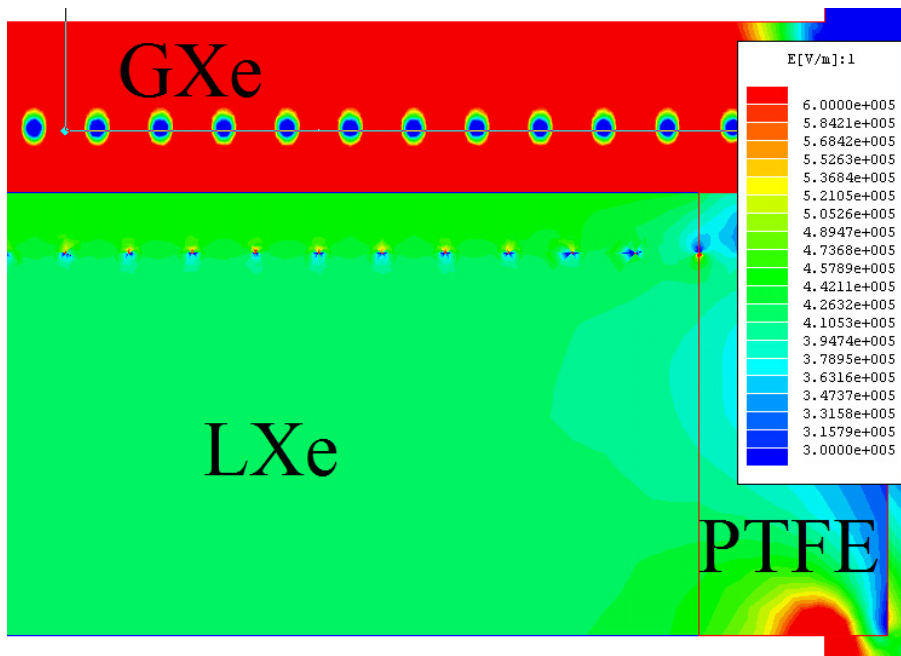
Figure 4.10: Electric field map of a two-phase setup with two wire grids (not visible) and two plates representing the PMT photocathode. The liquid level is between the two grids. The field is very uniform up to the edges because the grids extend into the PTFE walls and because the dielectric constants of the PTFE and LXe match well.

used for all grids. This dimension allowed for a large direct (>90%) transmission of light and charge.

Common ring materials are metals such as stainless steel and copper. Since we were interested in developing an individual wire charge readout system, we opted for $1/8''$ thick copper-plated Cirlex$^{\text{TM}}$, which is a thick polyimide adhesiveless laminate of the same material as Kapton. Cirlex is very strong and chemically resistant. Importantly, it has been shown by the Case group to not affect the electron drift length. The radioactivity of Kapton has been measured by the XENON collaboration to be 30-fold smaller than that of glass. Circuit patterns can be etched with laser or a milling machine. The former method is preferred as it leaves behind a much smoother service that is unlikely to trap dirt, but it is also more expensive and cannot be done in house. Figure 4.11 is pictures of a laser-etched Cirlex ring that was not used. The rings used in the measurements described in this thesis were etched with a milling machine.

Figure 4.11: A Cirlex ring with laser etched individual pads. The wires are BeCu 125 μm.

Regular lead-tin solder was initially used, but was later replaced with silver-tin solder (5% silver) because of its higher melting point temperature. Although, the melting point of lead-tin solder is about 165°C, it softens at ∼120°C. Silver-tin solder melts at 220°C and has been tested to hold wires well up to at least 160°C. The higher operating temperature is important since it permits high baking temperatures. Furthermore, silver-tin solder has greater sheer strength and resistance to creep. Although not an issue in our prototype detector, silver-tin solder presumably has a lower radioactivity than lead-tin solder as it has much less ^{210}Pb [255].

To ensure that the wires do not break or loosen when baking or cooling, the ring and wire materials are chosen so that the linear expansion coefficients (α) closely match. The stress on a wire upon cooling or heating to temperature T_C is

$$\sigma = E(\alpha_{wire} - \alpha_{ring})(T_0 - T_C), \tag{4.3}$$

where E is the Young's Modulus; α_{wire} and α_{ring} are the linear expansion coefficients of the
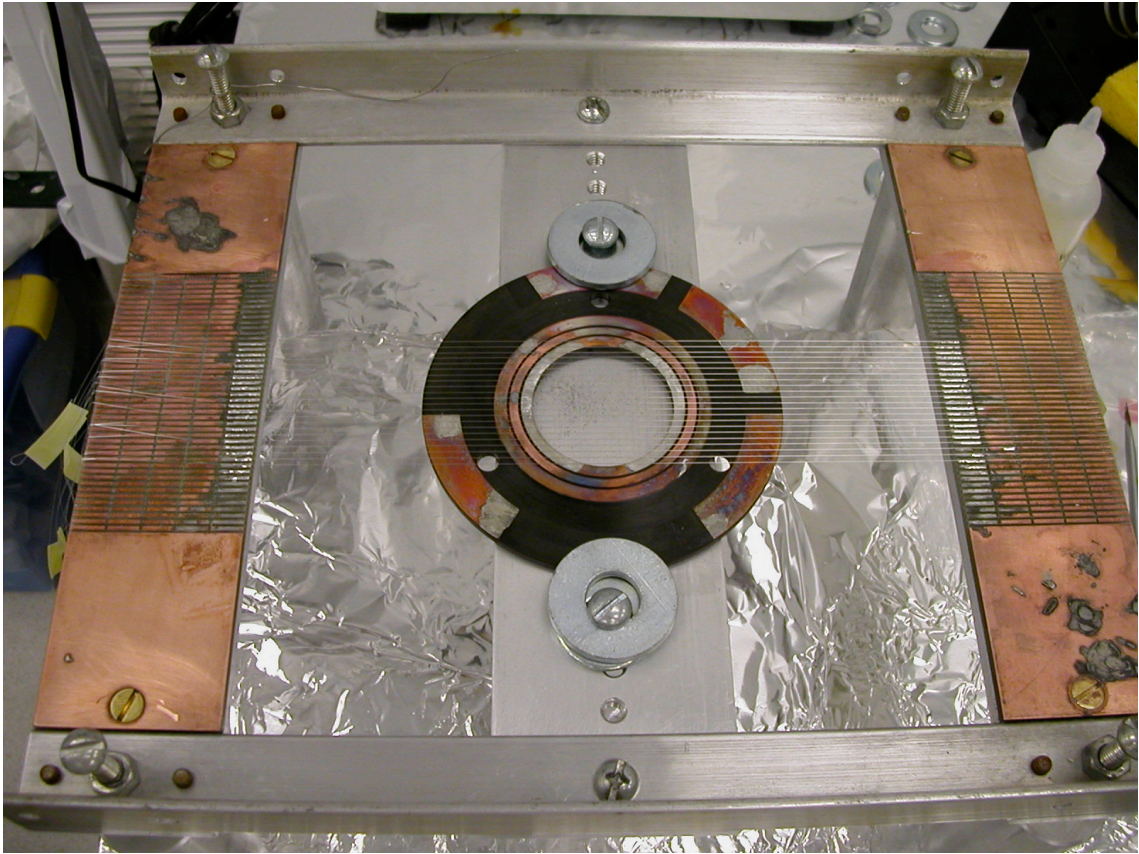
Figure 4.12: Cirlex ring on the wire transfer frame. The 125 μm BeCu wires were soldered under a tension of 40 g to the 2 mm spaced copper pads of the circuit boards. At this stage, the next step would be to solder the wires onto the inner copper ring. Completed wire grids can be seen in Figure 4.13.

wire and ring materials, respectively; T_0 is the room temperature; and T_C is the operating temperature. If the stress on a wire exceeds its yield point, then the wire may become permanently deformed. If $\alpha_{ring} > \alpha_{wire}$, then some tension needs to be applied when soldering the wire to the ring to ensure that the wire does not loosened when cooled. The necessary amount of tension is σA, where A is the cross sectional area of the wire. Note that Equation 4.3 is an approximation as it assumes that α is constant. For metals, α generally decreases as the temperature falls.

Figure 4.13: The Cirlex rings with 125 μm (left) and 40 μm (right) wires. The four on the periphery are the plates of the liquid level monitoring capacitor. Rings of this form were use for most of the measurements described in this thesis. In the center of each ring is a PTFE reflector.

Construction of Wire Grids

The wire grids are created by soldering tensioned fine wires onto copper coated Cirlex rings. The wires are first soldered onto the wire transfer frame (Figure 4.12). The frame has two G-10 boards with rows of copper pads spaced 2 mm apart. To ensure accurate pitch, each copper pad has a slight indentation across the center of each pad where the wire sits. The wires are soldered one at a time, under tension, to the transfer frame. A wire is tensioned across the frame by taping one end of the wire directly to the edge of one of the G-10 boards and taping the other end to a calibrated mass which hangs off the edge of the other G-10 board. After attaching the wires, the Cirlex ring is placed underneath the row of wires and the copper pads of the ring are covered with a generous amount of flux. The flux is added for two reasons. It removes the oxidation on the copper surface to ensure good bonding. It also acts as a surfactant to increase the fluidity of the solder which allows for easier spreading and increased smoothness of the final surface which is important for minimizing discharges. The wires are carefully soldered onto the inner copper ring and are then cut

with a razor above the outer copper ring. The sharp ends of the wires are covered with solder. The flux, which is fairly corrosive, is immediately removed by flushing with alcohol or acetone.

Before employing the wire grids, they undergo a temperature cycle test. In this procedure, the grids are heated on a hot plate at 150°C for 10 minutes, allowed to cool back to room temperature and then are placed in a liquid nitrogen bath. The wires are check for tautness in the bath. This cycle is then repeated two more times and the grid is considered acceptable as long as none of the wires have loosened or snapped.

4.3.3   Photomultiplier Tubes

We used R6041 and R9288 Hamamatsu PMTs (as seen in Figure 5.29), which have the same compact profile with a $2''$ window but with different quantum efficiencies (QE). The QE of the PMTs vary with wavelength and are 7% and 24% respectively, at 175 nm. The 12-stage dynode PMTs have a first dynode electron collection efficiency of 70%. They were designed to have low background and be able to operate in liquid xenon, which is crucial for light collection. The PMTs were positively biased to a voltage of 700–1000 V.

4.3.4   Liquid Level Measurement System

The liquid level can be measured by exploiting the difference in dielectric constants of xenon gas ($\epsilon_g \approx 1$) and liquid ($\epsilon_l \approx 1.87$). The capacitance changes as the xenon gas between any two electrodes are displaced by liquid. Two configurations were considered – a short tube with a thin central wire and parallel plates. We opted for parallel plates for several reasons. Firstly, capillary action in a narrow tube may cause inaccuracies in the capacitance measurement. Secondly, with the use of Cirlex rings, the parallel plates could be etched onto the rings and thus eliminate any ambiguity to the vertical position of the plates relative to the grids. In this section, we first derive the relation between the parallel plate capacitance and the liquid level and then describe the liquid level measurement system used in the Case detectors.
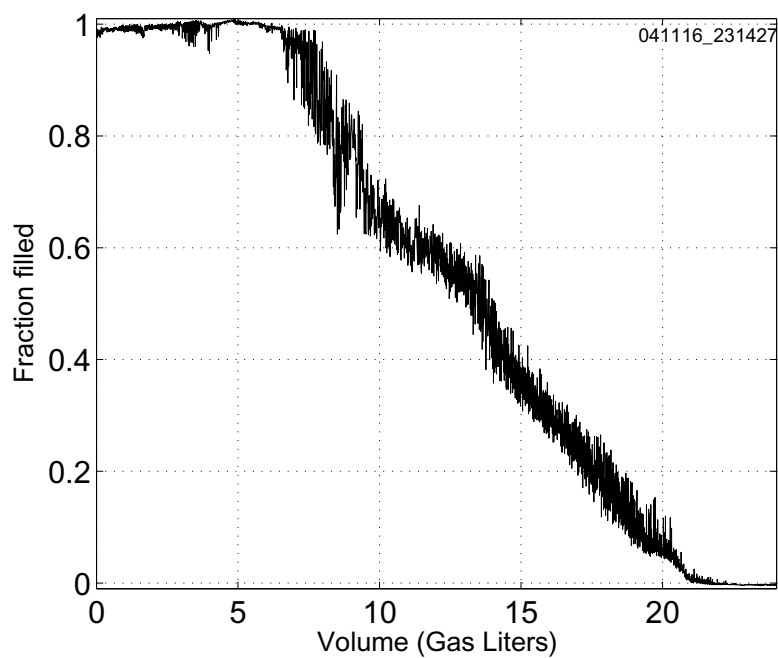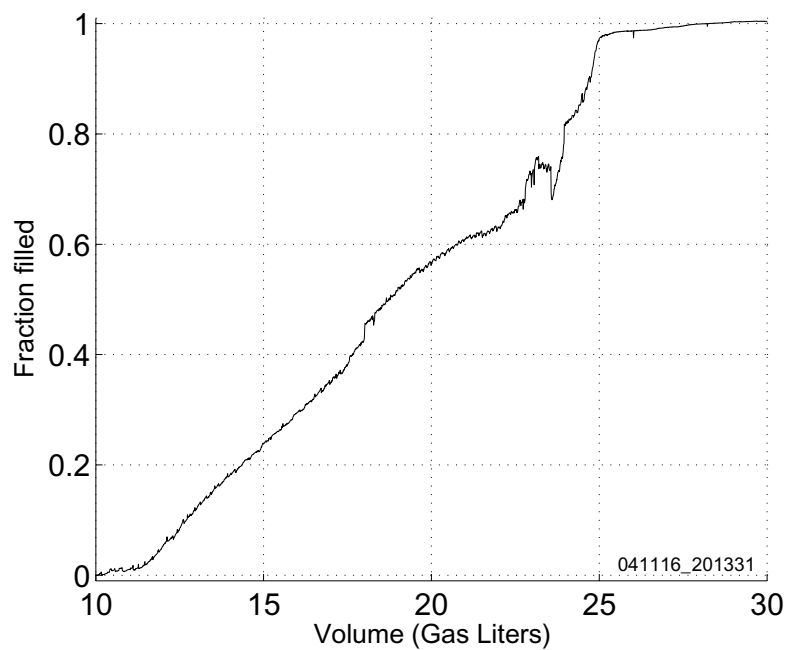
Figure 4.14: The liquid level (fraction filled) between the anode and gate wire grids versus volume while filling (above) and recuperating (below) at a constant rate. The erratic behavior at ∼0.7 are likely due the liquid adhering to the high voltage leads attached to the anode grid. The large waves seen during recuperation are likely due to the boiling in the outlet tube.

Consider two parallel plates of surface area A and gap distance d. The total capacitance is

$$\frac{1}{C_{tot}} = \frac{1}{C_1} + \frac{1}{C_2} \tag{4.4}$$

as this system is essentially two parallel plate capacitors in series – one capacitor including the liquid (C_1) and a second one including the gas (C_2). These two capacitances are

$$C_1 = \epsilon_0 \epsilon_l \frac{A}{z}, \tag{4.5}$$

$$C_2 = \epsilon_0 \epsilon_g \frac{A}{d-z}, \tag{4.6}$$

where z is the height of the liquid level above the bottom plate, and ϵ_g and ϵ_l are the dielectric constants of the gas and liquid, respectively. The total capacitance of completely empty and completely filled capacitors are

$$C_{empty} = \epsilon_0 \epsilon_g \frac{A}{d} \tag{4.7}$$

$$C_{filled} = \epsilon_0 \epsilon_l \frac{A}{d}. \tag{4.8}$$

Substituting these equations into 4.4, we obtain

$$C_{tot} = \frac{C_{empty}}{1 + (\frac{\epsilon_g}{\epsilon_l} - 1)\frac{z}{d}}. \tag{4.9}$$

The dielectric constants can be replaced with the measured empty (C_{empty}) and filled (C_{filled}) capacitance values:

$$C_{tot} = \frac{C_{empty}}{1 + (\frac{C_{empty}}{C_{filled}} - 1)\frac{z}{d}}. \tag{4.10}$$

We can take this equation and write the liquid level height, z, as a function of the total measured capacitance:

$$z(C_{tot}) = d\frac{\frac{C_{empty}}{C_{tot}} - 1}{\frac{C_{empty}}{C_{filled}} - 1}. \tag{4.11}$$

The $\sim$4 mm gap between the gate and anode grids is monitored by three parallel plate capacitors built onto the Cirlex rings (as seen in Figure 4.13). There is one reference capacitor that uses the Cirlex as the dielectric. The pads have a width of $\sim$1 cm and a
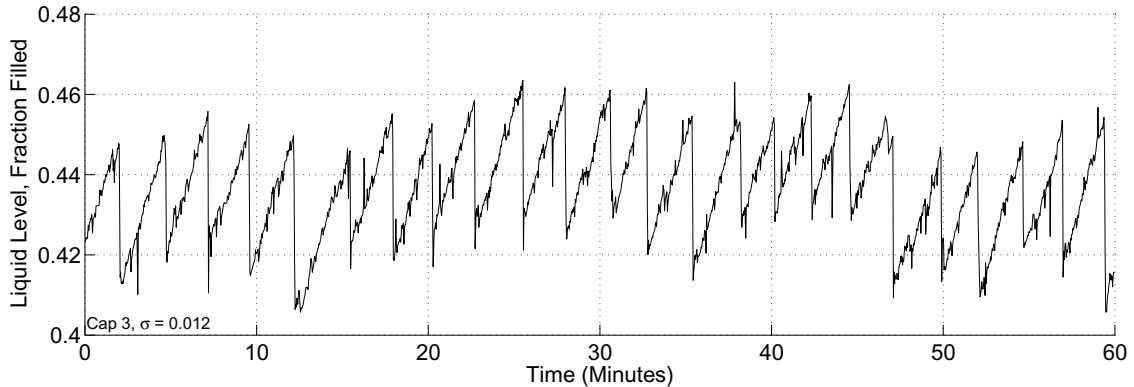
Figure 4.15: Liquid level (fraction filled) between the anode and gate wire grids at equilibrium. The gap between the anode and gate is 4 mm. The standard deviation of the fraction filled (liquid level) is 0.012 or (48 microns). The most likely explanation for the seesaw pattern is the gradually accumulation and sudden release of bubbles.

length of ~3 cm. The signals are carried by Kapton coated copper wires. A Smartec UTI board measures the capacitances by a three signal technique that removes the dependence on signal gain and offset and nullifies the effects of instabilities in the processor clock cycle [256]. The system is sensitive enough to measure the minute level changes due to the pull of the liquid towards the grids when the electric fields are turned on. At the beginning of every run, the empty and filled capacitance values are measured. Then the detector is leveled by adjusting the three height adjustment bolts on the aluminum frame of the cryostat. Figure 4.14 shows the liquid level during filling and recuperation at a constant flow rate. The nonlinearity at ~0.7 fraction filled is likely due to the liquid xenon interacting with the high voltage copper wires. The fluctuations are higher during recuperation because of the boiling occurring in the outlet line.

Immediately after filling the Xe can, there are typically large erratic swings in the liquid level due to falling droplets and escape of trapped bubbles. Several subsequent small fills and recuperations are required to achieve the desired level. After twelve or more hours, the liquid level always equilibrates to a see-saw wave with a period of several minutes (Figure 4.15). An explanation is the generation of bubbles by a hot spot at the joint between the bottom of the Xe can and the outlet tube. The bubbles slowly accumulate on a surface and
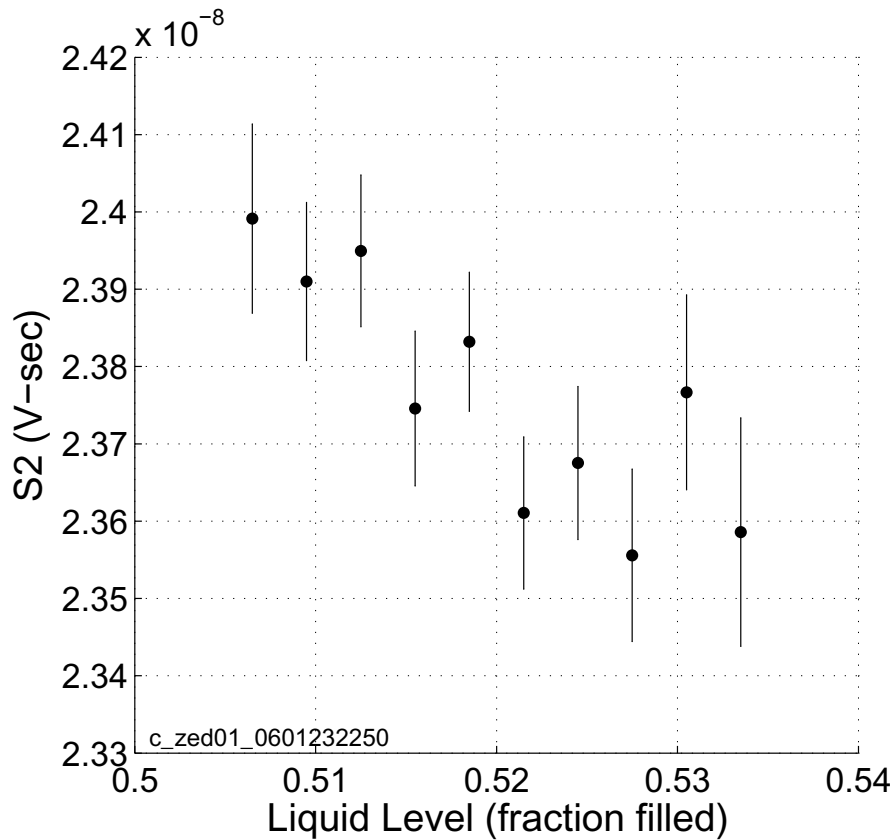
Figure 4.16: The Gaussian fit mean of $S2$ versus liquid level (fraction filled) for 122 keV gammas at a stable liquid level setting. The spread in liquid level is due to the see-saw fluctuations (as seen in Figure 4.15). A Gaussian function was fit to the $S2$ distribution of events in each liquid level bin. The error bars represent the statistical uncertainty to the Gaussian fits. There is an anti-correlation because an increase in liquid level decreases the electron path length in the gas. The amount of proportional scintillation follows Equation 3.19.

escape when they reach a certain size. This theory is supported by the disappearance of the waves upon heating the detector. Raising the temperature of the detector increases the gas pressure, which raises the energy barrier for nucleation. As previously noted, changes in the liquid level will alter the generation of proportional light. This see-saw fluctuation in the liquid level thus decreases the resolution of $S2$. In a ^{57}Co dataset with the average liquid level held constant, an anti-correlation between the liquid level and the $S2$ of the 122 keV gammas can be seen. Figure 4.16 is a plot of the $S2$ Gaussian fit means for several bins of liquid level. Recall that the amount of proportional light is dependent on the pressure,

Figure 4.17: The PTFE tube insulating the connection between the Gortex wire and high voltage feedthrough.

electric field, number of electrons extracted and the distance the electrons travels in the gas (Section 3.5.4). Although the number of electrons extracted can increase with an increase in liquid level since the electric field is higher (if the gas field is above 10 kV/cm, then there is no change), the electron travel distance is the overriding factor. A liquid level correction to the proportional light was shown to slightly improve the resolution but since running the UTI board introduces noise, the liquid level is usually only measured before and after taking a dataset.

4.3.5 Electrical Lines

Commercial SHV hermetic connectors mounted in 2-3/4″ Conflat flanges were used. These feedthroughs have a maximum voltage rating of 5 kV. Initially, single stranded bare 0.15″ diameter copper wires were used to carry the high voltage from the feedthrough to the wire grids but due to the lack of insulation these were replaced with Gortex^{TM}cable, which is

a multi-strand copper wire with plastic insulation, rated to several kV. There are several additional features to minimize electrical discharges. PTFE cylinders surround the point of connection between the feedthrough and Gortex cable (Figure 4.17). The connection between the Gortex wire and wire grid sits in the liquid where the break down electric field is very high. The PMT high voltage and signal lines are Kapton insulated coaxial cables designed for high vacuum systems and have a voltage rating of 1 kV. Several Bertan 375 high voltage power supplies were use to bias the grids. A system was later built to control these voltages with the DAQ computer. This allowed for the automated scanning across many electric field settings which significantly reduced the idle time of the detector. A Bertan 225 and a Ortec 556 are used to power the PMT's. The Bertan 225 can be set to shut off at a particular current to prevent damage to the PMT. All the high voltage power supplies output voltages with 20–30 kHz noise which are removed with simple LRC filters.

4.4   Detector Cleanliness

To reduce the introduction of impurities, we used parts that were known or expected to be compatible with liquid xenon. New or well cleaned tools are used in machining soft materials (such as PTFE) to avoid embedding impurities. Before assembly, all parts of the detector are cleaned in an ultrasonic bath filled first with acetone and then with ethanol, both heated to 50°C. Parts that are particularly dirty such as freshly machined parts are first bathed in detergent and water. Next, the parts are flushed with de-ionized water and transferred to a clean room where they are left to dry. All parts are handled with clean disposable nitrile gloves. Care is taken to ensure very limited exposure of nitrile gloves to the acetone bath as nitrile dissolves in it. If possible, parts are also stored in a dry box before usage to remove some of the absorbed moisture. The detector is then assembled in a ultra-low particulate environment provided by a bench with a horizontal HEPA filtered blower (Figure 4.18). Before closing up, the detector is brushed with pressurized dry air or nitrogen to remove residue dust which are a source of electrical discharges.

The detector is usually baked at 50°C (limited by PMT) while being evacuated for

Figure 4.18: Clean bench with HEPA filter unit and blower.

several days. After cooling down the detector, xenon is circulated for several days through the detector (where it liquefies and absorbs impurities) and through a hot metal getter purifier. For some experiments, the recirculation outlet was the tube welded to the bottom of the Xe can. A PTFE outlet tube was later routed directly to the active volume to more efficiently remove the impurities there. More information on this change can be found in Section 5.4.1.

4.5 DAQ

Two types of signals are recorded – the fast nanosecond time scale light pulses from the PMTs and the slower microsecond time scale charge signals from the spectroscopy amplifier. Figure 4.19 is a simple diagram of data acquisition system (DAQ), which was programmed in LabVIEW by Tom Shutt and Carl Eric Dahl. This section describes the PMT and charge
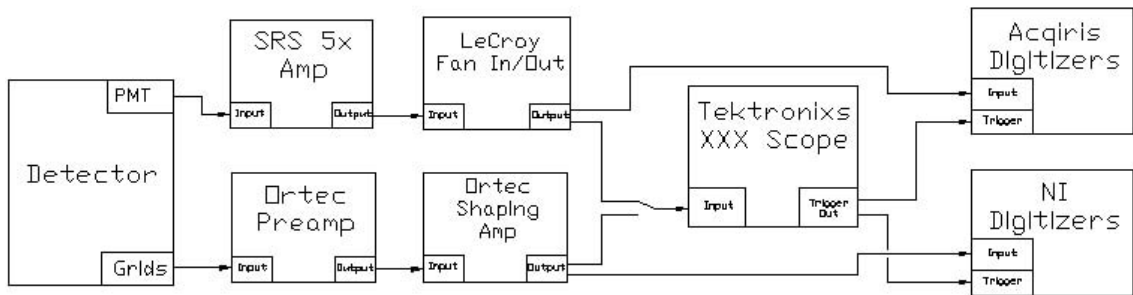
Figure 4.19: Simplified schematic of the data acquisition system used for light and charge measurements

DAQ systems.

4.5.1 Acquisition of PMT Signals

The PMTs signals are amplified near the signal feedthroughs with an SRS SR445A fast 5x amplifier to boost the signal-to-noise ratio. The amplified light signals are directed to a CAEN N401 Fan In/Out module. One set of signals is routed to the triggering system and another to the Acqiris cards. The triggering system consists of a Tektronics analog oscilloscope with a trigger out signal which is sent to the trigger input of the DAQ. For the two PMT setup, the DAQ is triggered by the signal from the bottom PMT as it collects more primarily light. The light signals are recorded by four 8-bit 500 MHz Acqiris digitizers. Two channels are needed for each PMT signal because of the great dynamic range in signal size and low resolution of the digitizers. The signals are stitched together in the data processing.

The primary light signal (S1) has a rise time of 5–10 ns and a fall time of about 50 ns. The pulse from the proportional light (S2) has a roughly Gaussian-shaped and a width of about 200 ns. The 500 MHz is well above the necessary sampling speed to capture the S1 and S2 pulses. Figure 4.20 is an example of the light signals from a 5 keV event in the bottom PMT of a Case two-PMT detector.

For some datasets, in particular the high statistics electron recoil datasets, we are primarily interested in low energy events. To conserve disk space, we sometimes implemented a high energy veto using gate/delay generators and multiple discriminators. For our setup,
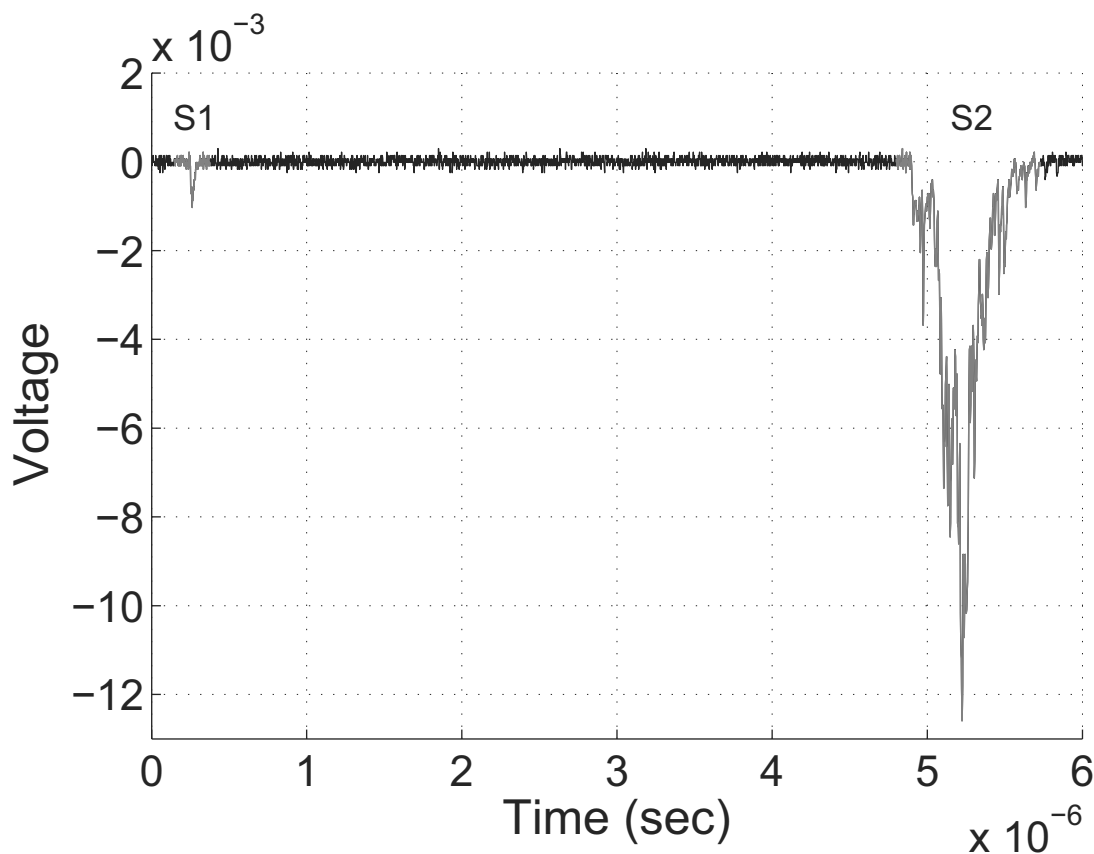
Figure 4.20: Light signal of a 5 keV nuclear recoil event with a charge of 25 electrons.

a Philips 794 quad gate/delay module was used. Figure 4.21 is a schematic of this setup which functions in the following manner (see Figure 4.22): an S1 signal in PMT#1 (the PMT in the liquid) triggers the gate/delay generator to create a trigger signal, which is delayed by the maximum drift time, Δt_{max}. If there is an S2 from PMT#2 following the S1 that is within the maximum drift time and has a height that exceeds the upper threshold, a positive gate signal is created lasting for Δt_{max}. This is the veto signal that inhibits the third gate/delay from generating a trigger signal for the DAQ. Thus, if there is an S1 trigger and an S2 pulse with height greater than the threshold, the S1 trigger will be inhibited by the veto signal. This configuration also rejects events that have an S1 below the trigger threshold in conjunction to an oversize S2. In such a case, the S2 provides the primary trigger and trigger for the veto. To determine the veto trigger threshold, some calibrated
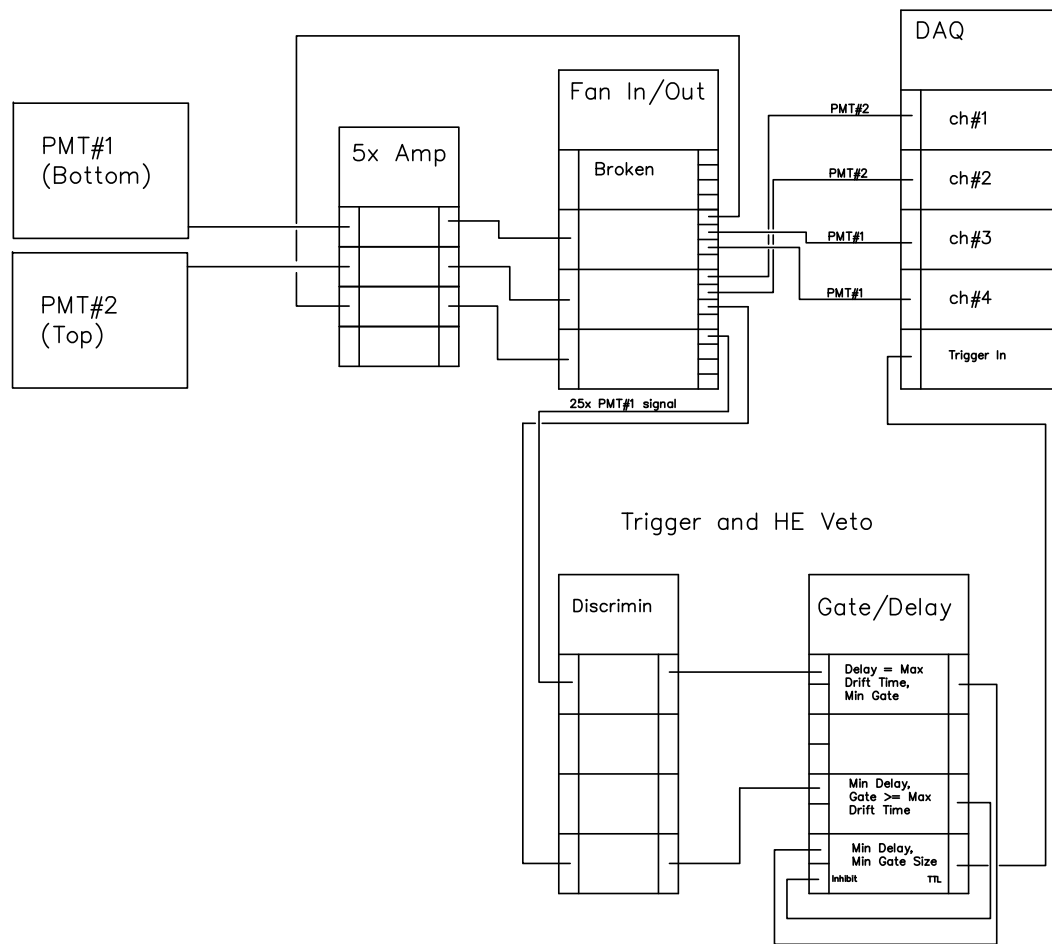
Figure 4.21: A schematic of the trigger setup with high energy veto. The signals are amplified by an SRS SR445A 5x amplifier. Copies are created with a CAEN N401 Fan In/Out. Three units on a Gate/Delay module are needed to create the veto logic. The system can be reverted to normal triggering (no veto) by disconnecting the line to the "inhibit" input.
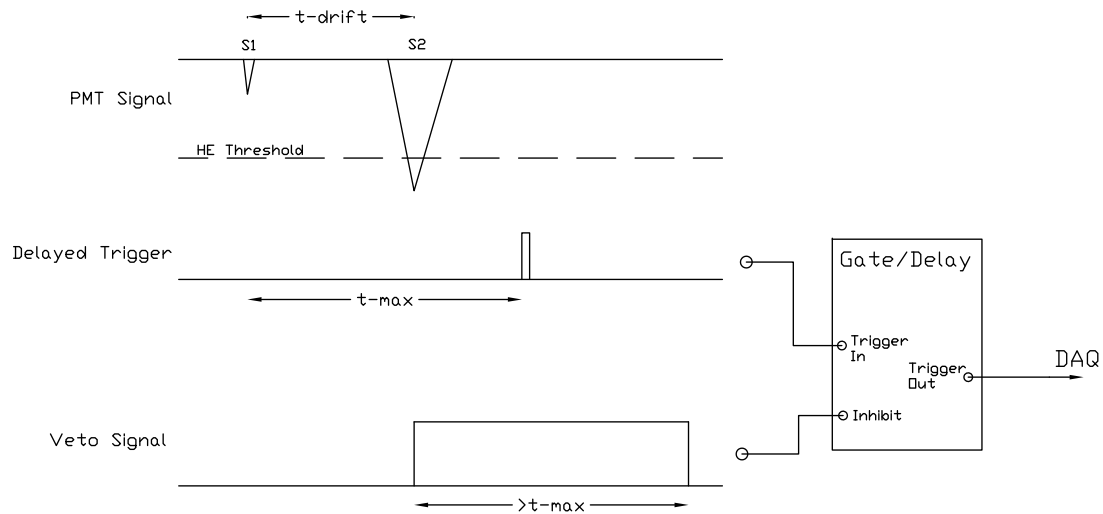
Figure 4.22: This diagram briefly describes the operation of the high energy veto. The S1 creates a trigger signal that is delayed by the maximum drift time. An S2 that exceeds the threshold creates a inhibit gate signal lasting at least as long as the maximum drift time. This inhibit signal negates the delayed S1 trigger signal and the event is rejected.

data is taken from which the S2 height threshold of the desired energy cut off is extrapolated. Note, that the S2 threshold must be generous to avoid cutting off the S1 pulse of same energy as there are large fluctuations between the sizes of the two pulses. Figure 4.23 is a histogram of $S2$ of two datasets, one without the veto and another with the veto at 30 keV.

4.5.2 Acquisition of Charge Signals

Direct charge measurements are made by integrating the charge with an Ortec 142AH pre-amplifier connected to the collecting electrode. Its feedback capacitance has been measured to an accuracy of $<1\%$ by muliple methods. Minimizing the input capacitance is crucial to lowering the noise so the shortest possible SHV cable ($\sim4''$) is used between the HV feedthough and the pre-amplifier input. The pre-amplifier signal has a rise time equal to the drift time of the electrons, which is usually about 5 μs. The integrated signal of the pre-amplifier is shaped and amplified by an Ortec 572 spectroscopy amplifier. The shaped signal is recorded by a National Instruments 6110 card, which has a sampling speed of 6
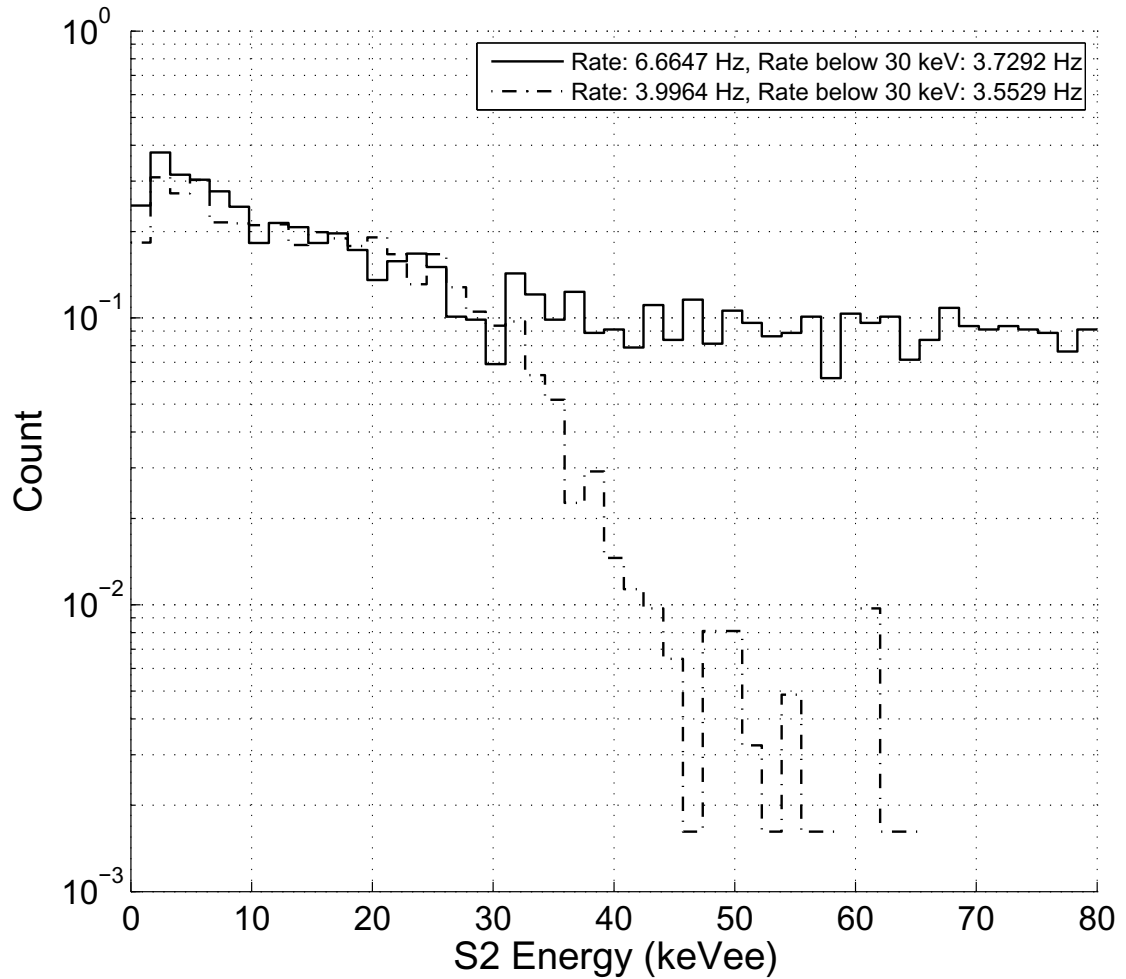
Figure 4.23: Histogram of $S2$ with and without the high energy veto. The high energy veto is at set at ~ 30 keV.

MHz and voltage resolution of 14 bits. The DAQ is triggered by the shaped signal. The DAQ can not be triggered by the pre-amplifier signal as it suffers from "flicker" noise.

4.6 Data Processing

After the data is written to hard disk, the files are compressed by creating new files that contain only the waveform of the pulses, omitting the sections of baseline that contain no useful information. Next, the basic quantities of the pulses are calculated and based on these values, the pulses are classified as S1, S2, charge pulses or noise. A framework was created
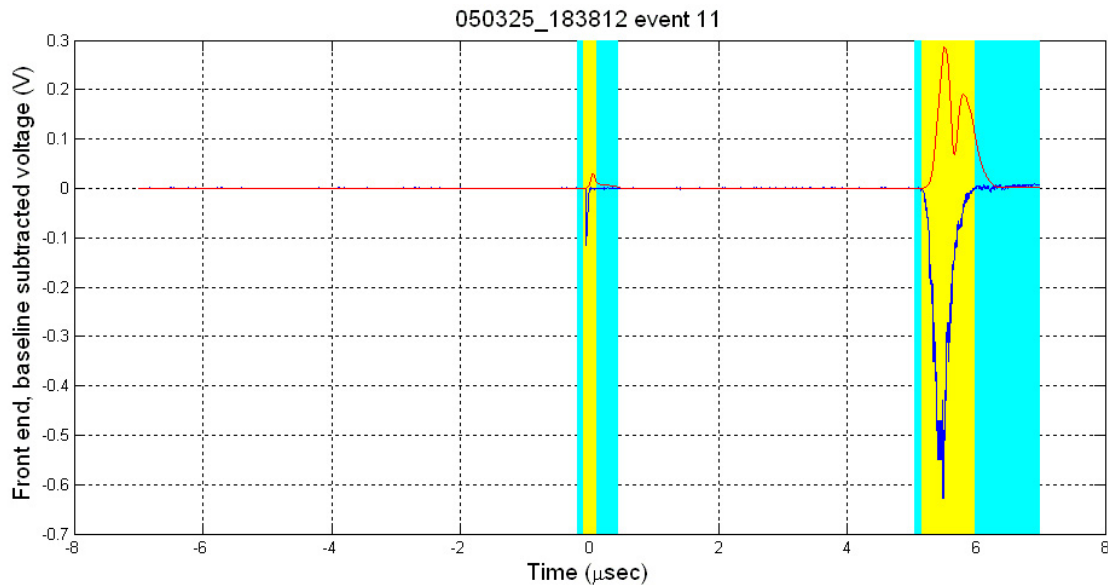
Figure 4.24: The blue line represents the original signal. The sections with a filtered signal (red line) above a particular threshold are highlighted yellow. The sections highlighted cyan indicate the sections that are saved to the new files.

to distribute these jobs across multiple computers. This section describes these steps in processing the data. Most of the work on the file compression was done by Carl Eric Darl. The event reconstruction and job distribution portions were programmed primarily by the author.

4.6.1 Data Compression

The light data requires a great deal of storage space. Two 10 μs PMT signals recorded at a speed of 500 Mhz and resolution of 8 bits requires 80 kb or 10 kB of disk space. A million such events total 10 GB. Although the cost of hard disk space to store this data is not expensive, the transfer of such large files across the internet is problematic. For a full scale detector with scores of PMTs and a much longer maximum electron drift distance, the size of raw signal data is prohibitively large. Recognizing that most of the signal traces contain only small fluctuations around the baseline, these files can be compressed with fairly simple algorithms. Only the pulse waveforms, the pulse locations, and the baselines are saved to smaller files. With this information, a good approximation of the original waveforms can be

reconstructed. The pulses are identified by applying various filters. First, the baseline of the signal is subtracted and then the slow baseline shifts ($\sim$1 μs) are removed with a high-pass filter. Next, the absolute value of the filtered signal is smoothed out with a Gaussian filter. The sections of the final filtered signal that are above a certain threshold are saved. Small segments preceding and following these sections are also saved. This procedure reduces the size of the data by a factor of $\sim$10. Figure 4.24 shows the original and filtered pulses.

4.6.2   Event Reconstruction

After the data is compressed, key characteristic values are calculated for the pulses and saved to file. These quantities include the pulse integral, height, rise time, fall time, start time, and the width at 10% and 50% of the maximum amplitude. Temporal moments such as the mean ($\mu = [\Sigma_i t_i V(t_i)]/[\Sigma_i V(t_i)]$), skewness, and kurtosis are also calculated. Skewness or the third standardized moment, is $\gamma_1 = \frac{\mu_3}{\sigma^3}$, where $\mu_3 = [\Sigma_i (t_i - \mu)^3 V(t_i)]/[\Sigma_i V(t_i)]$ and $\sigma = \sqrt{[\Sigma_i (t_i V(t_i) - \mu)^2]/[\Sigma_i V(t_i)]}$. This quantity reflects the asymmetry of a distribution. Kurtosis is $\gamma_2 = \frac{\mu_4}{\sigma^4} - 3$ where $\mu_4 = [\Sigma_i (t_i - \mu)^4 V(t_i)]/[\Sigma_i V(t_i)]$, and describes how peaked or flat a distribution is relative to the Gaussian distribution. A template pulse is also fit to the pulses to measure how closely the pulses conform to the expected pulse shape and to also provide a better estimate of the pulse height. This is important particularly for small charge signal pulses, where the height of the pulse is exaggerated by the noise fluctuations. The templates are average pulses.

In the next step, the pulses are classified based on the pulse shape. The most important quantities for discriminating light pulses are the pulse widths and rise times. For two-phase data, a good event is one that has a single S1 and single S2, within the maximum drift time expected. Since the Case prototype detectors had at most one PMT in the gas, there was no x–y position reconstruction capability. The z coordinate is provided by the drift time.

4.6.3   Computing Job Distribution

The compression of signals and calculation of pulse values demand a large amount of computational power so multiple computers are employed. With the data sets split among many files, there naturally exists a large number of discrete jobs that can distributed among several computers. A multiple-slave system was setup in Matlab to handle job processing. The process starts with one of the computers creating a database file that categorizes which datasets that have been processed. Maintaining a database file is faster than requiring that each computer scour the hard drives every time that a job is needed. After the database file is created, all the computers take turns accessing the database file to check out jobs. Only one computer can access the database at any given time to prevent multiple computer from checking out the same job. The required data file is first copied over to the local hard drive. Once a computer finishes a job, it copies over the compressed data or pulse shape quantity file, deletes local copies of the files related to the job, and finishes up by marking the job as complete. Every hour or so, one of the computers checks to make sure that the database file is consistent with the actual processing state.

Chapter 5

Liquid Xenon Detector Research and Development

5.1 Introduction

In 1993, the ICARUS collaboration demonstrated discrimination between alpha and gamma ray events by measuring the primary and proportional signals of a two-phase liquid xenon time projection chamber [257]. An article published in 2003, showed the results of a two-phase xenon time projection chamber, which detected Xe recoils and distinguished them from electron recoils but lacked statistics and a clearly defined energy axis [258]. When the XENON collaboration formed in 2003, no two-phase liquid xenon detector had yet been employed for WIMP search. In fact, no one had determined the ultimate performance of the technology. Before starting on XENON10, several smaller prototypes were built by the Case Western group and our collaborators to gain experience with two-phase detectors, make calibration and discrimination measurements and explore alternative techniques for potential integration into the full scale detector. This chapter summarizes some of the basic research and development performed by the Case group, which is lead by Tom Shutt. The first two sections describes our measurements of discrimination by charge $(\log_{10}(S2/S1))$ and by shape of the primary scintillation pulse. The effectiveness of applying both princi-

ples simultaneously (as is done for two-phase liquid argon detectors) is also explored. The following section describes the use of a wavelength shifter in an attempt to improve light collection. The next section shows our operation of a detector with electron multiplication running stably in two-phase. This demonstration is important because the use of a photo-cathode (to convert primary scintillation photons into electrons) along with a direct charge measurement system can be used in place of PMTs, which are expensive and radioactive. The charge multiplication results are used to project the discrimination performance of a detector with charge readout and PMT in the liquid. The final section shows the results of a detailed measurement of the recombination fluctuations of 122 keV electron recoils, which can be used to test recombination models.

5.2   Charge-Based Discrimination

When work began on the Xed prototypes in the summer of 2003, the ultimate discrimination power of liquid xenon two-phase detectors had yet to be measured. Before observing Xe recoils, we observed the recoils of ^{206}Pb nuclei down to 20 keVr in our Xed1a detector, which had only a single PMT in the gas. The ^{206}Pb recoils were from alpha decays of an internal ^{210}Po source. Shortly afterward in November 2004, we measured the field and energy dependence of the Xe nuclear recoil ionization yield and discrimination efficiency. Some of these results are described in Section 3.4 and [19].

This section describes the results of a follow up measurement of the discrimination efficiency with a higher light collection efficiency setup yielding a much lower energy threshold and higher discrimination efficiency. Unforeseen structures in the two bands were observed which fortuitously resulted in high background rejection down to 2 keVr. These results established that this type of detector had the potential to set new cross section limits. The next section describes the pulse shape discrimination using the same data.
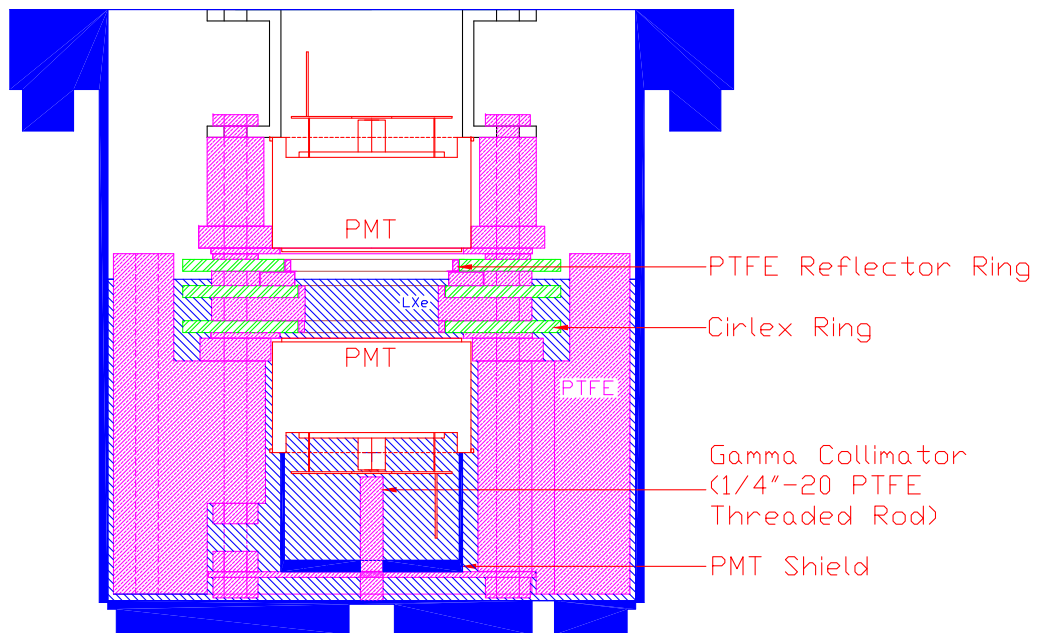
Figure 5.1: Diagram of Xed1b detector which has two PMTs and five wire grids on three Cirlex boards. The $1/4''$ PTFE rod surrounded by the more attenuating LXe serves as the gamma collimator. Teflon reflectors line the inside of the active volume. The large PTFE block serves as filler material to lessen the amount of the LXe needed. Each PMT has a metal can surrounding the PMT at the base for electrical shielding.

5.2.1 Experimental Setup

The Xed1b detector had two Hamamatsu PMTs and five wire grid electrodes. Figure 5.1 is a CAD diagram of the Xed1b prototype used for the discrimination measurements. Figure 5.2 shows the detector from above with the PMT in the gas ("top") removed. Figure 5.3 is a view of the bottom of the detector with the lid of the stainless steel can shield removed. The base of the PMT in the liquid ("bottom") can be seen in this photo. The bottom PMT is a R9288 with a QE of 23%. The top PMT is a R6041 with a QE of 6%. The five wire grids are refered to, from top to bottom, as "top", "anode", "gate", "cathode", and "bottom". The top most Cirlex ring which holds the top and anode grids can be seen in Figure 5.3. Each wire grid had 20 wires spaced 2 mm apart. The top and anode grids consisted 125 μm gold plated aluminum wires. The gate, cathode and bottom grids were made of 40 μm BeCu. The cathode and gate, which defined the active volume, were separated by 1 cm. As with other detectors, a $1/4''$ diameter PTFE rod surrounded by LXe below the detector serves as a gamma collimator. The signal and high voltage pins on the PMT circuit board are electrically shielded by metal cans. One of these shields can be seen in Figure 5.3. Unlike Xed1a which had reflectors only in the liquid region, Xed1b had PTFE reflectors covering the active and gas regions. These reflectors not only help increase the light signal but also decrease the positional dependence. Figures 4.8(a) and 4.8(b) are light collection maps of the bottom and top PMTs, respectively, created by the photon propagation Monte Carlo. The detector is surrounded by a large PTFE block (see Figures 5.2 and 5.3) that extends to the walls of the Xe can and serves as volume displacement.

To measure the discrimination performance of a dark matter detector, we must find the discriminant response (charge, light, pulse shape, etc.) to background and WIMP events. With these measurements, we can then define the WIMP acceptance window which is the region in discriminant space that has a low rate of background but high rate of WIMP events. As previously mentioned, the dominant source of background are electron recoils from Compton scatters of high energy gammas (see Section 3.4 for information on gamma interactions with xenon). For background calibration, a hot gamma source is typically used
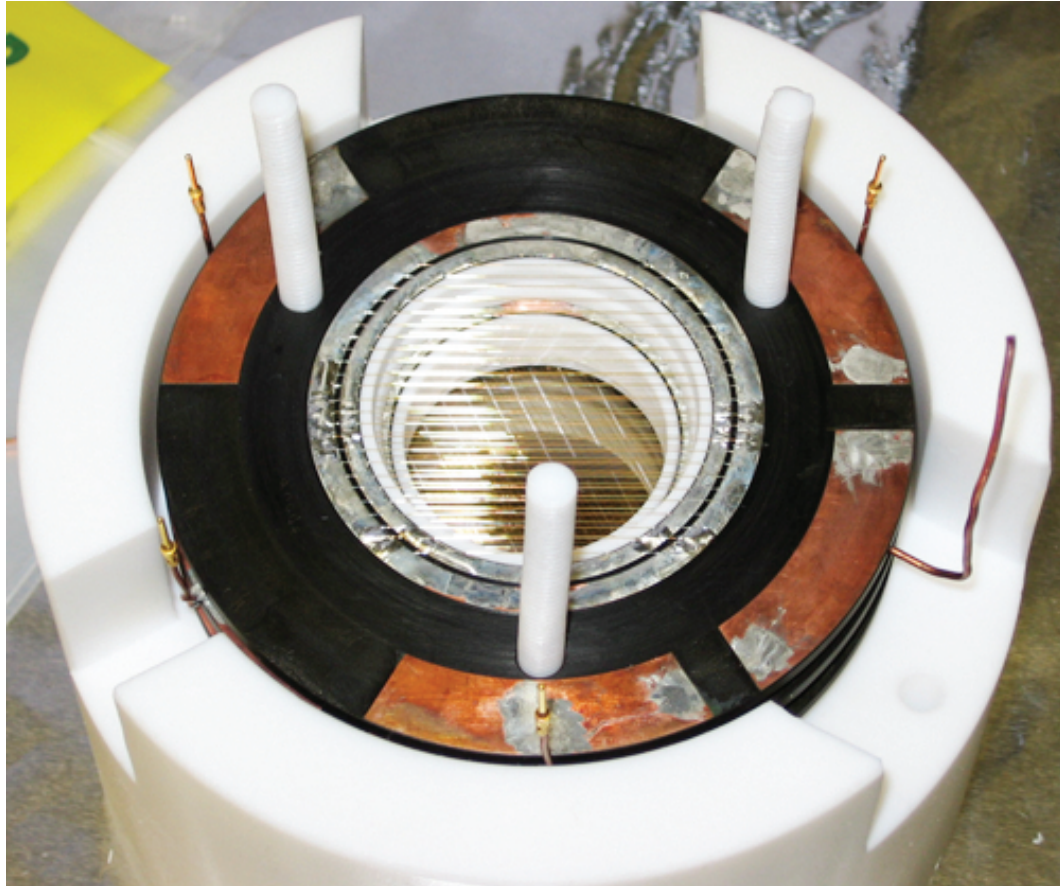
Figure 5.2: View from above the detector with the top PMT removed. The white rings are the PTFE reflectors. The detector is surrounded by a volume displacing PTFE block. The pins are connections for the parallel plate capacitors.
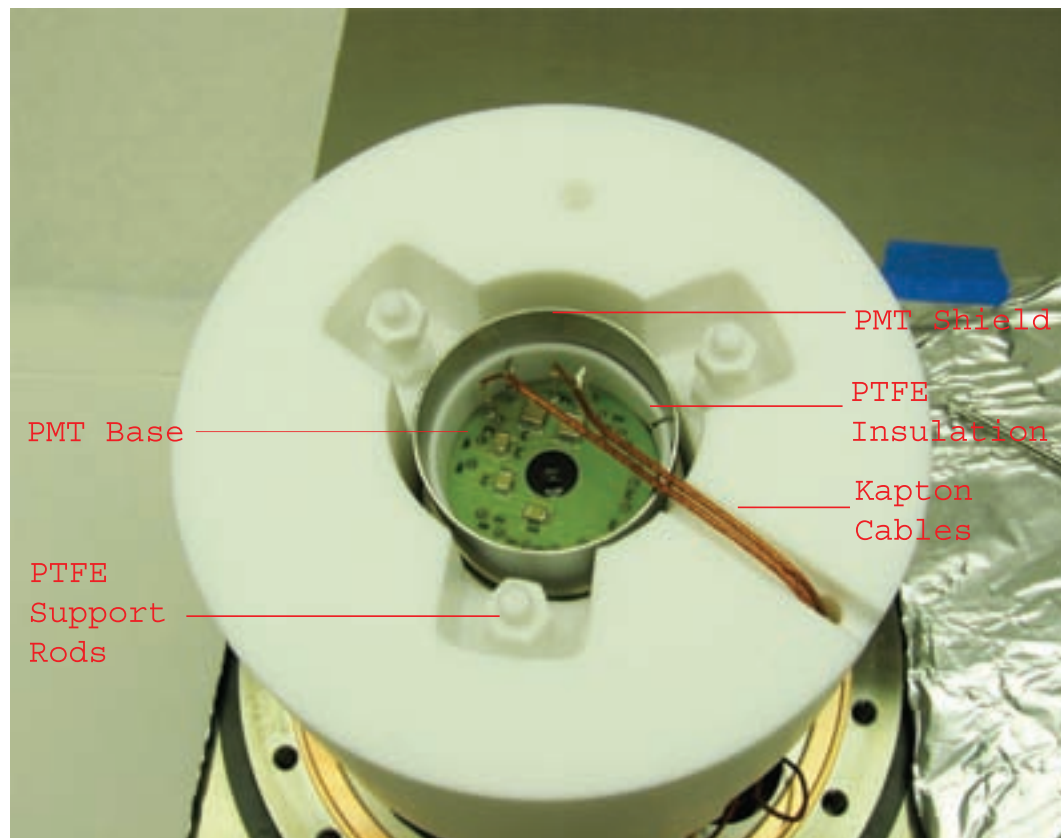
Figure 5.3: This photo shows the bottom of the detector with the lid of the stainless steel PMT shield removed. Many components can be seen: the PMT shield can; the PMT base; the Kapton-coated coax wires that carry the high voltage and signal; the strip of Teflon that lines the inside of the PMT shield can and serves as an insulating barrier; the three $1/4''$ threaded PTFE support rods.
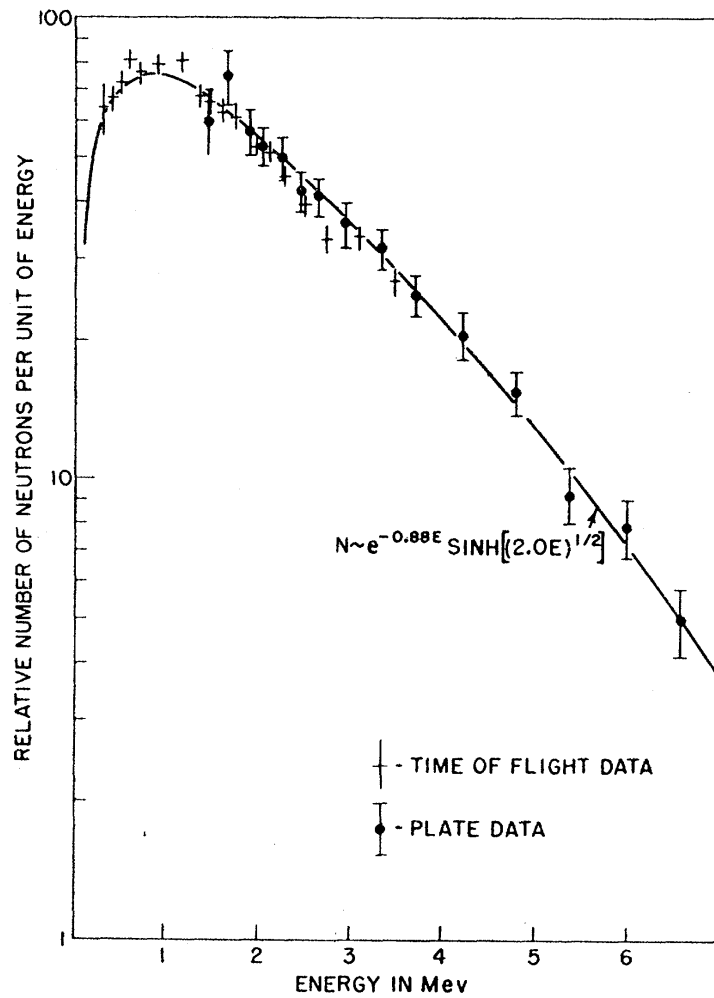
Figure 5.4: The ^{252}Cf neutron energy spectrum [44]. The most probable and mean neutron energies are 0.7 MeV and 2.1 MeV, respectively.
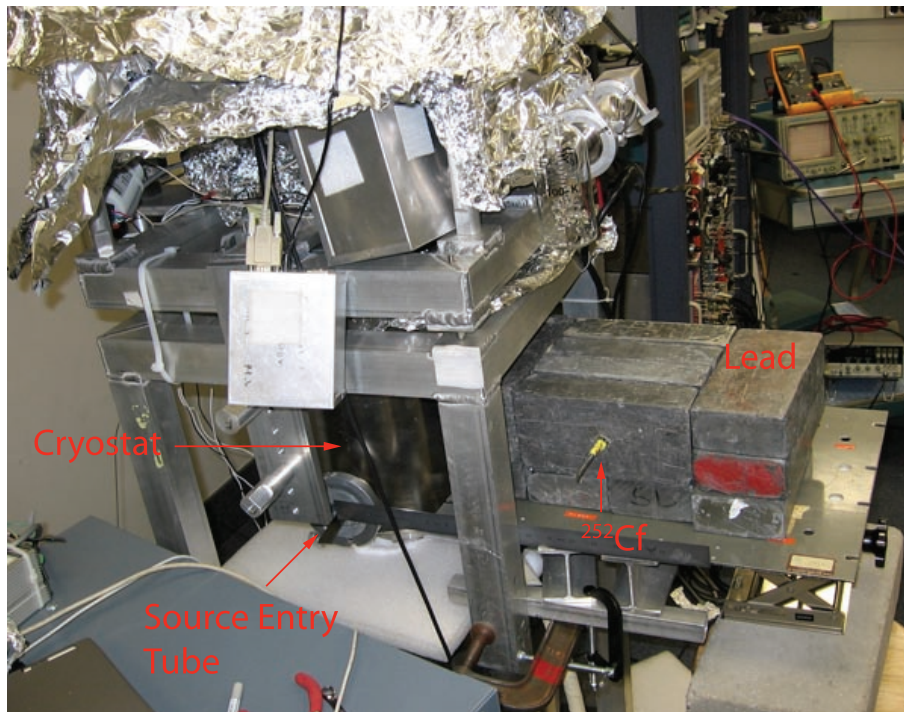
Figure 5.5: The lead enclosure for blocking out much of gammas from the ^{252}Cf source. The source entry tube can also be seen in this photo.

rather than background in order to obtain a large number of events in a reasonable period of time. To calibrate the response to WIMPs, a neutron source is used. Neutrons with an energy of $\sim$1 MeV mimic the response of $\sim$10 keV WIMPs. High energy gammas were provided by a ^{133}Ba source which was placed approximately 15$''$ away from the center of the detector. A 25 μCi ^{252}Cf source provided neutrons with a falling exponential energy spectrum (as seen in Figure 5.4). The most probable and mean neutron energies are 0.7 MeV and 2.1 MeV, respectively [259]. Many more gammas are emitted than neutrons – the gamma emission rate of ^{252}Cf is 1.8×10^8 s$^{-1}\mu$g^{-1} versus 2.34×10^6 s$^{-1}\mu$g^{-1} of neutrons – necessitating the use of a lead shield (see Figure 5.5). The ^{252}Cf source was located 14$''$ away from the center of the detector with 10$''$ of lead in between. The lead placed behind the source reflected neutrons back towards the detector. The neutrons and gammas from these sources were not collimated.

At each drift field, a calibration (^{57}Co), gamma background (^{133}Ba) and neutron (^{252}Cf)
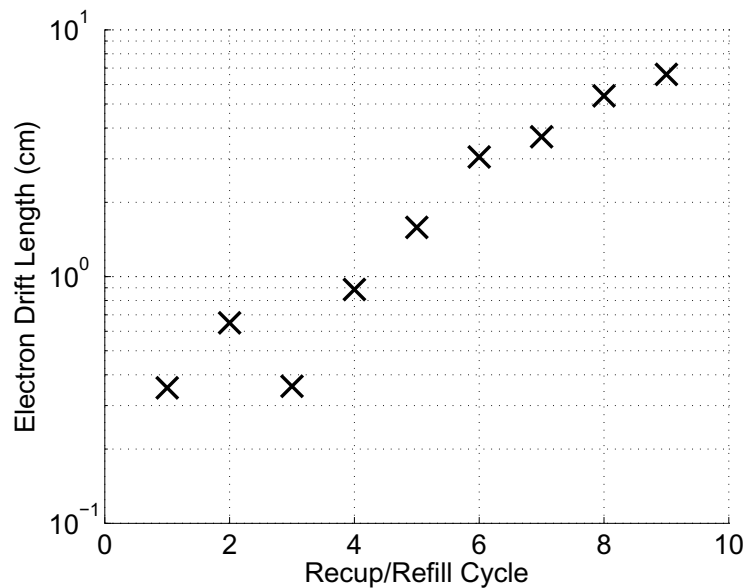
Figure 5.6: The evolution of the electron drift length as a function of xenon recuperation and refill cycles. The reason for the drop in purity at cycle number of 3 is unknown. The detector eventually reached a drift length of ∼20 cm.

data sets were taken. Data was taken at five electric fields: 0.06, 0.52, 0.88, 1.95, and 3.96 kV/cm. A constant gas field of 10 kV/cm was set (5 kV/cm in liquid), providing full extraction of electrons into the gas [38]. The top and bottom PMTs were biased to +825 V and +875 V, respectively. The gamma background and neutron datasets contained 5×10^5 to 1×10^6 events.

The temperature of the liquid xenon was 187.4 K and the pressure was 1970 torr. The liquid level sat halfway between the anode and gate electrodes which was separated by 4 mm. The electron drift length was initially observed to be only several centimeters. The detector was purified by completely recuperating the xenon and refilling the xenon several times, passing the gas through the SAES MonoTorr getter in each direction of the cycle. Figure 5.6 shows the evolution of the electron lifetime as a function of recuperation/refill cycle. The detector eventually reached a drift length of ∼20 cm which was constant throughout the rest of the run.

A general overview of the data processing is given in Section 4.6. A good event has one S1 and one S2 with a drift time within the range expected for the drift field. The pulse

integrals, $S1$ and $S2$, were corrected for depth dependence by using the response to 40 keV gammas from inelastic nuclear recoils in the ^{252}Cf dataset and calibrated with the 122 keV gammas. The nuclear recoil energy follows Equation 3.10. For simplicity, we assumed a constant value of $\mathcal{L}_{eff} = 0.2$ for the relative scintillation.

The measurement of the 122 keV gammas showed that the Xed1b detector had a primary light collection of 5.0 phe/keV at zero electric field for the bottom PMT. This corresponds to $\sim$50% of the photons striking this PMT. The energy threshold was $\sim$2 keVr which was set in the analysis. The charge threshold was $\sim$7 electrons which was set by the trigger threshold. Only the PMT in the liquid is used for the S1 since the PMT in the gas collects $\sim$1/5 as much light and has a far lower QE. The top and bottom PMTs collect roughly the same amount of proportional light. Either the top or bottom PMT is used for the S2, depending on the size of the signal. For S2 of $\lesssim$300 electrons, the bottom PMT is used because of its higher signal-to-noise ratio. However, for events of $\gtrsim$300 electrons, the top PMT is used. Due to the high amount of light generated and the higher quantum efficiency and higher PMT bias of the bottom PMT, the S2 signal in the bottom PMT was highly nonlinear above several hundred electrons. For this reason, the charge signal of the 122 keV can only be measured by the top PMT. In order to calibrate the $S2$ of the bottom PMT in terms of charge, we examine events with S2's that do not saturate the bottom PMT channel but are also above the threshold in the top PMT.

5.2.2 Results

As previously stated, the discrimination is rooted in the difference in linear energy transfer (LET), which manifests as $(S2/S1)_{\mathrm{ER}} > (S2/S1)_{\mathrm{NR}}$ (see Section 2.3.5). By convention, we use $\log_{10}(S2/S1)$ as the discrimination parameter. Figures 5.7(a) and 5.7(b) shows the $\log_{10}(S2/S1)$ versus energy of the ^{252}Cf and ^{133}Ba data sets, respectively, at 1.0 kV/cm. The nuclear recoil acceptance window is the region below the energy dependent mean of $\log_{10}(S2/S1)$. For all fields, the leakage is calculated for discrete energy bins with edges at 2, 6, 10, 20, 30, 40, 50, 60, 70, 80, and 90 keVr. The electron recoil leakage is defined as
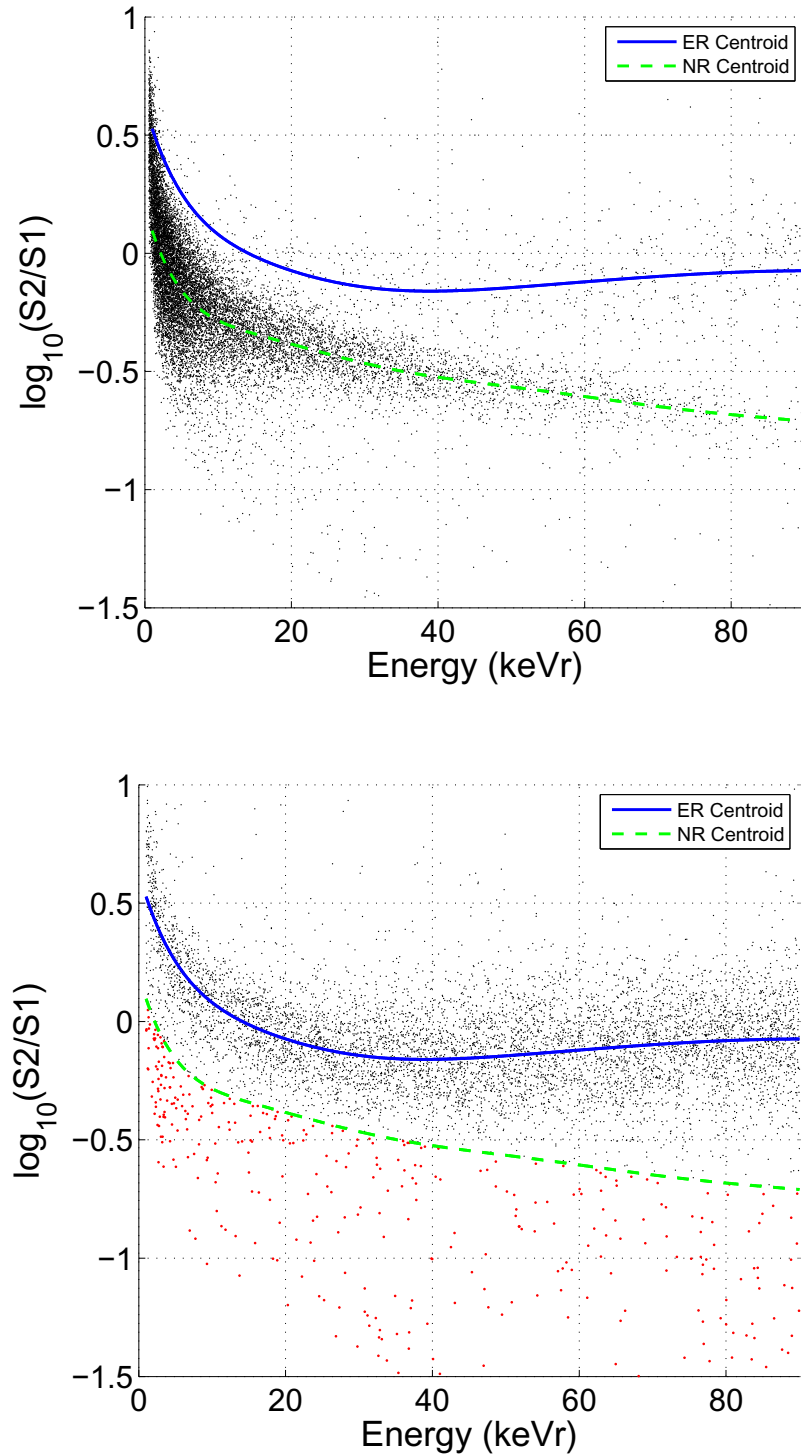
Figure 5.7: Scatter plot of $\log_{10}(S2/S1)$ versus recoil energy of the ^{252}Cf (top) and ^{133}Ba (bottom) data sets at 1.0 kV/cm drift field. The background leakage events have been highlighted red. Also plotted are the band centroids of the electron (blue) and nuclear (green) recoils.
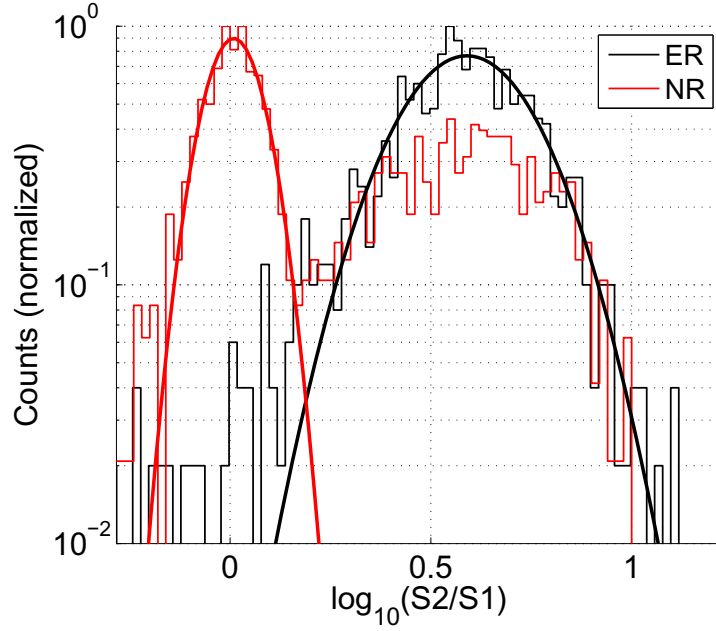
Figure 5.8: Histograms of and Gaussian fits to the $\Delta\log_{10}(S2/S1)$ of the electron and nuclear recoils peaks between 70 and 80 keVr at 0.88 kV/cm. $\Delta\log_{10}(S2/S1)$ is the $\log_{10}(S2/S1)$ subtracted by the mean of the nuclear recoils.

the fraction of events in the ^{133}Ba dataset that are in the nuclear recoil acceptance window. The discrimination efficiency is defined as one minus the leakage. We calculate two leakage quantities – actual and Gaussian. The actual leakage is determined by counting events inside and outside the acceptance window. For this quantity, a lower bound of $\mu - 2.5\sigma$ is included for the acceptance window to exclude events that are likely to be spurious. The Gaussian leakage assumes that the $\log_{10}(S2/S1)$ distribution is Gaussian and is calculated with two parameters: the Gaussian width of the electron recoil distribution and the distance between the means of the electron and nuclear recoil distributions. The electron and nuclear recoil energy dependent $\log_{10}(S2/S1)$ means are characterized by 10th order polynomials (these are represented by the lines in Figures 5.7(a) and 5.7(b)). These polynomials are calculated by iteratively fitting to the means of many overlapping energy bins, subtracting out the contour ("flattening") and then repeating until curvature is omitted. Fitting Gaussian functions to the flattened bands provide a truer estimate of the band width since a shift
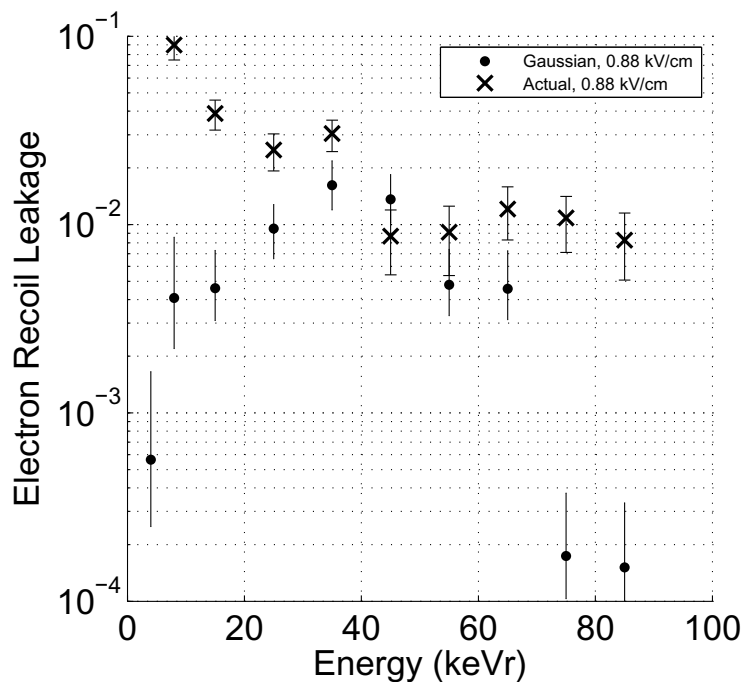
Figure 5.9: Actual and Gaussian electron recoil leakage versus energy at 0.88 kV/cm which is the drift field that provides the best performance. The error bars are statistical.

in $\log_{10}(S2/S1)$ within an energy bin would otherwise lead to an overestimate. Figure 5.8 shows the histograms of the $\log_{10}(S2/S1)$ of the ^{133}Ba and ^{252}Cf datasets with Gaussian fits between 70 and 80 keVr at 0.88 kV/cm.

Figure 5.9 is a plot of the actual and Gaussian leakages versus energy at 0.88 kV/cm, the drift field of the dataset that gives the best performance. In general, the actual leakage is much larger than the Gaussian leakage. We expected the actual leakage to be higher due to events that lose charge at the edges of the detector but can not be removed due to the lack of x-y position information. XENON10 and the ZEPLIN detectors confirmed this. Figure 5.11 shows the $\log_{10}(S2/S1)$ fit means of both recoils as a function of energy. There are several key features in this plot. Both bands turn up at lower energies because there are fewer ions with which the electrons can recombine with [60]. In our prior measurement with Xed1a, which had a much higher threshold of 20 keVr, the sharp upturn was apparent in the nuclear recoil band but it was unknown whether this feature would also be present in the
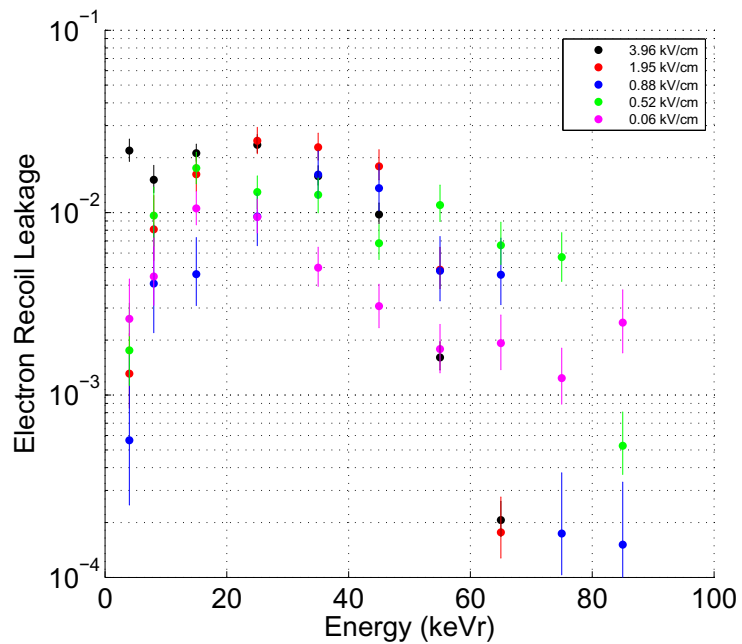
Figure 5.10: Gaussian electron recoil leakage versus energy at all five electric fields. The error bars are statistical.

electron recoil band. Had the electron band not shifted upward, the discrimination would have been far worse. This feature has been confirmed by XENON10 and other experiments [13, 207]. The $\log_{10}(S2/S1)$ of the electron recoils appear to be much more field dependent than that of the nuclear recoils which is a reflection of the difference in ionization density. A proposed model for the band turn-up at low energies will be part of a future publication by our group [260] and in another thesis [60].

In summary, we remeasured the discrimination efficiency of two-phase liquid xenon detectors to lower energies with a higher light collection efficiency prototype, finding a rejection efficiency that is >99.5% below 20 keVr. This observation matches the results of XENON10. The field and energy dependence of the band structures are also explored.
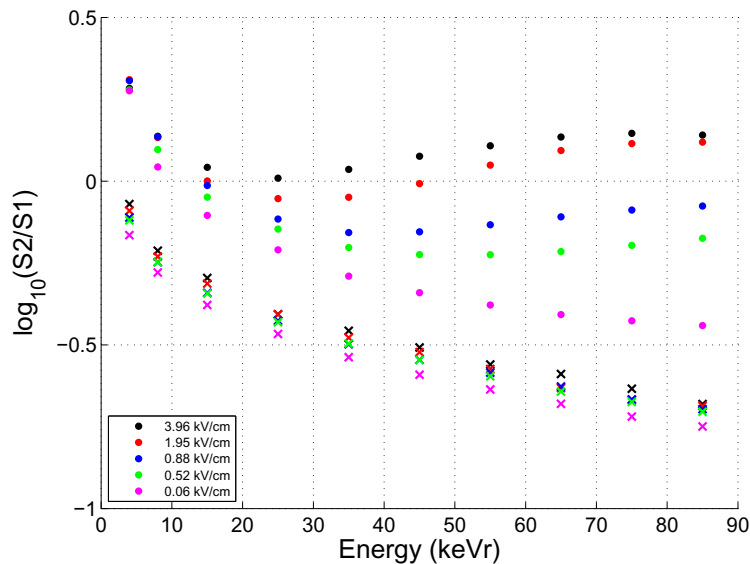
Figure 5.11: Fit means of the $\log_{10}(S2/S1)$ of the electron and nuclear recoils. The error bars are statistical.

5.3 Pulse Shape Discrimination

5.3.1 Introduction

As previously mentioned, the measurement of the scintillation light alone can also provide discrimination, albeit at a lower efficiency than charge-based discrimination (see Section 3.4). Dark matter detectors using pulse shape discrimination (PSD) with NaI [183], high pressure xenon gas [261], single phase liquid xenon, argon and neon [12, 195, 262, 263, 264], and two-phase argon [203, 265] have been employed or are currently under development, but thus far there has been no exploration of PSD in a two-phase liquid xenon time projection chamber. In a two-phase detector, $\log_{10}(S2/S1)$ can be used to clearly separate the electron and nuclear recoil events for better measurement of their respective pulse shapes. This section describes the measurements of the electric field and energy dependence of PSD in such a detector with the same data as that used to explore the charge-based discrimination described in the previous section. Also explored is the use of the prompt/total pulse shape quantity in conjunction with $\log_{10}(S2/S1)$ to further reduce the background beyond that achievable by either discriminant alone. Lastly, PSD performance is projected to larger

detectors using a pulse shape Monte Carlo.

5.3.2 Prompt/Total Method

The PSD performance was examined for various pulse shape quantities such as the width at half-max, integral/height, prompt/total fraction and a quantity called "multi-bin," which is a generalization of the prompt/total fraction to more than two bins (described in [200]). The prompt/total and multi-bin quantities provide equal discrimination efficiency in liquid xenon. Here, we describe only the results of prompt/total which is defined as

$$f_p = \frac{\int_{t_i}^{t_0 + t_{window}} V(t)\,dt}{\int_{t_i}^{t_f} V(t)\,dt}, \tag{5.1}$$

where $V(t)$ is the signal voltage, t_{window} is the prompt window size, $t_i = t_0 - 50$ ns, and $t_f = t_0 + 300$ ns, where t_0 is the time at which the pulse reaches 10% of the maximum amplitude on the leading edge. The optimal t_{window}, depends on the PMT, electronics, and detector size. For Xed1b, it is 10 ns and for the Monte Carlo pulses of larger detectors as described in the next section, $t_{window} = 36$ ns is used.

5.3.3 Pulse Shape Monte Carlo

A pulse shape Monte Carlo was developed to gain a better understanding of the f_p distribution and to project the PSD performance to larger detectors by incorporating a photon arrival time distribution. To simulate the S1 signal, we need the photon emission (excimer decay) probability distribution function (PDF), the photon arrival time PDF, PMT gain distribution, and photoelectron response waveform. The PMT gain distribution is the single photoelectron distribution from the photoelectron calibration dataset. The photon emission PDF is obtained by deconvolving the photoelectron response from the average S1 pulse. Deconvolving the arrival time is unnecessary due to the small size of the detector as confirmed by the photon propagation Monte Carlo (described in Section 4.3.1). The average pulses are calculated by lining up the pulses according to their t_0 and calculating the mean voltage for each time bin. This was done for electron and nuclear recoil events
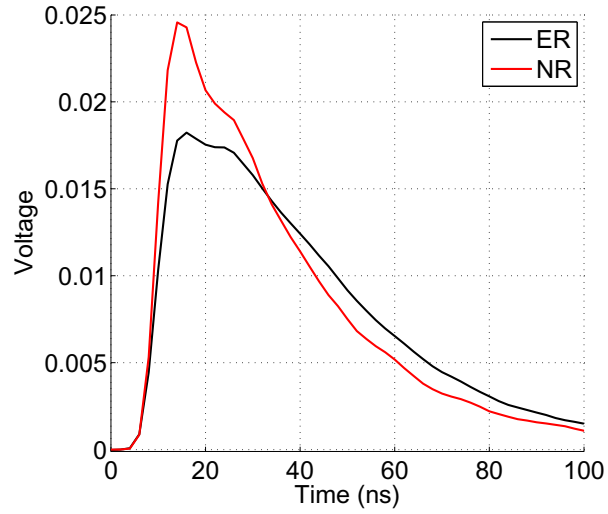
(a)
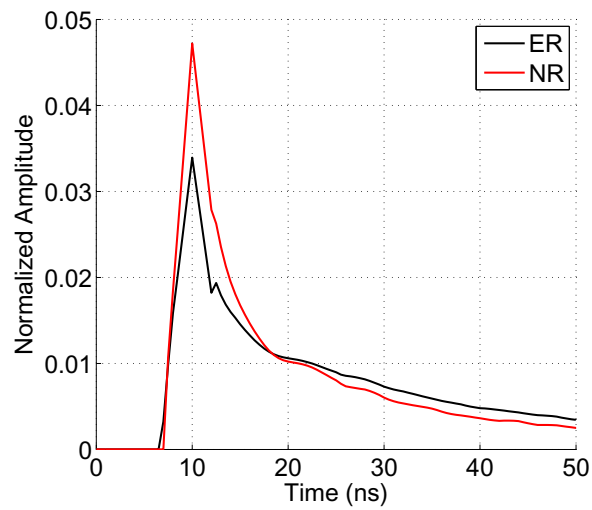
(b)

Figure 5.12: Average pulses (top) and corresponding photon emission probability distribution functions (bottom) for 78 keVr electron and nuclear recoils at 0.58 kV/cm as determined with the Case prototype.
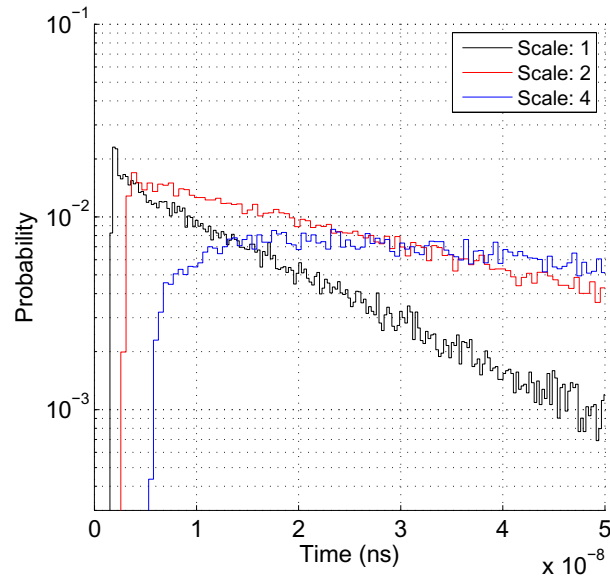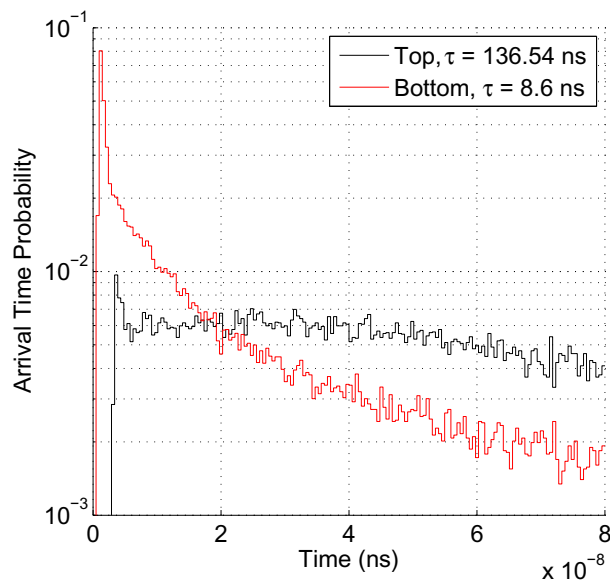
Figure 5.13: The distributions of photon arrival time to the bottom PMT array for various scales of LUX (top) and for events at the top and bottom of LUXx4 (bottom). The top plot represents an average of the active volume.
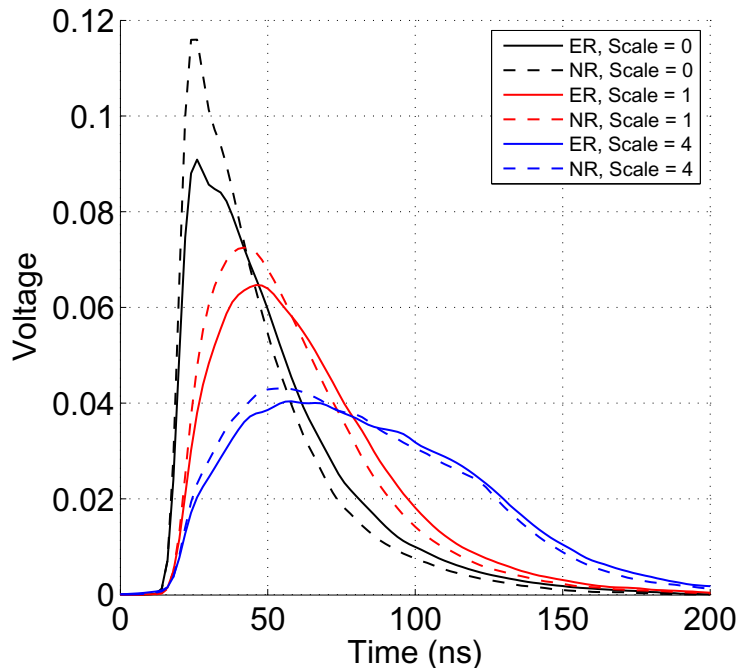
Figure 5.14: Electron and nuclear recoil pulses in various detectors generated by the Monte Carlo. The pulses become less distinct with increase in detector size as the fluctuations in arrival time dominate.

in 2 photoelectron bins. The PMT response to a single photoelectron was obtained in the same manner from the photoelectron calibration dataset. Figures 5.12(a) and 5.12(b) show the average S1 pulses and corresponding emission PDF for 78 keVr electron and nuclear recoils at 0.06 kV/cm.

The photon arrival time PDF for larger detectors was obtained with the previously mentioned photon propagation Monte Carlo. In addition to simulating Xed1b (to confirm the assumption of instantaneous photon arrival times), a next generation two-phase liquid xenon detector called the Large Underground Xenon Detector (LUX), and a detector with four times the dimensions of LUX (LUXx4) were also simulated. Nominal LUX active volume dimensions of 49 cm diameter and 54 cm height were used. LUX and LUXx4 have active masses of roughly 300 kg and 20,000 kg, respectively. Five aluminum meshes of 0.02 normal opacity are placed in same manner as in Xed1b. The arrival time distributions were simulated for 50 different (r, z) coordinates. Figure 5.13(a) shows the photon arrival time
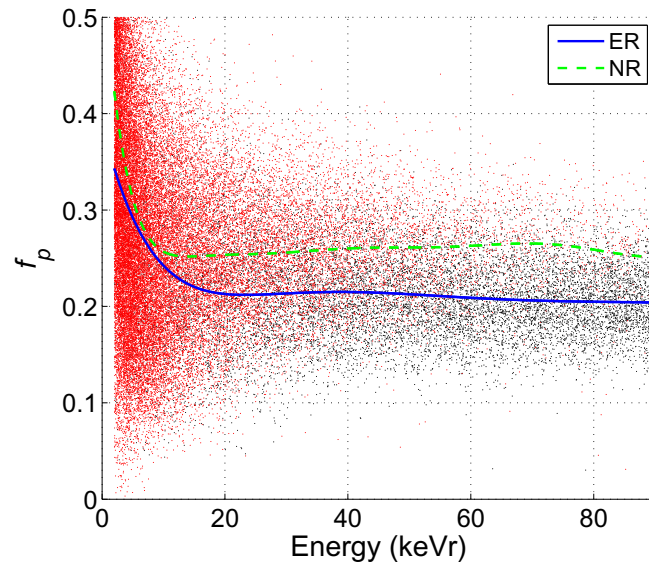
(a)
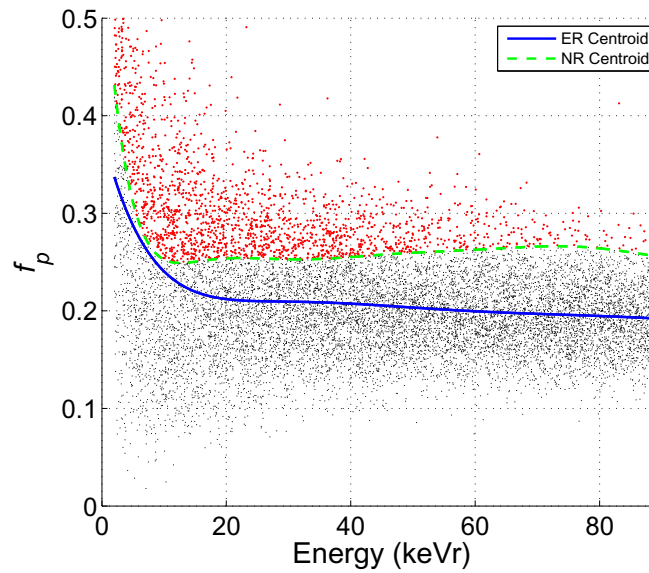
(b)

Figure 5.15: Plots of f_p versus energy of the nuclear (red) and electron (black) recoil events (top) of the ^{252}Cf data set and of the electron recoils events (bottom) of the ^{133}Ba data set at 0.06 kV/cm. The leakage events of the ^{133}Ba data set have been highlighted red. The nuclear and electron recoil centroids are indicated by the dashed green line and solid blue line, respectively.
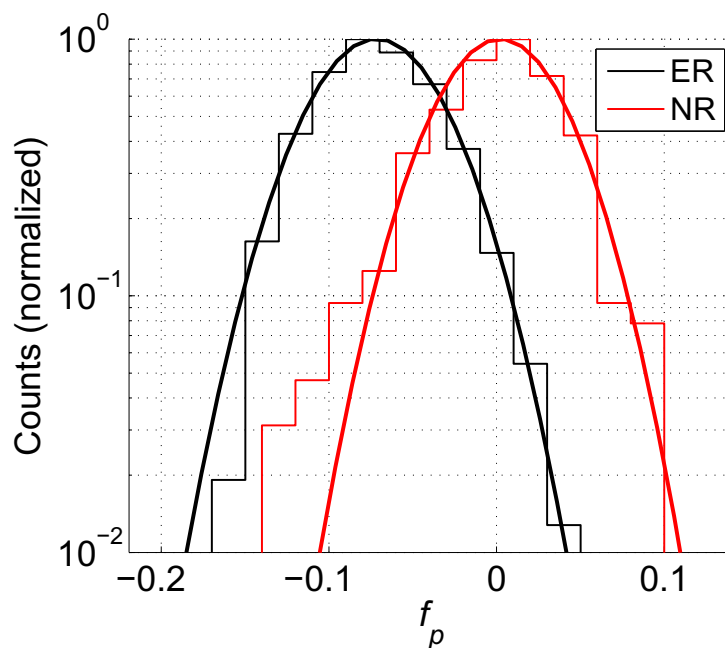
Figure 5.16: Histogram (normalized to amplitude of 1) of the f_p between 70 and 80 keVr of electron and nuclear recoil events at 0.06 kV/cm. Also included are the Gaussian fits to the peaks.

distribution for several scales of the LUX detector. Figure 5.13(b) shows the arrival time distribution for photons emitted near the top and bottom of the active volume of LUXx4. This plot shows that photons emitted from the top of the active region generally strike the bottom PMT array much later and with a significantly wider distribution in arrival times than those emitted from the bottom. Figure 5.14 shows the average electron and nuclear recoil pulses for the different sized detectors as created by the pulse shape Monte Carlo. The electron and nuclear recoil pulses become noticeably less distinct as the detector size is increased. At each electric field and for each of the three detectors, 24,000 light pulses of each recoil type were simulated between 0 and 100 keVr.

5.3.4 Results

Figure 5.15(a) is a scatter plot of f_p as a function of recoil energy for the ^{252}Cf dataset. Figure 5.15(b) is a similar plot of the ^{133}Ba data set with the leakage events highlighted.
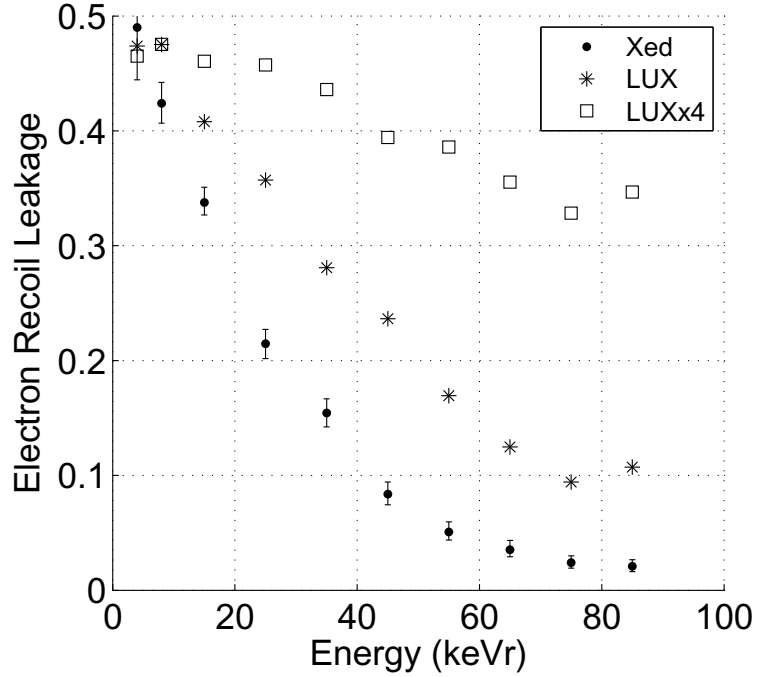
Figure 5.17: Gaussian leakage of f_p as a function of recoil energy at 0.06 kV/cm. Also included are the Monte Carlo predictions for larger detectors.

The nuclear recoil acceptance window is the region above the energy dependent nuclear recoil mean as indicated by the green dashed line. The leakage is calculated in a fashion that is identical to that used for $\log_{10}(S2/S1)$ in the previous section (Section 5.2.2). The 10th order polynomial fits to the band mean can be see in Figures 5.15(a) and 5.15(b). Figure 5.16 shows the histograms of f_p between 55 and 60 keVr for the ^{133}Ba and ^{252}Cf (excluding the ER events) at 0.06 kV/cm.

Figure 5.17 shows the electron recoil leakage as a function of energy at 0.06 kV/cm which is the drift field that provides the lowest leakage. Also included in this plot are the Monte Carlo predictions of the detector-averaged leakage for LUX and LUXx4. We see that the PSD is very weak for LUXx4 and thus would probably never be used in such a large detector except for regions of the detector near the PMTs. The discrimination efficiency of LUX is ~90% for recoil energy >70 keVr and steadily decreases with decreasing energy. The discrimination efficiency in Xed1b is ≥95% at energies above 50 keVr but is much lower below 20 keVr, which is the energy region of interest for dark matter detection. The error
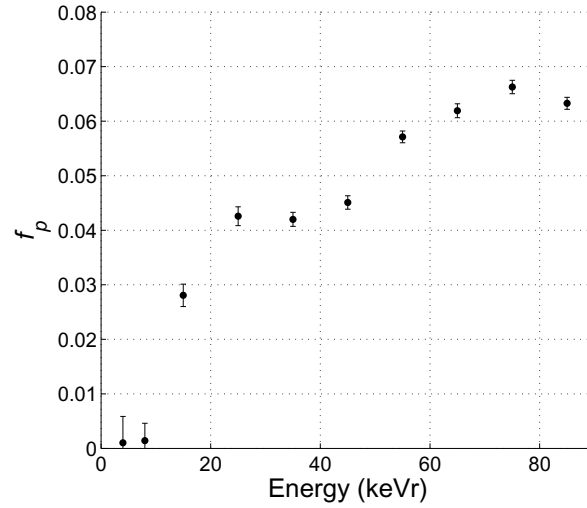
(a)
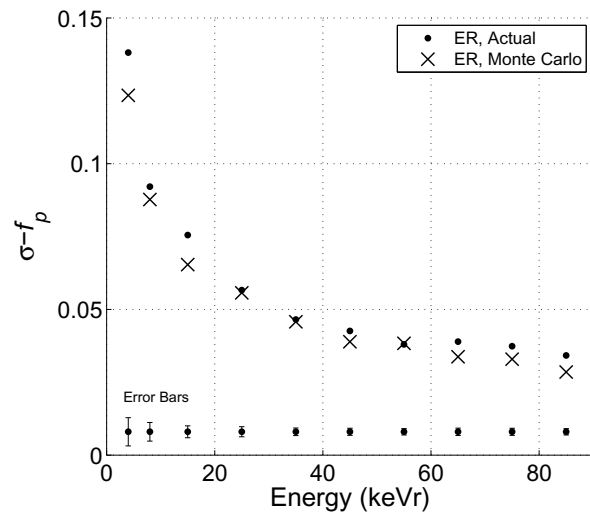
(b)

Figure 5.18: The energy dependence of the electron and nuclear recoil f_p band separation (top) and fit sigmas (bottom) of the electron recoils at 0.06 kV/cm drift field. The error bars represent the statistical error.

bars of the leakage include only the statistical fit uncertainties. The existence of systematic shifts in the pulse shape between the electron and nuclear recoil datasets would manifest as a shift in the f_p of the electron recoil as they are present in both datasets. Several changes could lead to a change in pulse shape: the introduction of an impurity that captures and emits light with a decay time, a drastic shift in the geometry or a change in the electronics. None of these changes are likely to have occurred and in any case, the fit mean of the electron recoil pulse shape of the ^{252}Cf and ^{133}Ba datasets agree within error.

Figures 5.18(a) and 5.18(b) show the band separation and electron recoil band width as a function of energy, respectively. These figures reveal that the rise in leakage with decreasing energy is a result of the convergence of the two bands and an increase in the band width. The convergence of the f_p of the electron and nuclear recoils can be explained by the convergence in LET (see Figure 3.9). Also included in Figure 5.18(b) are the Monte Carlo data band widths, which match well with the data indicating that band width is dominated by statistical fluctuations. The slightly higher width in the actual data suggests that some other intrinsic component (e.g. recombination fluctuations) that is not included in the Monte Carlo is apparently making a small contribution to the band width. The data shown in these plots can be used to estimate the discrimination performance of a detector with higher light collection. We obtain the intrinsic component to the width as the difference between between the Monte Carlo and observed widths. The band width at energy E of a detector with a factor x higher light collection is the sum (quadrature) of the Monte Carlo width at $x \times E$ plus the intrinsic width at E. Here, we see that although an improvement in the light collection would result in a large reduction in the band width below 20 keVr, the leakage is unlikely to drop meaningfully as the band separation is near zero.

Figure 5.19 is a plot of the field dependence of the leakage between 60 and 80 keVr. The leakage increases as the electric field is increased. The band width appears to be independent of the electric field (Figure 5.20(b)) as expected since the Monte Carlo shows that the width is dominated by statistical fluctuations which do not change with electric
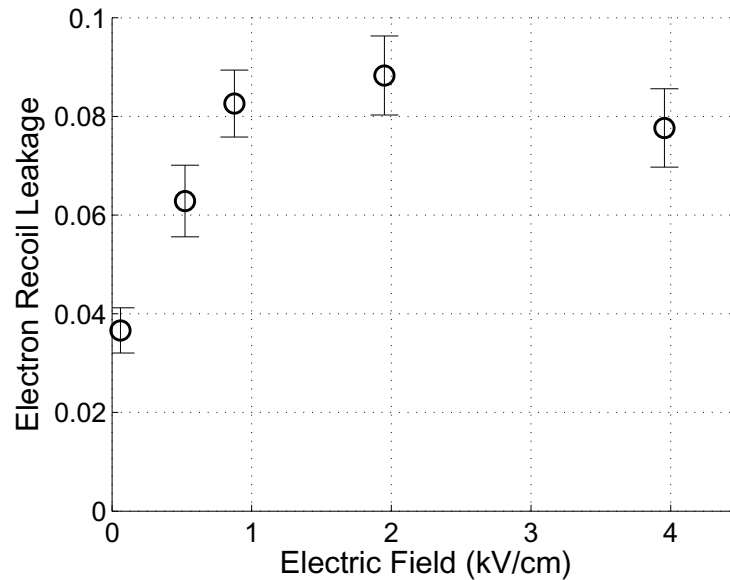
Figure 5.19: Leakage versus electric field between 60 and 80 keVr using f_p. The error bars represent the statistical uncertainty.

field. The trend in the leakage can be explained by the change in the f_p mean (Figure 5.20(a)). The f_p of nuclear recoils appears to be field independent while that of the electron recoils possesses a strong field dependence below ~ 1 kV/cm, similar to the behavior of the electron recoil charge yield. The change in the tail is attributed to the removal of electrons from the event site. As the electric field is increased, the electrons that would have otherwise recombined at longer time scales are swept away by the electric field. The presence of electrons may also be changing f_p by converting singlets to triplets [240, 22]. On the other hand, the charge yield of the nuclear recoils changes little with field [19] as does the pulse shape. This mechanism suggests that a correlation should be observed between mean f_p and $\log_{10}(S2/S1)$, as the latter parameter is a measure of charge yield. A positive correlation is observed for the mean values across electric fields (Figure 5.21), however, the correlation at an electric field is roughly zero. The correlation is either nonexistent or is masked by the much large statistical fluctuations.

The electron recoil leakage can be reduced by changing from the usual nuclear recoil window defined by $\log_{10}(S2/S1)$ to a two-dimensional window in $\log_{10}(S2/S1)$-f_p space
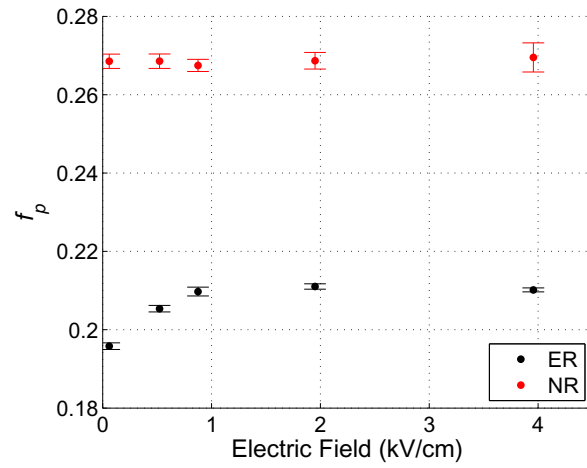
(a)
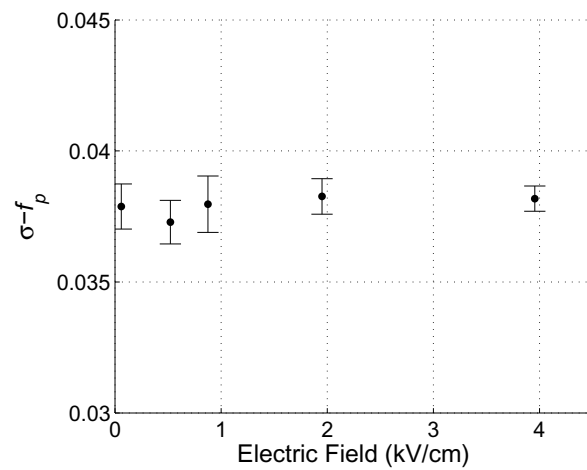
(b)

Figure 5.20: The Gaussian fit means for electron and nuclear recoils (top) and fit sigmas for electron recoils (bottom) between 60 and 80 keVr as functions of the electric field. The error bars represent the statistical uncertainty.
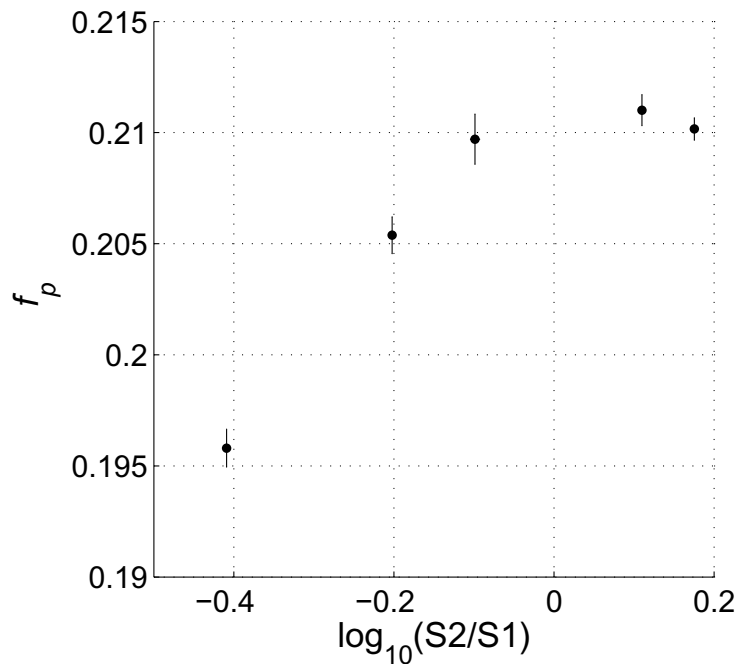
Figure 5.21: Plot of the mean f_p versus the mean $\log_{10}(S2/S1)$ between 60 and 80 keVr at five different electric fields. The error bars represent the statistical uncertainty.

("2D window") as the discriminants are not redundant. For simplicity, the acceptance window is defined by a diagonal straight line cut through the center of the nuclear recoil cluster, retaining the 50% acceptance for nuclear recoils. For projections to larger scale detectors, the fits to the $\log_{10}(S2/S1)$ of the real data is used in conjunction with the fits to f_p of the Monte Carlo data. Figures 5.22(a) and 5.22(b) are scatter plots of f_p versus $\log_{10}(S2/S1)$ of the [133]Ba and [252]Cf data between 70 and 80 keVr at 0.06 kV/cm, with the $\log_{10}(S2/S1)$ and 2D windows, respectively. The circled dots are the electron recoil leakage events. Figure 5.23 shows the leakages with the two different windows in Xed1b and the projected performance for LUX. The results for LUXx4 are omitted because the improvement is minuscule. The error bars are statistical. In Xed1b, the reduction in Gaussian leakage below 30 keVr is 16% and for LUX, 5%. Note that these are detector averages. The fluctuations in photon arrival time of events near the bottom of the detector are smaller than average (Figure 5.13(b)) thus the performance of this technique in such regions would be better than that shown in Figure 5.23.
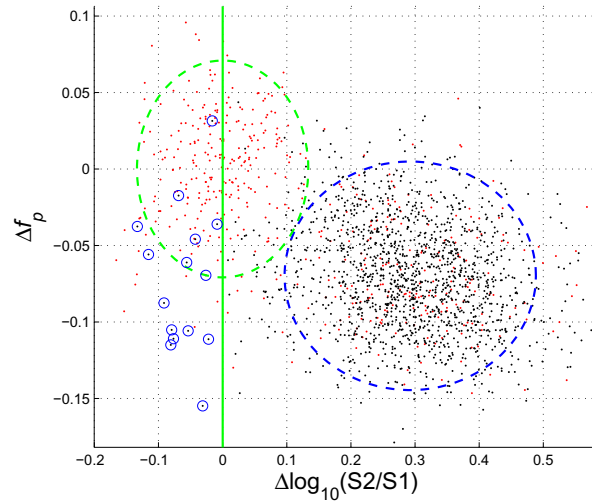
(a) f_p versus $\log_{10}(S2/S1)$ with usual cut in $\log_{10}(S2/S1)$.
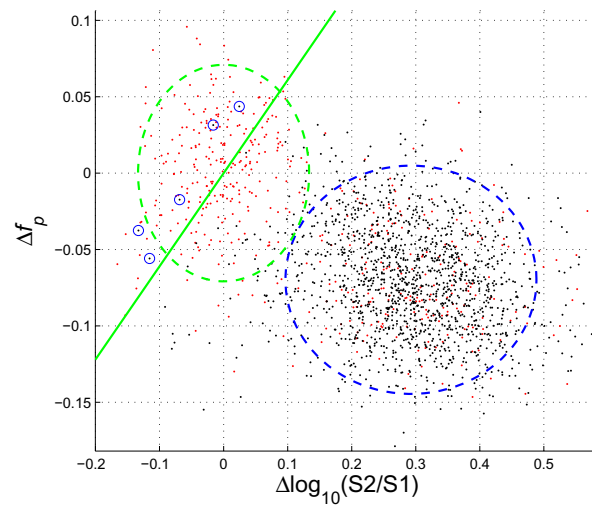
(b) f_p versus $\log_{10}(S2/S1)$ with diagonal cut.

Figure 5.22: Scatter plots of f_p versus $\log_{10}(S2/S1)$ between 60 and 80 keVr at 0.06 kV/cm with the $\log_{10}(S2/S1)$ (top) and 2D window (bottom) cuts shown. Both the ^{133}Ba (black) and ^{252}Cf (red) points are plotted with respect to the nuclear recoil mean. The blue circle highlights ER leakage events. The dashed lines are the 2σ ellipses.
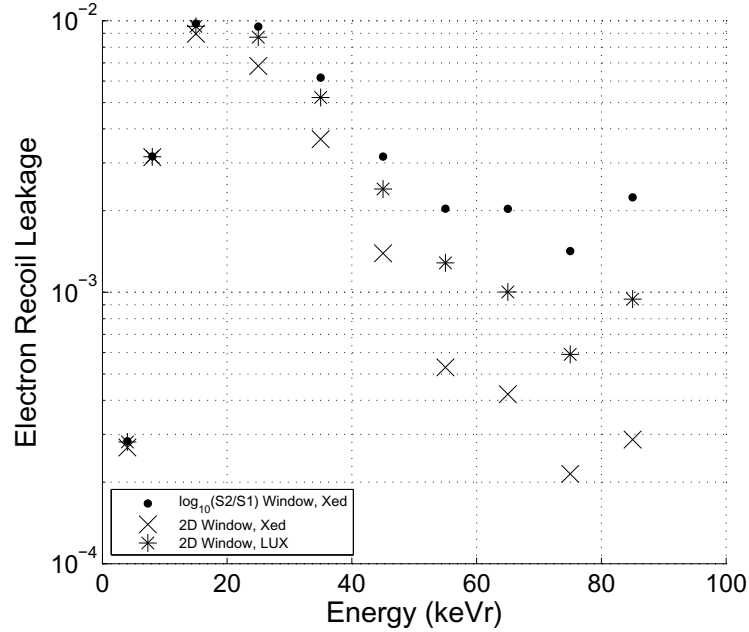
Figure 5.23: Electron recoil leakage versus recoil energy with $\log_{10}(S2/S1)$ and 2D window at 0.06 kV/cm. The predicted 2D window leakage in LUX is also shown.

In summary, we have measured the field and energy dependence of pulse shape discrimination in a two-phase liquid xenon detector. By using $\log_{10}(S2/S1)$, we were able to cleanly separate the electron and nuclear recoils for a more robust measurement of the respective pulse shapes. With the aid of a pulse shape Monte Carlo, we find that the width of the pulse shape bands are dominated by statistics; other processes like recombination fluctuations contribute little. We observe no apparent correlation between the fluctuations of pulse shape and $\log_{10}(S2/S1)$ at an electric field. A significant increase in light collection is unlikely to meaningfully increase the PSD efficiency at low energies relevant to dark matter searches. Although, the discrimination by pulse shape is poor, it can be used with the charge measurement to reduce the leakage beyond that achievable by either method alone. Finally, the pulse shape Monte Carlo is used to project the performances of PSD and 2D-window to larger detectors.

5.4 Use of a Wavelength Shifter in a Two-Phase Xenon Detector

The discrimination performance of liquid xenon dark matter detectors greatly depends on the light collection efficiency as the statistical fluctuation of the primary light signal is a limiting factor at recoil energies of several keVs [266, 267, 60]. XENON10 and the Case prototypes with two PMTs achieve a light collection efficiency of about one photoelectron (pe) per keVr (slightly field dependent). The use of wavelength shifters have been used in LXe scintillation detectors [266]. Shifting the emission spectrum to longer wavelengths can boost the light signal in several ways. First, the reflectance of PTFE and other materials are generally higher for photons of higher wavelength. As previously stated, the reflectance at 175 nm has been reported to be between 55% and 95% (see Section 4.3.1 on discussion on reflectors). The reflectance at 350 nm has been measured to be 98.5% [45]. Spectralon, a proprietary form of PTFE created by Labsphere, has a reflectance that rises from 98% at 300 nm to >99% above 400 nm [45]. The spectral reflectance of Spectralon, PTFE and other reflectors to photons of wavelength <220 nm can be seen in Figure 4.7. The reflectance to photons of wavelength >300 nm is shown in Figure 5.24. Secondly, the Rayleigh scattering length increases with wavelength as λ^4 (see Equation 3.21) [251]. Extending the Rayleigh scattering length decreases the total travel distance of the photons, which decreases the likelihood for absorption by impurities in LXe (assuming that the wavelength shifted photons are not more readily absorbed by impurities). Finally, the quantum efficiency of photomultiplier tubes typically increases with wavelength. For example, work at the Jefferson Lab concluded that the deposition of p-terphenyl (p-TP) onto the glass windows of Burle 8854 PMTs increased their quantum efficiency in the blue range by about 40% [268].

A group exploring the benefits of using wavelength shifters in dark matter detectors has successfully operated a NaI detector with p-TP wavelength shifter at 160 K [269]. ICARUS T600 [205], ArDM [205], and WARP [203] are three argon detectors that use the wavelength shifter tetraphenylbutadiene (TPB). TPB has also been used in a liquid neon detector [72].
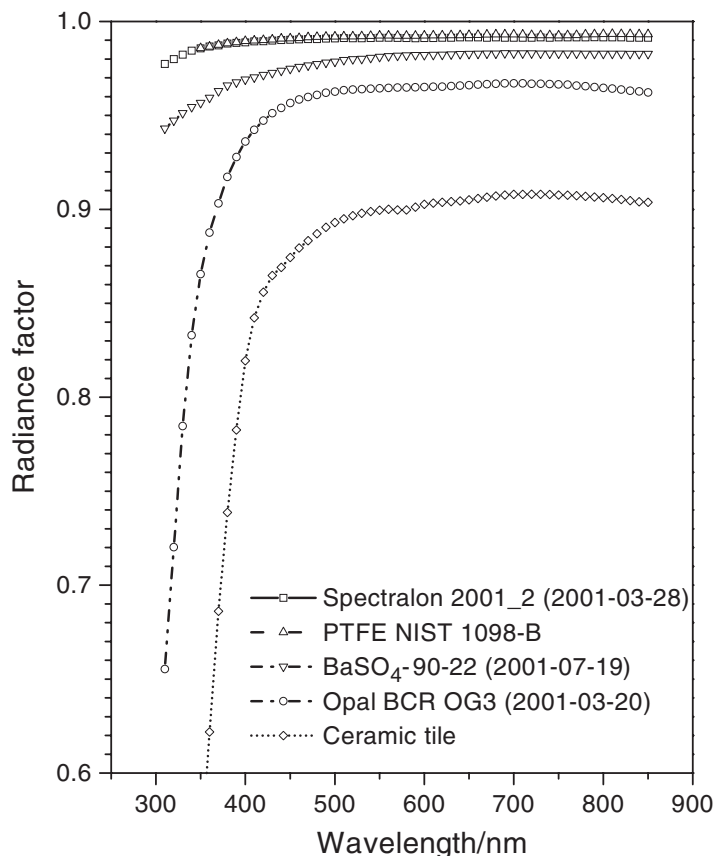
Figure 5.24: Spectral diffuse reflectance of some common reflectors as a function of wavelength above 300 nm [45].

Wavelength shifters are required in argon and neon detectors because of their low wavelength emission (128 nm and 77 nm, respectively). We are unaware of any published results on the use of a wavelength shifter in a two-phase xenon detector. In this section, we report the results of running such a detector with vacuum-deposited p-TP.

5.4.1 Detector

Figure 5.25 is a CAD diagram of the Spectralon detector, Xed1f. Figure 5.26 is a photo of the detector with the top reflector removed. This detector consisted of five wire grids and a single 2″ diameter Hamamatsu R9288 PMT in the liquid. The high voltage and signal connections at the PMT were shielded with a stainless steel cup. The wire grid
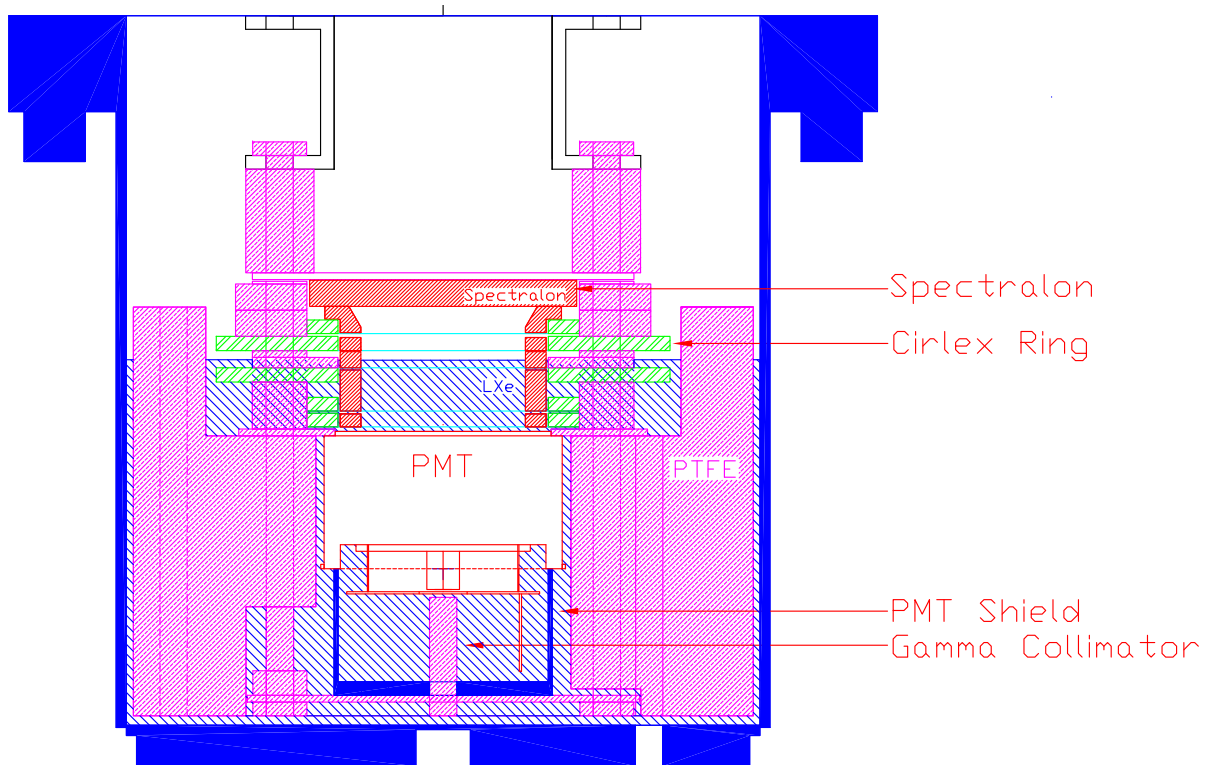
Figure 5.25: CAD diagram of the Xed1f detector with Spectralon reflectors.
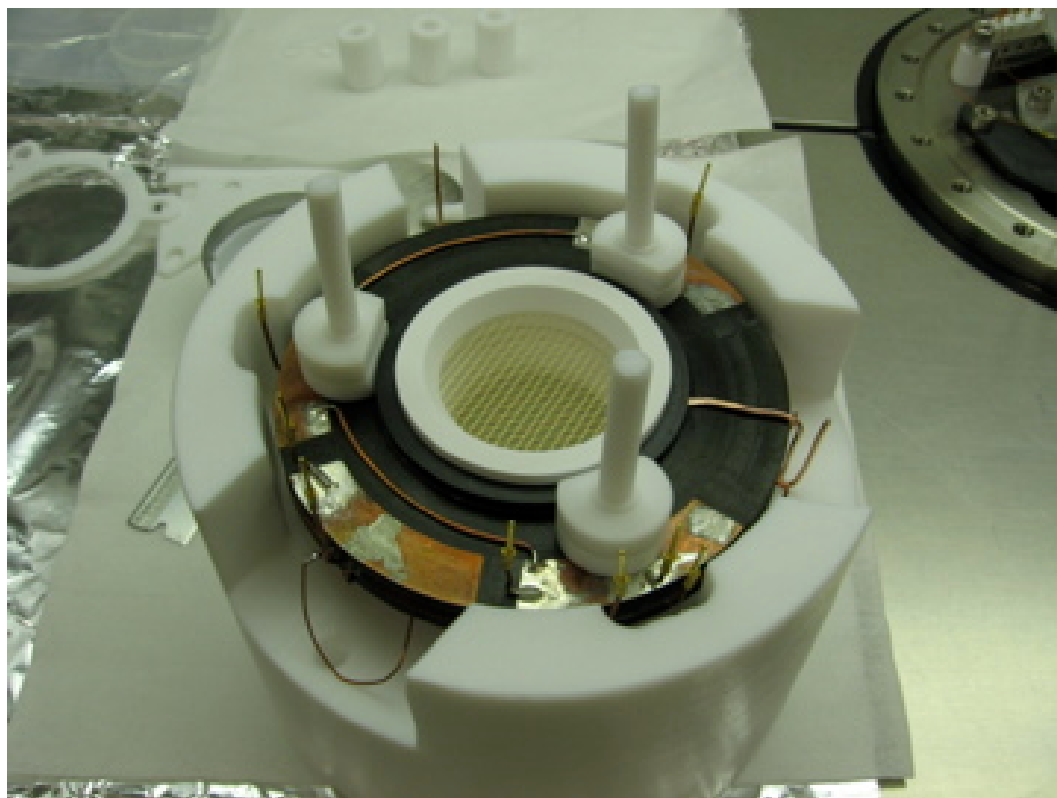
Figure 5.26: Detector with p-terphenyl coated Spectralon pieces. The top Spectralon reflector has been removed to show the active volume.

just below the liquid level (gate) consisted of 40 μm diameter BeCu wires; the other four had 125 micrometer diameter gold-plated aluminum wires. The active volume was defined by the cathode and gate grids and had a depth of 1.0 cm and a diameter of 3.83 cm. Five Optical-Grade Spectralon reflectors – five rings and one circular plate – surrounded the active volume. Since the reflectance of Spectralon is very sensitive to impurities such as oils, we had the manufacturer of Spectralon, LabSphere, machine the the parts. We chose Spectralon over Teflon even though the literature shows identical reflectance at high wavelengths because the Spectralon is likely generated under more controlled conditions and thus is less likely to show the large variations in reflectance that has been observed for Teflon at 175 nm. Its reflectance is a function of thickness (as seen in Figure 5.27) – the reflectance is 0.935 at 1 mm and rises to $\sim$99% at 5 mm and levels off. All five reflector pieces have a thickness of at least 5 mm. Spectralon is extremely hydrophobic as it has a

Wavelength 325 nm
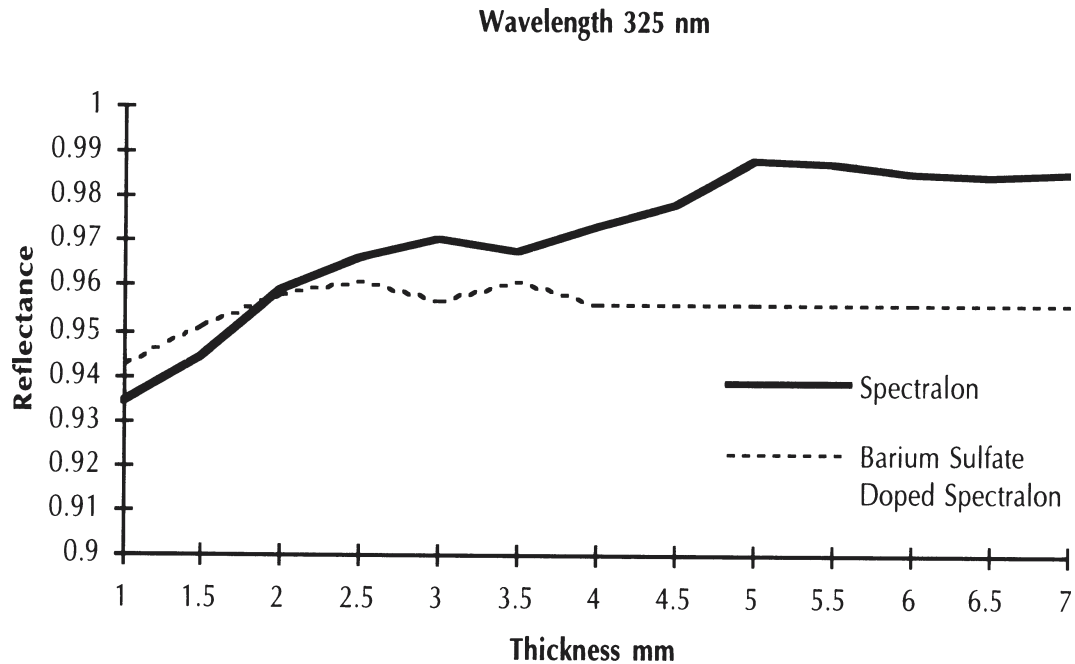
Figure 5.27: The reflectance of Spectralon and Spectralon doped with barium sulfate to 325 nm photons as a function of thickness [46].

water permeability of <0.001%. This is important as water is one of the primary charge-collecting impurities of liquid xenon (see Section 3.5.2 for information on electron-capturing impurities in liquid xenon). The PMT and the inside surfaces of the reflectors were coated with a wavelength shifter.

A ^{57}Co source was placed in the source entry tube underneath the detector (as seen in Figure 4.1). The 122 keV gammas are collimated by the PTFE $1/4''$ rod (as seen in Figure 5.25), which is surrounded by liquid xenon which is more absorbent of gammas. This collimates the gammas to a ~1.5 cm diameter column.

5.4.2 Selection of Wavelength Shifter

A number of solid wavelength shifters have been considered for noble gas detectors including trans-stilbene, TPB, sodium solicylate, diphenylstilbene and p-TP [270, 222]. We selected p-TP because it has been used in previous high-pressure xenon gas scintillation and electro-luminescence detectors (see [271] and references therein). Among the wavelength shifters,
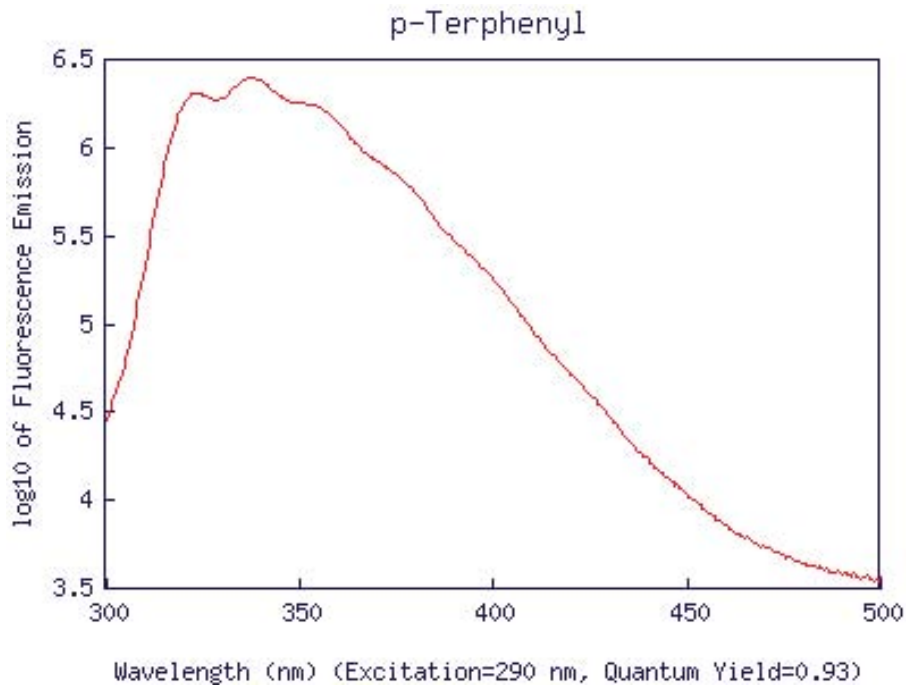
Figure 5.28: P-terphenyl emission spectrum [47].

p-TP has the best record in applications for noble gas detectors because of its reasonable stability in vacuum, low hygroscopy, chemical inertness, and extreme radiation hardness. Several studies have proven that p-TP does not contaminate pressurized xenon gas and helium with electronegative impurities and has been demonstrated to have a >90% quantum efficiency for converting 175 nm photons into 340 nm ones [272]. Spectralon has a reflectance of 98.5% at 340 nm [45]. Figure 5.28 shows the emission specturm of p-TP [47].

5.4.3   Vacuum Deposition of Wavelength Shifter

There are several common ways of depositing wavelength shifters. One method is to spray coat the items with a mixture of p-TP dissolved in toluene. Another is by polymer matrix coating. In this technique, the wavelength shifter and a plastic is dissolved in toluene, and the mixture is coated onto the parts and allowed to dry. The most complicated method is by evaporation in a vacuum chamber. We opted for this technique because it affords the best purity, uniformity and control of thickness [273]. A standard vacuum thermo-deposition

system was used to deposit 0.5 mg cm^{-2} of p-TP on the Spectralon reflectors and the window of the PMT. Before deposition, the p-TP was baked at 50°C in vacuum to remove absorbed water and other impurities. The sublimation began at a pressure of 2×10^{-7} torr and temperature of 160°C. The coated pieces were allowed to cool down in the nitrogen atmosphere before removal. The thickness of deposited layers was estimated by measuring the change in the mass of the p-TP and calculating, by geometry, the fraction of p-TP that lands on the Spectralon pieces. Before usage, the coated pieces were stored in a dry box to prevent absorption of water which can lower the quantum efficiency of p-TP [274].

5.4.4 Light Collection Efficiency

The expected number of photoelectrons generated for an event of energy E is

$$N_{pe} = (E/w_{ph}) \cdot LCE \cdot QE, \qquad (5.2)$$

where w_{ph} is the energy required to generate one photon (15.2±0.3 eV at zero field from the calibration measurement described in [275]), LCE is the light collection efficiency, and QE is the quantum efficiency of the PMT. The number of photons emitted is E/w_{ph}. The number of photons expected to strike the photocathode is N_{pe}/QE. With N_{pe}, we have the LCE of the detector. The N_{pe} is just the $S1$ of the 122 keV electron recoils divided by the mean single photoelectron response and thus only two datasets were needed. Both zero field datasets were taken with the detector at 175 K and liquid level above the surface of the top Spectralon disc reflector. Only events within the space 4–6 mm above the cathode are used. With this cut and the collimation by the Teflon rod, only events at the center of the active volume are considered. The peaks are fit with Gaussian functions. This setup had a photoelectron conversion efficiency of 6.5 pe/keV at zero drift electric field. This value has a statistical uncertainty of less than 1%.

To correctly assess the affect of using a wavelength shifter, a similar single PMT detector with no wavelength shifter should also have been tested but the experiment was terminated due to the very poor charge collection caused by the p-TP (see next section). The closest comparison that can be made is with the performance of the bottom PMT of the two PMT

Xed1b detector running in two-phase. The bottom PMT in the prototype with Teflon reflectors was 5.0 pe/keV. The light collection efficiencies of the Teflon and Spectralon setup were 47±1% and 57±1%, respectively – the Spectralon setup has 21% higher light collection than the Teflon setup. Note that part of the difference in the light collection efficiency is due to the difference in the detector configurations. In the two-PMT setup, the photons that leave the liquid are unlikely to reenter it and be collected by the bottom PMT.

There are several potential sources of systematic error in the light collection efficiency values. The first is the nonlinearity in the PMT signal response to larger S1's due to the current output limitations of the PMT. This effect was determined to be negligible for the signals of this experiment. The second is the possible change in quantum efficiencies when cooled to cryogenic temperatures. Having observed no change in the QE's by changing the temperature from 165 to 185 K, we assumed that these values are constant with temperature. The errors given for LCE are due to uncertainties in w_{ph}. A homemade light propagation Monte Carlo written in MATLAB was used to determine the reflectance of the Teflon given the observed light collection and determine the expected light collection efficiency of the wavelength shifter plus Spectralon setup. Simulated photons reflect diffusely off non-metal surfaces and shift in wavelength before reflecting off surfaces covered with p-TP. Photons are propagated until absorption. Refractive indices of 1.68 [42] and 1.51 (given by the PMT manufacturer) were used for the LXe and PMT glass, respectively, and values of 30 and 100 cm were used for the Rayleigh and absorption scattering lengths [222, 39]. Reflectance values of 0.40 and 0.35 were used for scattering wavelength shifted photons off BeCu (assumed to be the same as Cu) and Au, respectively [276]. The reflectance of BeCu and Au below 200 nm could not be found and likely varied greatly depending on the surface quality. Since varying the reflectance of BeCu at 175 nm from 0 to 1 shifts the LCE by less than 1%, a value of 0 was arbitrarily chosen. The reflectance of Au is 0.3 near 200 nm [276]. Assuming that the Au reflectance at 175 nm is 0.3±0.3, the Monte Carlo can match the LCE of the two PMT Teflon setup with Teflon reflectance of 0.85±0.05. This
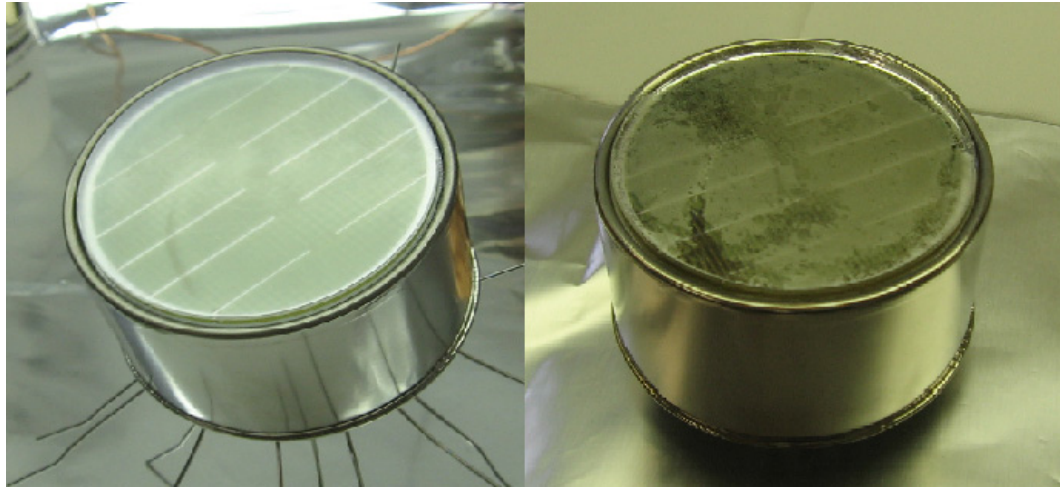
Figure 5.29: The p-TP coated PMT before and after the experiment. Some of the p-TP clearly dissolved into the liquid xenon.

value falls within the range of previous observations (see Section 4.3.1) but is much lower than that seen in XENON10, which saw a reflectance of >98%. The presense of embedded light-absorbing impurities or degradation by UV light may be reasons for the difference [254]. There is also the possibility that the Monte Carlo underestimated the reflectance by omission of certain detector details such as small gaps between reflectors rings which would have otherwise absorbed light and decreased the expected number of collected photons. A LCE of 67±2% (error from the uncertainty in Au reflectance) was expected for the Spectralon setup based on the Monte Carlo. A post-run inspection revealed that some of the p-TP had migrated to other parts of the detector, which could account for the lower than expected LCE. Figure 5.29 shows the p-TP-coated PMT before and after the experiment, showing that large amounts of the p-TP had been removed. The omission of small gaps between reflector rings in the Monte Carlo may also have contributed to the discrepancy in light collection efficiency.

5.4.5 Electron Lifetime

To measure the effects of impurities on the charge collection in LXe, ^{57}Co datasets were taken with the detector running in two-phase configuration at 175 K. The electric field in
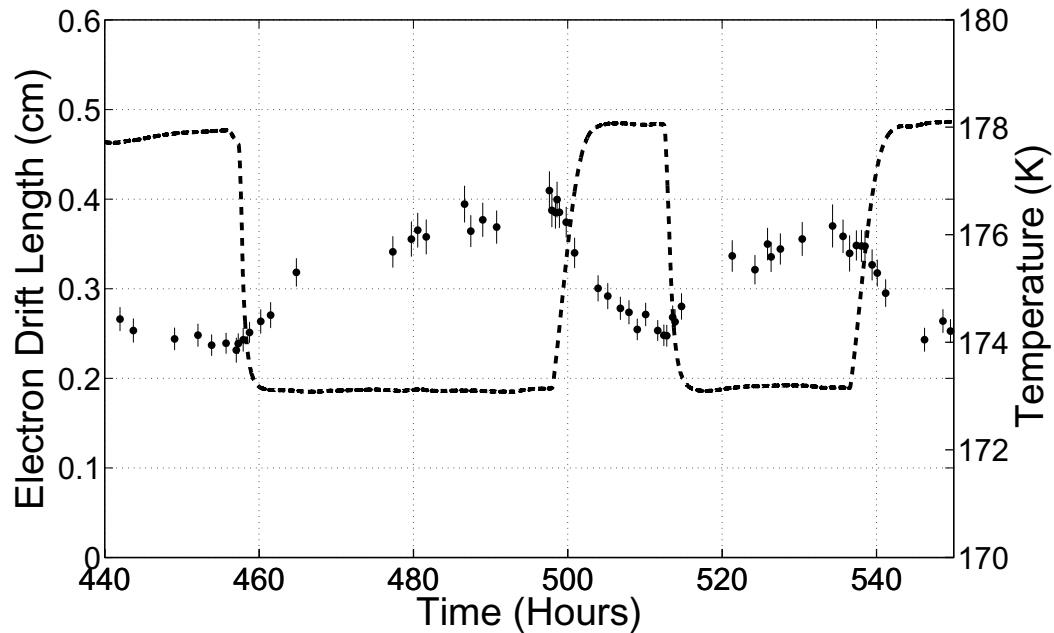
Figure 5.30: Electron drift length (dots) and temperature (dashed line) versus time. There is clearly an anti-correlation between the drift length and temperature that can be explained by the temperature-dependent solubility of p-TP. The error bars are statistical errors of the fit.

the active volume was 1 kV/cm. The field underneath the liquid surface was 5 kV/cm which provided full electron extraction. The liquid level was set halfway between the anode and gate grids. The electron lifetime and drift length were extracted as described in Section 3.5.2. The electron drift length has routinely been measured to be greater than ∼100 cm in our prototypes without p-TP. However, in this detector, the electron drift length stabilized at ∼0.4 cm after more than a week of recirculation. Various attempts at purifying the xenon did not improve the situation. This included recirculating the xenon through the metal getter purifier at different flow rates and modifying the detector to improve the efficiency by which the liquid in active volume of the detector was passed through the purifier. This final modification involved adding a PTFE outlet tube directly to the active volume (Figure 5.31). Furthermore, no vacuum leaks were found in the detector or associated plumbing and a subsequent run with a detector devoid of the wavelength shifter showed excellent purity, thus the equipment was likely not at fault. The impurity problem was likely related to the

presence of the wavelength shifter.

Influence of Electric Field Strength

At a fixed recirculation flow rate and xenon temperature, we measured the electron lifetime as a function of the drift electric field. Electron life time drops with increasing electric field strength (as seen in Figure 5.32) corresponding to an electron attachment rate that increases with field like N_2O (see Figure 3.18).

Influence of Temperature

A potentially more important insight into the impurity issue was revealed by the observation that the drift length did not further decrease over time when recirculation purification was turned off. This is in marked contrast to the common situation early in a run when outgassing appears to be the dominant source of impurities. Moreover, in static conditions with no recirculation, the drift length was inversely related to the temperature by an apparently fixed relationship that was reversible over several cycles of temperature (as shown in Figure 5.30). This strong and reversible correlation between the drift length and temperature suggests that the p-TP is dissolved in the LXe at a level determined by a temperature-dependent solubility. Molecules of p-TP may be acting as acceptors themselves or be facilitating their capture by other impurities by slowing down their drift velocity.

Compounds with higher molecular weight are likely to have lower solubility in LXe. From this point of view, it looks reasonable to repeat the experiment with heavier members of p-N-phenyl family such as p-quaterphenyl (p4P), p-quinquephenyl (p5P), and p-sexiphenyl (p6P); Table 5.1 shows their properties. In fact, p4P has been used as an effective extreme-ultra-violet wavelength shifter in the past (see, for example, [277]) and has demonstrated emission and absorption spectra similar to that of p-TP [278]. Also, p-N-phenyls have demonstrated high chemical stability and high luminescence quantum yield in the blue range [279]. All of them can be deposited by evaporation with the sublimation temperature elevated for heavier members. These organic substances attract attention because of their
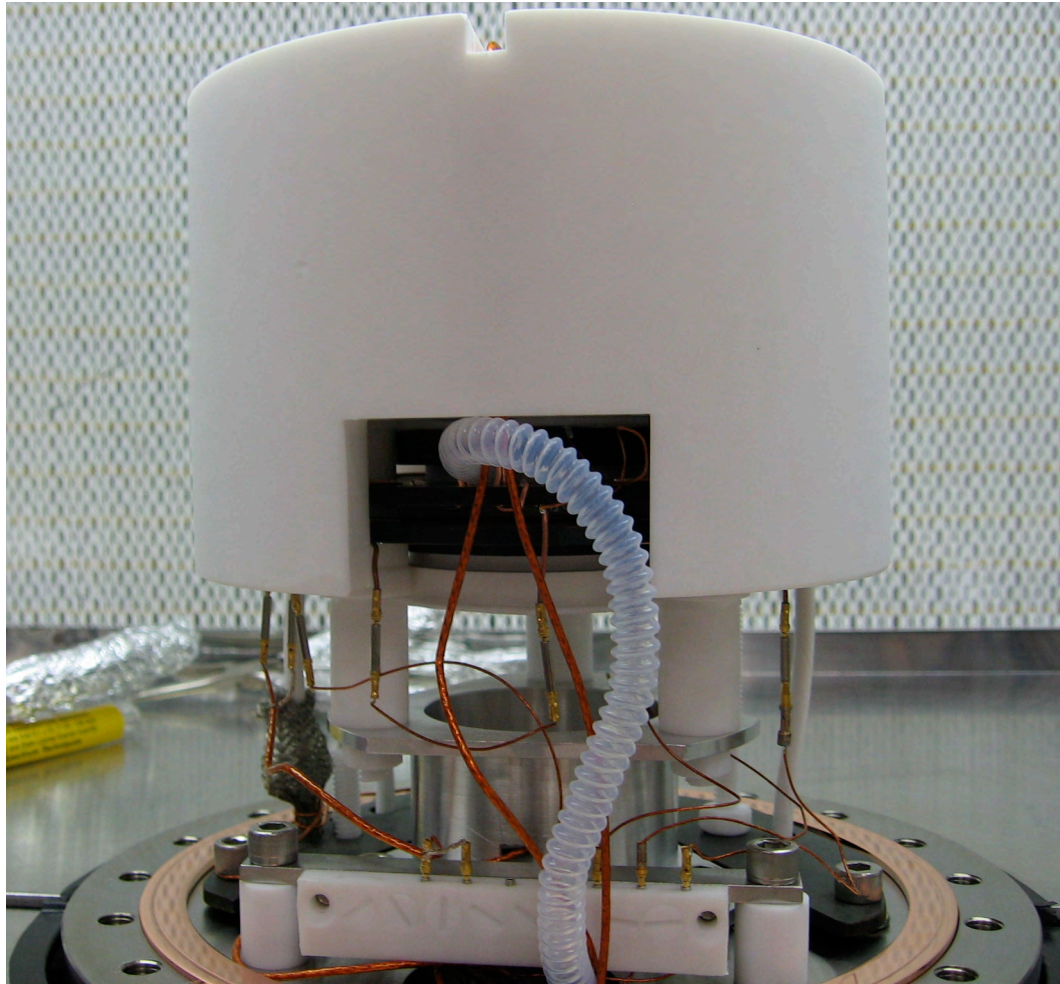
Figure 5.31: The PTFE outlet tube connected to the active volume of the detector which is shown here upside down in the clean bench. The liquid xenon was originally pulled out from underneath the detector but in an attempt to better clean the impurities out of the active volume, the PTFE outlet tube was connected coupled to this region.
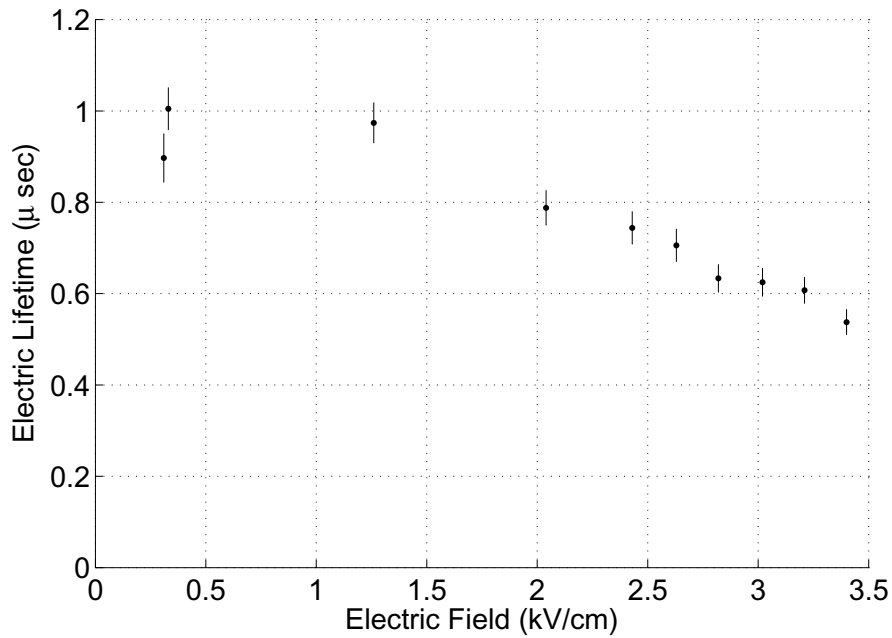
Figure 5.32: The electron lifetime versus the electric field.

Table 5.1: Properties of p-N-phenyls. p3P = para-terphenyl; p4P = para-terphenyl; p5P = p-Quinquephenyl; p6P = p-Sexiphenyl

	p3P	p4P	p5P	p6P
Molecular Weight	230.1	306.41	382.50	458.59
Melting Point (°C)	212	>300	381	475.16

potential use in organic light-emitting diodes, organic field-effect transistors, and solar cells [280]. As previously mentioned, some argon and neon detectors use TPB. However, these detectors operate at a far lower temperature and thus it is not clear that TPB would work in liquid xenon.

In summary, we have demonstrated the use of a wavelength shifter in a LXe detector. Our first choice of p-TP as the wavelength shifter results in unacceptable levels of charge loss, but other promising wavelength shifter materials with potentially lower solubility in LXe remain an attractive option.
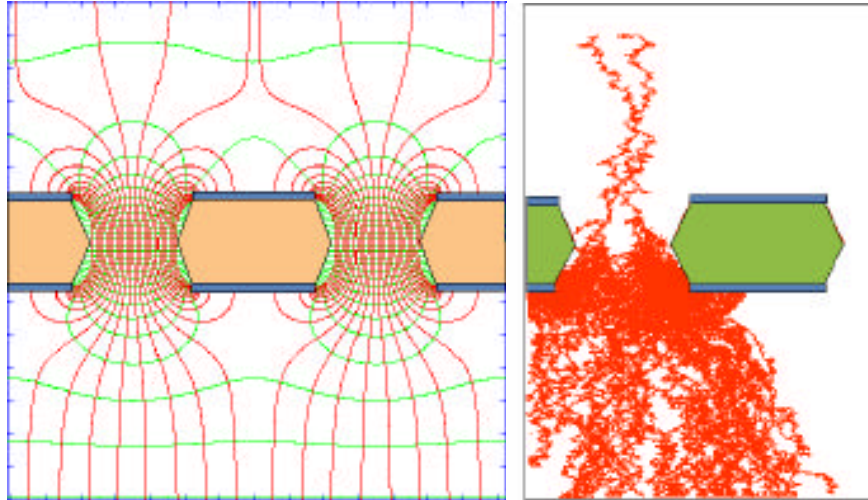
Figure 5.33: Electric field and tracks of electrons in an avalanche across a GEM [48].

5.5 Charge Multiplication

5.5.1 Introduction

Measuring proportional scintillation is an excellent way of achieving a charge measurement with low threshold and high resolution. However, this standard method requires many photomultiplier tubes which are a large source of radioactivity. The Hamamatsu PMTs used in our prototypes are also expensive ($\sim$\$2000 each), fragile, and require several months to manufacture. Charges can be directly measured with a charge sensitive amplifier attached to the anode electrode. However, directly measuring the charges of several tens of electrons is a very difficult task given the typical amount of electronics noise. The charges can be measured if the electrons are multiplied through ionization avalanches in high electric fields around thin wires or other micro structures. This method can lessen the number of PMTs or eliminate them completely. In the latter case, the primary light can be measured by having a cathode plate covered with a photocathode material (such as CsI) for converting the primary light into electrons. In a detector with photocathode, the proportional light of one set of electrons can produce a set of even more electrons. This mechanism can grow and eventually evaporate the photocathode. A solution is to include a fast high voltage

switch to turn off the extraction field for a certain amount of time after the necessary pulses have been recorded. If the necessary quantum efficiency for the photocathode cannot be achieved, the bottom PMT array can be retained to measure the primary and proportional scintillation while two perpendicular sets of wire grids in the gas would provide position sensitivity and a second measurement of the ionization. The ArDM is a two-phase liquid argon dark matter detector under development that has such a configuration [205].

This section reviews prior research performed with noble elements, gives a basic overview of the physics of charge amplification, and presents the results the of measurements performed in our two-phase xenon prototype.

5.5.2 Previous Work on Electron Multiplication

Electron multiplication was demonstrated 30 years ago in liquid xenon using thin wires with a thickness of several microns [281]. The fragility of the fine wires motivated the exploration of microstrips. One such experiment used microstrips of 8 μm wires on an insulating borosilicate substrate, which observed a gain of about 10 in LXe [282].

Electron multiplication with a triple Gas Electron Multiplier (GEM) structure has been demonstrated in two-phase detectors using argon, xenon, and xenon doped with methane (CH_4) by Bondar et al [49]. Figure 5.33 is a plot of the electric fields and electron tracks of an avalanche around a GEM hole. Methane is added as a quenching gas, which usually increases the maximum gain and stability by suppressing feedback (by blocking photons from initiating secondary avalanches). However, its use in a dark matter detector would be problematic as methane would also suppress the S1 signal. Figure 5.34 shows the gain in pure and CH_4-doped xenon versus the voltage difference across the GEM. The detector obtained a reproducible ~5000 gain stable to 6 hours with saturated argon vapors at a pressure of 0.76 (85 K) and 1 atm (87 K). However, such high gains could not be achieved with saturated xenon vapors. The detector obtained a maximum gain of ~200 with pure xenon at 0.88 atm (163 K) and 0.99 atm (165 K) and was able to operate stably for a half-hour with a gain of 80. The addition of 2% CH_4 to saturated xenon vapors did not
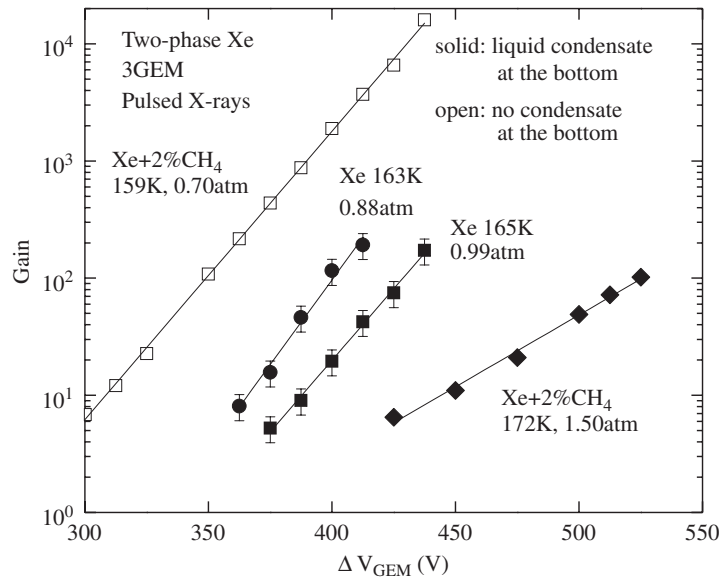
Figure 5.34: Two phase (solid) and single phase (open) gas gain versus voltage difference across each GEM of a three GEM structure [49]. The presence of saturated vapors appears to limit the gain to ∼200, with or without methane.

increase the maximum gain. However, in single-phase with a nonsaturated mixture at 0.70 atm (159 K), a maximum gain of 10^4 was obtained. Other detectors with electron multipling structures have also observed limitations in the maximum gain with pure xenon [283] and CH_4-doped mixtures [284] operating in two-phase. The former also could not operate for periods greater than a half-hour, presumably because of the condensation on the multiplication structures. A GEM detector with pure xenon was able to operate in two-phase with a gain of 25 for several hours [283]. It is not clear how this detector was able to run stably for such an extended period while the others could not.

Both the primary light and charge must be measured for background discrimination. Measuring the primary scintillation requires a photocathode such as CsI or NaI. A GEM detector with one side coated with CsI in pure xenon has been successfully demonstrated at room temperature, measuring 5.9 keV and 22 keV gammas from ^{55}Fe and ^{109}Cd [50]. Figure 5.35 shows the charge signal including the pulses induced by the scintillation (equivalent to S1) and ionization. The primary light signal is enhanced by the generation of proportional
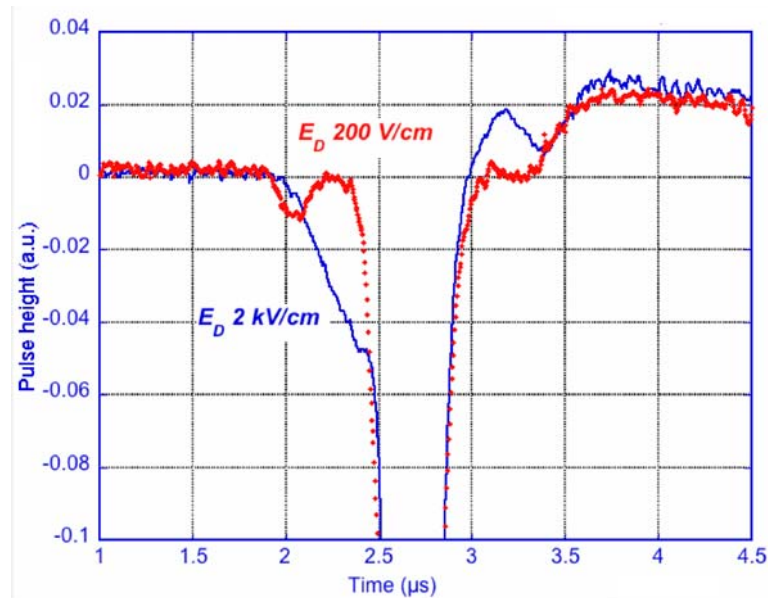
Figure 5.35: Charge signal of prompt scintillation followed by the proportional scintillation of the ionization from 22 keV gammas of ^{109}Cd at two drift electric fields [50]. At 200 V/cm, two distinct pulses can be observed. At 2 kV/cm, ramping signal is due to the formation of proportional scintillation by the primary light induced electrons.

scintillation. The simultaneous measurement of the primary light and charge by photocathode and GEM in a two-phase argon detector has been demonstrated [51]. The three GEM structure has CsI deposited on the first GEM. The detector had a primary light collection efficiency of only $\sim 10^{-3}$, presumably limited by the backscattering of photoelectrons into the CsI and poor collection of photoelectrons into the GEM holes. Figure 5.36 shows the average charge signal with scintillation and ionization pulses induced by betas from ^{90}Sr. No reference could be found for a xenon detector with photocathode and charge multiplication running in two-phase. CsI was tested in a Case prototype with a PMT in the gas and a CsI-covered aluminum cathode. The CsI coating was achieved by evaporation in a vacuum chamber. The detector was able to observe the proportional light (S3) emitted from electrons induced by the primary light and the proportion light (S4) from S2 induced electrons. Fast high voltage switching was successfully demonstrated. Our collaborators at Columbia also demonstrated such a detector [285].
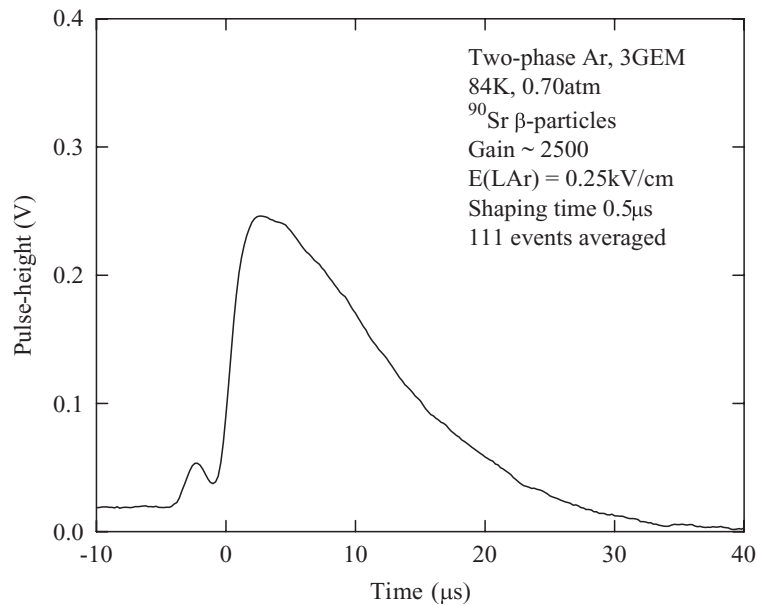
Figure 5.36: Averaged charge signal with scintillation and ionization signals induced by betas from ^{90}Sr in a two-phase Ar triple GEM detector with CsI [51].

5.5.3   Basics of Ionization Multiplication

In this section, a brief overview of the physics of electron multiplication and a derivation of an equation for the electron multiplication factor (or gain) value are given for the case of a wire grid. A more complete overview can be found in [286].

Electron multiplication occurs when an electron accelerating in an electric field acquires enough energy in between collisions to ionize a xenon atom. The change in the number of electrons of an avalanche of size N over a distance dr is

$$dN = N\alpha dr, \tag{5.3}$$

where α is the first Townsend coefficient which is the number of ionizations per unit length or the inverse of the mean free path between ionizations. The first Townsend coefficient is determined by excitation and ionization cross sections and on various transfer mechanisms. Due to its complexity, α must be measured for each gas mixture. Figure 5.38 shows α for several gases. Since the mean free path of the electrons scale with density, α should scale
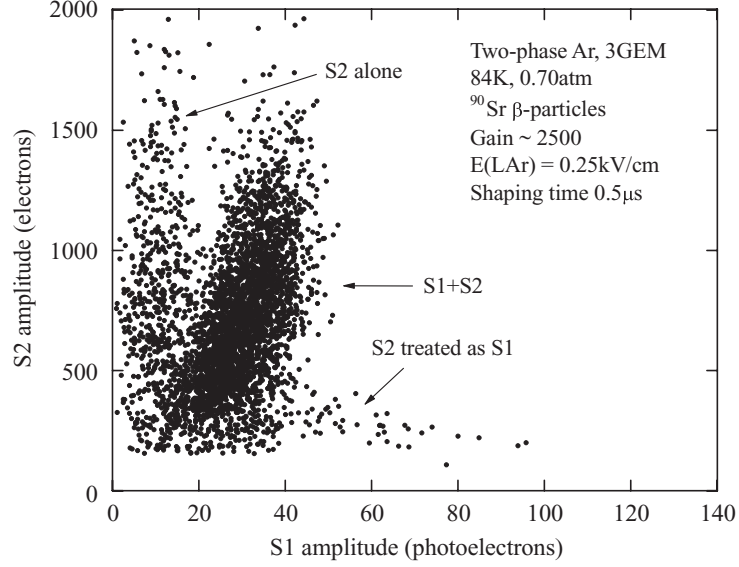
Figure 5.37: Scatter plot of $S1$ and $S2$ of events induced by betas from ^{90}Sr in a two-phase Ar triple GEM detector with CsI [51].

accordingly:

$$\alpha \left(\frac{E}{\rho}, \rho \right) = \alpha \left(\frac{E}{\rho_0}, \rho_0 \right) \times \frac{\rho}{\rho_0}, \tag{5.4}$$

where ρ_0 is the density at room temperature. If we assume that the avalanche starts near the surface of the wire, we can use the equation for the field around a single wire of infinite extent which is

$$E(r) = \frac{\lambda}{2\pi\epsilon_0 \, r}, \tag{5.5}$$

where λ is the charge density and r is the radius of the wire. An electron experiences increasing electric fields as it falls onto the wire and at a particular field, E_{min}, an electron will have a high probability of acquiring enough energy in between collisions to ionize a xenon atom. Integrating Equation 5.3 from where the avalanche starts ($r = r_{min}$) to the surface of the wire ($r = a$) gives

$$
\begin{aligned}
M &= \exp \left(\int_{r_{min}}^{a} \alpha(r) \, dr \right) & (5.6) \\
&= \exp \left(\int_{E_{min}}^{E(a)} \frac{\alpha(E)}{dE/dr} \, dE \right), & (5.7)
\end{aligned}
$$
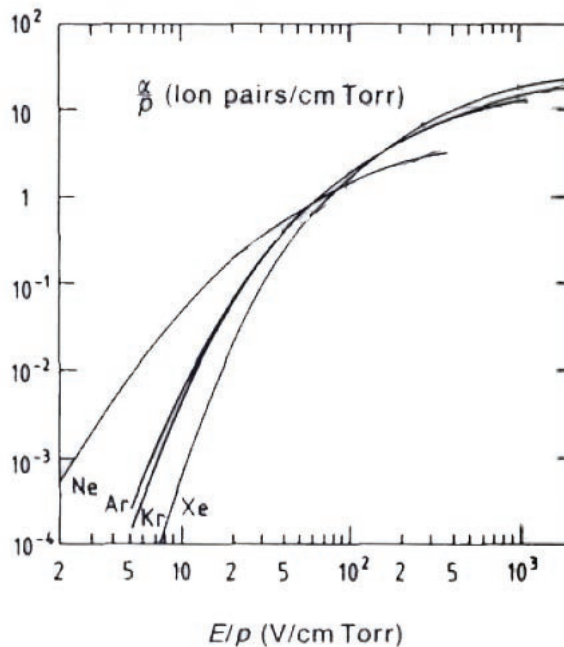
Figure 5.38: First Townsend coefficient divided by pressure, α/p, versus E/p for neon, argon, krypton and xenon gases [52].

where E_{min} is the field at r_{min}. Substituting in Equation 5.5 for E gives

$$M = \exp\left(\int_{E_{min}}^{E(a)} \frac{\lambda\,\alpha(E)}{2\pi\epsilon_0\,E^2}\,dE\right). \tag{5.8}$$

To proceed further with this integral, a functional form of the α is needed. In the region of E/P between 10^2 to 10^3 V cm^{-1} torr^{-1}, α is roughly linear with E (as seen in Figure 5.38), and thus we can substitute $\alpha = \beta E$ into Equation 5.8:

$$M \;=\; \exp\left(\int_{E_{min}}^{E(a)} \frac{\lambda\beta E}{2\pi\epsilon_0 E^2}\,dE\right) \tag{5.9}$$

$$\;=\; \exp\left[\frac{\beta\lambda}{2\pi\epsilon_0}\ln\left(\frac{\lambda}{2\pi\epsilon_0 a E_{min}}\right)\right]. \tag{5.10}$$

We can derive a relation between β and the average potential difference required to produce an electron. The potential difference between the surface of the wire $(r = a)$ and the point
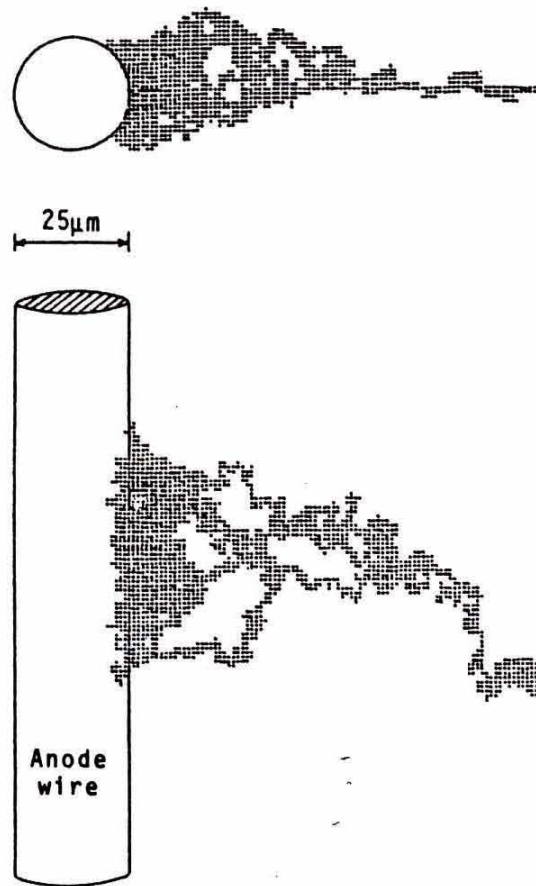
Figure 5.39: Two views of a computer simulated electron avalanche around a μm diameter wire [53].

where electron multiplication begins is

$$V(a) - V(r_{min}) = \int_a^{r_{min}} E(r)\, dr \tag{5.11}$$

$$= \frac{\lambda}{2\pi\epsilon_0} \ln\left(\frac{r_{min}}{a}\right) \tag{5.12}$$

$$= \frac{\lambda}{2\pi\epsilon_0} \ln\left(\frac{\lambda}{2\pi\epsilon_0 a E_{min}}\right). \tag{5.13}$$

Let ΔV be the average potential required to produce an electron. The number of multiplications in the avalanche is

$$Z = \frac{V(a) - V(r_{min})}{\Delta V}, \tag{5.14}$$

and the number of electrons is

$$M = 2^Z. \tag{5.15}$$

Equating Equations 5.13 and 5.15 gives the relation between β and ΔV:

$$\beta = \frac{\ln 2}{\Delta V}. \tag{5.16}$$

E_{min} scales with density as $E_{min}(\rho_0)\frac{\rho}{\rho_0}$ (since the mean free path of electrons scale with ρ^{-1}). Substituting this into Equation 5.13 and replacing $\frac{\lambda}{2\pi\epsilon_0}$ with $aE(a)$, we obtain

$$M = \exp\left[aE(a)\,\beta\,\ln\left(\frac{E(a)}{E_{min}(\rho_0)(\rho/\rho_0)}\right)\right] \tag{5.17}$$

$$= \left(\frac{E(a)}{E_{min}(\rho_0)(\rho/\rho_0)}\right)^{aE(a)\beta}. \tag{5.18}$$

$E(a)$ can be written in terms of the uniform drift electric fields above and below the wire grid of pitch b [287]

$$E_{above} - E_{below} = \Delta E = \frac{2\pi a}{b}E(a). \tag{5.19}$$

Substituting Equation 5.19 into Equation 5.18 gives

$$M = \left(\frac{\frac{b}{2\pi a}\Delta E}{E_{min}(\rho_0)(\rho/\rho_0)}\right)^{\frac{1}{2\pi}\beta b\Delta E}. \tag{5.20}$$

We can see from this equation that consistency in the dimensions of the detector is important. In the case of an infinite wire grid with 40 μm wires at 2 mm pitch and with a symmetrical electric field of 8 kV/cm above and below the grid, a 5% spread in the wire diameter will give a gain resolution of $\sigma/\mu \approx 100\%$. A 5% variation in the pitch also leads to a similar variation in gain. Similarly, small imperfections in the placement of the wire grid with respect to surrounding electrodes will distort the field leading to large spatial variations in the gain. Maintaining a constant gas density is also crucial hence the importance of a good cryostat. Calculating the partial derivative of M in Equation (5.20) with respect to ρ gives

$$\frac{dG}{G} = -\frac{1}{2\pi}\beta b\Delta E\frac{d\rho}{\rho}. \tag{5.21}$$

A small fractional change in density results in an approximately equal fractional change in gain. The calculation for a GEM is more difficult to perform given the more complicated

electric field. The gain can be calculated numerically by first obtaining a map of the electric field with a program like Maxwell$^{\circledR}$, and then propagating the electrons with the map while calculating the number of electrons according to Equation (5.3).

Deviation from Proportionality

Several processes can introduce deviations in proportionality or cause breakdown. If the gain is too high, the accumulation of positive ions can distort the electric field. The front end of the avalanche between the wire and the ions will feel a reduced field while the electrons in the tail will experience an enhanced field, moving the starting avalanche point farther away from the wire. This effect can lead to two different modes of behavior. If the photons can travel greater distances, multiple avalanches can develop simultaneously from a single event. The signal size is independent of the number of initial electrons. On the other hand, in the "limited streamer" mode, the UV photons ionize near their creation point. These photons also ionize the tail end of the avalanche, creating more positive ions which move the initial avalanche point farther and farther away. Once the streamer reaches a certain length the number electrons collected in an avalanche become almost independent of the initial number of charges. This occurs because the electric field becomes weaker as the avalanches are created farther away from the wire. Breakdown, or electric discharges, is also a limiting factor in electron multiplying detectors and there are different models of how this may proceed. The Townsend mechanism describes breakdown in terms of secondary electrons emitted when avalanche photons or back drifting ions strike the cathode [288]. These electrons lead to another avalanche. The first avalanche contains MN_0 electrons, where N_0 is the number of initial electrons generated by the event. The number of electrons in the second avalanche is

$$N_2 = \gamma M^2 N_0, \tag{5.22}$$

where γ is feedback coefficient or number of feedback electrons created per avalanche electron and is usually called the second Townsend coefficient. The ith avalanche contains

$$N_i = (\gamma G)^{i-1} G N_0 ` \tag{5.23}$$

electrons. If $(\gamma G) < 1$, the total number of electrons collected is

$$
\begin{aligned}
N_{tot} &= \sum_{i=0}^{\infty} (\gamma G)^{i-1} G N_0 & (5.24) \\
&= \frac{G N_0}{1 - \gamma G}, & (5.25)
\end{aligned}
$$

and if $(\gamma G) \geq 1$, then the sum diverges – this is the Townsend criterion for gas breakdown. However, the Townsend model cannot explain breakdown that occurs faster than the time it takes for the electron to drift from the cathode to the anode nor situations where the cathode is far removed from the anode. Another model involves "streamers" that form due the presence of ion space charges [288]. An avalanche produces a bulk of slow moving ions which distort the field. The field between the head of the avalanche and the anode is enhanced relative to the normal field. The field between the head of the avalanche and the ion space changes is decreased while the field behind these ions is enhanced. Photons from the main avalanche, if they are absorbed shortly after they are emitted, will generate new auxiliary avalanches in the regions of enhanced fields. This yields fast "streamers" in the front and end of the avalanche that result in breakdown.

5.5.4 Measurements with Case Detector

This experiments had several objectives. First, we wanted to establish that stable electron multiplication could be achieved with a two-phase LXe time projection chamber with fine wire electrode meshes. Secondly, we wanted to measure how the gain varied with the electric field. Finally, we wanted to combine these results with the two-phase measurements of electron and nuclear recoils with a two-PMT setup (described in the next section) to see if a charge readout system could be accomplished without decreasing discrimination. This section describes the fulfillment of these objectives.

5.5.5 Detector Description

The Xed1c (as seen in Figure 5.40) was similar the wavelength shifter detector (described in the last section) except that the top grid was an aluminum plate and the reflectors were
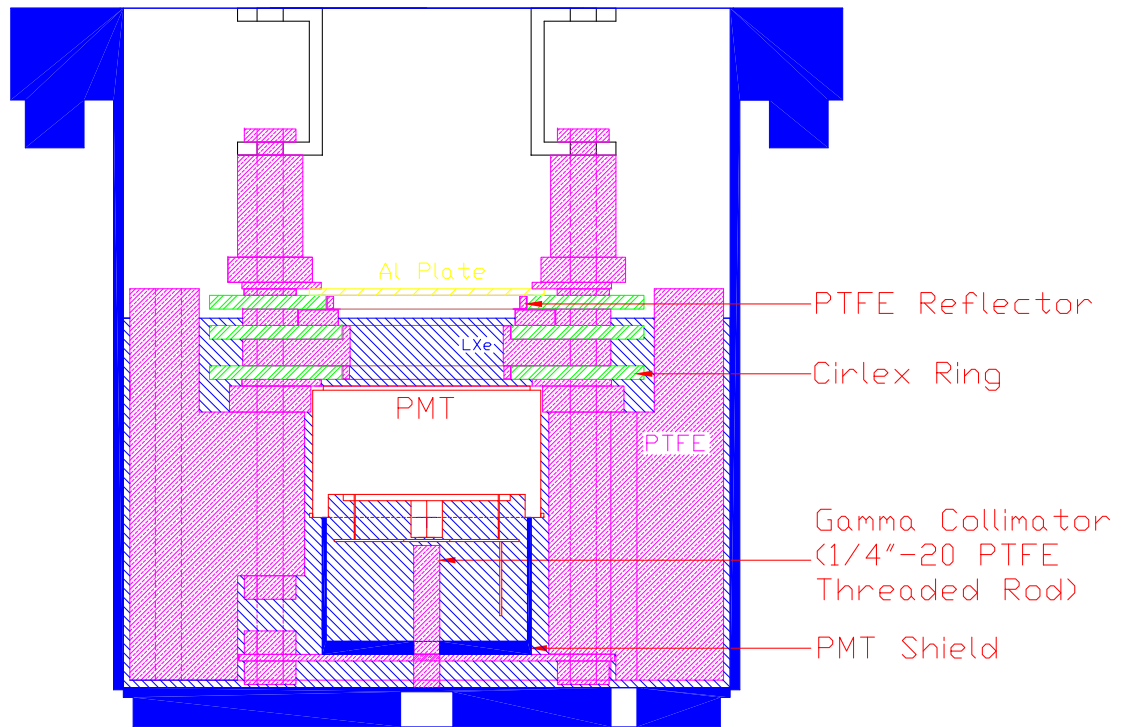
Figure 5.40: The Xed1c detector used to measure electron multiplication. This detector had a R9288 Hamamatsu PMT, four 40 μm wire grids and an aluminum plate.
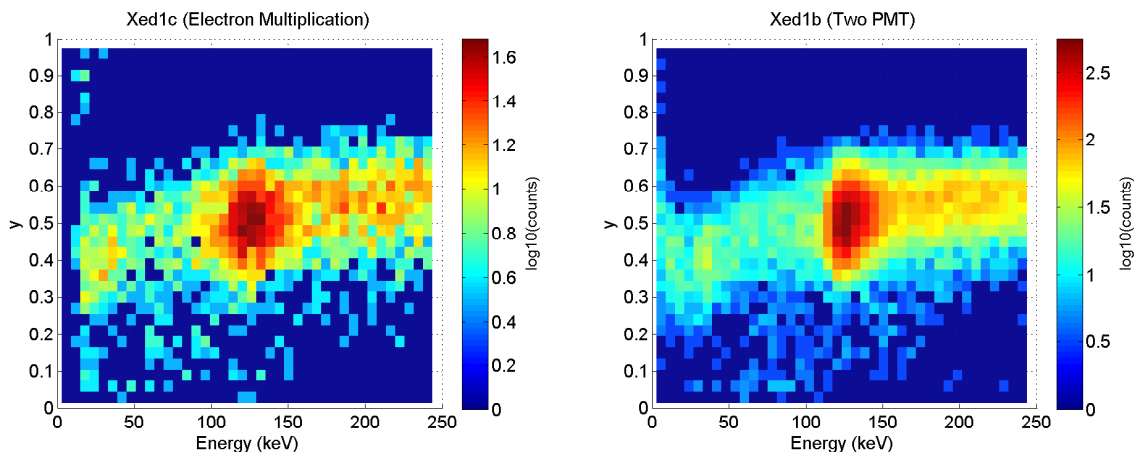
Figure 5.41: Plot of $y = N_e/(N_\gamma + N_e)$ versus energy for the data set having a gain of 58 (left) and data set taken with the Xed1b detector with two PMTs (right). The energy is $w_{max} \cdot (N_\gamma + N_e)$, as described in the text.

made of PTFE. It had a Hamamatsu R9288 PMT in the liquid. In addition to the aluminum plate, it had four wire grids all of which contained 40 μm beryllium-copper wires at a pitch of 2 mm soldered onto Cirlex rings. The anode grid is directly above the liquid surface. The active region had a height of 0.95 cm and a diameter of 3.73 cm. The ^{57}Co source was placed in the source tube underneath the detector.

The DAQ setup for charge and light measurements is described in Section 4.5. The Ortec 572 shaping amplifier was set to an amplification of 10× and shaping time of 6 μs.

5.5.6 Data

Gas gain data with ^{57}Co was taken at five different liquid-to-gas extraction fields (between liquid surface and anode) – 5.9, 6.2, 6.4, 6.7, and 6.9 kV/cm – with the drift field (active region) at 0.5 kV/cm for all datasets. A summary of the data set settings is given in Table 5.2. The voltages were set such that the fields about the anode grid were symmetrical, making the equipotentials near the wire surface circular. This symmetry decreased the position dependence of the avalanche gain. The systematic uncertainty in the extraction fields and drift fields are 11% and 8.5%, respectively, due primarily to uncertainties in the distances between the wire grids. The electrons were pulled through the gate grid with 100%

Table 5.2: Data sets. E_{below} is the field between the liquid surface and anode. E_{above} is the field between the anode and top electrodes. All electric field values are in units of kV/cm.

Name	E_{below}	E_{above}	$E(a)$	Effective Gain
c_xed1c_0607061359	-5.9 ± 0.5	6.0 ± 0.7	190.2 ± 10.5	$7.2 \pm 2.1_{sys} \pm 0.1_{stat}$
c_xed1c_0607061518	-6.2 ± 0.5	6.2 ± 0.7	197.0 ± 10.9	$11.1 \pm 2.9_{sys} \pm 0.1_{stat}$
c_xed1c_0607061752	-6.4 ± 0.6	6.5 ± 0.7	206.1 ± 11.4	$19.7 \pm 4.5_{sys} \pm 0.1_{stat}$
c_xed1c_0607061845	-6.7 ± 0.6	6.8 ± 0.8	214.0 ± 11.8	$33.7 \pm 6.9_{sys} \pm 0.4_{stat}$
c_xed1c_0607061937	-6.9 ± 0.6	7.0 ± 0.8	222.0 ± 12.3	$57.8 \pm 10.6_{sys} \pm 0.5_{stat}$
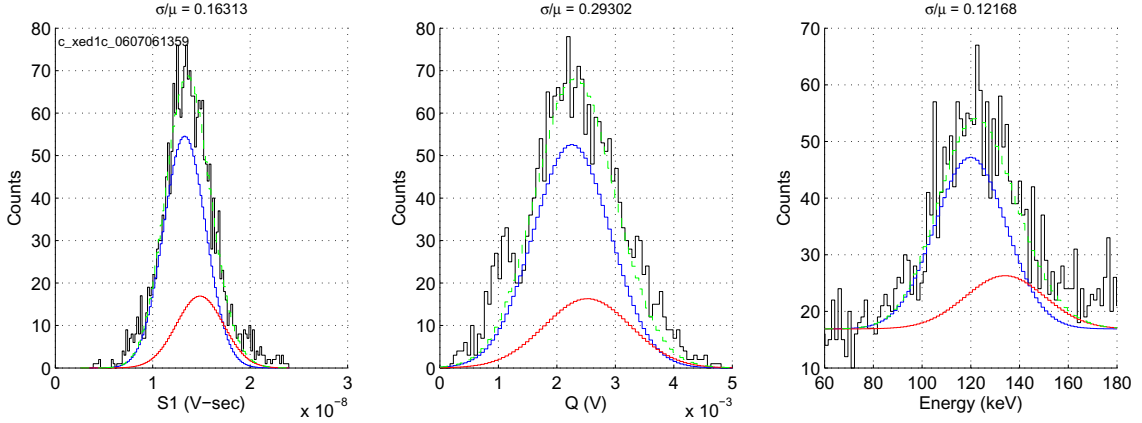
Figure 5.42: Histogram and fits of $S1$, the charge (Q), and energy ($w_{max} \cdot (N_\gamma + N_e)$) of dataset c_xed1c_0607061937.

transmission. Under these fields, the efficiency for extracting electrons into the gas ranged from 0.51 to 0.72 [38] and have a systematic uncertainty of $\sim 23\%$ due to the uncertainty in the extraction field. Typically, the extraction field is set at 10 kV/cm for 100% extraction but such a high field would lead to breakdown. The charge and light of the 122 keV gammas have been well calibrated [275, 267]. With this calibration measurement and knowledge of the extraction efficiency, the number of electrons entering the avalanche is known. The test input of the preamp was pulsed with a waveform generator to measure the electronics noise. Figure 5.41 is a scatter plot of the discriminate $N_e/(N_\gamma + N_e)$ versus energy of the highest gain dataset, where N_e is the number of electrons that escape recombination and N_γ is the number of primary scintillation photons. Also shown is the ^{57}Co data taken with the two-PMT electroluminescence Xed1b detector (see Section 5.2.1).

'

The peaks were fit with a double Gaussian function containing three free parameters:

$$y(a, x_0, \sigma, x) = a \cdot e^{-\frac{1}{2}(\frac{x-x_0}{\sigma})^2} + 0.3 \cdot a \cdot e^{-\frac{1}{2}(\frac{x-x_0 \cdot (136.47/122.06)}{\sigma \cdot (136.47/122.06)})^2}. \tag{5.26}$$

Two Gaussians are needed as 122 keV and 136 keV gamma distributions overlap. The ratio of 136.5 keV to 122.0 keV gamma event rates in the center of the active volume was measured to be 0.30±0.05 in a separate measurement with a two PMT detector (Xed1b as described in Section 5.2.1) and agrees with the predicted value. Use of this function assumes that both the fit means and sigmas scale with energy; the latter assumption is appropriate because the instrumental fluctuations, which scale with energy, dominate. The background rate was roughly 1/3 that of the ^{57}Co event rate. The effect of background is minimized by implementing an energy and drift time cut. Here, energy is defined as $E = w_{max} \cdot (N_\gamma + N_e$ where w_{max} is the average energy to produced either an exciton or ion. As this quantity is not affected by recombination fluctuations, cutting in it removes background events that leak into the peak by fluctuations in recombination. The drift time includes only events at the bottom 2.5 mm of the active volume where the ^{57}Co events dominate due to proximity to the source.

5.5.7 Results I. Basic Results

The peak voltages of the pulses from the shaping amplifier are proportional to the electron multiplication factor. The effective gas gain is defined as the fit mean voltage of the peak, divided by the voltage of the expected signal without gas gain: $V = \epsilon e N_e / C_f$, where $N_e = 4.45 \times 10^3$ is the number of electrons extracted from the event site, ϵ is the electron extraction efficiency, e is the elementary charge, and C_f is the feedback capacitance. The voltage ratio is not equal to the actual gain due to short the integration time and the signal induction onto other electrodes [289]. Figure 5.43 is a plot of the effective gain as a function of the electric field on the wire surface. We were able to run the detector for more than a day at a maximum effective gain of ~58. At very high unstable gains, multiple pulses could be seen separated in time by the electron drift time. This suggests that photon feedback on the cathode wires as the limitation on gain.
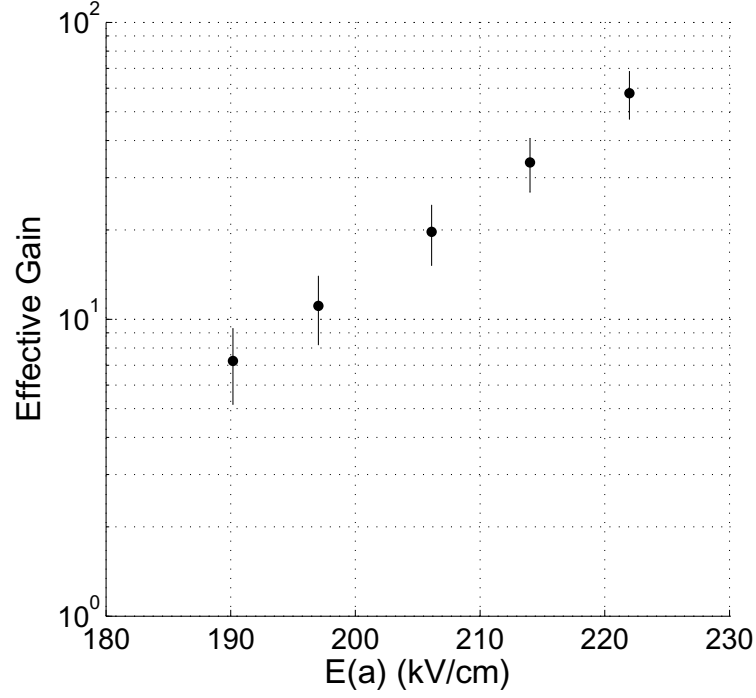
Figure 5.43: Gain versus the electric field on the surface of the wire. The highest measured stable gain was $57.8 \pm 10.6_{sys} \pm 0.5_{sys}$. The error bars represent the systematic errors.

5.5.8 Results II. Discrimination Projection

For a charge readout system to be viable for dark matter searches, the charge resolution of the readout must be comparable to that achieved by the typical PMT setup in order to have similar electron recoil discrimination power. In this section, we first decompose the various components of the charge signal variance of Xed1c and another detector by Sakurai and Ramsey [290]. Then, we make electron recoil discrimination projections to lower energy for hypothetical detectors with a PMT in the liquid of the same performance as in Xed1b and a charge readout system with lower electronics noise, higher gain and the instrumental fluctuations of the Xed1c and Sakurai detector. No projection is made for a CsI detector with no PMTs.

The charge variance in units of energy can be written as

$$\sigma_E^2 = \alpha E + \beta E^2 + \sigma_{recomb}(E)^2 + \sigma_{noise}^2, \qquad (5.27)$$
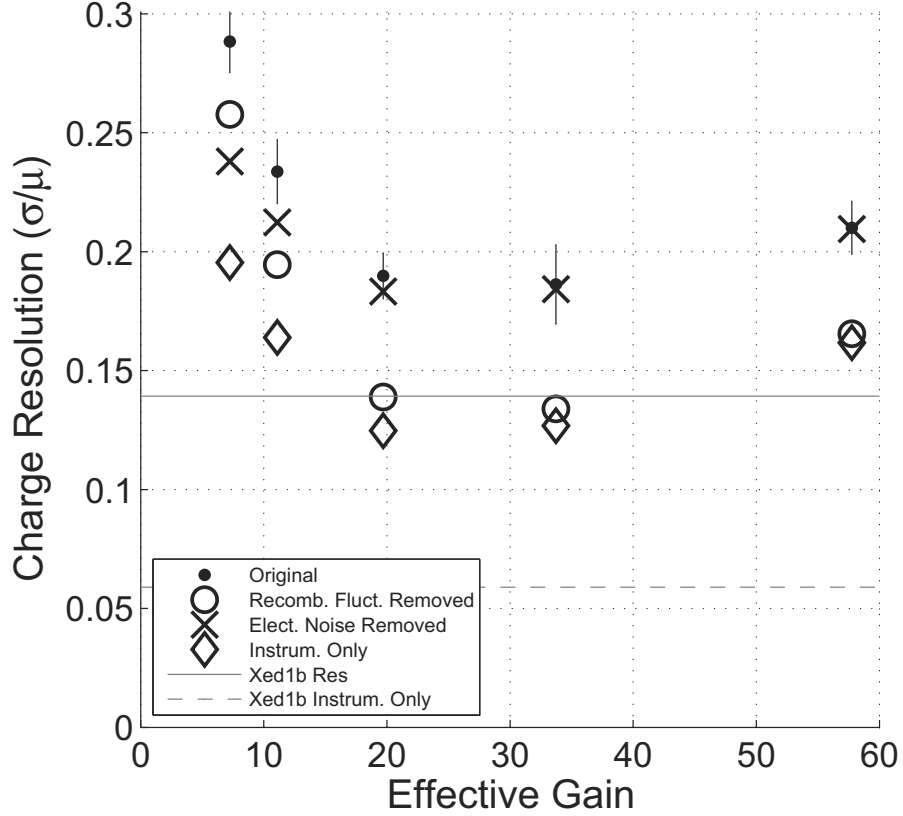
Figure 5.44: The charge resolution versus gain. Also plotted are the resolution values with various components removed. The resolution value with statistical fluctuations, recombination fluctuations and noise removed is the square-root of instrumental coefficient, β, of equation 5.27. The error bars represent the systematic errors. Also shown are the $S2$ resolution and instrumental component as seen in the two PMT Xed1b detector.

where α and β are the coefficients of the statistical and instrumental fluctuation components, respectively; σ^2_{recomb} is the energy dependent recombination fluctuation term; and σ^2_{noise} is the contribution from the electronics noise. The instrumental coefficient is obtained by subtracting the total variance by all the other components at 122 keV.

The statistical coefficient, with terms representing the fluctuations in gain, extraction and number of initial ions, is

$$\alpha = \frac{bw_i}{\epsilon(1-r)} + \frac{1-\epsilon}{\epsilon(1-r)} \cdot w_i + Fw_i, \tag{5.28}$$

where $b = \sigma^2_A/\overline{A}^2$ is the relative variance of the gain of a single electron avalanche as given by the Polya distribution for A [291, 292, 293] and has been determined in a Monte Carlo

simulation to be about 0.85 for 50 μm wires [294]; $w_i = 15.6$ eV is the average energy for generating an ion-electron pair in liquid xenon [295]; ϵ is the liquid-to-gas electron extraction efficiency; $r = 0.45$ is the fraction of recombination at 0.5 kV/cm for 122 keV gammas (as determined by a separate measurement); and $F \approx 0.05$ is the Fano factor [296, 297]. The quantity $w_i/(\epsilon(1-r))$ is effectively the average energy required to generate an electron that reaches the gas phase. The extraction efficiency, ϵ, is the only quantity that changes with dataset and is equal to 0.62 in the third (and best resolution) dataset, giving $\alpha = 0.057$ keV.

The recombination fluctuation variance is

$$\sigma_{recomb}^2 = \frac{\sigma_r^2(E)}{(1-r)^2}E^2. \tag{5.29}$$

At 0.5 kV/cm, $\sigma_r = 0.071 \pm 0.002$ for 122 keV gammas, giving $\sigma_{recomb}^2 = 94.0$ keV^2. The calculation of σ_r at an energy is described in Section 5.6 and in [275, 267].

The electronics noise term in units of energy is

$$\sigma_{noise} = \frac{w_i \sigma_{N_e}}{\overline{A}\epsilon(1-r)} \tag{5.30}$$

$$= \frac{w_i C_f \sigma_V}{e\overline{A}\epsilon(1-r)}, \tag{5.31}$$

where $\sigma_{N_e} = C_f \sigma_V/e$ is the rms of the noise in units of electrons, σ_V is the electronics noise and is the width of the test pulse distribution, e is the charge of an electron and $C_f = 1.15$ pF is the feedback capacitance of the preamplifier. Note that the electronics noise term is gain dependent whereas the statistical component is not. For the third data set of Xed1c, $\sigma_{noise} = 6.11$ keV (2640 electrons). Subtracting from σ_E^2 the terms for statistical, recombination and noise fluctuations, we obtain for Xed1c an instrumental coefficient $\beta = 0.0225$. For comparison, the instrumental coefficient of the proportional light signal of the two-PMT detector described in the next section is $\sim$0.004. Figure 5.44 is a plot the resolution versus gain, including resolution values with various components removed. We observe the instrumental coefficient changing with gain, which could be an indication that the background events are affecting the Gaussian fits. Also included for comparison are
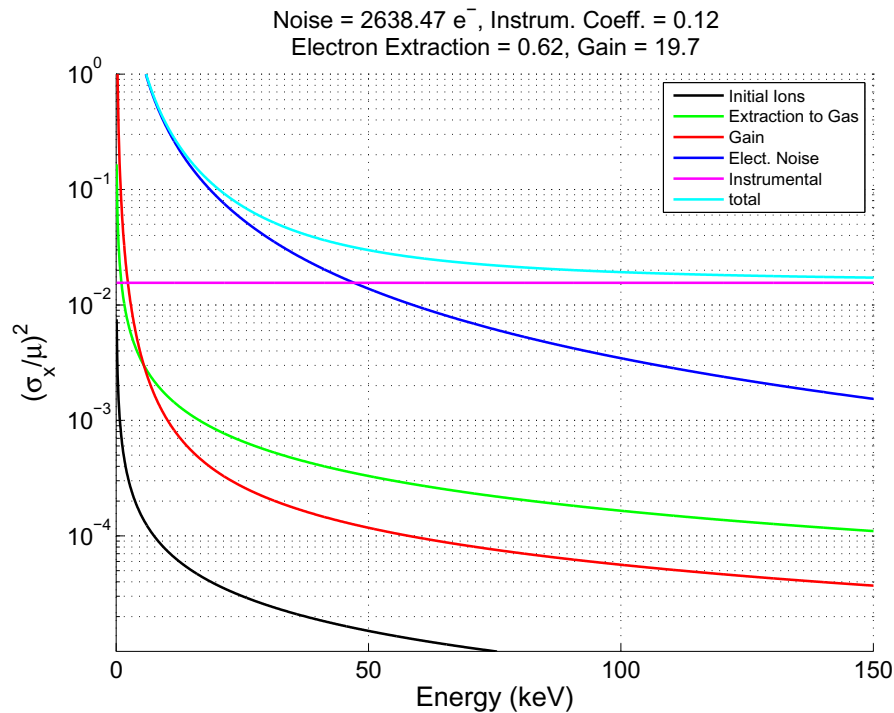
Figure 5.45: The relative variances of all components (except recombination fluctuations) that contribute to the charge resolution of the data set with gain 19.7. We see that the electronics noise and instrumental fluctuations dominate at low energies. Fortunately, these components can be reduced.

the $S2$ resolution and its instrumental component as seen in the two-PMT Xed1b detector. The great difference in instrumental components are unsurprising given the exponential dependency of the multiplication to wire diameter and pitch (Equation 5.20).

Figure 5.45 shows the relative variances of the various components (except for recombination fluctuations) as a function of energy for Xed1c at gain 20. Here, we see that contributions from gain, number of initial ions and extraction are negligible compared to instrumental and electronics noise. Fortunately, these two important components are also not intrinsic. The extraction fluctuations can be omitted by establishing a high enough electric field at the liquid surface so that extraction is 100%; this would entail thickening the anode wires to lower the gain in order to operate stably.

The same decomposition is performed on data taken with a single wire proportional counter detector by Sakurai and Ramsey. This detector was used to measure the wire
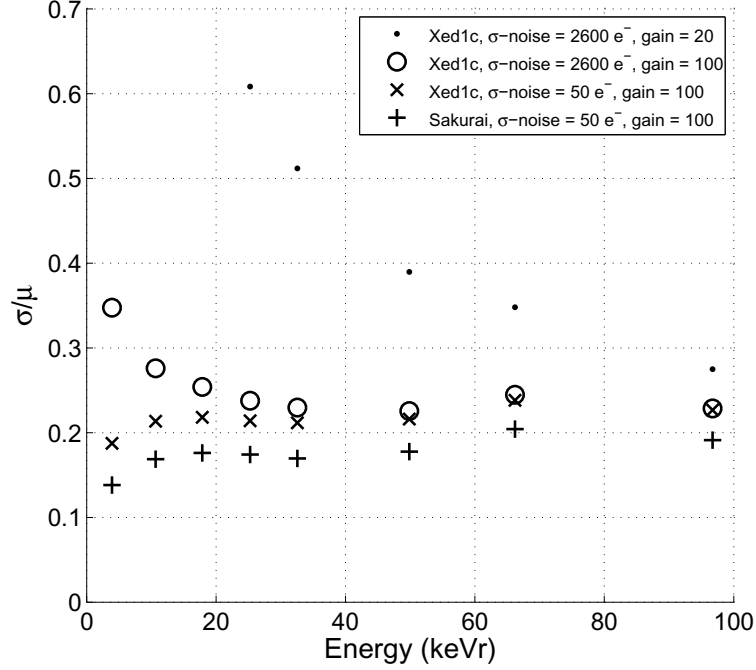
Figure 5.46: Charge resolution versus energy for detectors of various instrumental components, electronics noise and gain.

diameter dependence of the charge signal resolution using pure and CH_4-doped xenon at room temperature [290]. The gas was irradiated with 22 keV gammas from ^{109}Cd. With 50 μm wires (the diameter closest to ours), an energy resolution of 3.2% was observed, corresponding to an energy variance of 0.49 keV^2. For the Sakurai detector, the statistical fluctuation coefficient is

$$\alpha = (b + F) \cdot w_i^{gas}, \tag{5.32}$$

where $w_i^{gas} = 0.0215$ keV is the average energy to create an ion-electron pair in xenon gas [247], giving $\alpha = 0.0193$ keV, which is lower than that of Xed1c because of the absence of fluctuations in liquid-to-gas electron extraction. Recombination fluctuations are minor in the gas phase and the electronics noise is not known – for simplicity both the recombination and noise variance terms are set to zero. This gives an instrumental coefficient of $\beta = 1.35 \times 10^{-4}$. This value is significantly smaller than that of Xed1c, which reflects the great differences in instrumental complexities.

To project the discrimination for other detectors, the electron and nuclear recoil band
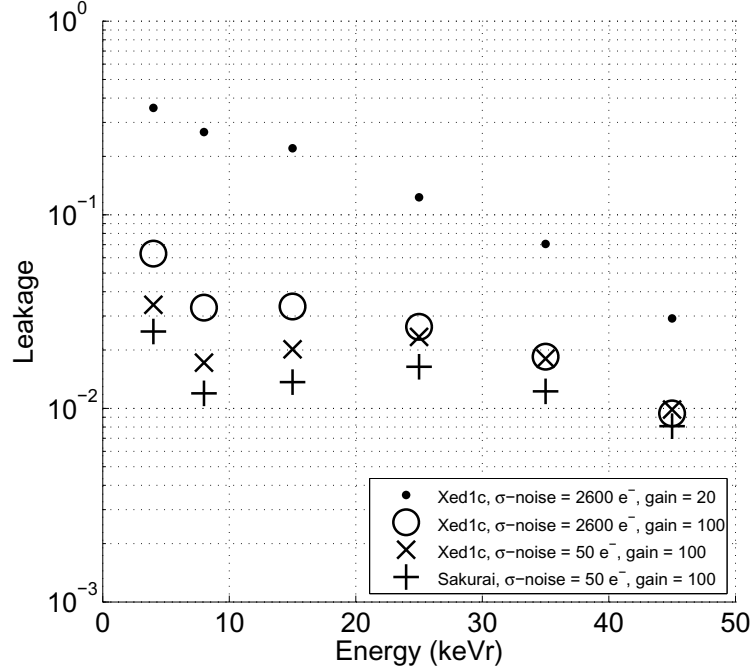
Figure 5.47: Electron recoil leakage versus energy of various instrumental components, electronics noise and gain..

data described in Section 5.2 is needed for two reasons: to obtain the energy dependent separation between the electron and nuclear recoils in $\log_{10}(S2/S1)$ and to get the intrinsic fluctuations (initial ions and recombination) in the charge and light signals. The decomposition of the signals is described in another Ph.D. thesis [60]). To create the fake data, we first simulated the intrinsic fluctuations in charge and light and then include statistical and instrumental fluctuations. We projected the performance of four detectors which have no fluctuations in extraction ($\epsilon = 1$) and drift field of 0.88 kV/cm, the field of the discrimination dataset that gives the best background rejection. We used the instrumental fluctuations of Xed1c and the Sakurai detector and varied the electronics noise and gain. Members of the Cryogenic Dark Matter Search (CDMS) collaboration have constructed charge amplifiers with a rms noise of 120 electrons by moving the primary stages of electronics into the cryostat [298]. As the electronics noise can probably be lowered to ∼50 electrons [299], we used this as a lower limit and the noise observed in Xed1c as an upper bound. We limited the maximum gain to 100 as groups have only been able to operate

stably with gain of several scores. Two sets of data were simulated for each detector. The first set contains electron recoil events of discrete energies between 2 and 100 keVr and was used for obtaining the charge resolution as a function of energy. The second set contains nuclear and electron recoil events (200,000 of each) simulated across a continuous band of energy between 2 and 50 keVr and is used for projecting discrimination. The discriminant used is $\log_{10}(Q/S1)$, where Q is the charge. The method for calculating the discrimination efficiency is the same as that used for real data as described in Section 5.2. Figure 5.46 shows the charge resolution of the charge signal versus recoil energy at 0.88 kV/cm. The legend indicates the instrumental coefficient, noise and gain of the detectors simulated. Figure 5.47 shows electron recoil leakage versus recoil energy. Reducing the noise component (Equation 5.30) has the greatest impact on the performance. The Xed1c and Sakurai instrumental fluctuations at 5 keVee are $\sigma_{instr} = \sqrt{\beta E} = 0.06$ keVee and 0.75 keVee, respectively. Lowering the noise to 50 electrons and increasing the gain to 100, lowers σ_{noise} from 6.11 keVee to 0.023 keVee and thus lowering the noise and/or increasing the gain has a much greater impact on discrimination than lower instrumental fluctuations. The detector with instrumental fluctuations of the Sakurai detector, noise of 50 electrons and gain of 100 displays a performance that is slightly inferior to that of Xed1b; the average leakage below 20 keVr is about 1.5%, whereas in Xed1b it is 0.5%. The results of this detector can be viewed as an estimate of the upper limit to the performance of this technology since full detectors are likely to have greater instrumental fluctuations and electronics noise.

In summary, we have demonstrated, for the first time, charge multiplication in a two-phase xenon detector with fine wire mesh electrodes. Also important was the stability obtained for over a day. The contributions to the charge resolution were decomposed and extrapolated to lower energies to understand which factors were important. By combining the instrumental and statistical fluctuations with intrinsic fluctuations in the light and charge signals, the discrimination performance of charge gain detectors were projected. The projections indicated that the performance of this technology can nearly reach that accomplished by the typical electroluminescence charge-readout technique if electronics noise is

greatly reduced and the gain is moderately increased.

5.6 Recombination Fluctuations in Electron Recombination

5.6.1 Introduction

Fluctuations in ionization and scintillation signals of liquid xenon detectors have been observed to be much larger than that predicted by Poisson statistics. The Fano factor is defined as $F = \sigma_e / N_e$ [300] and describes the deviation of fluctuations from Poisson statistics. Poisson statistics corresponds to $F = 1$ and for many materials, $F < 1$ is observed (germanium, for example, has $F = 0.129$ [301]) as expected since the ionization processes are not independent. In the Case xenon detectors, the observed fluctuations in the charge signal correspond to $F > 10$ whereas the theoretical value is about 0.05 [296]. This discrepancy has been observed by many groups and has been presumed to be due to fluctuations in the fraction of recombination from event to event [243, 302]. Thomas et al proposed that the basis of the recombination fluctuations is the statistical fluctuations in the ionization density along the track of the primary particle [303].

This section describes a simple model by which the recombination fluctuations manifest in the primary light and charge signal and show how measurement of the spread of these two quantities can be used to obtain the recombination fluctuation. This method is applied to a two-phase measurement of 122 keV electron recoils at many electric fields. A binomial-like behavior in recombination fluctuation is discovered. An effort to model recombination fluctuations of this experiment is described in another dissertation [60].

5.6.2 Recombination Fluctuations Model

Radiation interacts with xenon by generating excitation and ionization. A review of the basic processes is given in Section 3.4. Recall that any electron that recombines yields a photon. This mechanism leads to a 1-to-1 anticorrelation in the calibrated $S1$ and $S2$ that can be seen across electric fields (as the mean fraction of recombination is changed) and

also at a field as the fraction of recombination fluctuates as the track structures vary from event to event. The equations describing the number of electron (N_e) and photons (N_{ph}) emitted can be written as

$$N_e = N_i \cdot (1 - r) + C_1, \tag{5.33}$$

$$N_{ph} = N_{ex} + N_i\, r + C_2, \tag{5.34}$$

$$N_{tot} = N_e + N_{ph} = N_i + N_{ex}, \tag{5.35}$$

where N_i and N_{ex} are the number of initial ions and excitons, respectively; r is the fraction of initial ions that recombine; and C_1 and C_2 represent the instrumental fluctuations that average to zero. This assumes that recombination is the only process that can occur after the initial generation of excitation and ionization that gives a correlation between $S1$ and $S2$. The initial number of ions, N_i, is equal to gamma energy divided by $w_i = 15.6$ eV, the average energy to create an electron-ion pair [295]. To obtain the fluctuation in recombination fraction, σ_r, we first calculate their respective error propagation equations:

$$\sigma_{N_e}^2 = (1 - r)^2 \sigma_{N_i}^2 + N_i^2 \sigma_r^2 + \sigma_{C_1}^2 \tag{5.36}$$

$$\sigma_{N_{ph}}^2 = \sigma_{N_{ex}}^2 + r^2 \sigma_{N_i}^2 + N_i^2 \sigma_r^2 + \sigma_{C_2}^2 \tag{5.37}$$

$$\sigma_{N_{tot}}^2 = \sigma_{N_i}^2 + \sigma_{N_{ex}}^2 + \sigma_{C_1}^2 + \sigma_{C_2}^2 \tag{5.38}$$

The difference of $\sigma_{N_e} + \sigma_{N_{ph}}$ and $\sigma_{N_{tot}}^2$ removes the instrumental components and gives

$$\sigma_{N_e}^2 + \sigma_{N_{ph}}^2 - \sigma_{N_{tot}}^2 = -2((1 - r)r\sigma_{N_i}^2 - N_i^2\sigma_r^2). \tag{5.39}$$

Replacing the term $\sigma_{N_i}^2$ with FN_i, where F is the Fano factor for ionization and then solving for σ_r, we obtain

$$\sigma_r = \frac{1}{N_i}\sqrt{(1 - r)rFN_i + \frac{1}{2}(\sigma_{N_e}^2 + \sigma_{N_{ph}}^2 - \sigma_{N_{tot}}^2)}. \tag{5.40}$$

The Fano factor is $\sim$0.05 [296, 297] which makes the first term of Equation 5.40 negligible.

5.6.3   Experimental Setup

The Xed1h detector used for this measurement is essentially the same as Xed1b (Figure 5.1, Section 5.2.1), except for the replacement of the PMT in the gas (R6041, QE $= 7\%$) with one
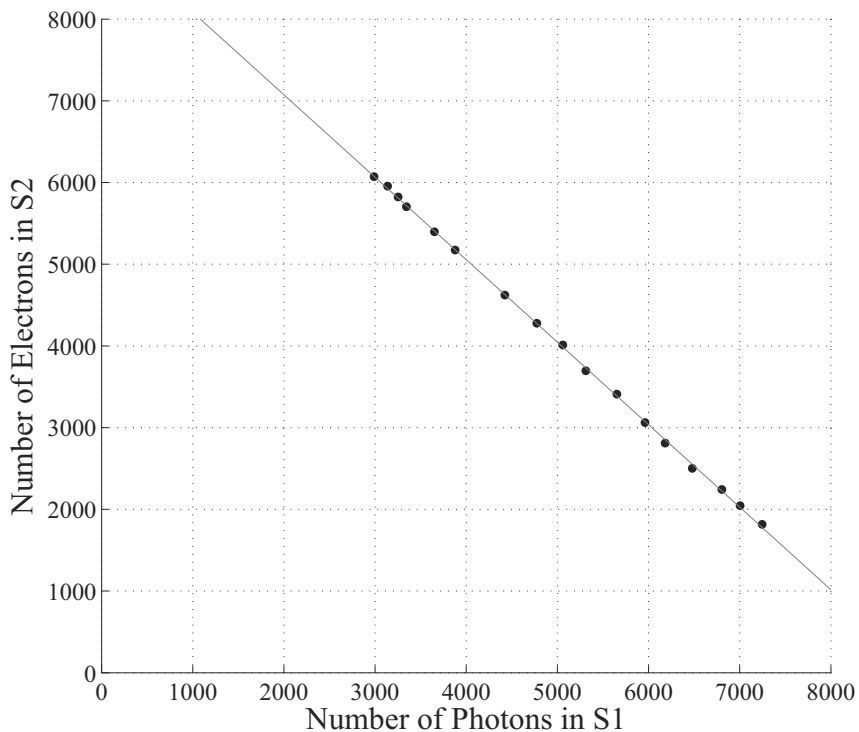
Figure 5.48: Number of photons in S1 versus number of electrons in S2 with best fit line of slope $-1.010 \pm 0.033_{\text{sys}}$ and y-intercept $9093 \pm 162_{\text{sys}}$. The statistical error is <1% for both quantities.

having a higher quantum efficiency (R9288, QE = 24%). As with previous measurements, the ^{57}Co source sat directly underneath the detector and was collimiated by the PTFE rod. Data with ^{57}Co was taken at seventeen different electric fields ranging from $\sim$0 to 4.5 kV/cm.

5.6.4 Analysis and Results

The $S1$ and $S2$ are calibrated using the single-phase ^{57}Co data. To calculate the recombination fluctuations, we need the variances of the peak in $S1$, $S2$ and N_{tot}. Because of the presence of 136.5 keV gammas, the peaks are fit to the double-Gaussian function with three fit parameters (Equation 5.26).

Figure 5.48 is a plot of $S1$ versus $S2$. The quantities are calibrated with the highest field dataset where the calculated electric field has the lowest systematic error and the
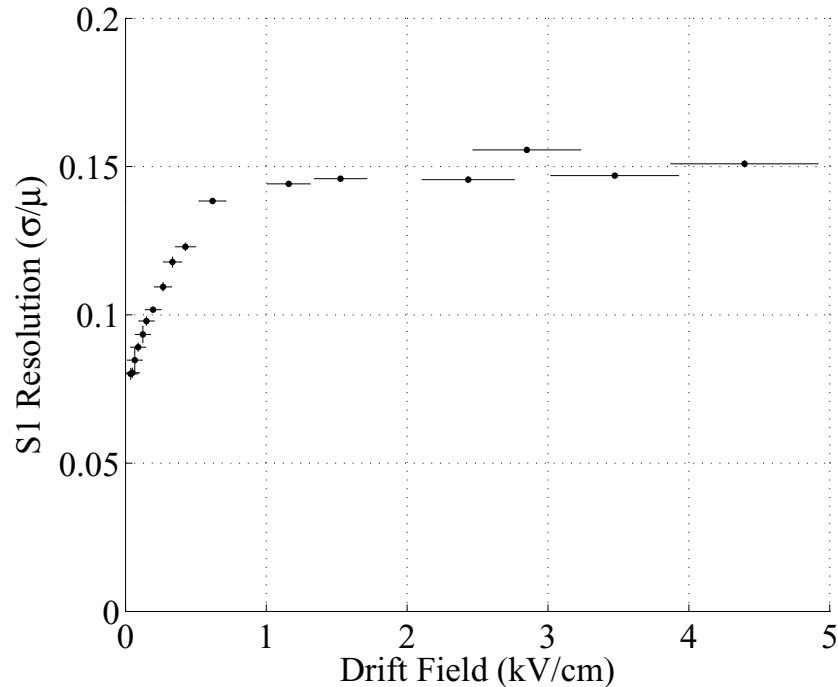
Figure 5.49: $S1$ resolution of 122 keV gammas versus drift field. The error bars represent the systematic uncertainty.

photon and electron yields change the least with field, thus providing the calibration with the lowest systematic errors. The lack of curvature in the data points shows that the calibration coefficient were constant with changing electric field and supports the idea that recombination model described in Section 5.6.2 is correct. The S1 calibration is unlikely to have drifted as this quantity is not dependent on the electric field, temperature or pressure of the system, unlike that of S2. Thus the deviations of the points from the best-fit line are more likely due to drifts in the S2 calibration. The points deviate in $S2$ from the line by at most ∼2%. The pressure fluctuated by ∼ 0.1% and thus could not have been the source of this fluctuation. It was likely due to fluctuations in the liquid level as it has been observed to fluctuate by up to 4% over the span of ∼10 hours. Figures 5.49 and 5.50 show the $S1$ and $S2$ resolutions (σ/μ), respectively, as a function of the electric field. Figure 5.51 is a plot of the various σ_N values that enter into σ_r (Equation 5.40). In Figure 5.51, we see that σ_r exhibits a binomial-like behavior with r and has a peak at $r \approx 0.4$ (as do σ_{ph} and
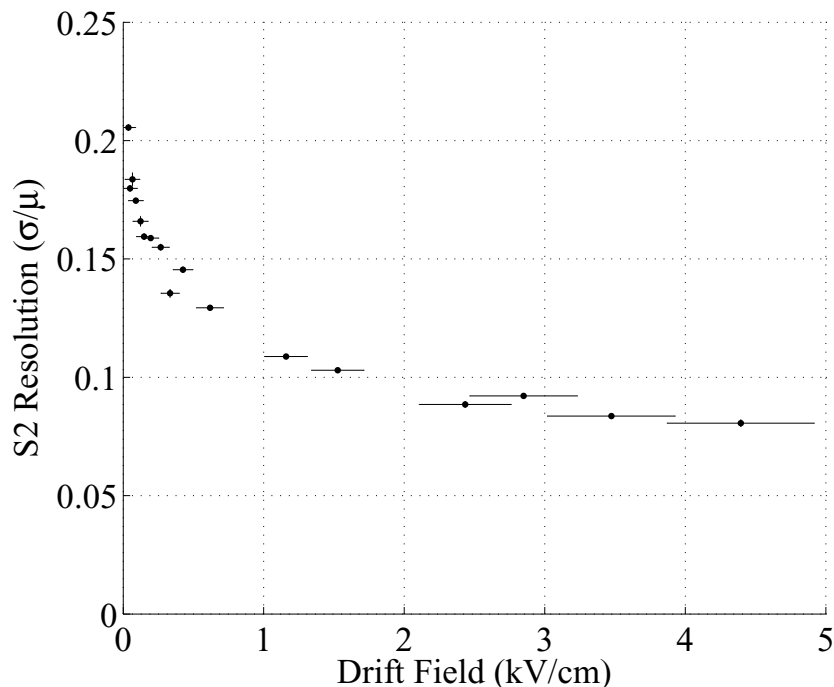
Figure 5.50: $S2$ resolution of 122 keV gammas versus drift field. The error bars represent the systematic uncertainty.

σ_e), which is off by ~0.1 from where the peak would be for a binomial distribution. The observed variances are ~100–$150\times$ that given by binomial statistics. The systematic errors in r and σ_r are due to several uncertainties: the drift field due to errors in the dimensions between wire grids, the ratio of 122 keV to 136 keV gammas, and the S2 production. The uncertainty in the highest drift field value leads to an uncertainty in the calibration in light and charge. The ratio of 136.5 keV to 122 keV gammas has been measured to be 0.3 ± 0.05 in another experiment. The long time scale $\sim4\%$ fluctuations in the liquid level also contribute to the uncertainty in the calibration of S2. The errors bars in σ_r and r displayed in Figure 5.52 represent the total error. The systematic error in r is $\sim4\times$ larger than the statistical portion.

In this section, we described the extraction of the spread in fraction of recombination of electron recoils at an energy. Another dissertation [60] describes an attempt to model recombinations fluctuations by implementing the Thomas-Imel box model [304] on simu-
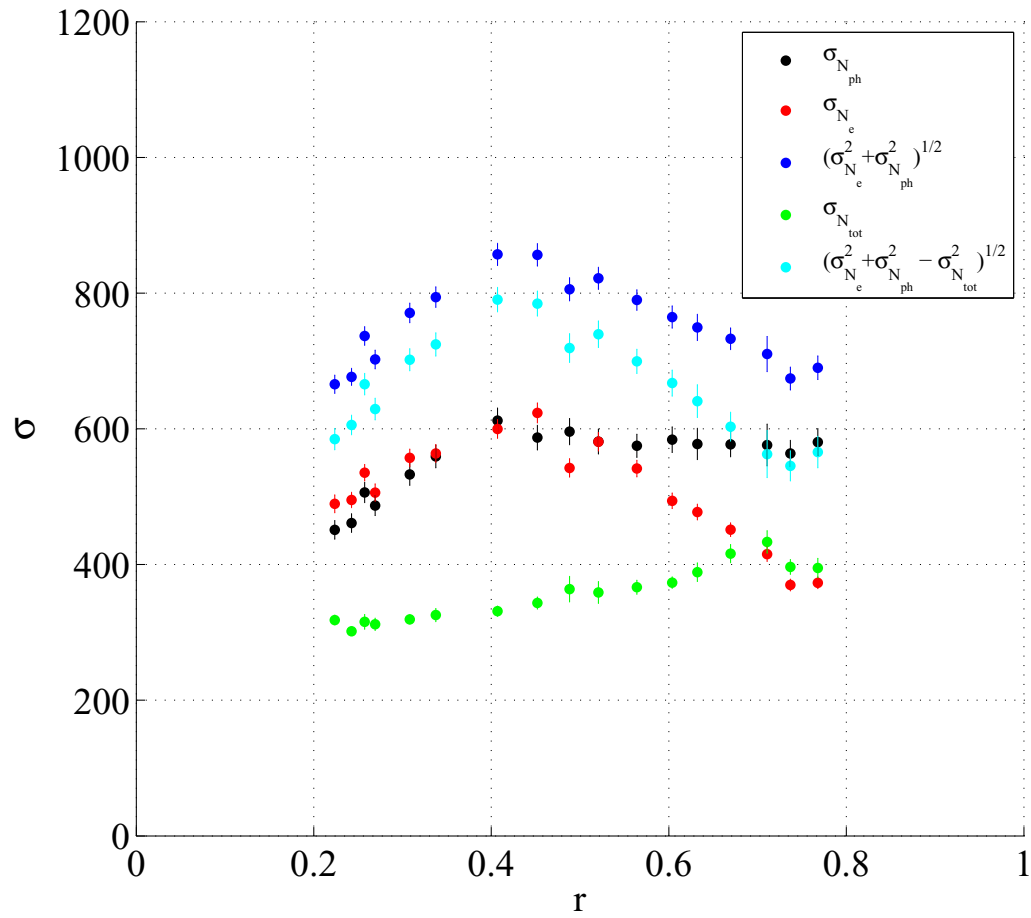
Figure 5.51: Gaussian fit σ values versus recombination fraction. The error bars represent the systematic errors. The statistical errors are $\sim 1/5$ the systematic ones.
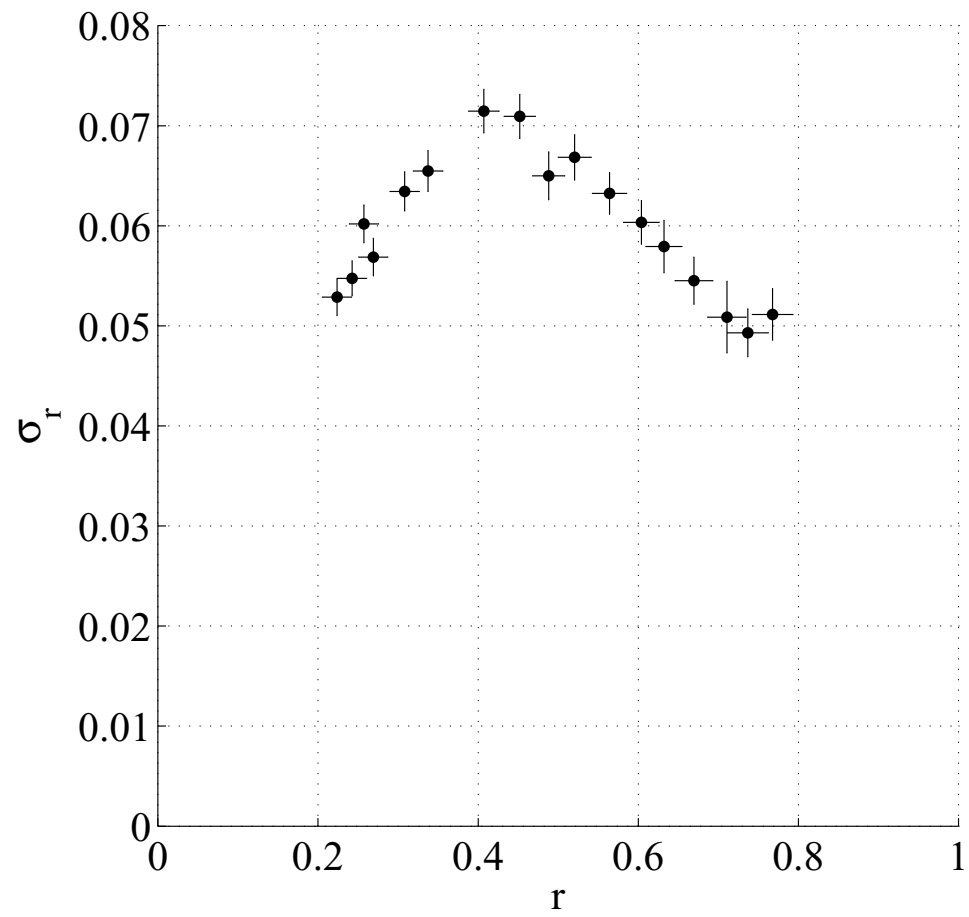
Figure 5.52: Recombination fluctuation versus recombination fraction

lated electron and nuclear recoil ionization tracks. A probe of σ_r at lower energies would be useful to dark matter searches. By obtaining the energy and field dependence of σ_r, the discrimination performance of future detectors can be extrapolated by including their projected statistical and instrumental fluctuations. This analysis would also allow us to determine the electric field that achieves the optimal discrimination efficiency. Note, however, that the procedure described in this section only applies to a peak of known energy. Rather than performing this procedure, the energy dependence of σ_r at a field can be deduced from the $\log_{10}(S2/S1)$ by subtracting out known contributions of statistical and instrumental fluctuations and then assuming that the remaining spread is due purely to recombination fluctuations. This procedure obtains σ_r in a less direct fashion than the method described here but it is the only realistic way of accomplishing the task. Implementation of this procedure along with projections of discrimination performance of detectors of various light collection efficiencies is also shown in [60].

Chapter 6

XENON10

6.1 Introduction

The XENON10 collaboration, which formed in 2002, included professors, students, and technicians from Columbia University, RWTH Aachen University, Brown University, University of Coimbra, Case Western University, Princeton University, Livermore National Laboratory, Rice University, Yale University, University of L'Aquila, and Gran Sasso National Laboratory. Before building a full-scale dark matter detector, the XENON10 collaboration assembled several prototypes. The largest test detector was XENON3 [305], which was a 3 kg module with full 3D position reconstruction capability. After demonstrating proof of concept and measuring the limits of this technology, the collaboration began work in December 2005 on XENON10, a 10 kg module for taking dark matter data. The detector was largely built at Nevis Laboratories of Columbia University. Once basic tests were conducted, the detector was disassembled and reassembled at Gran Sasso National Laboratory in Italy, where it ran from April 2006 to August 2007. WIMP search data was taken and cross section upper limits were reported [13, 70].

6.2 Detector and Supporting Systems

The XENON10 experiment contained components that were similar to that of the Case setup but of larger scale and greater complexity. Other components like the Pb/poly shield was not needed for the prototypes but was required for XENON10 because of the need for passive background removal. The data acquisition was considerably more complicated as many more PMT signals needed to be recorded. The gas system of XENON10 did not differ considerable from the Case system because the storage and flow requirements were similar.

This section describes the XENON10 detector, cryostat, data acquisition system, gas system and radiation shield.

6.2.1 XENON10 Detector

The XENON10 detector was a two-phase time projection chamber with an active LXe mass (volume) of 13.5 kg (5 liters), four electrode meshes and two PMT arrays containing 89 Hamamatsu R8520 PMTs. The total xenon mass was $\sim$22 kg. Figure 6.1 is a 2D CAD diagrams of the detector. Figure 6.2 shows several members of the XENON10 collaboration assembling the detector in a cleanroom.

The PMTs have a $1''$ by $1''$ window covered with bialkali Rb-Cs-Sn photocathode and have a QE of $23.7\pm1.9\%$ at 178 nm. The effective quantum efficiency of the PMT is the QE multiplied by the electron collection efficiency of the first dynode, which is $75\pm5\%$. Figure 6.3(a) shows the bottom PMT array which contained 41 PMTs and sat 1 cm below the cathode mesh. Figure 6.3(b) shows the top PMT array which contained 48 PMTs. The gap distance between the PMT windows and top mesh was 1.3 cm. This array contained one dead PMT (#48) which was not a significant lost as this PMT sat on the periphery. The high voltages were provided with a CAEN A1733. Multi-pin Kyocera feedthroughs were used to bring high voltage into the detector. Standard single-straned kapton coated wires (from MDC) were used to bring the high voltages from the feedthroughs to the PMTs.

The reflective PTFE tube (seen in Figure 6.3(b)) had an inner diameter of 20 cm. This piece defined the diameter of the active volume. Another PTFE ring wrapped around this
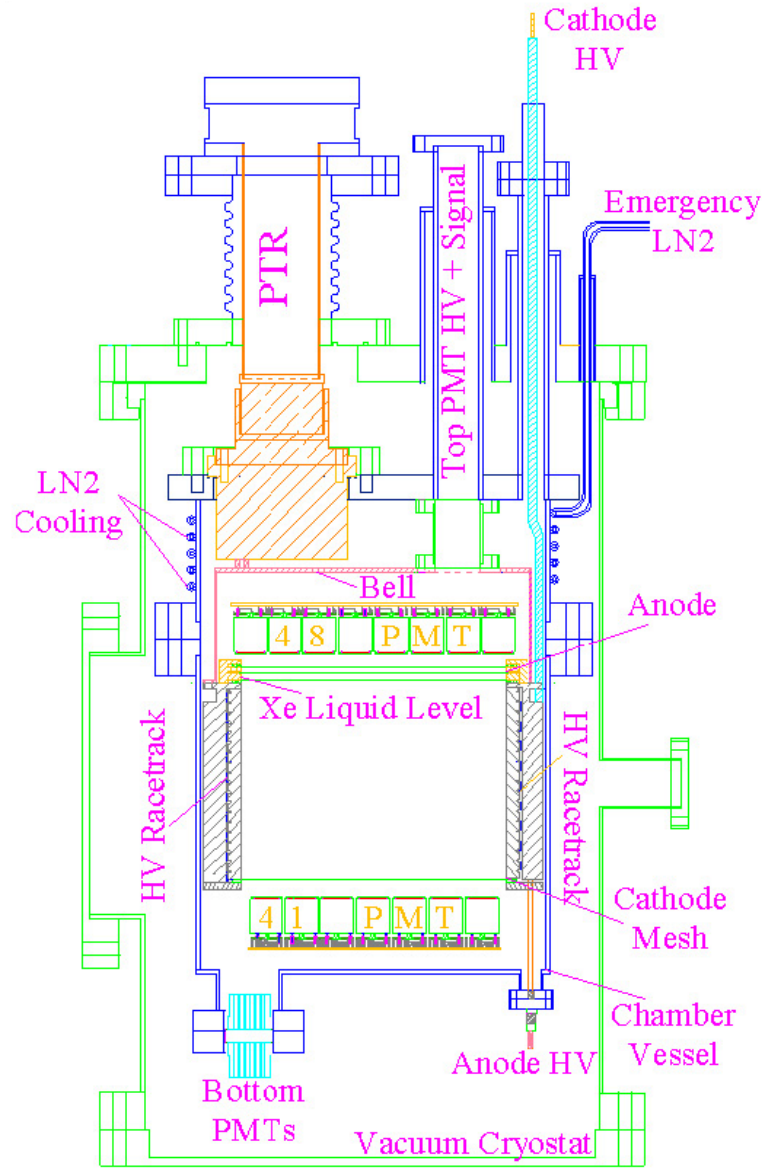
Figure 6.1: Schematic of XENON10 detector and cryostat.

Figure 6.2: Assembly of XENON10 detector in cleanroom by several members of the XENON collaboration. From right to left: K. Giboni (Columbia), R. Gomez (Rice), and M. Yamashita (Columbia).
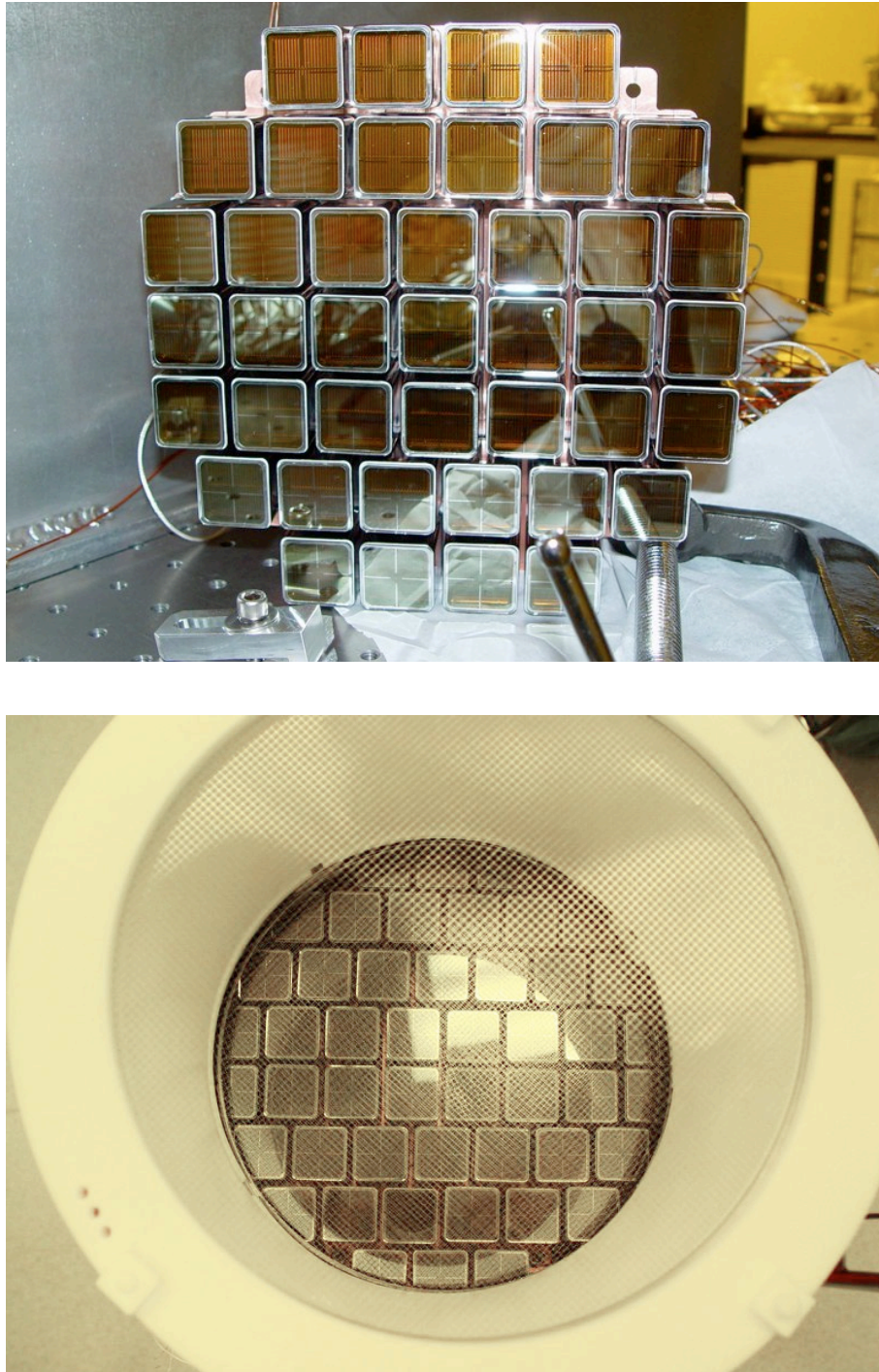
Figure 6.3: View of the bottom (top figure) and top (bottom figure) PMT arrays. The bottom and top arrays contain 41 and 48 Hamamatsu R8520 PMTs, respectively. Also seen in the bottom figure are the stainless steel meshes and PTFE reflector ring.

Figure 6.4: View of the top three of the electrode meshes and the outer PTFE ring.

one for additional LXe displacement.

The detector had four 0.203 mm thick 304 stainless steel meshes which were electro-formed and electropolished to minimize electrical discharges. The gate and cathode meshes, separated by 15 cm, defined the vertical bounds of the active volume. The anode and top meshes sat above the liquid level. The gate–anode and anode-top mesh gap distances were both 5 mm. The dimensions of mesh holes were 2.0 mm by 2.0 mm and the bars had a width of 0.182 mm. The meshes had a normal optical transparency of ∼84%. The placement of the top three rings can be see in Figure 6.4.

Embedded in the inner PTFE tube were copper field-shaping rings that established a uniform field in the active region (see Figure 6.5). These were needed as the height to diameter ratio was quite large unlike that of the Case prototypes. The voltage divider

Figure 6.5: Copper field shaping rings with high voltage divider on the PTFE tube.

network consists of nineteen 1 GΩ resistors. Figure 6.6 shows the electric field as simulated with Comsol Multiphysics modeling software. The electric field was uniform up to ∼3 mm from the PTFE walls.

The high voltages for the gate, anode, top were provided by a CAEN A1733. SHV cables carried the voltages to the cryostat and in the vacuum, PTFE insulated wire was used. In the detector, bare wire was used, which is acceptable as the LXe is an excellent insulator. A Heinzinger PNC high voltage power supply was used to bias the cathode mesh. The high voltage was brought to the detector with a custom-made PTFE insulated feedthrough.

The detector was kept at 177 K which gave a gas pressure of 2.11 atm. The liquid level was measured to a precision of 1 mm with a cylindrical capacitor and was usually kept at 2 mm above the gate electrode. For the data described in this chapter, the top and gate meshes were biased to -1.15 kV. The anode and cathode were biased to +3.15 kV and -12 kV, respectively. These voltages established a drift field of ∼0.73 kV/cm and a gas field of ∼13 kV/cm.
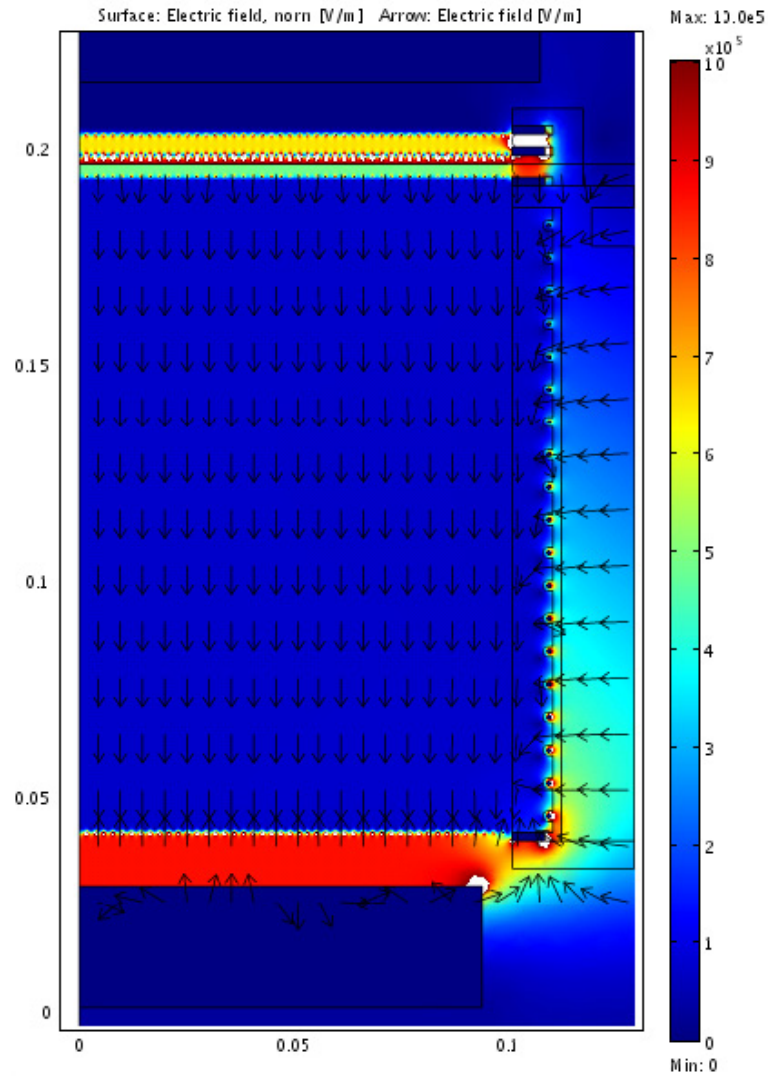
Figure 6.6: Simulated map of the electric field in XENON10. Field shaping rings keep the fields in the active region uniform. The field in the region between the cathode and bottom field array is reversed and very strong ($\sim$9 kV/cm). This map was generated using COMSOL Multiphysics software.
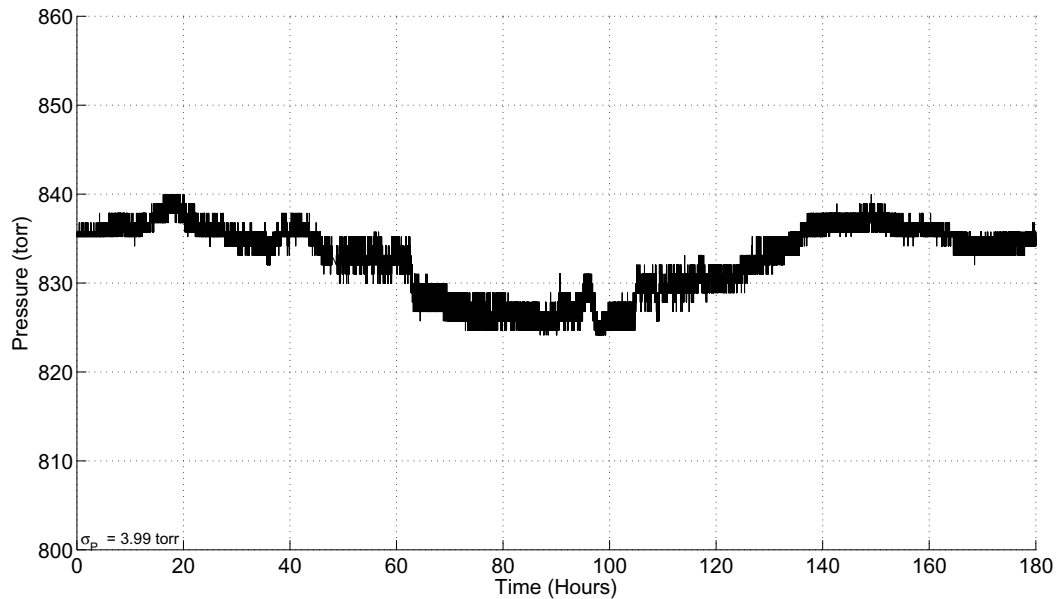
Figure 6.7: The xenon gas pressure as a function of time over period of 5 days. The standard deviation of the pressure over this period was 3.99 torr. The standard deviation over any 20 hour period was ∼1 torr.

6.2.2 Cryostat

A custom-made vaccum cryostat thermally insulated the detector can. The cryostat was cooled with a pulse tube refrigerator (PTR), which has a cooling capacity of about 100 W. The temperature was stabilized to ∼0.05 K by a LakeShore 304 controller, several resistive Pt temperature sensors and several heaters. Figure 6.7 shows the pressure over a period of several days.

There were several heat loads in the detector: radiation, conduction, convection, xenon recirculation and resistive (ohmic). The black-body radiative load follows Stefan-Boltzmann law (Equation 4.2). The inside surfaces of the detector were primarily stainless steel which has an emissivity of ∼0.15. The detector temperature was 177 K while the ambient temperature was ∼283 K and the inner surface area was ∼0.5 m^2 giving a radiative load of ∼23 W. A 10-layer aluminized-mylar (same material as that used in the Case cryostat) was later added which decreased this load by roughly a factor of 10. The conductive heat load included leakages through the stainless steel cylindrical ports, electric lines, and xenon

plumbing. This heat load follows equation Equation 4.1 and was <10 W. The residue gas ($P \sim 2.7 \times 10^{-3}$ torr) added a heat load of ~50 W, although the 10-layer aluminized insulation likely reduced this as it likely decreased the mean-free-path of the gas molecules. The liquification of the xenon presented another heat load which is

$$P = \dot{M}(C\Delta T + L) \tag{6.1}$$

where $\dot{M} = \rho \times \dot{V} = (5.4 \text{ g/l}) \times (2.3 \text{ l/min}) = 0.2$ g/sec is the mass flow, $C = 0.158$ J g^{-1} K^{-1} is the the heat capacity [306], $L = 95.7401$ J g^{-1} is the latent heat of vaporization [306] and $\Delta T = 300 - 177$ K $= 123$ K is the temperature difference. The recirculation heat load was about 24 W.

The PMTs introduced only a small amount of heat. The PMT bases had a voltage of ~780 V across 12.6 MΩ voltage dividing network. The power dissipated by the PMTs was # of PMTs$\times \frac{V^2}{R} = 89 \times \frac{780^2}{12.6 \times 10^6} = 4.3$ W. The voltage divider chain for the field shaping rings emited <20 mW.

6.2.3 Emergency Precautions

The accidental lost of cooling power can be disastrous in liquid xenon detectors. Each Hamamatsu 8520 PMT cost ~$1,000 and require many months to remanufacture. Furthermore, the evaporation of liquid xenon can lead to an explosion, causing significant damage to the lab and resulting in the lost of xenon. Several precautions were taken to prevent this from occurring. An emergency cooling system was built into the cryostat which consisted of a dewar containing liquid nitrogen, a solenoid valve, and an insulated line for carrying the nitrogen to copper coils on the detector can. The solenoid valves automatically turn on upon loss of power to keep the detector can cooled. In addition, the detector had a burst disc with a rupture pressure of ~4 atm to protect the PMTs which implode at ~7 atms. Furthermore, system vitals were constantly monitored above ground at all hours. Finally, a text messaging system was set up to alert cell phones of system abnormalities.
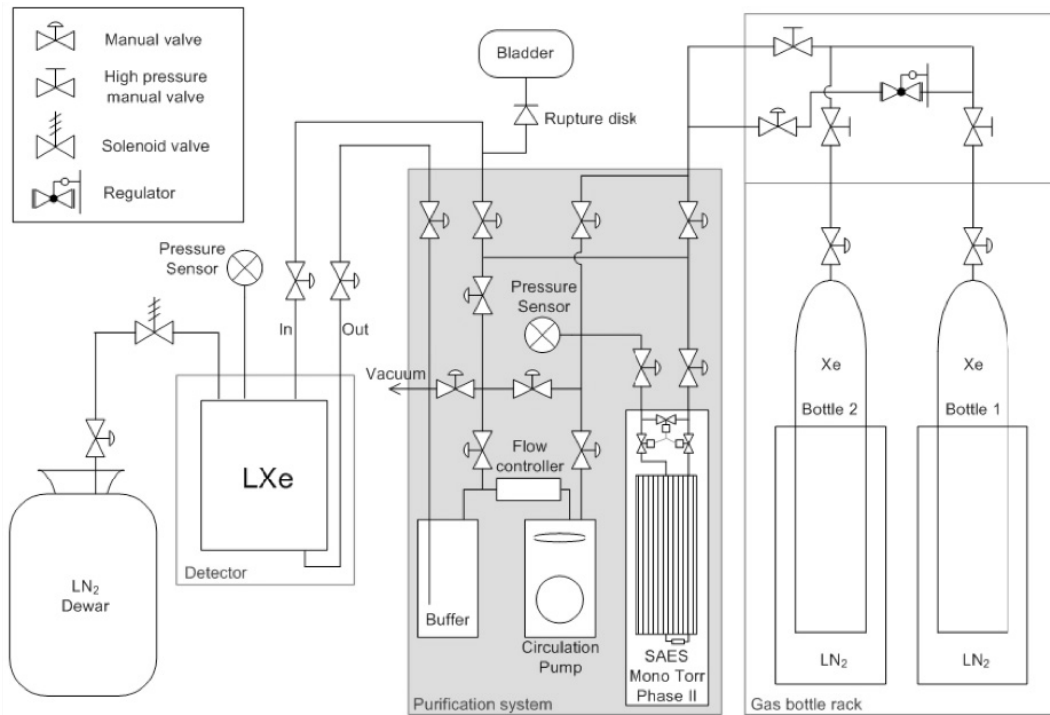
Figure 6.8: Schematic diagram of the XENON10 gas system. Figure of courtesy of Coimbra University.

6.2.4 Gas System

The XENON10 gas system consisted of a bottle rack containing two gas bottles and a gas panel containing a sealed diaphragm pump, SAES PS4 getter, mass flow controller and many high purity valves. It is very similar to the one being used at Case (see Section 4.2). Oxisorb purifiers cannot be used because of residual ^{238}U and ^{232}Th [307]. The amount of xenon in each bottle was tracked with a strain gauge. Figure 6.8 is a schematic diagram showing all the components and connections. Figure 6.9 is a photo of the gas panel mounted onto the lead shield.

A small dedicated LXe drift chamber for continuous monitoring of the electron lifetime was attached to the bottom of the detector. The device consisted of a solid cathode and anode, two meshes in between for shielding the solid electrodes and a series of field shaping rings. See Figure 6.10 for a picture of this device. The electrons are generated by pulsing the CsI on the cathode with a burst of light from an external xenon lamp. The lifetime value

Figure 6.9: XENON10 gas system panel, which was largely developed by members at Coimbra University.
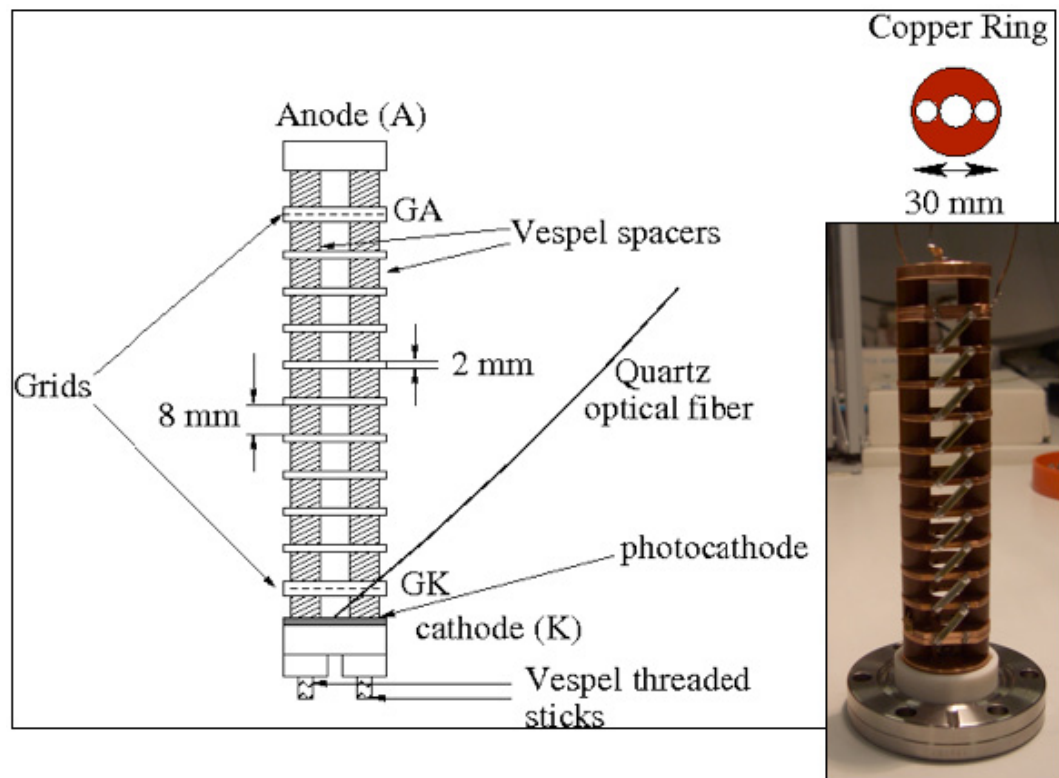
Figure 6.10: XENON10 purity monitor developed by group at University of L'Aquila.
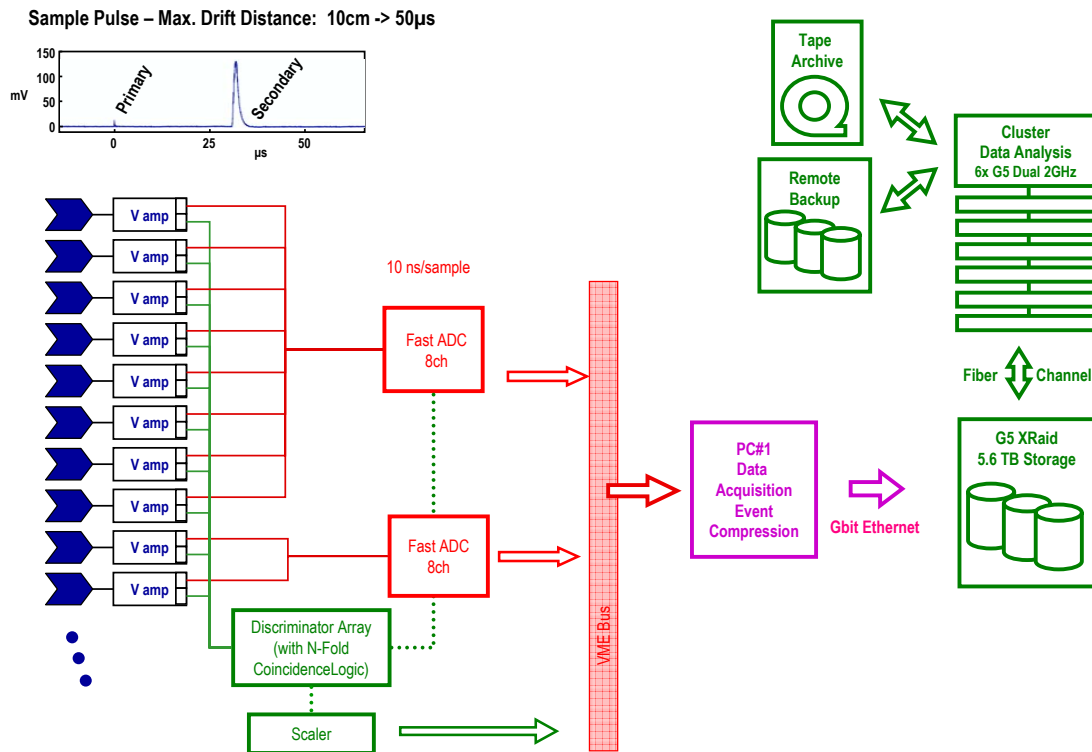
Figure 6.11: Diagram of the XENON10 DAQ

is extracted from the charge signal of the anode and cathode. The device was extensively tested but was ultimately not implemented due to the head load it introduced. For more information on this device and its measurements, see [59]. See Section 6.4.1 for information on the results of the electron lifetime measurements.

6.2.5 DAQ

This section briefly describes the data acquisition system (DAQ) shown in Figure 6.11. Each PMT signal was amplified by a Phillips 776 10x amplifier (each module contained 16 inputs) which has two outputs for each input. One output was routed to one of the inputs of the SIS-3301 14-bit 105 MHz digitizer and the other was directed to the discriminator. These digitizers sampled quickly enough to capture the shape of the S1 and S2 pulses, which have widths of several tens and several hundreds of nanoseconds, respectively. Figure 6.12
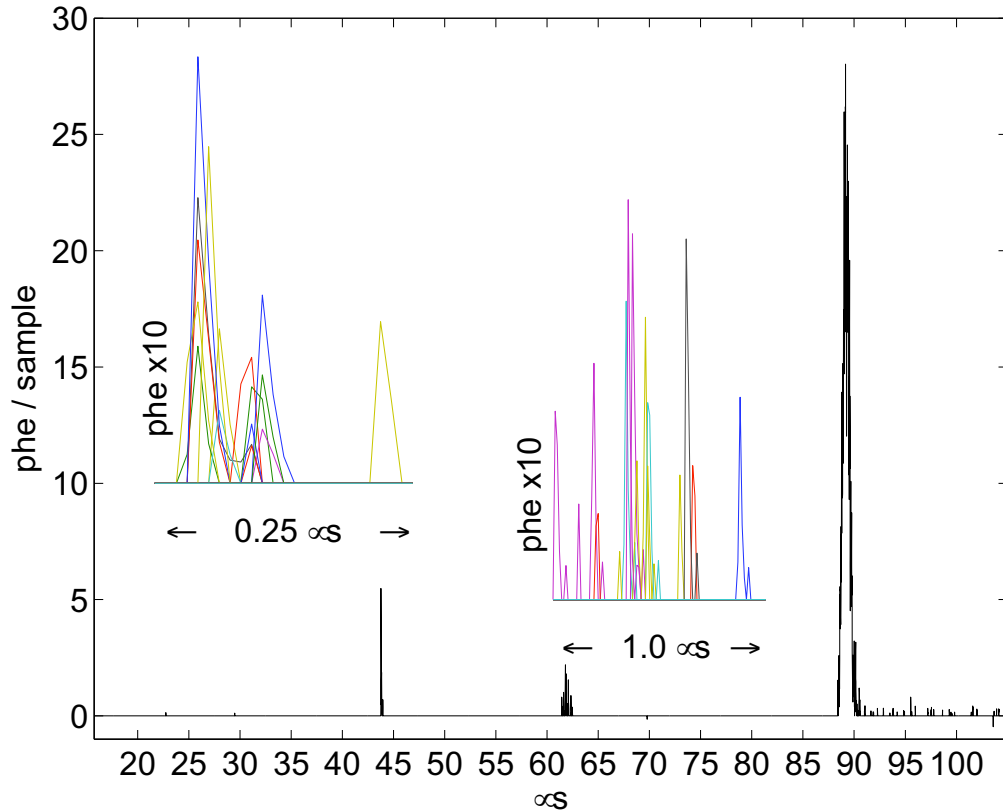
Figure 6.12: The PMT traces of an nuclear recoil event. The left inset shows the individual traces of the S1 pulse which contains ∼19 phe. The right inset shows that of the single electron S2. The large pulse on the right is the S2 of ∼1630 phe. Plot courtesy of P. Sorensen [54].

shows the traces of a nuclear recoil event. Although, more information on the S1 could have been saved with faster cards (like the 500 MHz Acqiris cards used with the Case detectors) this would have cost significantly more.

The digitizer captured the 80 μs (maximum drift time) segment preceding the trigger and 80 μs segment following the trigger for each PMT. The pre-trigger section was required to record lower energy events that were triggered by the S2. The storage size of an event was 14 bits $\times$ 88 channels $\times$ 160 μs $\times$ 105 MHz = 20,697,600 bits = 2.47 MB. Storing a 400,000 event dataset would have required nearly a terabyte of disk space. At the time of the experiment, redundant storage of this amount would have cost several thousands of

dollars. Fortunately, much of the trace does not contain useful information. A compression technique was applied (different from that used for the Case data; see Section 4.6.1) which reduced the size of the files by more than an order of magnitude. First, the segments of the signal that deviated little from baseline were set to baseline. Next the files were compressed with, gzip, which worked well with on these files as they contained much redundancy. More information on the compression procedure can be found in [60, 54]. The compression applied on Case data is described in Section .

Several trigger setups were explored. The S1-based triggered required a signal coincidence of ≥ 6 on the PMTs of the bottom array. The trigger for each PMT was adjusted so that there was a $\sim 80\%$ acceptance for a single photo-electron. One problem with the S1-based trigger was the high rate of S1 only events due to a large amount of xenon outside of the active region with no electric field. Also explored was an S2-based trigger which used the sum the signal of the 34 central PMTs of the top array. This trigger system was capable of triggering off of single electrons with an efficiency of $> 80\%$ and provided a much lower energy threshold than the S1 trigger as the S2 generally contains much more light. The threshold was set to trigger off of S2's of 4 electrons with a 100% efficiency. Because it afforded a lower threshold and avoided the S1 only events, this trigger setup was used for the WIMP search data. A more complete description can be found in [308].

6.2.6 Radiation Background Sources and XENON10 Shield

The rate of WIMP interactions is much lower than that of ambient background radiation. Most of the background in dark matter experiments is from Compton scattering of high energy gammas. Although electron recoils can be discriminated against in two-phase LXe time projection chambers, the rejection efficiency is not high enough to adequately suppress them to below expected WIMP rates and thus passive shielding is required. Passive shielding is also needed to block high energy neutrons from muon spallation and decay of radioisotopes as their response is indistinguishable from that of WIMPs. These external backgrounds are generally suppressed by running the detector underground in a plastic and lead shield.
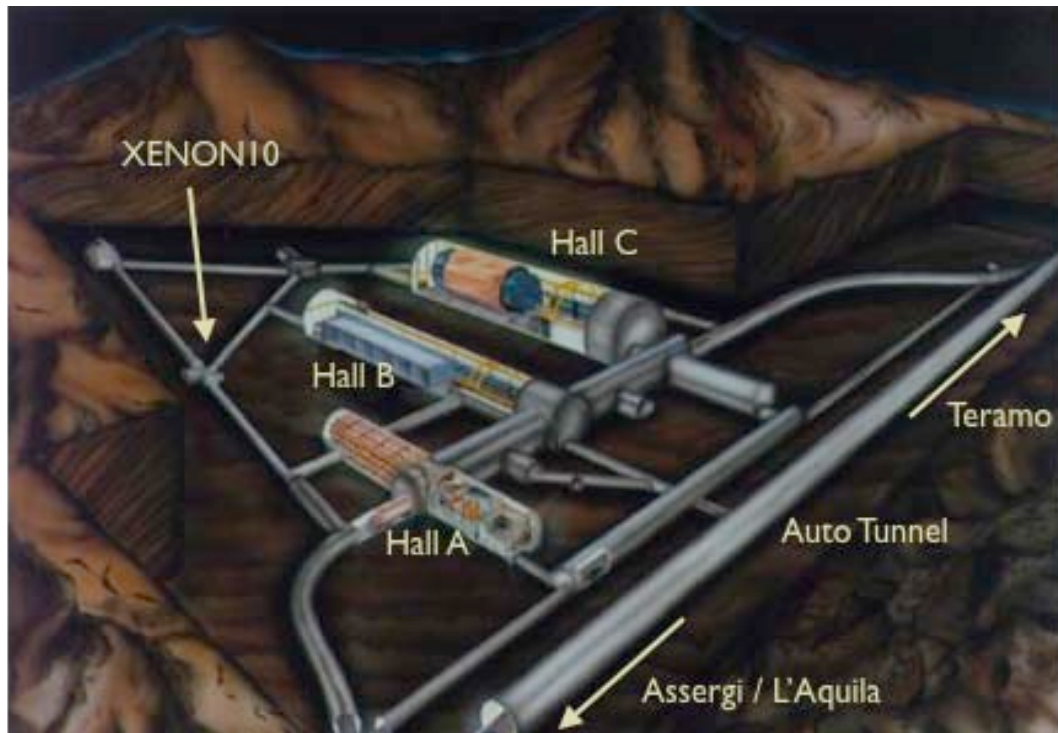
Figure 6.13: Diagram of the Gran Sasso National Laboratories with the location of XENON10 indicated.

Care must also be taken to ensure that the materials of the detector, cryostat and shield are radiopure.

In this section, we give a general overview of background sources, a description of the XENON10 shield, a survey of background in XENON10 and the performance of the shield in removing these sources.

General Overview of Background Sources

There are many sources of background radiation. In describing the background, we divide the sources into two groups: those induced by muons and those induced by non-muon sources, primarily those of primordial heavy isotopes. An complete survey of background sources relevant to low-background detectors is given in [55].

Much tertiary radioactivity stems from three primordial sources: ^{238}U, ^{232}Th and ^{40}K. The half-life of these elements are 4.47, 14.1 and 1.25 billion years, respectively. The

average concentration of ^{238}U/^{232}Th/^{40}K in the upper crust is 36/44/850 Bq/kg [55]. The concentration of these elements are likely to be the same in buildings and common detector materials as they are not separated in the extraction of materials from ores. A key exception is copper which is purified of these contaminants in repeated electrolytic dissolution and redeposition cycles as it has a high redox potential relative to that of U, Th and K.

Figure 6.14 describes the ^{238}U and ^{232}Th decay chains, which release a slew of alphas, betas, and gammas. Also released are neutrons from (α,n) reactions, in particular by alphas from U and Th on lighter elements. Nearby rock emits neutrons from (α,n) reactions of U and Th decay with a flux of $\sim$2 n/m^2/day [309].

^{238}U decays into ^{222}Rn, which is by far the strongest airborne radioactive source. The outdoor concentration of radon is typically several Bq/m^3 [310]. The average indoor concentration of ^{222}Rn is roughly 40 Bq/m^3 [55]. ^{220}Rn is not as important because of its shorter half-life of 55.6 seconds compared to 3.82 days of ^{222}Rn. More importantly, the progenies of ^{220}Rn are short lived – the half-life of ^{212}Pb is 10.64 hours which is by far the largest half-life of isotopes in the ^{220}Rn chain. On the other hand, ^{222}Rn eventually decays to ^{210}Pb which has a half-life of 22.3 years and will release two betas and an alpha before transforming into the stable ^{206}Pb. All surfaces become radioactive from ^{222}Rn by the plate-out effect where by its charged radioactive daughters attach themselves to aerosols and collect onto surfaces, especially statically charged surfaces of materials such as plastic and glass. The decays at the edges of the detector can be misinterpreted as nuclear recoils and charged daughters can also migrate guided by the electric field toward grids – these events can be removed by position cuts. Covering parts with foils and keeping them in a radon free environments can lessen the contamination.

^{40}K decays can decay to ^{40}Ar by electron capture or positron emission (11.2%), the latter of which also emits a 1.46 MeV gamma ray, or to ^{40}Ca by beta decay (88.8%) with a 1.32 MeV end-point energy. Potassium is an essential element for several bodily functions and ^{40}K, comprising 0.012% of all potassium, is taken up just like regular potassium (^{39}K). The ^{40}K activity in the average human is approximately several kBq. To block the transfer
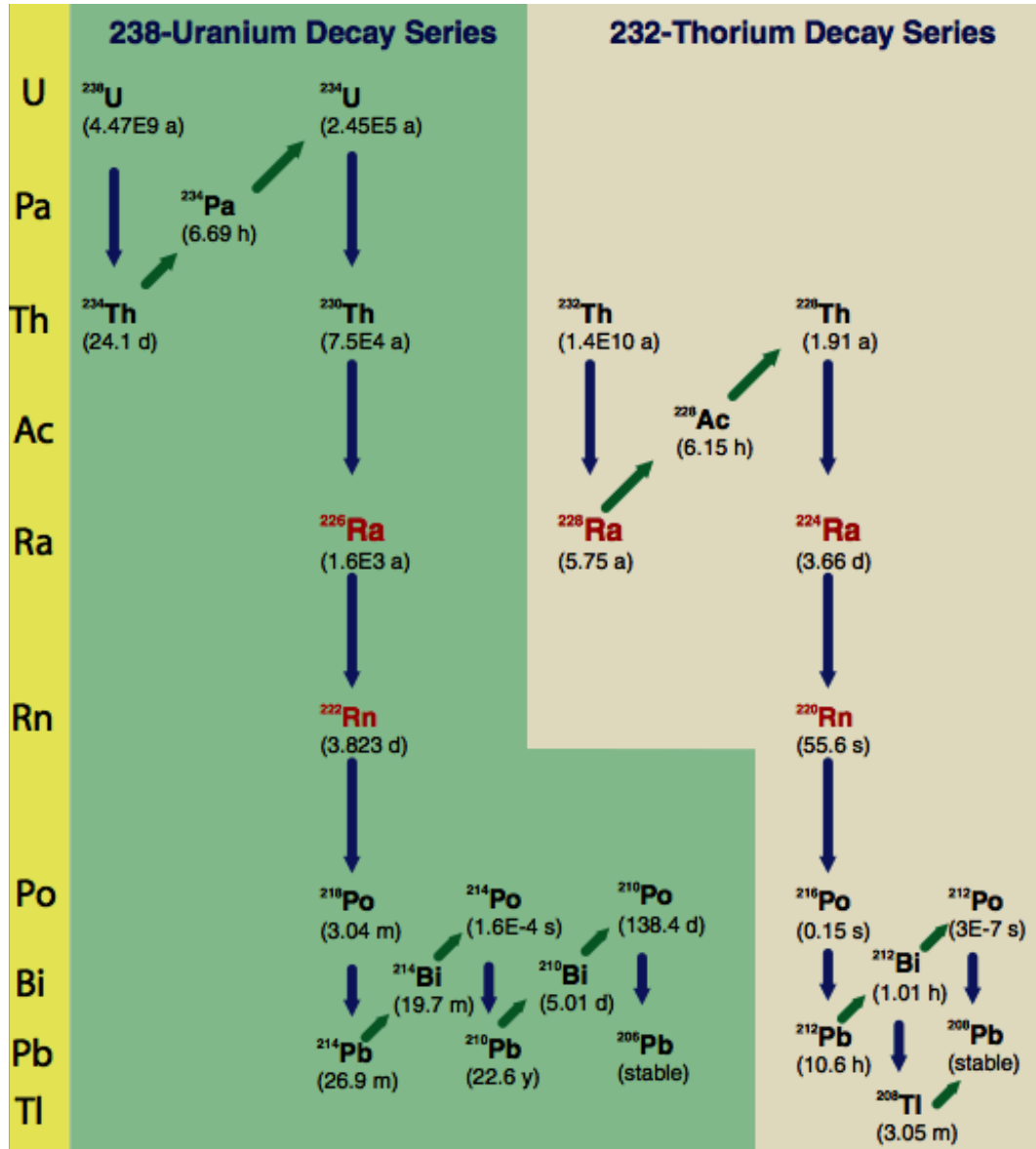
Figure 6.14: ^{238}U and ^{232}Th decay chains.

of ^{40}K to the detector via bodily fluids, gloves must be worn in handling and parts must be cleaned.

^{85}Kr is produced in small amounts by cosmic rays on ^{84}Kr. The abundance of ^{85}Kr in the atmosphere increased dramatically with the advent of nuclear energy but has since declined sharply due to cessation of atmospheric nuclear weapons test coupled with its short 10.76 year half-life. Fission of ^{235}U results in two large fragments of mass number between 90 and 140 and several neutrons. About 3 ^{85}Kr atoms produced per 1000 fissions. Nuclear reprocessing (to retrieve usable sources) releases ^{85}Kr into the atmosphere and results in an average concentration of 30 mBq/m^3 air [55].

Many plastic materials consist primarily of C, H and O and thus have ^{3}H (tritium) and ^{14}C, which are radioactive. Although, plastics usually derive from petroleum sources that contain very little of these two sources, they may be introduced by additives and catalysts and by the machining of these materials [55].

The lead used as shields typically has ^{210}Pb which beta-decays with a half-life of 22 years to ^{210}Bi, which in turn beta decays with a half-life of 5 days to ^{210}Po (see Figure 6.14). The betas of ^{210}Pb are unlikely to escape the lead but the 1.16 MeV beta produces a bremsstrahlung continuum with a maximum at 170 keV and characteristic x-rays with energies 72.8, 75.0, 84.9 and 87.4 keV. Concentrations of ^{210}Pb have been measured from detection limit up to 2500 Bq/kg [311]. Lead can be further contaminated with ^{210}Pb by the antimony added for hardening or by the coal used in smelting. Lead commonly used for underground experiments have a contamination of about 200 Bq/kg. Lead with activities of 5, 20 and 50 Bq/kg can be obtained at higher prices. Supplies of low activity lead produced several half-lives ago are limited to sources such as old lead pipes and ship ballast. Ancient Roman lead found in the Mediterranean sea have a ^{210}Pb activity of several mBq/kg, the lowest ever reported [312]. As previously mentioned, silver-tin solder can be used in place of common lead-tin solder which can have high concentrations on ^{210}Pb.

Cosmic rays generate a slew of particles. The relative intensity of $\pi^{\pm}$:p:e^-:n:$\mu^{\pm}$ is 1:13:340:480:1420 at the surface of the earth [55]. The cosmic-ray-generated neutrons do
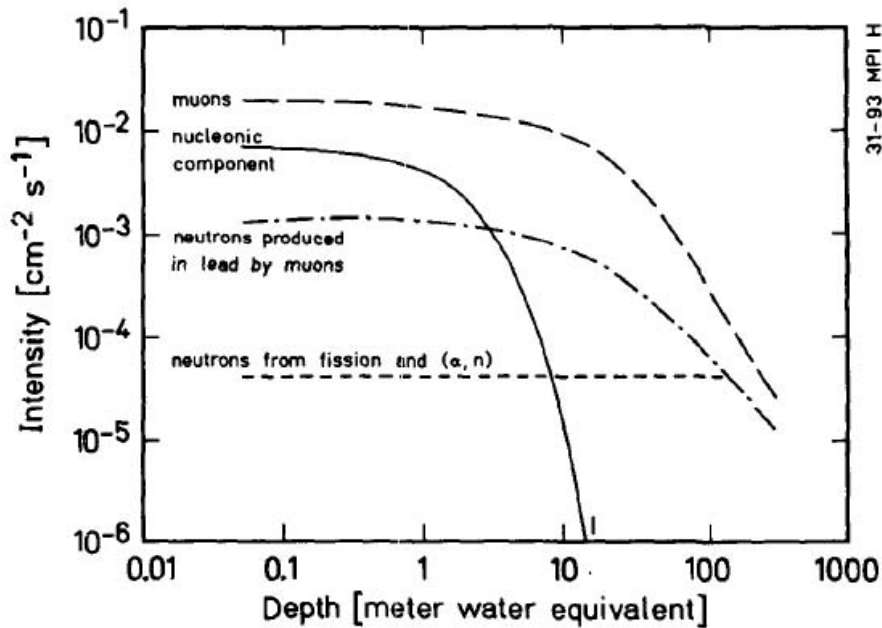
Figure 6.15: The intensity of cosmic ray daughters and tertiary-produced neutrons as a function of depth [55].

not reach underground event sites as they have a mean length of 200 g cm^{-2}, while muons are attenuated with 2 kg cm^{-2}, thus muons are the only cosmic ray daughters that affect underground experiments. Figure 6.15 shows the intensity of cosmic ray daughters as a function of depth. At sea level, the flux of muons is roughly 0.02 cm^{-2}s^{-1} and depends on such variables as the geomagnetic latitude and the phase of the solar cycle. Figure 6.16 shows the muon intensity as a function of depth.

XENON10 Shield

Much of the work on the XENON10 shield was done by the Brown University group. Figure 6.17 is a 3D CAD diagram of the XENON10 shield with the sliding door open. Neutrons were moderated by a 20 cm thick layer of high density polyethylene (HDPE) weighing 1.56 tonnes. Gammas were blocked by 20 cm layer of Pb weighing 33 tonnes which surrounds the polyethylene. The standard outer lead has an activity of 560 Bq/kg. The inside layer of lead has an activity of 17 Bq/kg. The shield was supported with steel beams. One
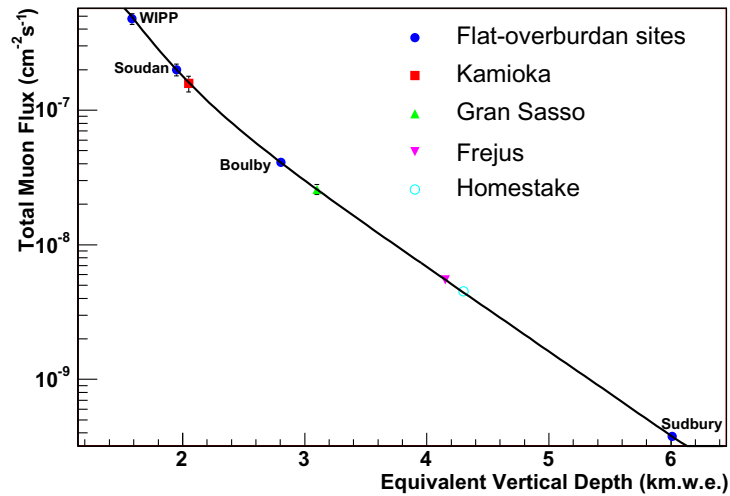
Figure 6.16: Muon flux versus depth with the depth of several labs indicated [56].

wall of the shield and the base of the detector sat on a sliding rail. The electrical and gas lines penetrated the shield through zig-zag pathways to remove direct penetration paths for external gammas. To remove radon emanating from parts inside the shield, the shield cavity was purged with 0.5 l/min of nitrogen gas provided by a dewar of liquid nitrogen. The LXe surrounding the active volume also served well as a shield as LXe is dense and is free of radioactive isotopes (if ^{85}Kr is removed). Figure 3.6(b) shows the attenuation length of gammas in liquid xenon. Outer sections of the active volume can be excluded with event position information.

External Background at Gran Sasso and Shield Performance

Muons The 1400 meters (3800 mwe) of rock provided by the Gran Sasso mountains cut the muon rate by about a factor of 10^6 to 22.3 ± 2.6 m^{-2} day^{-1} [56]. The average muon energy at LNGS is 270 ± 18 GeV [313]. In the 58.6 live-days WIMP search data, 69 potential muon events were found, 47 of which appeared to have entered the top of the detector, which agrees with the expected rate [54].
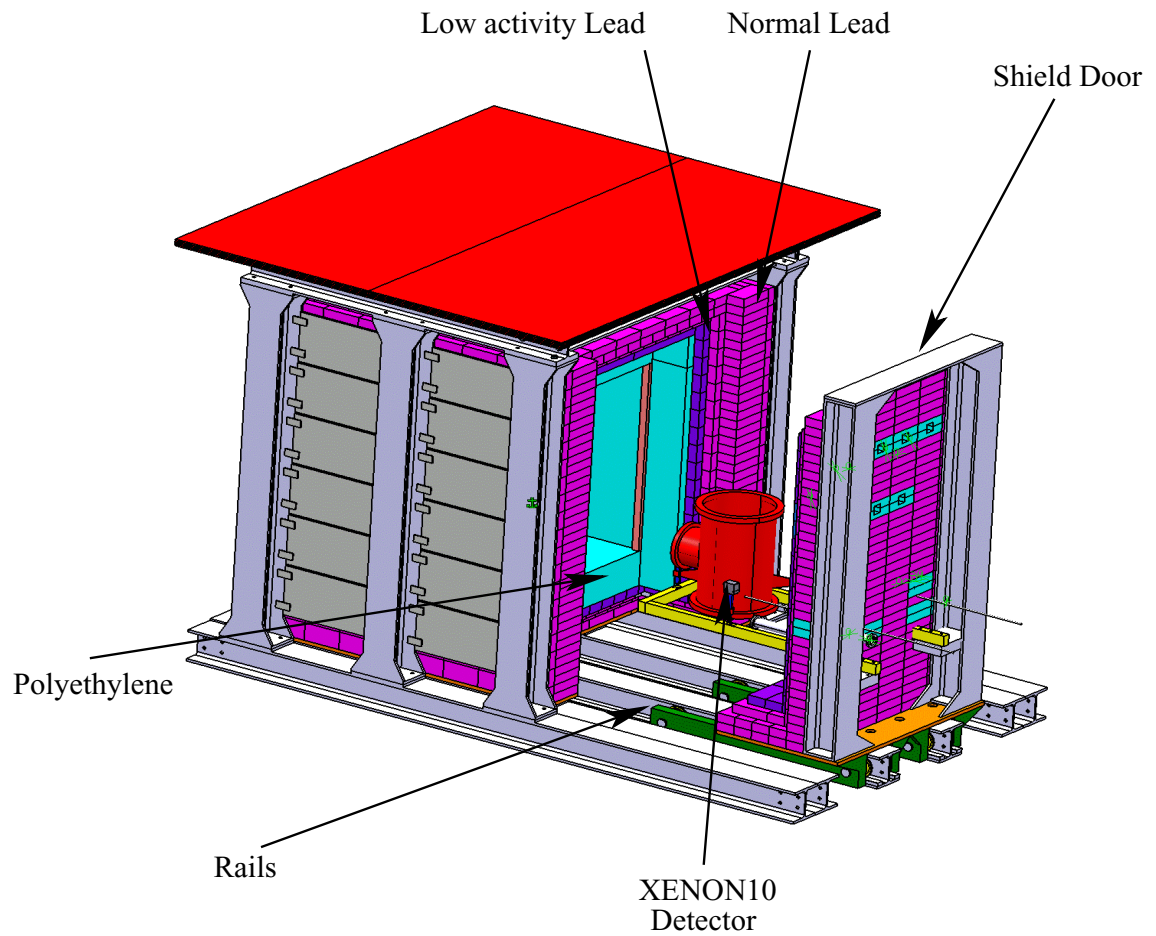
Figure 6.17: 3D CAD drawing of the XENON10 shield with the sliding door open. The lower activity and standard lead have activities of 17 and 560 Bq/kg, respectively. Drawing by L. Tatananni (LNGS Engineering staff).
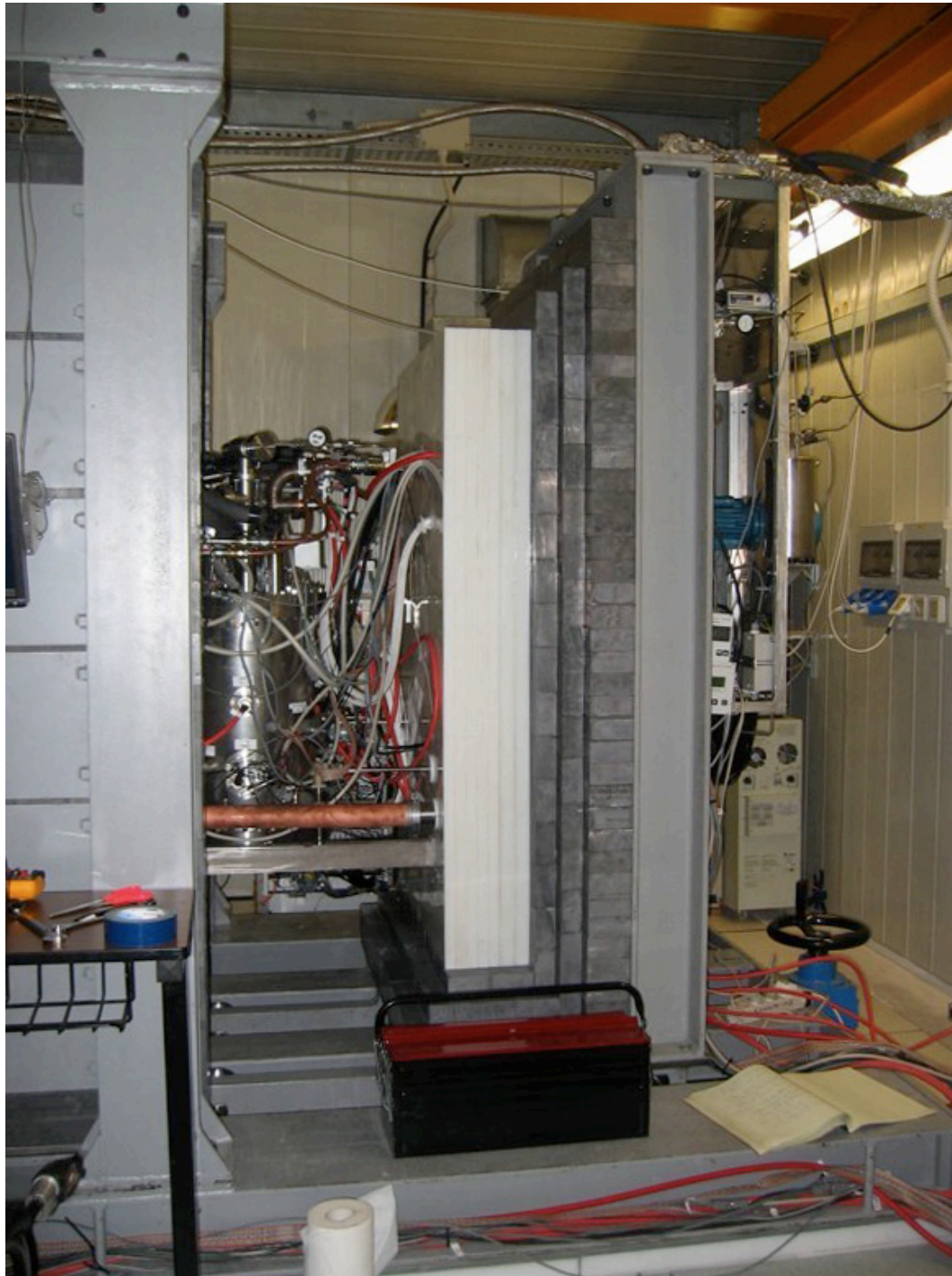
Figure 6.18: View of the detector with the shield open.

Table 6.1: Interaction lengths of high energy neutrons in polyethylene [75].

Energy (MeV)	σ (barn)	λ_{att} (cm)	$\exp(20 \text{ cm}/\lambda_{att})$
0.1	28	0.893	5.3×10^9
1	6	4.17	121
10	2.5	10	7.4
100	0.42	59.5	1.4
1000	0.28	89.3	1.25

Gamma rays from external sources   The U and Th of surround rock can give an event rate of 10^4 counts kg^{-1} keVee^{-1} day^{-1}. The Pb of the shield results in a 10^6 reduction of the gamma background from the rock, predicting a rate of < 0.05 dru in the detector cavity [54]. A higher rate was observed presumably due to radio impurities in the detector.

Neutrons from external sources   The neutron flux in Gran Sasso National Laboratory has been simulated [57]. The neutrons from radioactive decays of nearby rock at the depth of 3000-4000 mwe is roughly three orders of magnitudes higher than that derived from cosmic rays. Figure 6.19 is a plot of the neutron flux spectrum in Hall A and C. Although the neutron production rate in Hall C rock is more than 10 times lower than that of Hall A, the total rate in Hall C is only slightly lower. It was found that the neutron flux from the rock was reduced by the concrete which could be as thick as 1 m in some sections and thus, the neutrons emitted was dominated by that from the concrete. It was also determined that the rate was dependent on its water content as water is a good neutron moderator (see Figure 6.19).

Moderating the energy of a neutron to $\sim$100 keV eliminates the possibility of it generating a perceptible response in the detector. With 20 cm of HDPE, a factor 100 (60) reduction in flux of 1 MeV (6 MeV) neutrons was expected [54]. Table 6.1 gives the attenuation lengths and factors of neutrons at various energies [75]. The 20 cm Pb further reduced the neutron flux by an order of magnitude. Monte Carlo simulations predicted a neutron rate of <0.1 neutron/2 month/10 kg from ambient sources (non-muon) in the recoil window of 5 to 25 keVr [308].
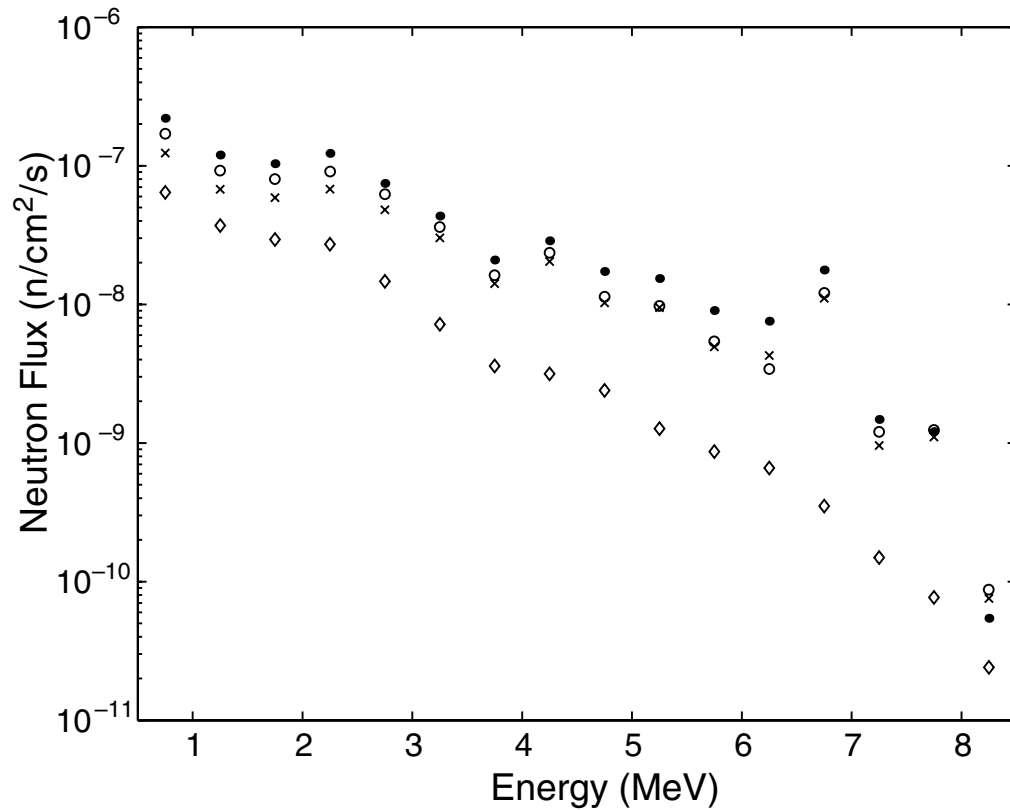
Figure 6.19: Neutron flux at the Gran Sasso National Laboratory, solid circle: Hall A, dry concrete, ×: Hall A, wet concrete, diamond: Hall A, dry concrete, fission reactions only and open circles: Hall C, dry concrete. Each point shows the integral flux in a 0.5 MeV energy bin. This plot is from [57].

Cosmic-ray generated neutrons Figure 6.20 shows the differential energy spectrum of muon-induced neutrons at various underground sites [56]. Muons on detector material will also generate neutrons. The production rate of muon-induced neutrons in various shield materials is shown in Figure 6.21. The rate of cosmic ray derived neutrons from the detector is estimated to be similar to that of ambient neutrons and the rate of muon-induced neutrons from surrounding rock is expected to be an order of magnitude lower.

Background from Detector and Shield

Table 6.2 gives a summary of the primary contributions of various materials to the background. The contents of the materials were either measured with a HPGe detector or found
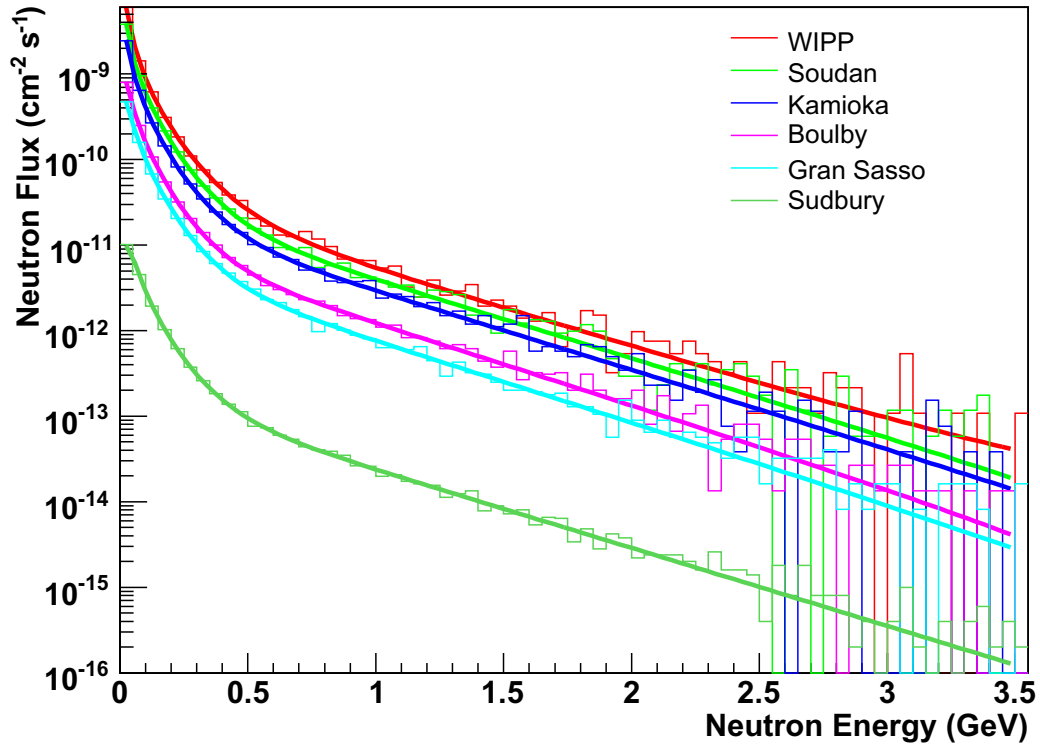
Figure 6.20: Differential energy spectrum of muon-induced neutrons at various underground sites. This plot is from [56].

in literature. The primary sources of electromagnetic radioactivity are the decay of U, Th, K, and Co in the stainless steel of the the detector and cryostat and the decay of ^{85}Kr in xenon. With the nitrogen purge, the contribution from radon is insignificant. Figure 6.22 shows radon activity as a function time.

The initial xenon used had a ^{85}Kr contamination of $\sim$25 ppm but was later replaced with xenon from Spectra Gas certified to contain $\sim$7 ppb of ^{85}Kr. The Kr removal system developed by the Case group purified 25 kg of xenon to <3 ppt but was not used for WIMP search data. This xenon would have given an event rate of $\sim$2$\times$10^{-4} dru as opposed to 0.43 dru expected from the xenon with 7 ppb ^{85}Kr [308].

Neutrons can also be generated inside the polyethylene shield. Neutron emission via spontaneous fission of U and Th can coincide with the emission of several MeV of gammas and thus can be discriminated against. Table 6.3 shows the expected neutron emission
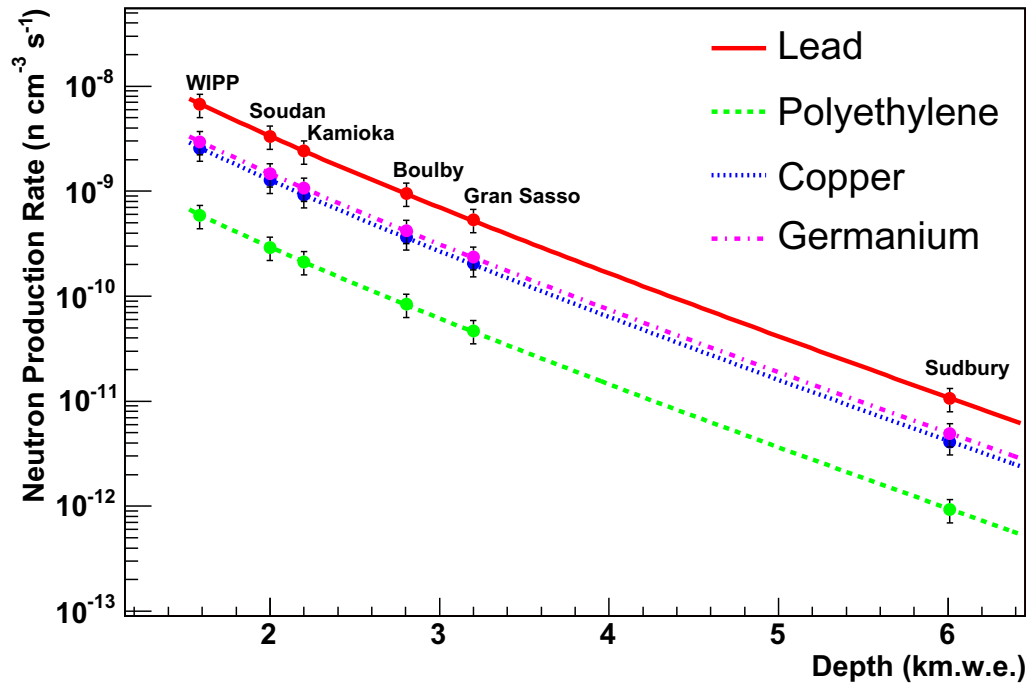
Figure 6.21: Rate production of muon-induced neutrons in common detector shielding materials as a function of depth with various underground sites indicated

rate of detector materials. Most of these neutrons are not expected to single scatter in the xenon. Preliminary estimates indicated that $<<1$ neutron/2 month/10 kg was expected to single scatter with a recoil energy between 5 and 25 keVr.

6.3 Data Processing

After the data was taken, we had to reconstruct detector interactions and the discrimination power depended on how accurately we were able to accomplish this. This required correcting the scintillation signals, filtering out bad events and categorizing the good events. This section describes the steps in processing the XENON10 data.

For cross checking purposes, two analysis groups were formed, one using ROOT (a data analysis package created by CERN) and the other using MATLAB (a commercial package created by The MathWorks). The analysis is only common in the signal compression stage.

Table 6.2: Radioactivity of various materials of the detector. The isotope activities are gives as 90% C. L. upper limits. The event rate is that of the 5.4 kg fiducial volume between 1.3 and 6.6 keVee (5 and 25 keVr). This table is from [54] from which more information on internal sources can be found.

Material	Mass (kg)	^{235}U,^{238}U	^{232}Th	^{40}K	^{60}Co	Event Rate (dru)
Vacuum cryostat steel	110	29	4	6	25	0.044
Detector vessel steel	33	29	4	6	100	0.176
Teflon	10	0.4	0.2	60	-	0.001
Kyocera A479SS	3	250	40	75	4	0.022
89 PMTs (PMTs + bases)	2.047	3.87	1.13	11.2	0.83	0.103
^{210}Pb (17 Bq/kg)	6370	-	-	-	-	0.045
Xe (7 ppb ^{85}Kr)	23	-	-	-	-	0.430
^{222}Rn (<5 Bq/m3)	<0.6	-	-	-	-	<0.010
Total (Monte Carlo)						0.83
Total (Data)						1.10±0.03

Table 6.3: Calculated neutron production per month from ^{238}U and ^{232}Th in XENON10. Table courtesy of P. Sorensen [54].

Component	^{238}U, (α, n)	^{232}Th Fission	^{238}U Fission	Total
89 PMTs	0.25	0.24	0.29	0.78
89 Bases	2.95	1.22	0.56	4.73
5 HV feed-through	2.61	0.91	2.12	5.64
143 kg stainless steel	2.94	1.75	11.72	16.41
10 kg Teflon	0.78	0.50	0.01	1.29
Total	9.53	4.62	14.70	28.85
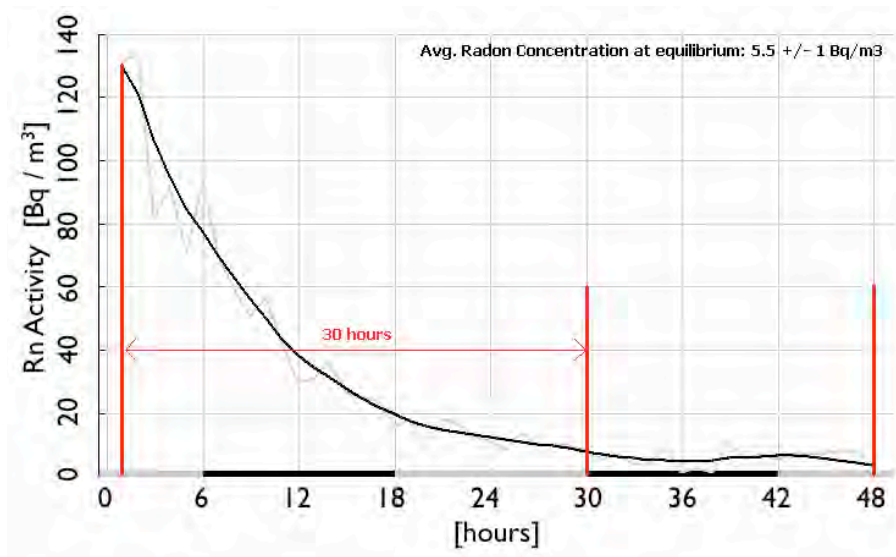
Figure 6.22: Radon activity inside the shield cavity as a function of time starting at the close of shield. Plot courtesy of S. Fiorucci.

Since the author was a member of the MATLAB analysis group, all the work in this section will be described from the MATLAB analysis perspective unless indicated otherwise. The author was involved primarily in defining and testing the position corrections and cuts.

6.3.1   Pulse Identification and Event Reconstruction

The first step of this stage is to load the 88 traces of each PMT into memory. Next the baselines are removed based on the first 50 samples of each trace. The amplitude is converted into units of photoelectrons/10 ns which is a convenient unit as the integral of a time bin ($\sim$10 ns) is roughly a photoelectron. For each event, several pulse shape quantities are computed for the n largest pulses found in the trace which are then saved to disk. These valves include the pulse height, integral, and time of X% of max amplitudes, where X is 10, 50 and 100.

In the next stage of processing, the files containing the basic pulse shape quantities are loaded into memory and the pulses are categorized as S1 and S2 according to the size, width and rise time of the pulses. The quantities of the S1 and S2 are saved to another smaller file. Some of these new values include the pulse start times (time of 10% max amplitude on

the leading edge), the width at 10% max amplitude, width at half max, the drift time (the difference between the S2 and S1 start times) and (x, y) positions.

6.3.2 Position Reconstruction

Accurate position reconstruction is important as regions near the walls of the active volume need to be excluded. The depth is provided by the drift time. The hit-pattern of proportion light on the top PMT array is used for reconstructing (x, y). The proportional light was always roughly uniform on the bottom PMT array and thus provided no position information. In the analysis, two sets of (x, y) position values are calculated. The first value is calculated by the "center-of-gravity" method:

$$X_{CG} = \sum_i X_i^{PMT} \times ss2_i, \tag{6.2}$$

$$Y_{CG} = \sum_i Y_i^{PMT} \times ss2_i, \tag{6.3}$$

where X_i^{PMT} and Y_i^{PMT} are the x and y coordinates of the i-th PMT, $ss2_i$ is the integral of the S2 in the i-th PMT signal and the summation is over only the PMTs of the top array. Although the center-of-gravity coordinates have a bias toward the center of the detector, they can be calculated very quickly. The "minimum-χ^2" method is a more accurate method that involves comparing the $ss2_i$ to a set of those simulated in 1 mm intervals in x and y coordinates by GEANT4, a general particle simulation package (the photon propagation Monte Carlo described earlier in Section 4.3.1 generated the same results but was not used). The χ^2 quantity,

$$\chi^2(x, y) = \sum_i \frac{(ss2_i - s_i(x, y))^2}{\sigma_i^2}, \tag{6.4}$$

is calculated for every simulated point, where $s_i(x, y)$ is the $ss2_i$ simulated at position (x, y) and σ_i is the uncertainty in the measured and simulated signals in the i-th PMT. The uncertainties in the simulated signal is insignificant compared to that of the actual signal. The fluctuations in the PMT gain and initial number of photoelectrons contribute to fluctuations in the measured signal. At first, the coordinate corresponding to the minimum value of $\chi^2(x, y)$ was chosen as the reconstructed position but it was found that taking a
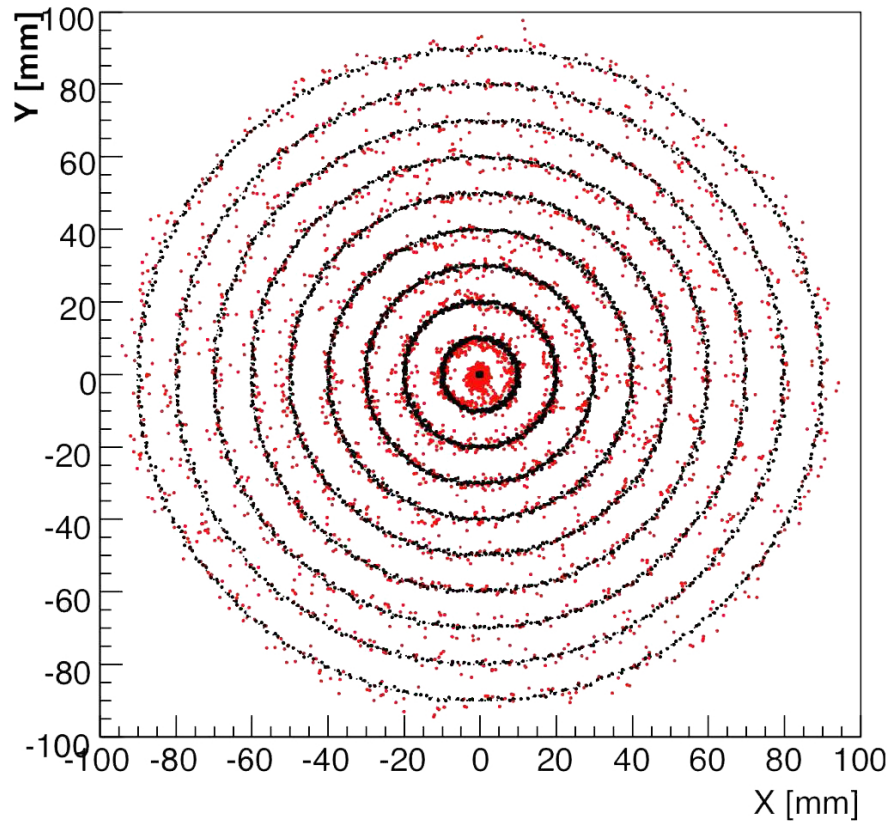
Figure 6.23: The black dots represent the actual location of simulated 10 keVr nuclear recoil events. The red dots represent the minimum-χ^2 positions. Plot courtesy of K. Ni [58].

weighted average of the positions corresponding to the three lowest $\chi^2(x,y)$ values would give a more accurate value. Figure 6.23 compares the actual and reconstructed position of 10 keVr nuclear recoil events in XENON10. Figure 6.24 shows the resolution of position reconstruction as a function of radius.

The minimum-χ^2 method is very slow requiring several milliseconds per event. The processing can be sped up by at least an order of magnitude by calculating the $\chi^2(x,y)$ for only a subset of positions around an approximate (x,y). For a rough location, the center-of-gravity coordinates or the position as calculated by minimum-χ^2 method using a much coarser set of $s_i(x,y)$ can be used. These ideas were tested but were not well developed in time for the final analysis.

In the ROOT analysis, another method was implement which was a neural network
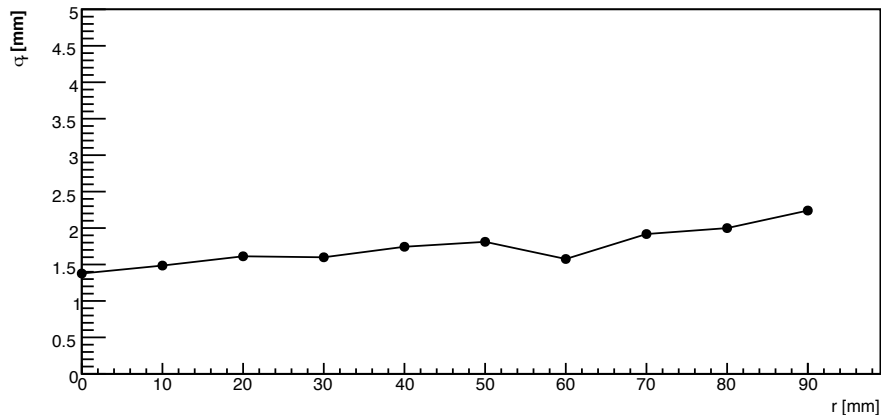
Figure 6.24: The spread (σ_r) in reconstructed position of 10 keVr nuclear recoil events as a function of radius. The resolution worsens with radius as less light is collected. Plot courtesy of K. Ni [58].

trained with Monte Carlo data. This method was more computationally intensive but was able to reconstruct the position with $\sim$100% better resolution than the minimum-χ^2 technique and thus was implemented in final analysis. The neural network is superior to the minimum-χ^2 technique because it is able to "learn" subtle patterns in the Monte Carlo data and better extrapolate points between the positions for which the proportional light is simulated.

6.3.3 Basic Cuts

In the analysis, the cuts were divided into three levels. The most basic cuts, QC0 (quality cuts, level 0), removed all events that could not be considered WIMP candidates such noise events, events that saturate the PMTs, and multiple scatters. The second level cuts, QC1, is the fiducial volume cut which excluded the edges of the active volume which have a high background rate and greater incidence of distorted events. The QC2 level cuts, removed anomalous events that may be misinterpreted as WIMP events such as those that multiple scatter with at least once vertex in the region underneath the cathode.

This section will describe QC0 and QC1 cuts. A description of QC2 will be given in Section 6.7.2.
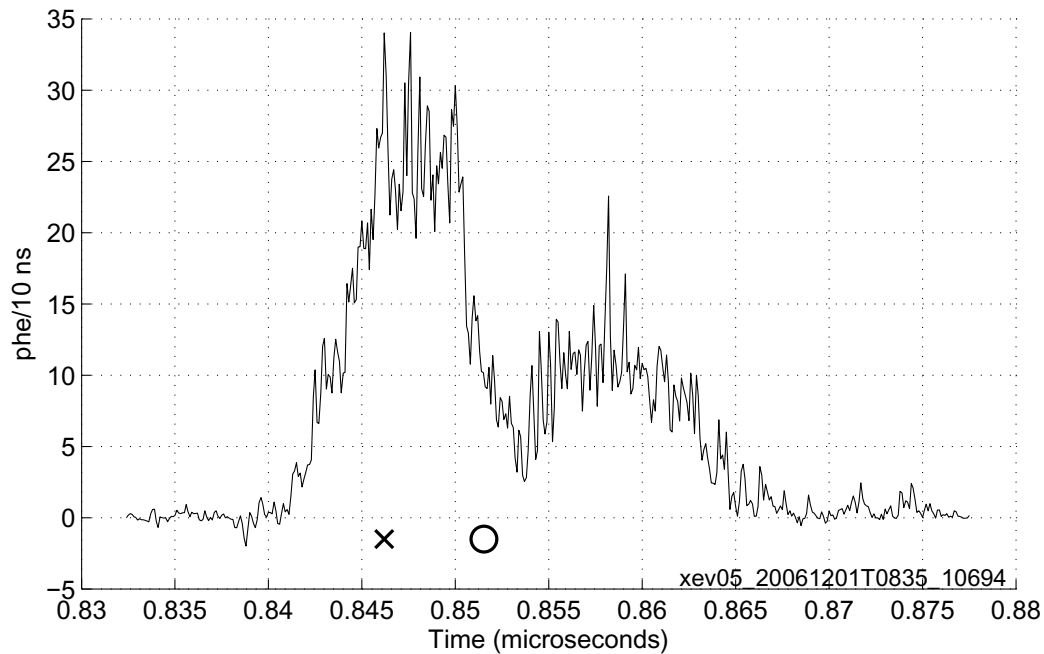
Figure 6.25: The x represents the t_{peak} and the circle represents t_{mean}, the first temporal moment.

QC0 Cuts

The QC0 level cuts had an efficiency of $\sim$99% for removing undesired events. Here, we describe all the cuts comprising QC0.

Single S1 and Single S2 Because WIMPs are expected to scatter once, only events with a single S1 and single S2 are accepted. This criteria also removes coincidence events which can be problematic as it is unclear which S1 is associated with which S2. In most instances of multiple scattering, the S2's are distinct and the requirement of a single S2 is sufficient to remove such events. However, if the vertices are not sufficiently separated in z, the S2 of a double scatter may appear as a single pulse with two peaks. The pulse finding algorithm views this as a single S2 pulse and thus such events are not rejected by the single S2 scatter cut. Such pulses can be recognized by a parameter that is the difference between the mean pulse time or the first temporal moment ($t_{mean} = (\sum_i t_i V_i)/(\sum_i V_i)$, where t_i and V_i are the time and signal voltage, respectively, of the i-th time bin) and the time of the peak, t_{peak}.
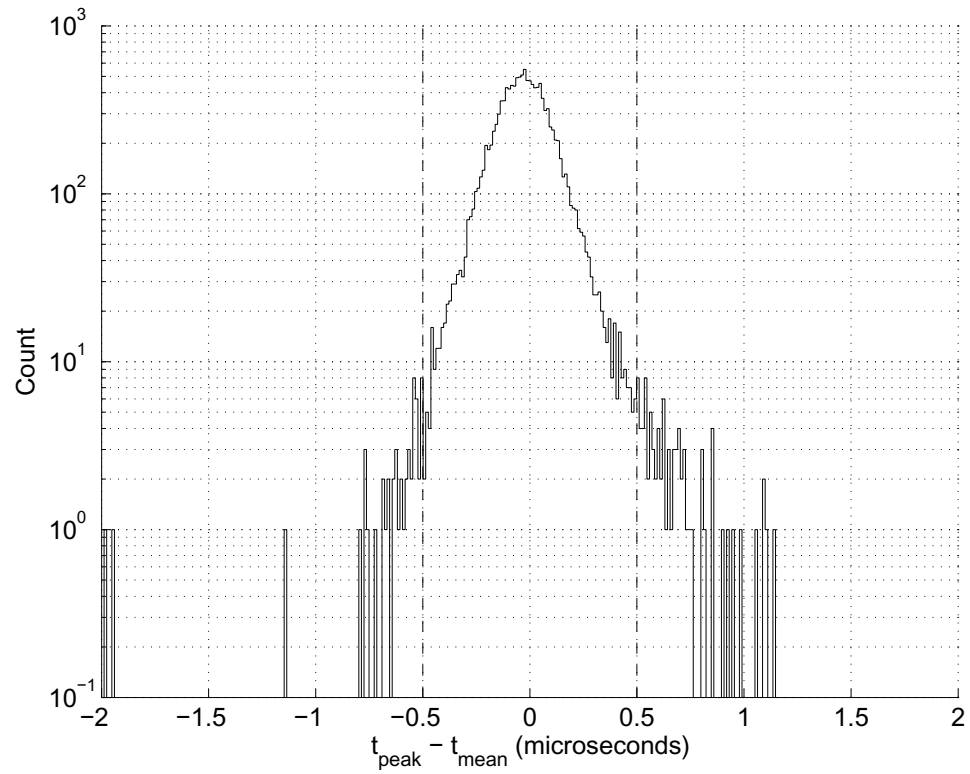
Figure 6.26: This is histogram of the $t_{peak} - t_{mean}$, the time of the peak subtracted by the first temporal moment (defined in the text) of S2 pulses. The outliers represent S2 pulses that have two or more peaks that was interpreted as a single pulse in the pulse finding routines. Such multiple scatters can be removed with this parameter. The vertical lines represent the conservative cut limits.
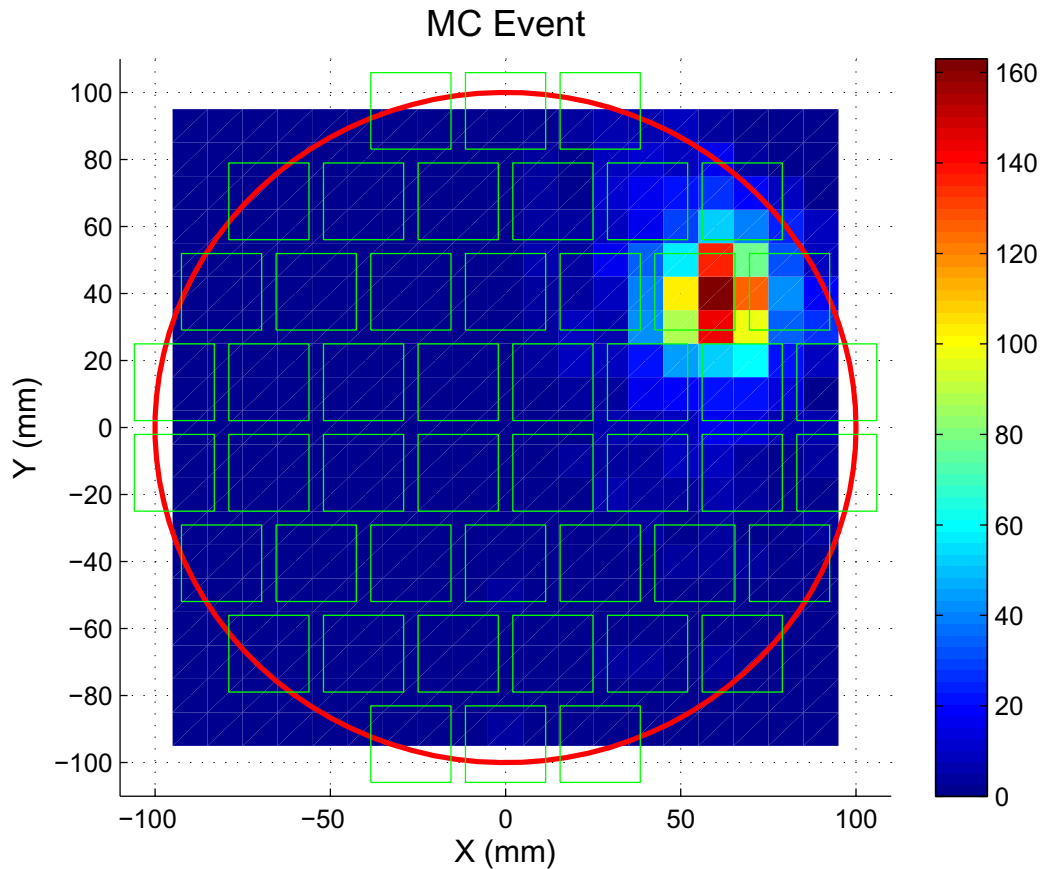
Figure 6.27: Map of final positions of S2 photons on the top PMT array. Most of photons strike two or three PMTs directly above the point at which S2 light is generated.

Normal S2's have a roughly Gaussian shape and $t_{peak} - t_{mean} \approx 0$ sec. For double-pulsed S2's, t_{mean} lies between the two peaks while the t_{peak}'s will be in the middle of the larger peak. Figure 6.25 shows an S2 with two peaks with the t_{mean} and t_{peak} indicated. Figure 6.26 is a histogram of the distribution the $t_{peak} - t_{mean}$ distribution. Virtually all of the events that lie outside of the $\pm 0.5 \mu$s bounds are double scatter events.

If a particle scatters more than once at the same z by are sufficiently separted in (x, y), then the summed S2 pulse will appear as a single pulse. For such events, the hit-pattern of the top PMT array must be examined. According to photon propagation simulations, the proportional light from a single scatter is focused on the few PMTs directly above the point of generation. Figure 6.27 shows the distribution of the final photon positions
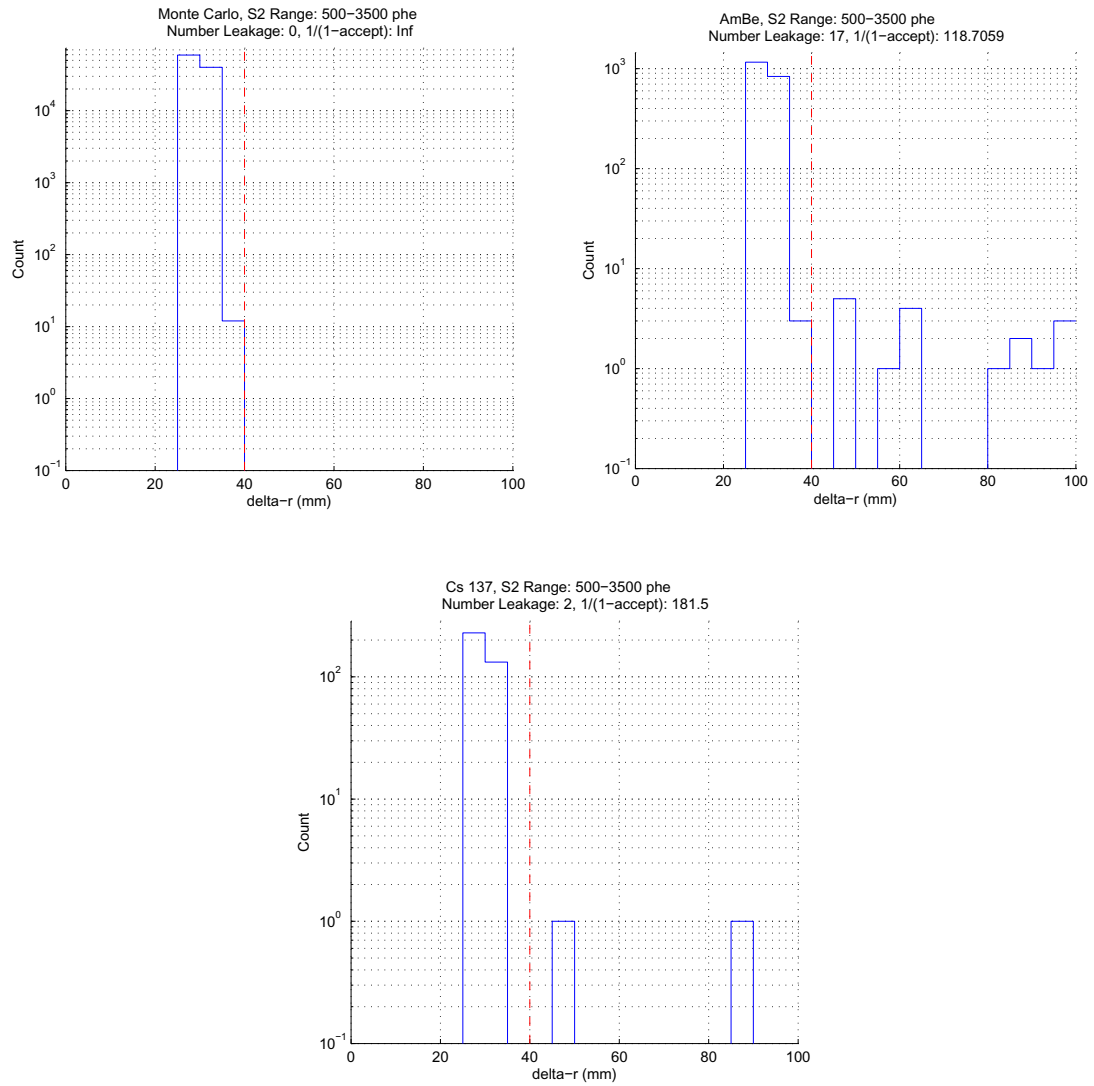
Figure 6.28: Histogram of the Δ_r between the PMT receiving the most and second-most light from Monte Carlo, AmBe and ^{137}Cs data for events with S2 between 500 and 3500 phe (40 and 120 keVr).

on the top PMT array for a single S2 pulse. On the other hand, an event with multiple scatters in the same z will generate a hit-patten with multiple "hot spots." A parameter which can remove such events and can be calculated quickly is the distance between the PMTs receiving the most and second-most light. The parameter, which we call Δ_r, will almost always be no greater than the distance between adjacent PMTs. Figure 6.28 shows histograms of this parameter for Monte Carlo, AmBe and ^{137}Cs data for events with a number of S2 photoelectrons between 500 and 3500, corresponding to an energy range of between roughly 20 and 140 keVr. The distance between adjacent PMTs is at most 30 cm. Any event with a high Δ_r is likely to be abnormal. The Monte Carlo showed that 0 out of 10^5 events had $Delta_r > 40$ cm, suggesting that actual events with $\Delta_r > 40$ cm were likely a double scatter or some other malformed event. Several events, possibly multiple scatters or other anomalous interactions, in the AmBe and ^{137}Cs are removed by this cut. Clearly, this cut needs greater sophistaication to account for multiple S2's of different sizes. Unfortunately, this cut was developed too late to be included in the final analysis.

Good baselines   This cut removed events whose baselines may have been calculated inaccurately by the presence of spurious pulses in first 50 samples. If samples in this segment exceeded a pre-defined threshold, the event was rejected.

Trace Edges   This cut eliminated events with an S1 or S2 at the edges of the traces. Such pulses may have distorted pulse shape quantities as a portion of the pulse's waveform may have been truncated.

S2 fraction of trace area   For normal events, the S2 should comprise nearly all of the total trace area. Some events have traces with slowly drifting baselines which can result in incorrect integral and height values. This cut removes all events with $S2$ to total trace integral ratio below 0.5 or greater than 0.999.

S2 top versus bottom   The actual and Monte Carlo data shows that~60% of the S2 signal should be collected by the top PMT array and that any large deviation is an indication
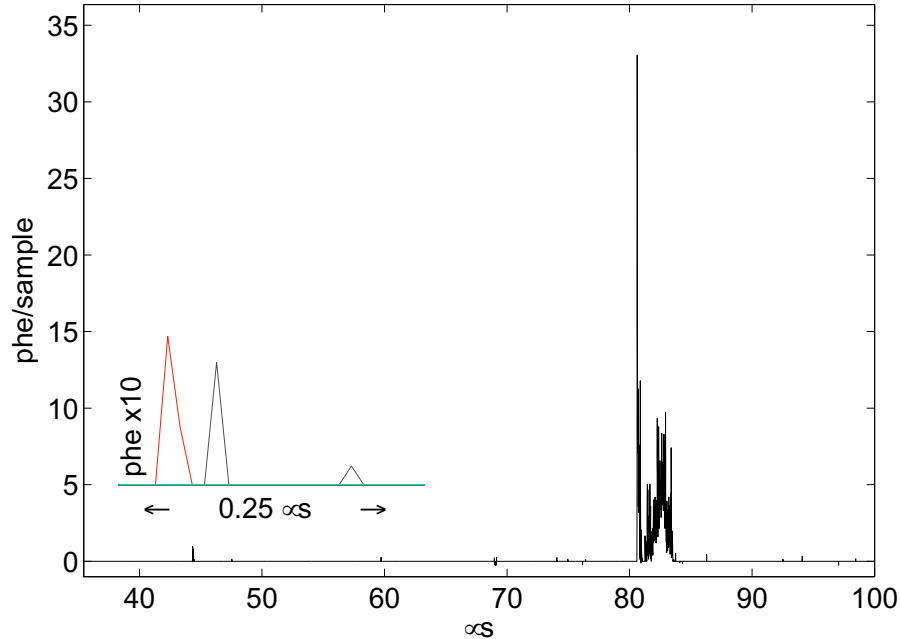
Figure 6.29: Signal trace of an event scattering immediately underneath the liquid level surface, resulting in a large S1 immediately preceding the S2. Such events are removed with the height/integral cut. Plot courtesy of P. Sorensen [54].

of something wrong. Events with an $S2_{top}/S2_{bottom} > 1.5$ are excluded by this cut.

S2 width The S2 width is determined by the distance that the electrons drift in the gas. The S2 pulse width must be between 0.45 and 2.25 μs. The range is very large because of the warping of the meshes (see Section 6.4.3).

PMT Saturation No WIMP event in the energy region of interest (5-25 keVr) are expected to saturate the digitizers. If any PMT signal of an event exceeds the limit of the DAQ channel, it is rejected.

S2 height/integral The height/integral of the pulse is a measure of the inverse of the pulse width. This cut removes broad pulses and pulses with an S1 attached to the front of the S2 (see Figure 6.29). The latter are events that occur near the liquid surface.
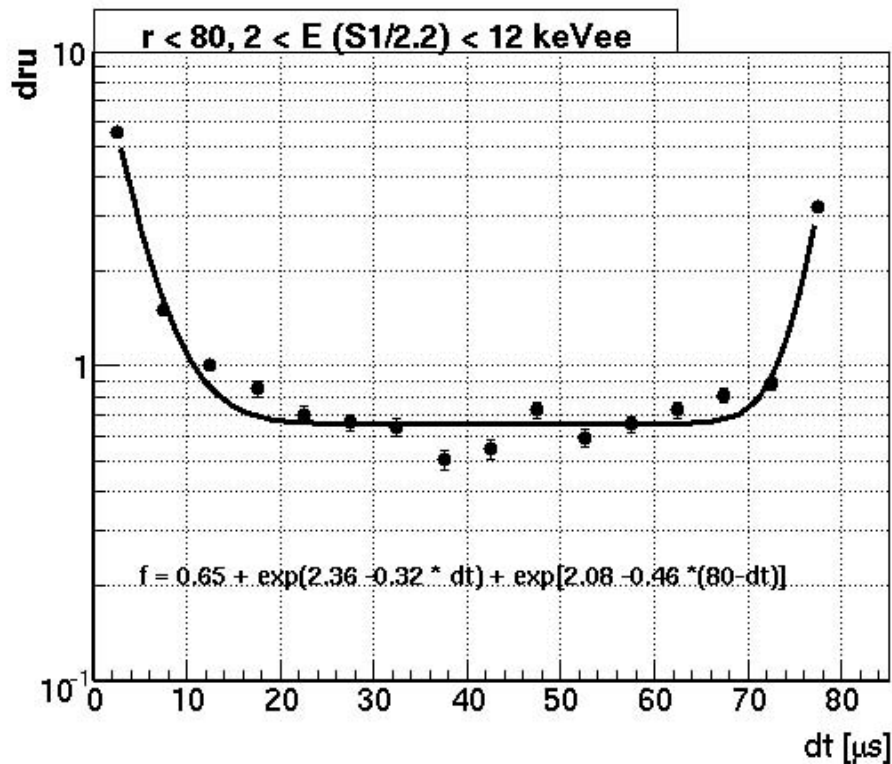
Figure 6.30: XENON10 background rate within r < 80 cm as a function of depth in the WIMP energy window.

S1 pulse shape cut The S1 must meet several requirements. PMTs can have sizable dark noise pulses that are indistinguishable from primary light pulses. Such pulses are filtered out by demanding that the primary light pulse be simultaneously present in several PMTs. At least 2 PMTs must have an S1 signal of >0.35 phe. Also, the width at 50% maximum amplitude of the S1 must be <0.30 μs. Finally, the S1 rise time, defined as the time difference between the 10% maximum amplitude of the rising edge to the time of the peak, must be between 10 to 50 ns.

Position Reconstruction Cut (χ^2 Cut) This cut excludes events with a minimum-$\chi^2 > 2$. Events with a high minimum-$\chi^2 > 2$ value are likely to be abnormal events.

QC1 Cuts – Fiducial Volume

Events occurring at the edges of the detector should be omitted from consideration for two reasons. Firstly, the edges will have more background events than the center due to the self-shielding afforded by liquid xenon (see Figure 3.6(b)). For example, a 1 MeV gamma has an attenuation length of ∼6 cm. In XENON10, the central portion had a background rate of 0.6 events/keVee/kg/day, while the edges saw 3 events/keVee/kg/day (see Figure 6.30). Secondly, electron recoil events that occur near the PTFE walls may suffer from charge loss and be misinterpreted as a nuclear recoil. Events near the PTFE walls and the electrode meshes may also experience a different electric field than those at the center.

The fiducial volume defined in the blind analysis of the WIMP search data has a mass of 5.4 kg. The fiducial volume was determined by analyzing the ^{137}Cs data and a portion of the WIMP search data. The fiducial volume cut has a radial limit of 80 cm and a drift time bound of 15 and 65 μs. An additional cut was used to exclude events underneath PMT #48, which was dead as the position of these events were not reconstructed well. This cut removed events with coordinates inside a circular area of radius 4.7 cm centered at the coordinate of the PMT.

6.4 Basic Performance of the Detector

6.4.1 Electron Lifetime

In the XENON10 detector, the events have a drift distance of up to 15 cm. This presented a much greater xenon purity challenge than that of the Case prototypes as these detectors had a depth of only 1 cm. A 20 cm electron drift length in Case detector would only result in a maximum charge loss of ∼5%, while in XENON10, the charge loss would have been ∼53%. The electron drift time (length) of ∼2 ms (∼430 cm) was attained after several months of recirculation purification. Figure 6.31 shows the evolution of the electron lifetime over a period of about a month while recirculating xenon through the getter.
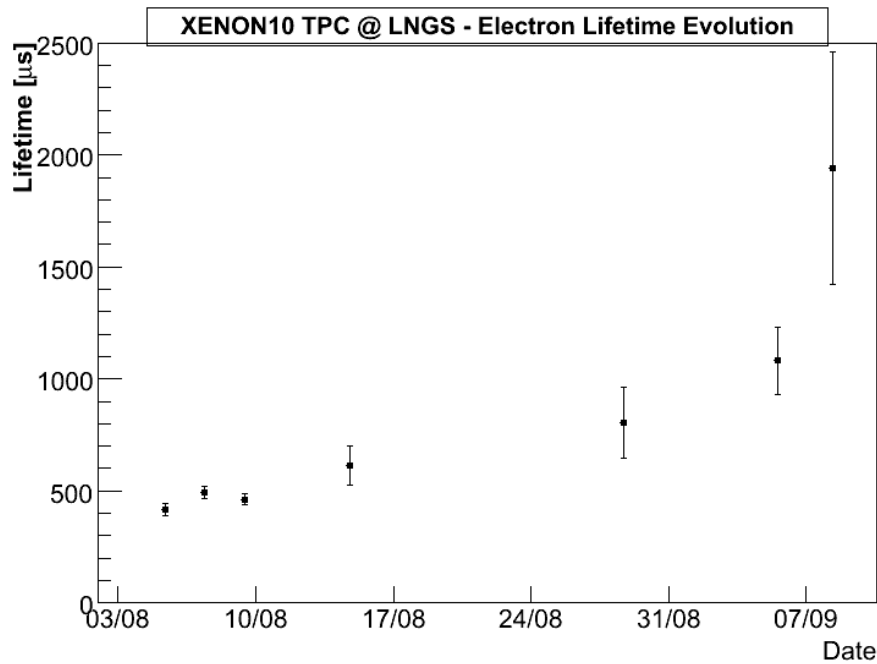
Figure 6.31: The evolution of the electron lifetime (as measured with ^{57}Co and ^{137}Cs) in XENON10 during about a month of recirculation purification. The time format is Date/Month (e.g. 03/08 is August 3rd). Plot courtesy of A. Ferella [59].

6.4.2 Signal Stability

A convenient gamma-ray line in LXe detectors for exploring stability is the ever-present 30 keV x-ray. This x-ray is emitted as following photo-absorption by a K-shell electron. This is usually accompanied by the photo-electron, but many of the background gammas are photo-absorbed in the dead xenon outside the active region. The x-ray may then travel through the PTFE wall to the active region and be measured alone. The range of the x-ray in liquid xenon is ~0.4 mm, so these events are only observed near the edges of the detector. Figure 6.32 is a plot of the $S1$ of this peak as a function of time. The fluctuations are less than 5% at 30 keV over a period of several months [59].
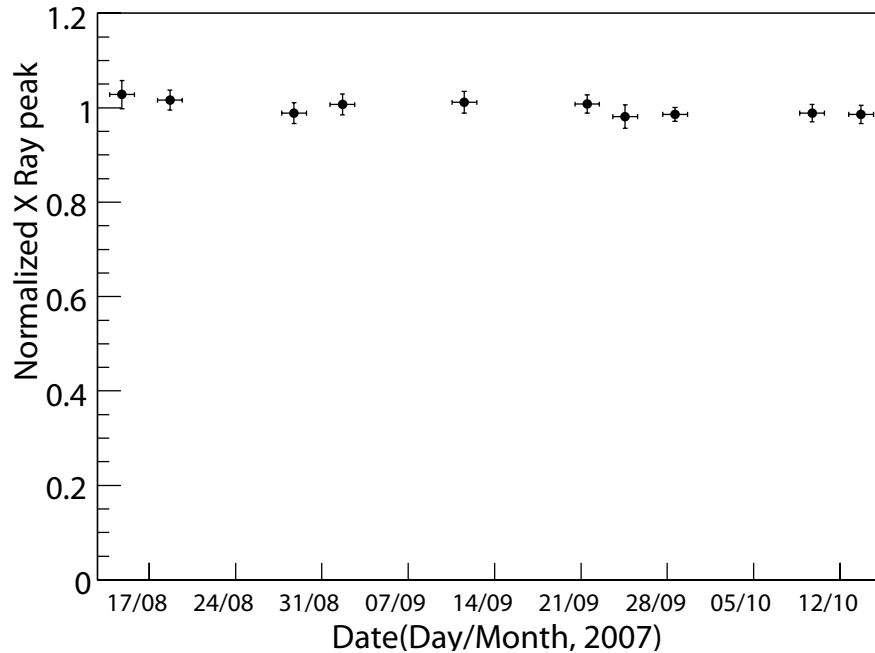
Figure 6.32: Normalized $S1$ of 30 keV background gammas. This plot indicates the stability of detector over a period of several months. Plot courtesy of A. Ferella [59].

6.4.3 Light Collection

Activated Xenon

A generic problem with using external gamma ray sources to probe a detector is that the lower energy gammas (e.g. 122 keV from ^{57}Co) do not adequately penetrate the center of the fiducial volume and higher energy sources (e.g. 662 keV from ^{137}Cs) are more likely to Compton scatter rather than photoabsorb, giving a continuum in recoil energy rather than a peak. This problem can be solved by having the xenon be not only the target but also the emitter by inducing delayed emissions of gammas with high energy inelastic nuclear recoils. The AmBe dataset contains 40 keV prompt gammas but there are only ∼2000 such events.

To get a higher rate without activating detector parts, a portion of xenon can be irradiated with a very hot source and then be mixed in with the xenon that is already in the detector. Prompt lines such as the 40 keV gamma cannot be used due to the delay from transferring the xenon. Two excited states with long half-lives are ^{129m}Xe and ^{131m}Xe,

which emit 236 keV and 164 keV gammas with half-lives of 8.9 and 11.8 days, respectively. The ^{129m}Xe and ^{131m}Xe can be created by neutron capture by ^{128}Xe and ^{130}Xe, respectively, or by inelastic scatter off of ^{129}Xe and ^{131}Xe, respectively. Members at Yale University irradiated a 1 kg of xenon with a ^{252}Cf source which emitted neutrons at a rate of 4×10^4 n/s. The xenon was activation was activated at Yale University and then shipped to Gran Sasso where a portion was included with the present xenon. This procedure was performed after taking the WIMP search data. A detail description of the preparation is provided elsewhere [236].

S1 Signal

The average number of photoelectrons observed in the primary light of 164 keV gammas was 2.9 phe/keVee (2.5 phe/keVee in bottom, 0.4 phe/keVee in top) at 0.73 kV/cm. The equivalent value at zero field is about 5.4 phe/keV (4.6 phe/keVee in bottom and 0.8 phe/keVee in top array) which is similar to that obtained by Xed1b, the Case prototype with two PMTs. About 8.6% of the primary scintillation photons are converted into photoelectrons. The light collection in XENON10 nearly matches that of two PMT Case prototype.

Figure 6.33 shows maps of the total primary light of 164 keV gammas collected by all PMTs and that collected by the bottom and top PMT arrays separately. Maps based on the 236 keV peaks are identical. The $S1$ varies with position in the expected manner. On average, the bottom array collects $\sim$6x more light due to the internal reflection at the liquid level surface. The collection of primary light increases with depth at all radii because a lower fraction of the light is absorbed by the PTFE (see Figure 6.34). The primary scintillation collection near the bottom decreases with increasing radii, also because of the greater absorption by the PTFE. However, an opposite trend is observed near the liquid level surface, contrary to that expected from the Monte Carlo studies. The reason for this is not known. These maps shows that two separate single-variable functional corrections for drift time and radius are inadequate. The use of this map in improving the resolution is described in later sections 6.6.2.
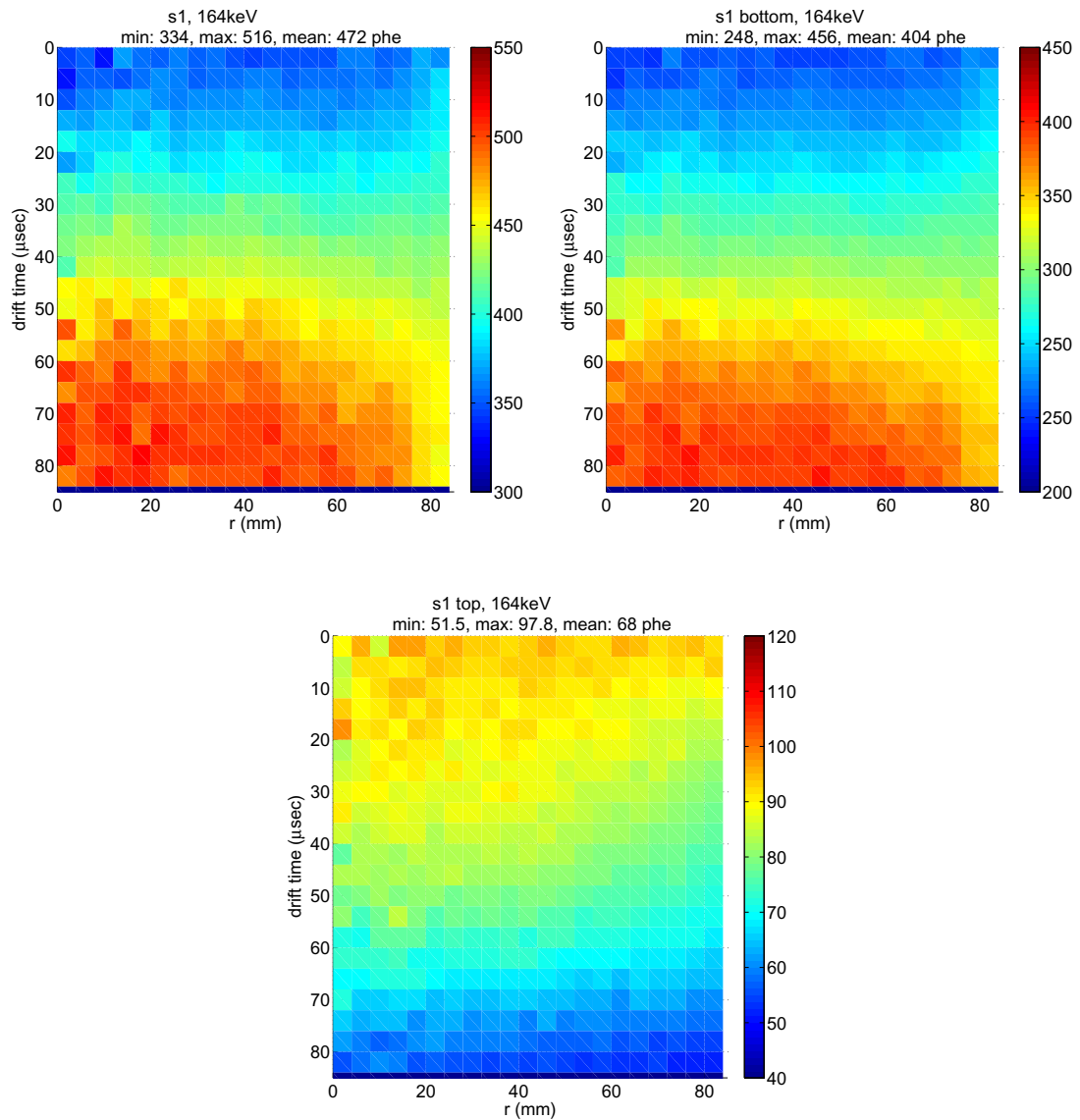
Figure 6.33: Map of the total $S1$ (6.33(a)), and $S1$ in the top (6.33(b)) and bottom (6.33(c)) arrays in drift time and radius based on the 164 keV gammas.
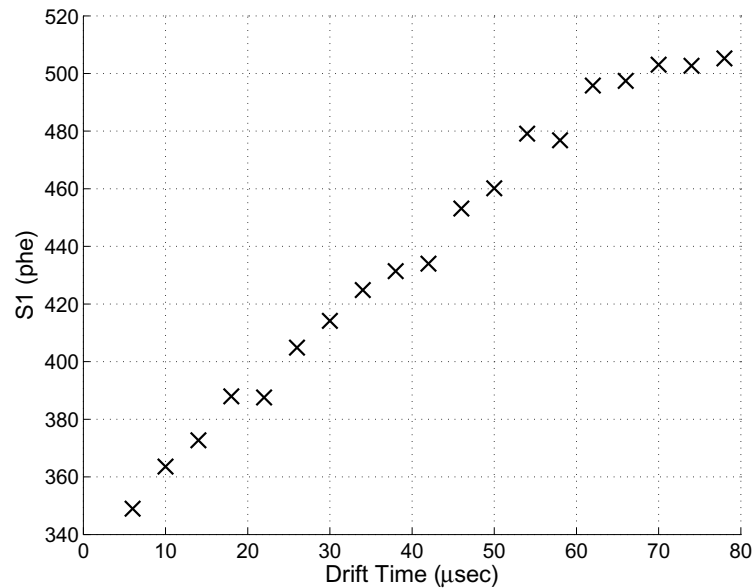
Figure 6.34: S1 light collection versus depth at r = 0 mm as measured using the 164 keV gammas. The basic trend is followed at all radii.

S2 Signal

Maps of the $S2$ and S2 width and 10% maximum amplitude were created using 40 keV and 164 keV gammas (See Figures 6.35(a) and 6.35(c)). Neither $S2$ map exhibits the fall off with radius as expected from Monte Carlo simulations. Instead they show a bump running along the 45 degree diagonal. The S2 width map shows a feature of the same angle. The two values actually appear to be anti-correlated suggesting a common mechanism which could be meshes having been warped by the contraction of the supporting structures. Figure 6.36 shows scatter plots and polynomial fits of $S2$ and S2 width at 10% versus the azimuthal angle for 40 keV gammas events between the radius of 50 and 70 mm. The regions of the map that have a higher $S2$ and smaller S2 width may be regions where the anode and gate mesh are closer together. Recall that the proportional scintillation is a function of the number of electrons, electric field and drift distance (see Equation 3.19). In this case, the proportional light was more sensitive to the electric field enhancement than to the decrease in drift distance, hence we observed a higher $S2$ in regions where the grids were closer together as indicated by the lower S2 width. The reason for the differences between the the
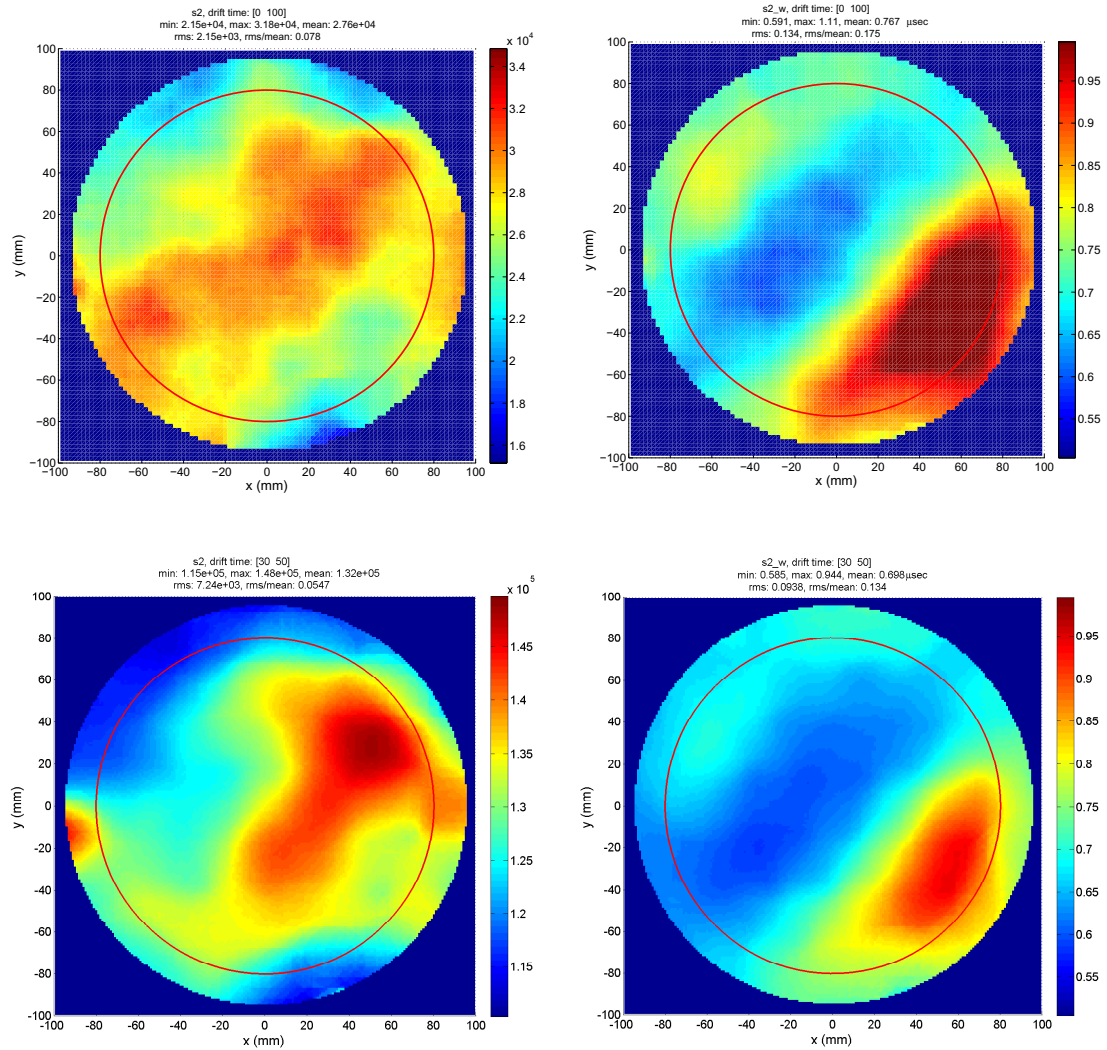
Figure 6.35: Maps of $S2$ (top-left) and S2 width at 10% max amplitude (top-right) of 40 keV gammas. Maps of $S2$ (bottom-left) and S2 width at 10% max amplitude (bottom-right) of 164 keV gammas.The asymmetrical pattern is likely due to a warping of the meshes.

$S2$ maps of the 40 keV and 164 keV is not known. The change may have been due to the change in liquid level that occurred upon adding the activated xenon.

The use of these maps to improve the $S2$ resolution and background discrimination are described in later sections (see Section 6.6.2 and 6.7, respectively).

6.5   Calibration

6.5.1   PMT Gain

The gain calibration of the PMTs was accomplished by measuring the single-photoelectron response to pulses of light from internal LEDs. In the Case detectors, the calibration was performed using the single photoelectrons that spontaneously emerged from the photocathode. The use of LEDs is superior as the pulse times are known which allows for a large reduction in noise events. The LED light is controlled with a pulse generator, which had a trigger signal directed to the DAQ. The LEDs were pulsed for 6 μs and a 50 ns wide window was integrated 4 μs after the end of the LED pulse. This window had a $\sim$20% probability of including one photoelectron pulse and a $\sim$2% of observing two or more photoelectrons. Figure 6.37 is a histogram of the single photoelectron in one of the PMTs. The PMT voltages were adjusted to achieve gains of $\sim$2 $\times$ 10^6. The PMTs were recalibrated every week or two to ensure that the small drifts in signal gain were accounted for. Figure 6.38 is a plot of the PMT gain as a function of time. Even with the PMT gains equalized, they did not exhibit the same level of response due to the differences in quantum efficiencies. A correction of the relative sensitivities of the PMTs is discussed in Section 6.6.1.

6.5.2   S1 and S2 Calibration

The nuclear recoil energy axis was not directly calibrated with a monoenergetic neutron source. As with the analysis of the Case data, single-phase relative scintillation factor (between electron and nuclear recoils) was used to calibrate the nuclear recoil energy units from the 122 keV peak. Figure 6.39 shows a histogram of the $S1$ of the ^{57}Co. The 122 keV
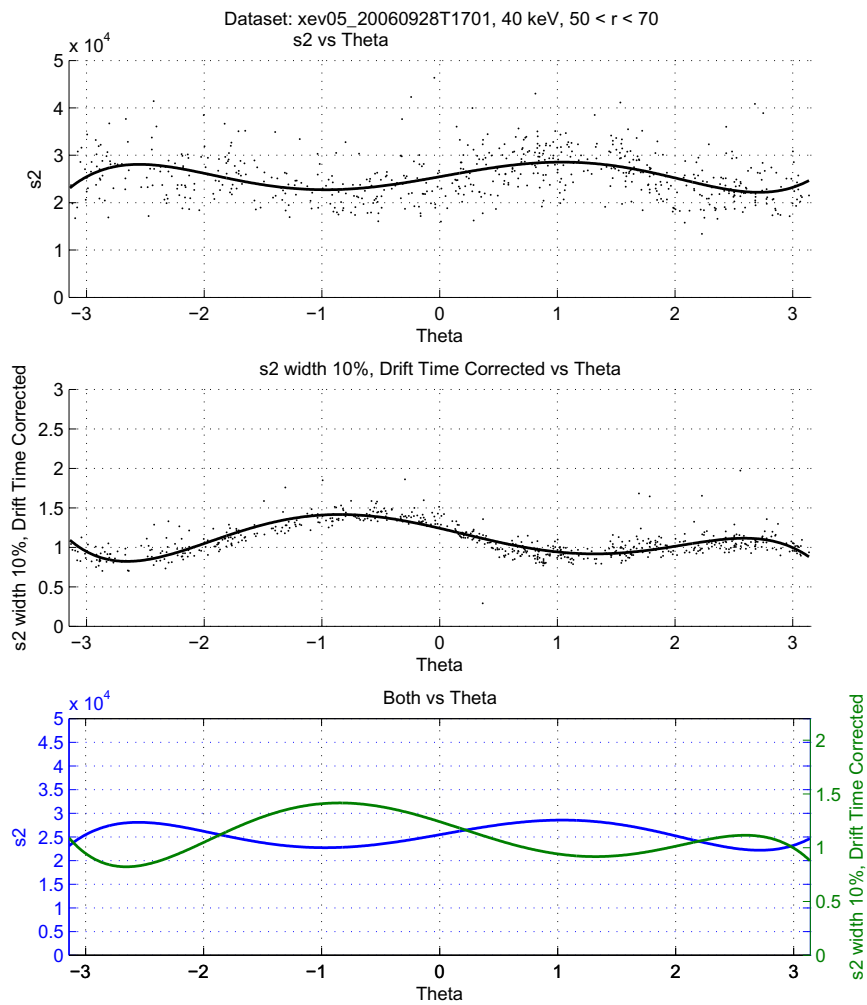
Figure 6.36: Scatter plot of $S2$ and S2 width at 10% versus data of 40 keV gammas between radius of 50 and 70 mm, showing the anti-correlation between the two variables.
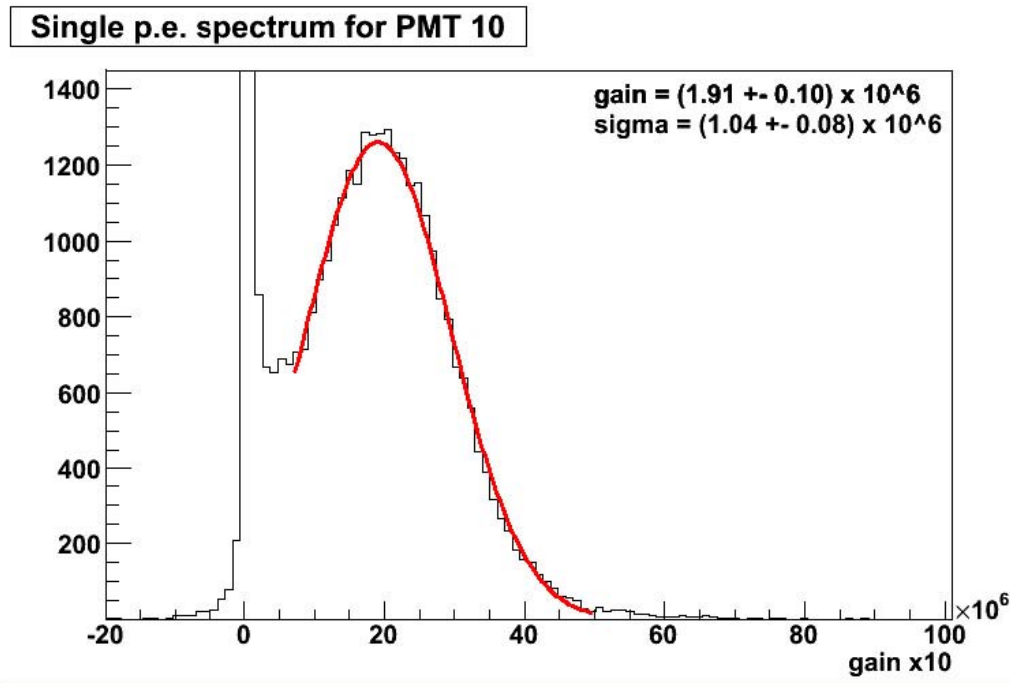
Figure 6.37: The single photoelectron spectrum of a PMT in XENON10. The sharp red peak is the noise and the blue broad distribution is the single photoelectron distribution.

gammas gives a volume averaged light yield of $L_y = 3.0 \pm 0.1_{sys} \pm 0.1_{stat}$ pe/keVee at 0.73 kV/cm after position-dependent corrections. The event energy is scaled linearly from this peak. The electron recoil energy is $E_{ER} = S1/L_y$, where $S1$ is in units of photoelectrons. As described before, the nuclear recoil energy is $E_{NR} = E_{ER}/L_y/\mathcal{L}_{eff} \cdot (S_{ER}/S_{NR})$, where $\mathcal{L}_{eff}$ is the scintillation yield of nuclear recoils relative to that of 122 keV gammas at zero electric field and S_{ER} and S_{NR} are the field dependent scintillation yields of electron and nuclear recoils, respectively, relative to their respective zero-field values. For simplicity, we assumed a constant $\mathcal{L}_{eff} = 0.19$. For more details on previous measurements of $\mathcal{L}_{eff}$, see Section 3.4. The $\mathcal{L}_{eff}$ was also extracted from the XENON10 data and is described in [30]. At a drift field of 0.73 kV/cm, $S_{ER} = 0.54$ and $S_{NR} = 0.93$. These values give a nuclear recoil light yield of 1.02 pe/keVr at 0.73 keVr. This value is was more or less field independent as the nuclear recoil light yield does not change much with field.

The measurement of $S2$ of single electrons provided the charge calibration. The origin of these electrons is unknown. Some possibilities include spontaneous emission from the
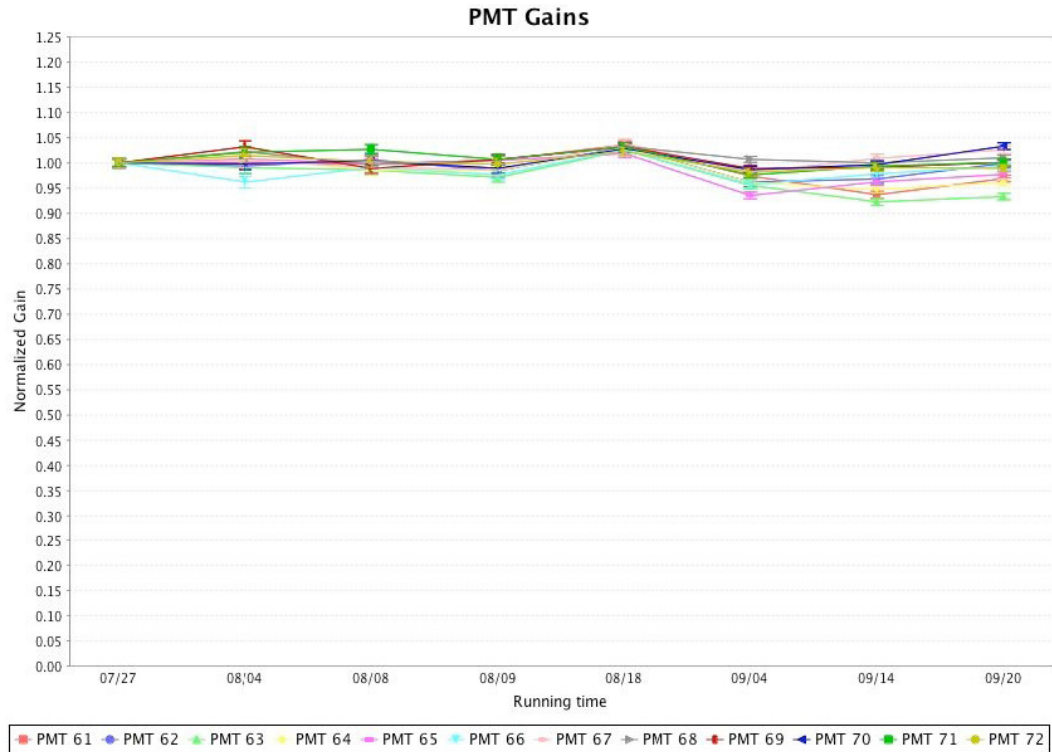
Figure 6.38: This is a figure of the gains of several PMTs as a function of time. The fluctuations are less than 5%. Plot courtesy of A. Ferella [59].

cathode mesh and the delayed drift of electrons due to temporary capture by impurities. Figure 6.40 is a 2D histogram of the single electrons as a function of the $S2$ in the top and bottom PMT arrays. The mean $S2$ light response per electron was 23.7 photoelectrons.

6.6   Signal Corrections

Instrumental fluctuations must be removed to minimize the electron recoil leakage. Here, we discuss two such corrections on the signals to remove these fluctuations. The next section on background discrimination shows how the leakage is reduced by applying these corrections.

6.6.1   PMT Relative Sensitivity Correction

The PMTs were not all uniform in response and the quantum efficiencies of each PMT at cryogenic temperature were not given. The QE values at room temperature were given but
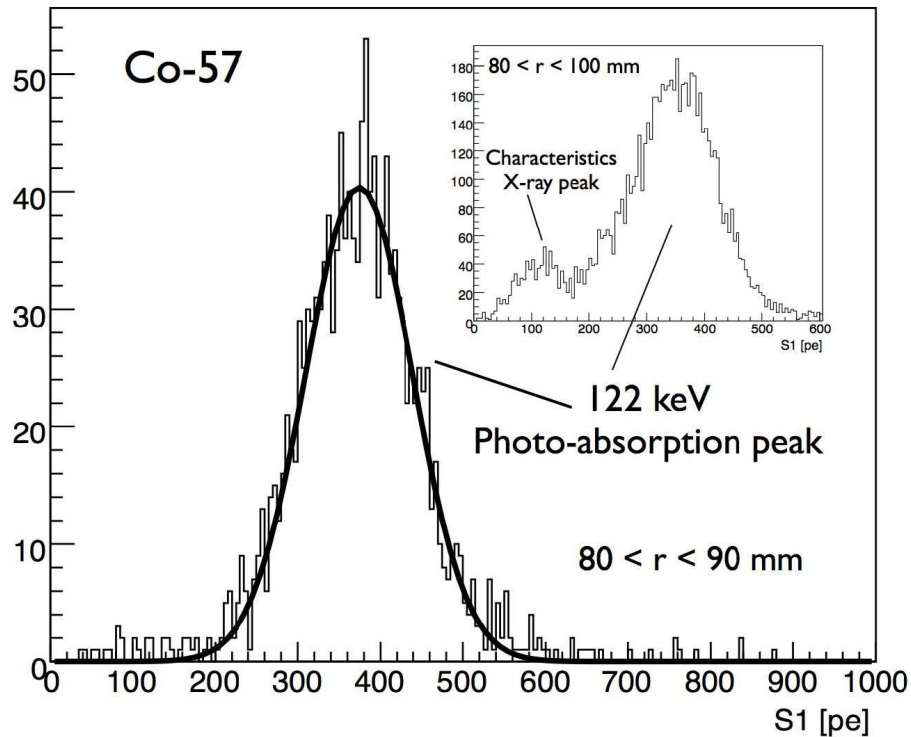
Figure 6.39: The $S1$ spectrum of 122 keV gammas from ^{57}Co in XENON10.

the QE has been observed to change with temperature in other experiments [314]. Note that the PMT gain measurements provide no information on the quantum efficiencies. Although, the absolute quantum efficiencies cannot be determined, we can obtain the relative sensitivities (RS) of the PMTs. This measurement is important for improving the position reconstruction because the reconstruction assumes a uniform response. The RS among the PMTs can be obtained by examining the response of all adjacent pairs of PMTs to the same amount of light. The MATLAB analysis used the primary light of events directly beneath the mean position of two PMTs. The ROOT analysis used proportional light. With the RS of all adjacent pairs, an overall RS map can be created, which can be used to normalize the response of all PMTs. A detailed explanation of the methods and results is explained in another thesis [54].
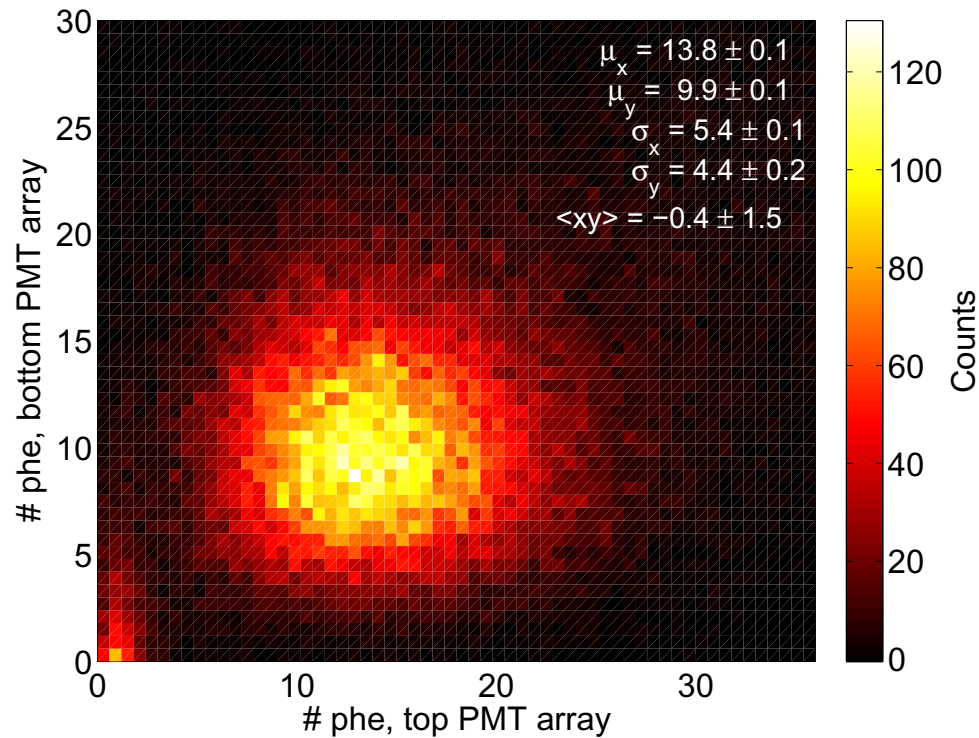
Figure 6.40: The 2D histogram of $S2$ from single electrons as a function of photoelectrons in the bottom array and top array. The average $S2$ per electron is 23.7 photoelectrons. Plot courtesy of C. E. Dahl [60].

6.6.2 Position Correction of Signals

As shown in Section 6.4.3, the light generation and collection varies greatly with position. Unlike the case with the Xed prototypes, the position variation can be completely removed since it has full 3D position reconstruction capability. A different multi-dimensional map is used for position correction when the RS correction is also applied. In this case, the maps are of the RS corrected signal. Figure 6.41(b) shows the histogram of the total $S1$ with and without correcting for position with the 2D map. Figure 6.41(b) displays histograms of the total $S2$ with and without position corrections. The improvements are also apparent in a 2D histogram plot of $S2$ versus $S1$ (Figure 6.42).
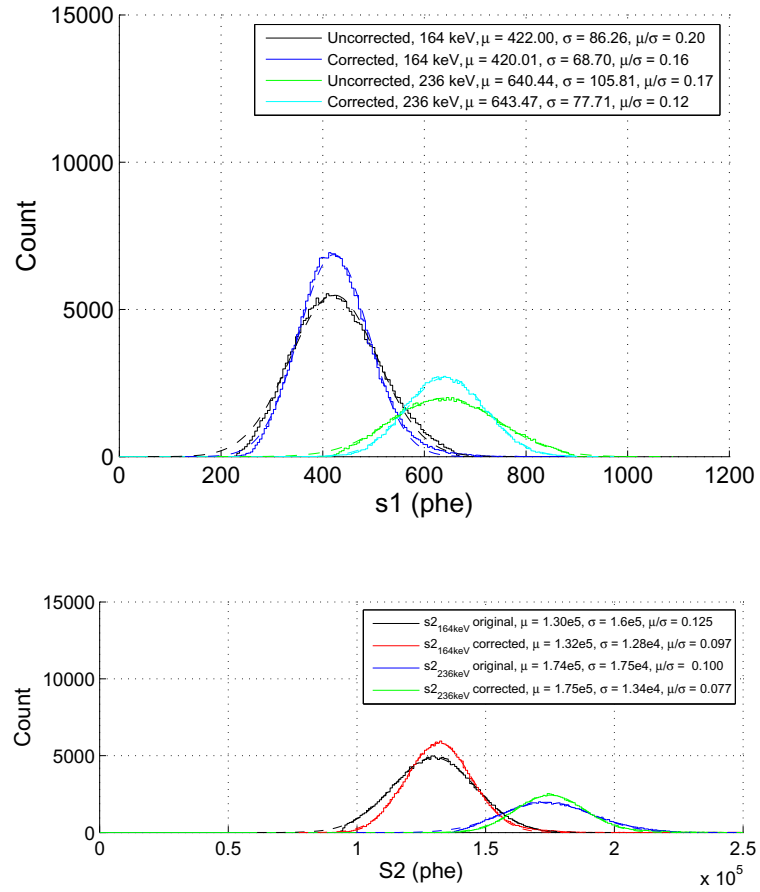
Figure 6.41: Histograms of $S1$ (top) and $S2$ (bottom) of the 164 keV and 236 keV with and without position corrections. The 2D maps used for correction are shown in Figures 6.33(a) and 6.35(c).
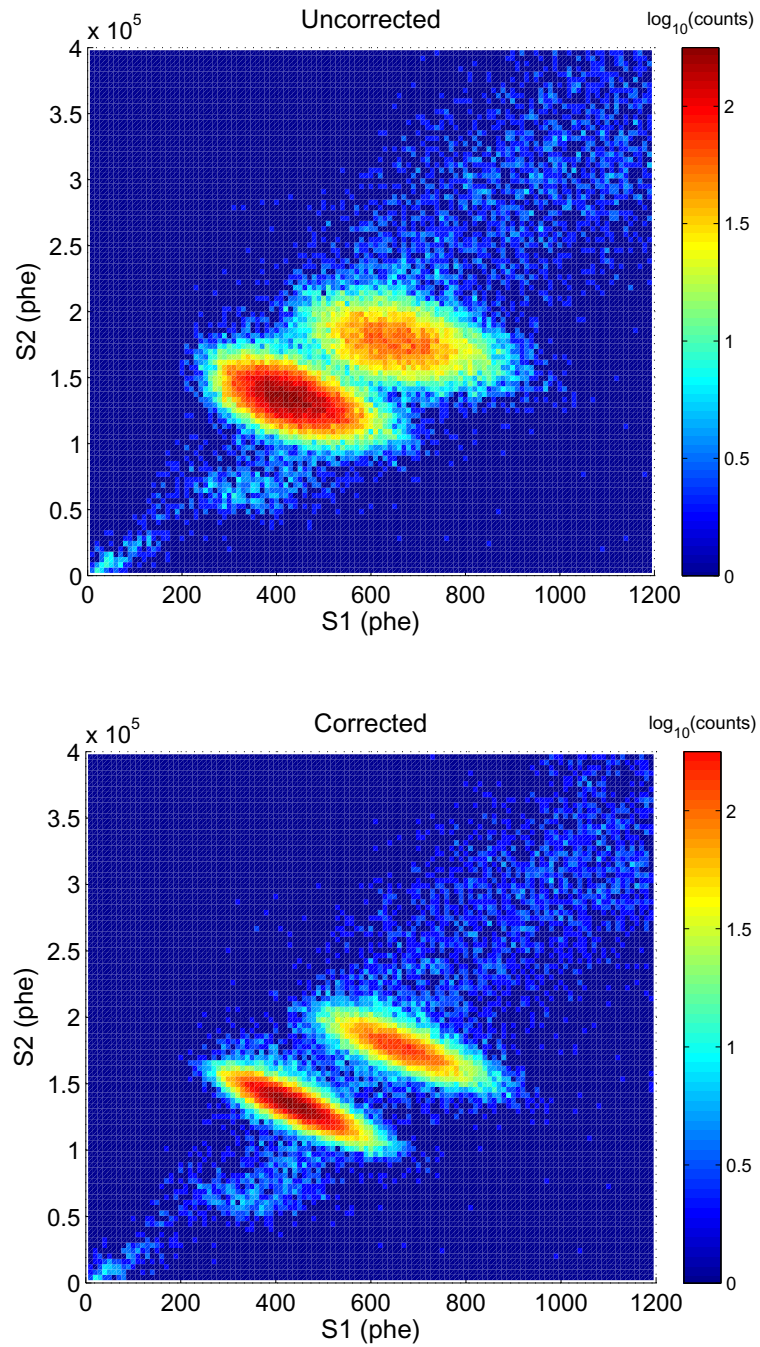
Figure 6.42: Histograms of $S2$ versus $S1$ of original and position corrected arrays from the activated xenon data. The 164 keV and 236 keV peaks are noticeably narrower along both axes.

6.7   Background Discrimination

Between mid-November of 2006 to December 1st, about 90 live days of ^{137}Cs data was taken for background calibration. A high energy veto with an upper energy threshold of $\sim$20 keV was used to save disk space. On December 1st, a data set with an americium-beryllium (AmBe) neutron source was recorded for nuclear recoil calibration. The neutrons are produced by the alphas via ^{9}Be$(\alpha, n)^{12}$C. These external radioactive sources were inserted through a $\sim$1/4" hole so as to not reduce the effectiveness of the Rn purge. There were several sets of WIMP search data. The first blind WIMP search data was taken starting in early October 2006 and ending in mid-February 2007. The WIMP search data was suspended for a short period to take aforementioned ^{137}Cs and AmBe data.

There are two categories of electron leakage events. The first class of events are true single-scatter electron recoils that sit on the lower end tail of the $\log_{10}(S2/S1)$ distribution but are in the nuclear recoil window. As will be shown, such leakage can be lessened by removing the instrumental fluctuations in the signals. The second class of leakage events are anomalous events that have a fraction of their charge signal missing. This section gives measurement of both types of backgrounds in XENON10 and the methods of minimizing them.

6.7.1   Gaussian Leakage

The procedure for determining the electron recoil Gaussian leakage in XENON10 is the same as that performed on data taken with the Case prototype. (See Section 5.2.2 for more details on the analysis procedure.) Briefly, the energy dependence of the $\log_{10}(S2/S1)$ mean of electron and nuclear recoils are characterized by 10th-degree polynomials and then the bands are "flattened" before being fit with Gaussian functions in discrete energy bins.

Different combinations of $S1$ and $S2$ corrections were explored. These corrections are described in Section 6.6. The position corrections were also tested with and without the RS correction. The nuclear recoil acceptance window is between the nuclear recoil mean (μ) and three sigmas below the mean ($\mu - 3\sigma$).

Figures 6.43(a) and 6.43(b) show the electron recoil band sigma and leakage, respectively, versus energy with and without corrections. The leakage value stated in the legend is that expected for the 58.6 live day exposure. For some reason, the position correction of the $S2$ worked better when the 40 keV electron recoil map was used, rather than the map based on the 164 keV gammas. As shown in the Section 6.4.3, the two maps are different although the diagonal feature is present in both.

6.7.2 Non-Gaussian Leakage

Sources of Non-Gaussian Leakage Events

In the ^{137}Cs data, the number of leakage events observed in the nuclear recoil acceptance window is larger than that expected from the tail of the Gaussian distribution. The ^{137}Cs data has 2273 events between 4.5 and 26.9 keVr (the WIMP energy window) after application of the first two sets of quality cuts (QC0 and QC1, as described in Section 6.3.3). In the tail of 0.5% Gaussian leakage, 23 events are observed corresponding to a leakage of ~1%. These anomalous events may be misconstructed events. As previously, mentioned, an electron recoil event can appear as a nuclear recoil event if some of its charge is lost. The events that lose charge due to interactions with the edges of the detector can be removed as their position is known. Events that scatter at least once in the active volume and at least once in a region where the primary light can be collected but not the ionization (Figure 6.44). Unfortunately, such events cannot be omitted by a simple fiducial volume cut. Most of these events (which we call "gamma-x") are those that have a vertex in the region between the cathode mesh and bottom PMT array (reverse-field region) where the electric field drifts the electrons downward. Some of these events may also be gammas that scatter once in the pocket of liquid xenon of the high voltage divider of the field shaping ring (see Figure).

QC2 Cuts

Cuts were developed to these anomalous events without severely lowering the acceptance for WIMPs. To accomplish this, the cuts were applied not only on the events of the ^{137}Cs
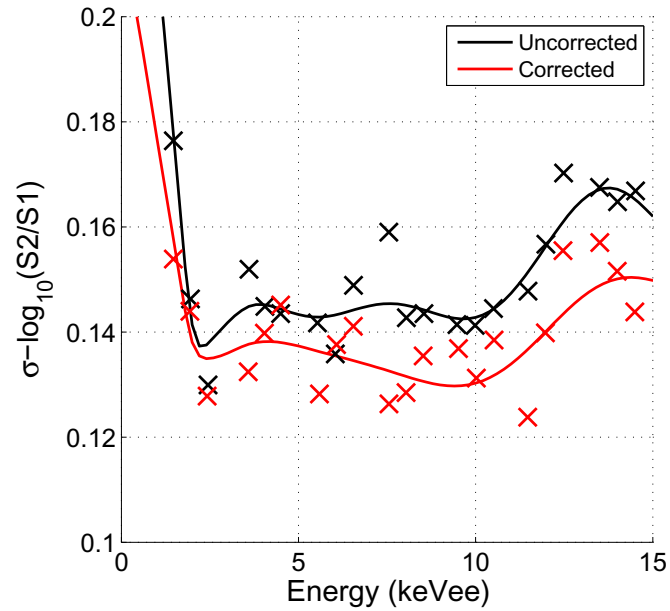
(a)
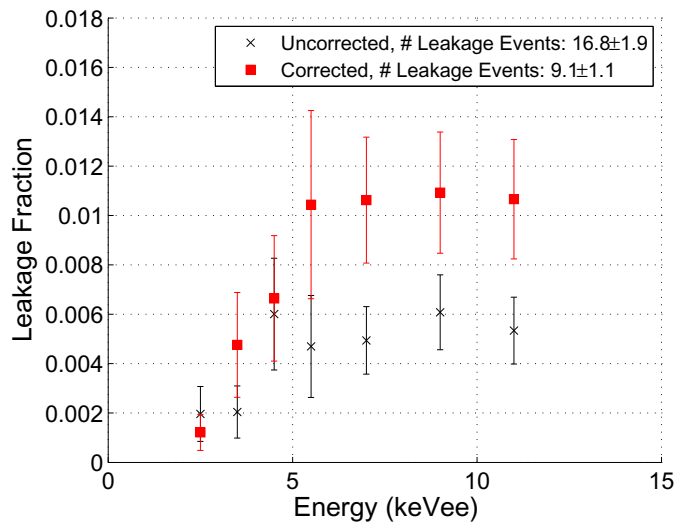
(b)

Figure 6.43: Top – The Gaussian width of $\log_{10}(S2/S1)$ versus energy of the ^{137}Cs data with and without corrections. Bottom – The electron recoil leakage fraction in the 50% acceptance nuclear recoil window as a function of energy, with and without corrections to the instrumental fluctuations as described in the text. The position dependence of $S1$ was removed with the 164 keV 2D $t_{drift} - r$ map. For $S2$, the position dependence was removed with the 40 keV $x - y$ map. The PMT relative sensitivity correction was also applied on the $S2$.
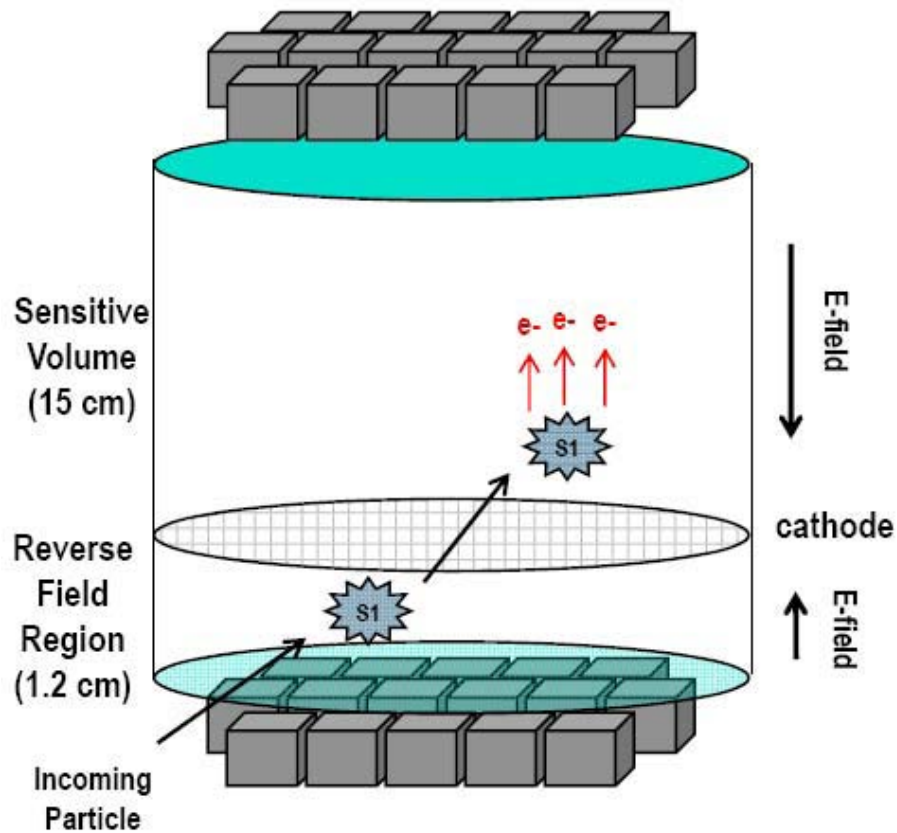
Figure 6.44: Diagram of a "gamma-x" event. Such an event scatters at least once in the region where charge cannot be collected (such as the space between the cathode mesh and bottom PMT array) and at least once in the fiducial volume. A portion of the charge does not participate in the generation of proportional light and thus the event has a lower $\log_{10}(S2/S1)$ than expected.

events but also on the nuclear recoil events of the AmBe dataset (with the nuclear recoils selected by a $\mu \pm 3\sigma$ cut in $\log_{10}(S2/S1)$). For both data sets, only events in the tail of 0.1% Gaussian leakage were examined.

Reverse-field region event cut (gamma-x cut)   Background simulations of gammas from PMT and other internal sources give a gamma-x event rate of ≤ 1 mdru [308]. The expected number of observed gamma-x events is 10^{-3}dru$\times$10keVee$\times$5.3kg$\times$59 days $= 3$ events. Fortunately, some of these events can be removed by examining the hit pattern on the bottom PMT array. Primary light emitted from the region between the cathode

Resistor Chain Pocket – filled with LXe
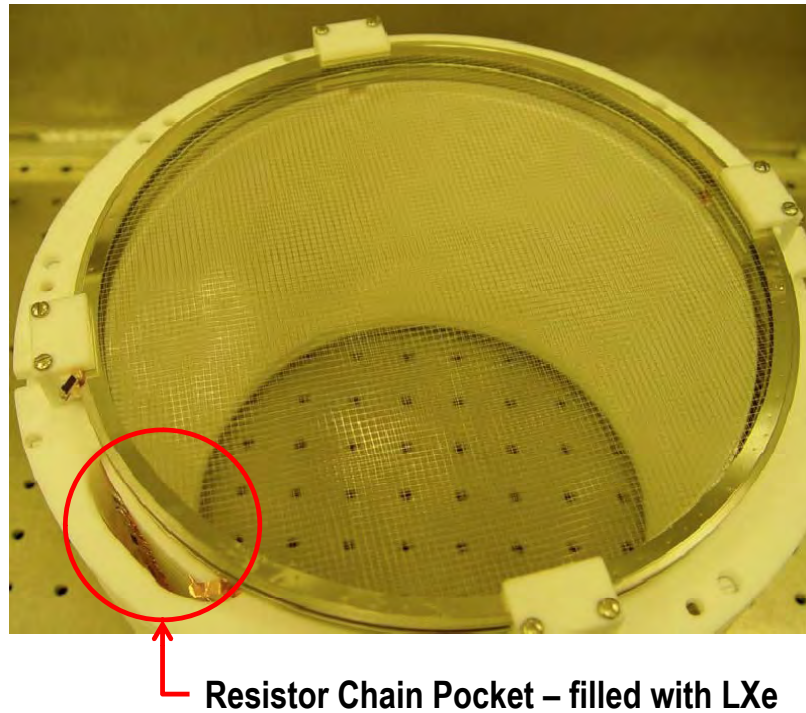
Figure 6.45: The gap in the PTFE spacer for the high voltage resistor chain which is filled with liquid xenon. Multiple scatter events with one vertex in this region can be interpreted as a nuclear recoil event as the charge here is not collected. Photo courtesy of L. De Viveiros.

and bottom PMT array is likely to be concentrated on a few nearby PMTs unlike that emitted from the active volume. Such events can be removed by cutting in a parameter which measures the localization of primary light on the bottom array. Several such parameterizations were explored. Some simpler parameters were $std(ss1_{bottom})/S1_{bottom}$ and $max(ss1_{bottom})/S1_{bottom}$, where $std(ss1_{bottom})$ is the standard deviation of $ss1_i$ of the bottom PMT array. $max(ss1_{bottom})$ is the size of the largest $ss1_i$ of the bottom PMT array. Both parameters increase with greater localization of light. Figure 6.46 is a scatter plot of $max(ss1_{bottom})/S1_{bottom}$ for the ^{137}Cs and AmBe data. This plot shows that some of the leakage events (indicated by green dots) of higher values of this parameter can be eliminated with a cut (blue line) without severely reducing the nuclear recoil acceptance. These simpler cuts were not implemented in the secondary (MATLAB) blind analysis. To remove gamma-x events, the ROOT analysis group used $std(ss1_{bottom})/S1_{bottom}$ which was also
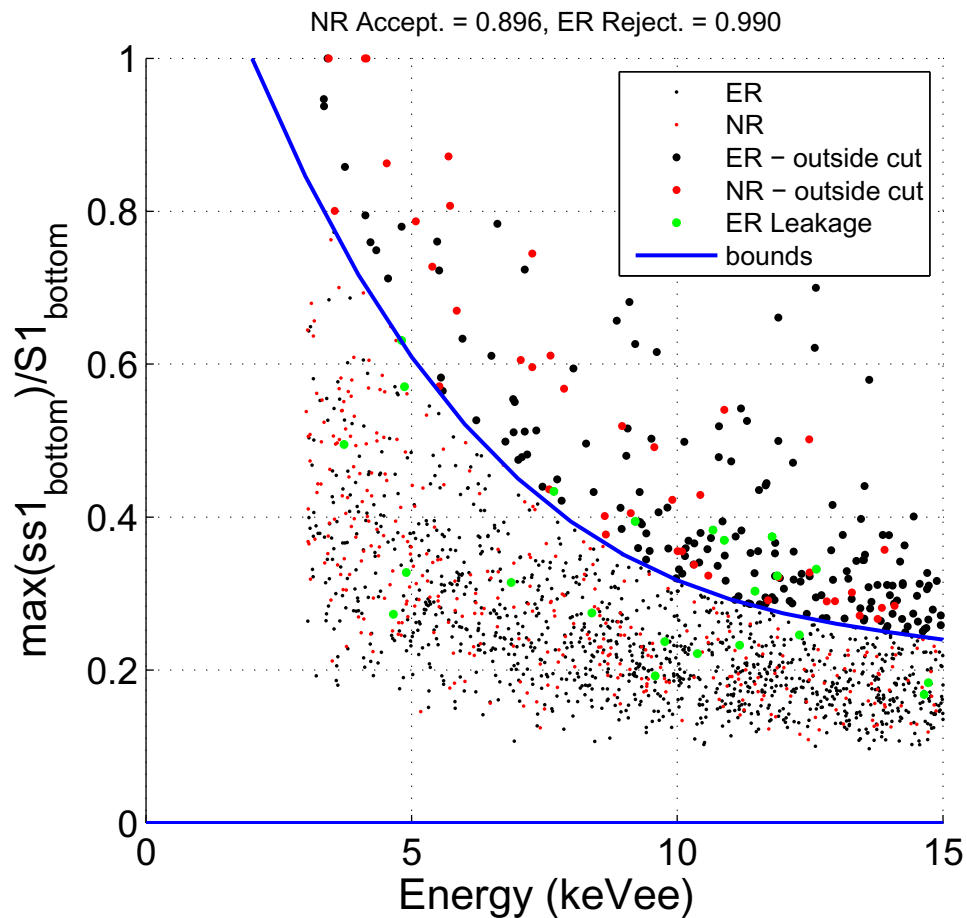
Figure 6.46: Scatter plot of $max(ss1_{bottom})/S1_{bottom}$ of the ^{137}Cs (black) and AmBe (red) events (only those in the WIMP window) as a function of energy. The electron recoil leakage events of the ^{137}Cs dataset are indicated by green dots. The events outside the bounds of this cut (blue line) are indicated by larger dots.

implemented in the blind analysis.

A more sophisticated and efficient set of cuts for removing gamma-x events was developed by Peter Sorenseon of the MATLAB analysis group. Only a brief description is given here (more details can be found in [54]). The parameters is $G_n = \sum_i ss1_i/S1_{bottom} \cdot \sqrt{S1}$ where the sum is over the n bottom array PMTs that receive the most light. The $\sqrt{S1}$ is present to reduce the energy dependence of the parameter. For $n = 1$, the parameter is more or less the same as the parameter described in the previous paragraph. For $n \geq 2$, the standard deviation of the x and y coordinates of the n PMTs must also fall within some
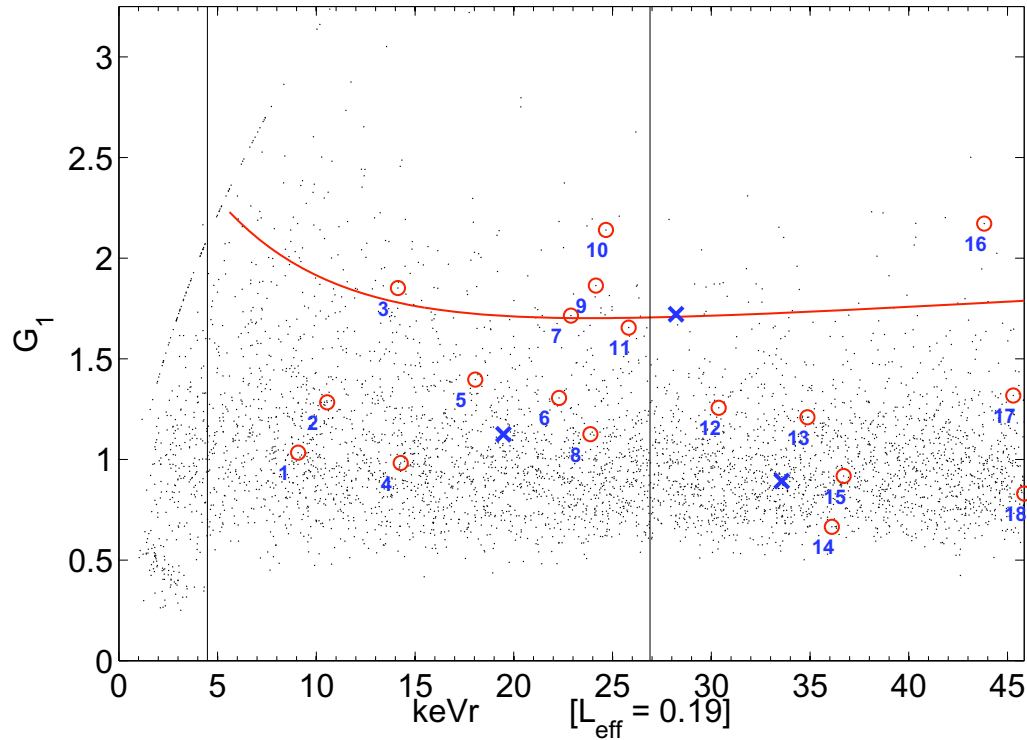
Figure 6.47: Plot of G_1 (as defined in the text) as a function of energy of the ^{137}Cs data. The red line indicates the upper bound for 95% acceptance as determined with a Monte Carlo. The leakage events in the 0.1% tail of Gaussian leakage are indicated by the red circles, four of which are excluded by this cut. The blue x's indicate extremely non-Gaussian events that lie beyond the $\mu - 3\sigma$ lower bound of the WIMP acceptance window. The arc of events on the upper left are events with all of the S1 light concentrated on one PMT. Plot courtesy of P. Sorensen [54].

upper limit. Cuts for n = 1, 2, 3 and 4 were calibrated with the help of a Monte Carlo. Figure 6.47 shows G_1 as a function of energy of the ^{137}Cs data. Figure 6.48 shows the G_2 as a function of energy and the standard deviations of the PMT coordinates.

Partial Gamma-X Cut   There exists a region within about 1 cm from the cathode where only a small portion of the ionization can escape. Multiple scatters with a vertex in this region will yield a small S2 pulse trailing the S1 by the maximum drift time. This secondary S2 may be < 5% the size of the primary S2 and consequently be ignored by the multiple S2 cut described earlier. The partial gamma-x cut removes such events.
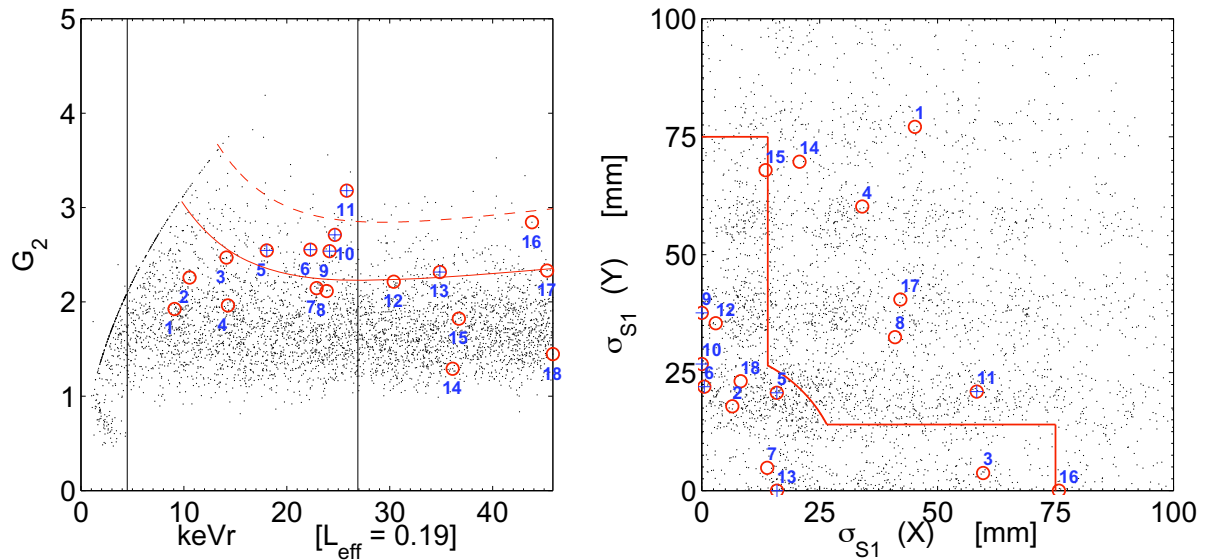
Figure 6.48: Right: Plot of G_2 (as defined in the text) of the ^{137}Cs data as a function of energy. Left: Plot of localization quantities. Events with G_2 above the dashed red line are always cut, while those above the solid line are cut only if $(\sigma_{S1}x)^2 + (\sigma_{S1}y)^2 < (30\text{mm})^2$, $(\sigma_{S1}x) < 14$ mm or $(\sigma_{S1}y) < 14$ mm as indicated by the red line of the left plot. The non-Gaussian events are indicated by red circles and those removed by this cut are marked with blue crosses. Plot courtesy of P. Sorensen [54].

$S1$ **edge-to-all ratio cut**   This cut removes events that may have scattered at the edges of the detector and thus may have lost some charge. The parameter is the sum of the S1 signal in PMTs on the outer edge of the bottom array divided by the total $S1$. The efficiency of this cut was determined with the same Monte Carlo as that used for the reverse-field region event cut. Figure 6.49 shows the hit-pattern of an event with a large fraction of light on the outer ring of PMTs.

S1 top fraction cut   The actual data and Monte Carlo photon propagation simulations show that most of the light should fall on the bottom PMT array. Large deviations would indicate something severely incorrect with the event. One anomaly that may result in a larger than expected proportion of the primary light falling on the top array is a scattering in the gas. Such occurrences are expected to be rare as the mass of the gas is much less than that of the liquid. Figure 6.50 shows the fraction of the $S1$ on the top PMT as a function
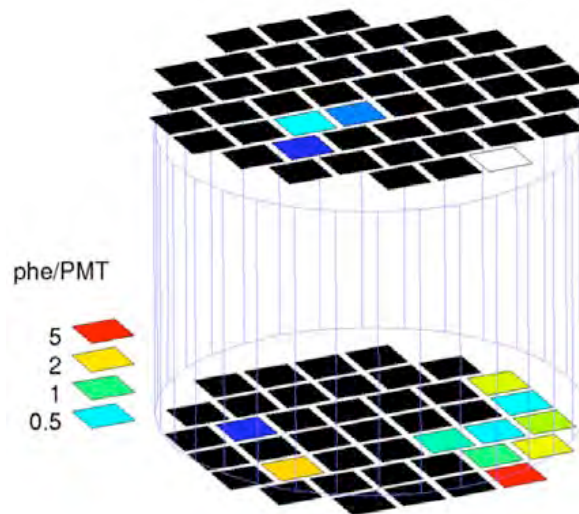
Figure 6.49: PMT hit pattern of an event with a large portion of the primary light concentrated at the edge indicating that they may have scattered at the edge of the detector and thus may have suffered charge loss. Such events are remove with the $S1$ edge-to-all ratio cut. Plot courtesy of P. Sorensen [54].

of energy of the ^{137}Cs dataset with the boundaries of 99% cut efficiency. The previously described Monte Carlo was used to help define the bounds.

Pulse Area Fraction   This cut parameter is $(S1+S2)/A$ where A is the total integral of the trace. Ideally most of the light should be from the primary and proportional scintillation signals. Events with values much lower than 1 may have problems with noise or may include light from abnormal sources. Some extraneously sources of light are proportional scintillation from electrons spontaneously emitted from the cathode and those photoionized by the proportional scintillation. Figure 6.51 shows this parameter plotted as a function of energy.

S1 width at 10% maximum amplitude   This cut removes events with an S1 width at 10% maximum amplitude of > 150 μs. This cut was motivated by the observation of 10 low $\log_{10}(S2/S1)$ with S1 width $> 200\mu$s. Assuming that the S1 decay probabilty distribution follows a simple exponential of fall time $\tau = 25$ ns, the probability of at least
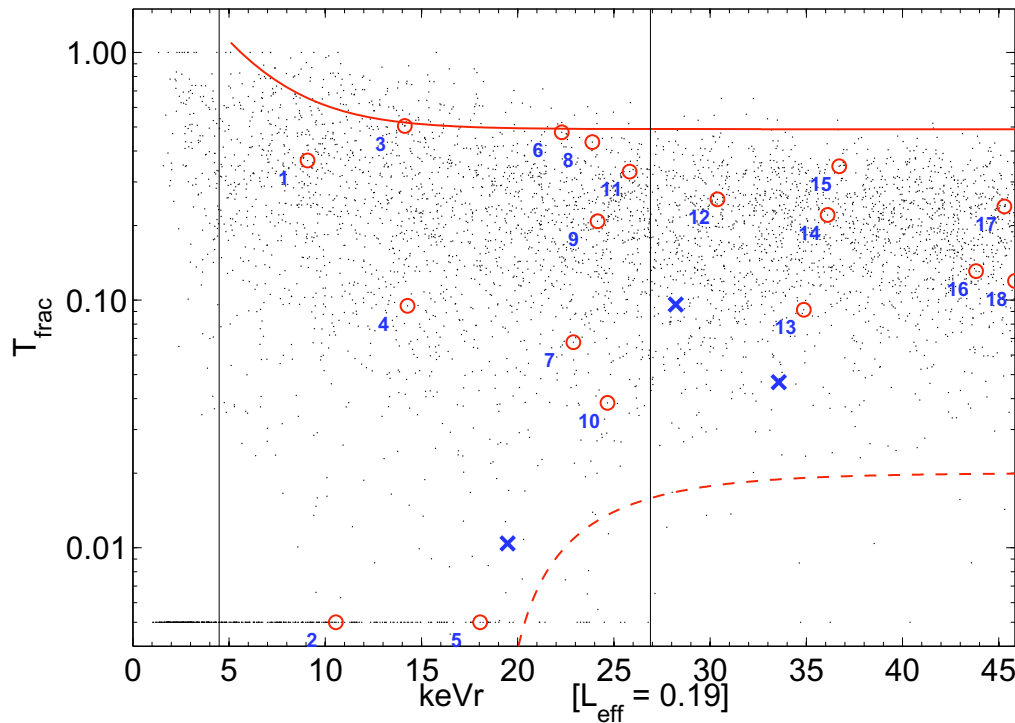
Figure 6.50: Plot of the fraction of proportional light signal in the top PMT array of the ^{137}Cs as a function of energy. The dashed lines indicate the bounds of the cut. The events of the 1% leakage tail are indicated by the red circles. The leakage events that lie beyond the $\mu - 3\sigma$ lower boundary of the WIMP acceptance window are indicated by the blue x's. The vertical lines indicate the lower and upper energy bounds. Plot courtesy of P. Sorensen [54].

one photoelectron occuring > 200 ns after the start of the pulse of N photoelectrons is

$$\sum_i^N (1 - \exp(200/25))^{N-i} (\exp(200/25))^i \approx \exp(200/25) = 3.4 \times 10^{-4}. \text{ About ten times more}$$

events with an S1 width $> 200 \mu$s was observed than expected and the cause is unknown.

Nuclear recoil Acceptance of QC2 cuts

The QC2 cuts were applied to the nuclear recoils events of the AmBe data to determine their affect on WIMP acceptance relative to the QC0 and QC1 cuts. To exclude electron recoil events, a $\mu \pm 3\sigma$ cut was applied around the nuclear recoil band. The reverse-field-region and edge-to-all cuts are responsible for most of the reduction in acceptance. Figure 6.52 is a plot of the nuclear recoil acceptance of the MATLAB QC2 cuts as a function of
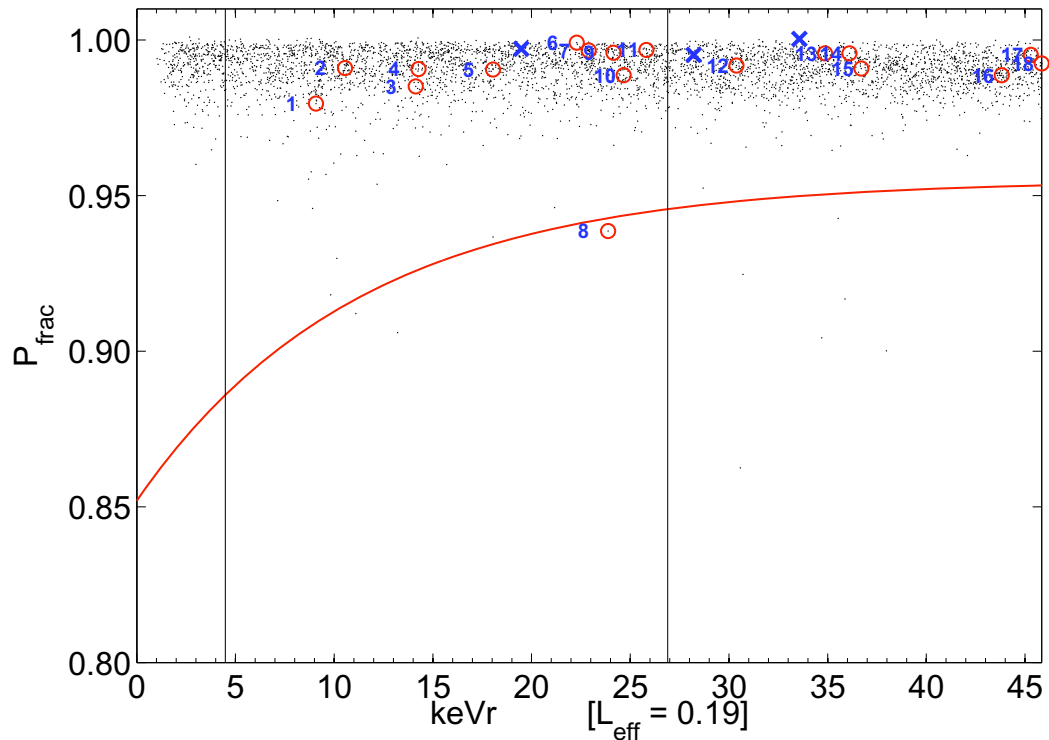
Figure 6.51: Plot of the pulse area fraction parameter versus energy of the ^{137}Cs data. The red line indicates the lower bound. The excluded event has a large amount of after-pulsing following the S2. Plot courtesy of P. Sorensen [54].

energy.

6.8   Dark Matter Limit

A blind analysis is important because it removes any opportunity for biasing the results. The blind portion of the WIMP search was locked away until all the cuts were defined. To check the quality of the WIMP search data without spoiling the analysis process, only sections of energy beyond the dark matter energy range were examined. By studying the ^{137}Cs and the unblind portion ($\sim$16 live days) of the WIMP search data, the cuts were fine tuned. Also set before the unblinding was the energy range (4.5–26.9 keVr), energy binning and the WIMP acceptance window ($\mu - 3\sigma$). Before unblinding, the ROOT analysis was deemed by vote to be the primary analysis whose results would be shown in publication.
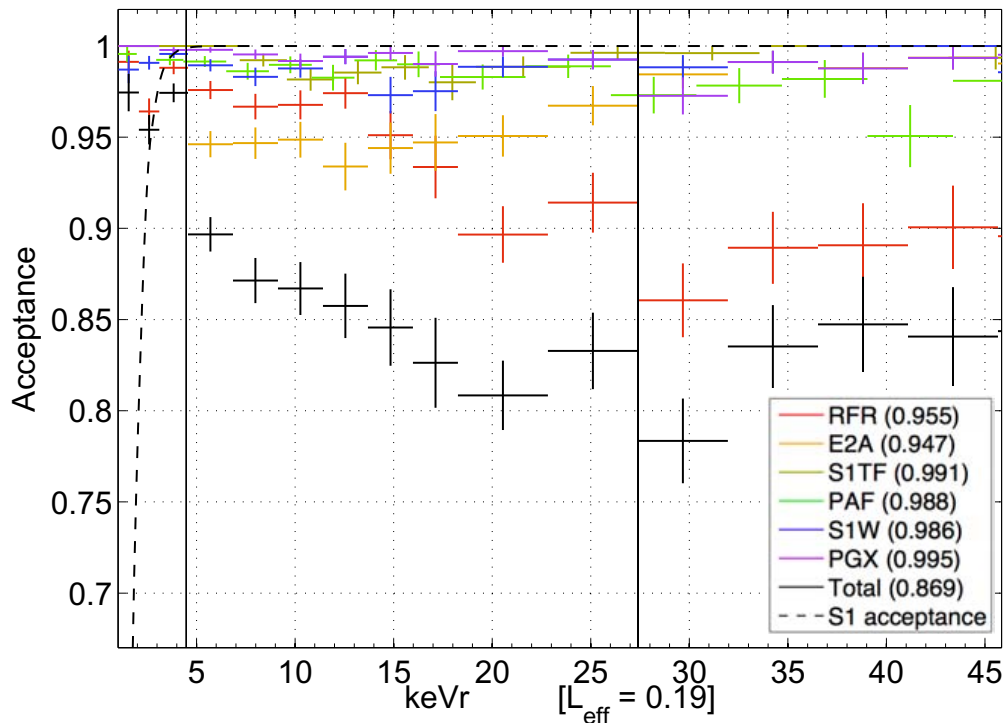
Figure 6.52: Nuclear recoil acceptance of QC2 cuts as a function of energy. The vertical lines indicate the 4.5 and 26.9 keVr energy bounds. The dashed line is the S1 acceptance. RFR – reverse field region (gamma-x cut). E2A – edge-to-tall area. S1TF – S1 top fraction. PAF – pulse area fraction. S1W – S1 width. PGX – partial gamma-x. Plot courtesy of P. Sorensen [54].

In this section, we discuss the results of the ROOT and MATLAB blind analysis of the 58.6 live days of WIMP search data.

6.8.1 WIMP Candidate Events of ROOT Analysis

The ROOT blind analysis revealed 10 candidate events in the WIMP window out of a total of 1815 events between 4.5 and 26.9 keVr after applying all cuts (QC2 cuts are described in [13]). Figure 6.53 is a plot of $\Delta \log_{10}(S2/S1)$ ($\log_{10}(S2/S1)$ centered on the electron recoil band centroid) as a function of energy of the WIMP search data. All leakage events can be explained as electron recoil background or as anomalous events. Five of the events (3, 4, 5, 7, and 9), which sit just underneath the upper bounds of the window, are consistent
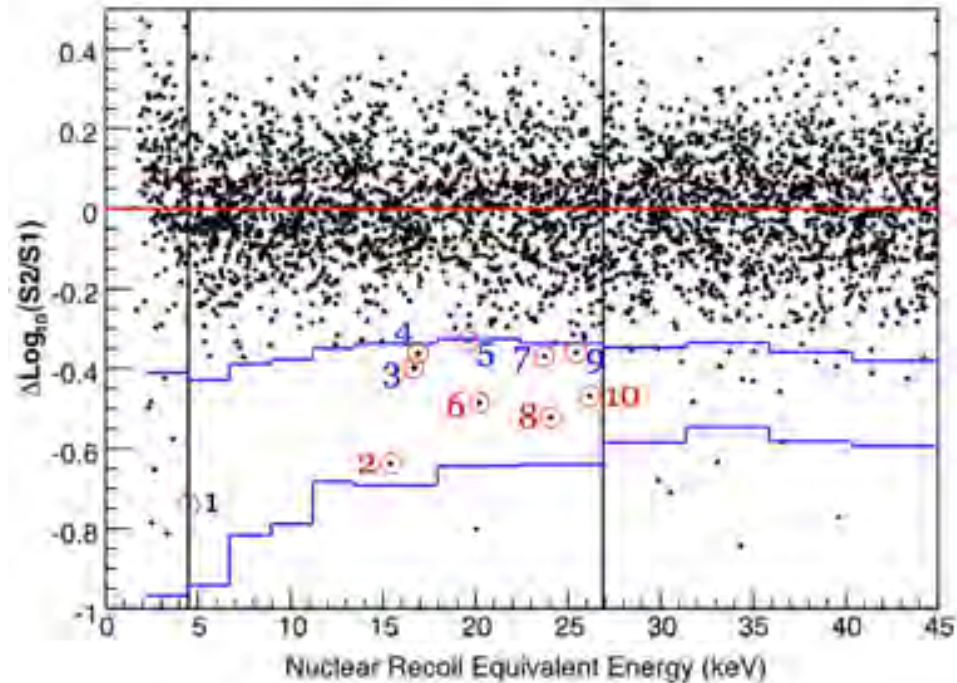
Figure 6.53: Plot of $\Delta \log_{10}(S2/S1)$ versus energy of 58.6 live days of WIMP search data in the ROOT analysis. $\Delta \log_{10}(S2/S1)$ is $\log_{10}(S2/S1)$ centered on the electron recoil mean. The WIMP acceptance window is defined by the two blue lines. The events with red circles are the leakage events. The ones which are labeled blue (near the top blue line) are those which are consistent with the Gaussian tail. The two vertical lines represent the 4.5 and 26.9 keVr energy bounds.

with statistical leakage of which $\sim$7 events were expected (see Figure 6.53). Events 2, 6, 8 and 10 are likely to be background events as they occur at the bottom of the fiducial volume (as seen in Figure 6.54) where a greater incidence of gamma-x events was expected. Furthermore, the energies of these events do not conform to that expected from the falling exponential recoil spectrum (Equation 2.24). The MATLAB analysis, with its more robust gamma-x cut (see Section 6.7.2) omitted events 6, 8, and 10. Event 1 was accepted because a noise glitch helped fulfill the S1 coincidence requirement.

6.8.2   WIMP Candidate Events of MATLAB Analysis

Only a brief summary of the blind MATLAB analysis will be given here; a complete account can be found in [54]. Figure 6.55 is a plot of $\Delta \log_{10}(S2/S1)$ versus energy of the WIMP
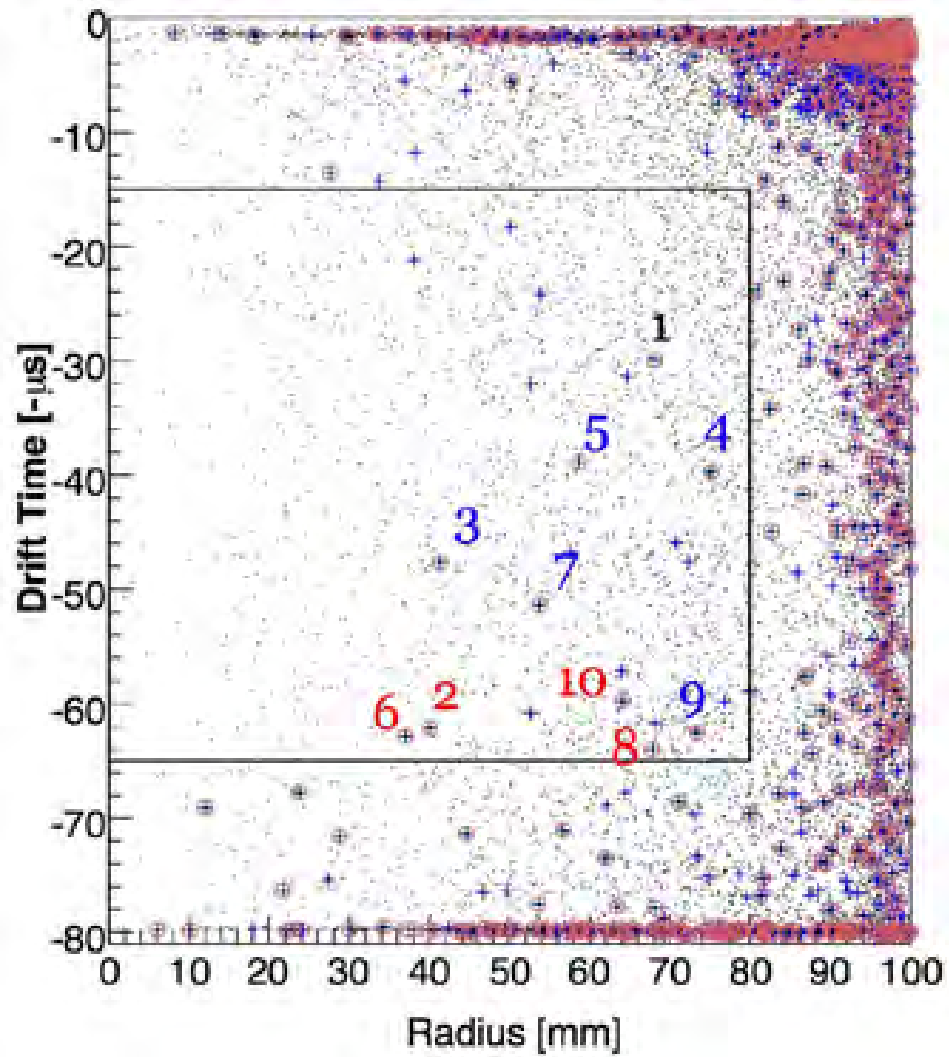
Figure 6.54: Position of events in the 4.5–26.9 keV nuclear recoil energy window in the ROOT analysis. The small dots, +'s and circles represent all events, events before application of QC2, and events after application of QC2, respectively.
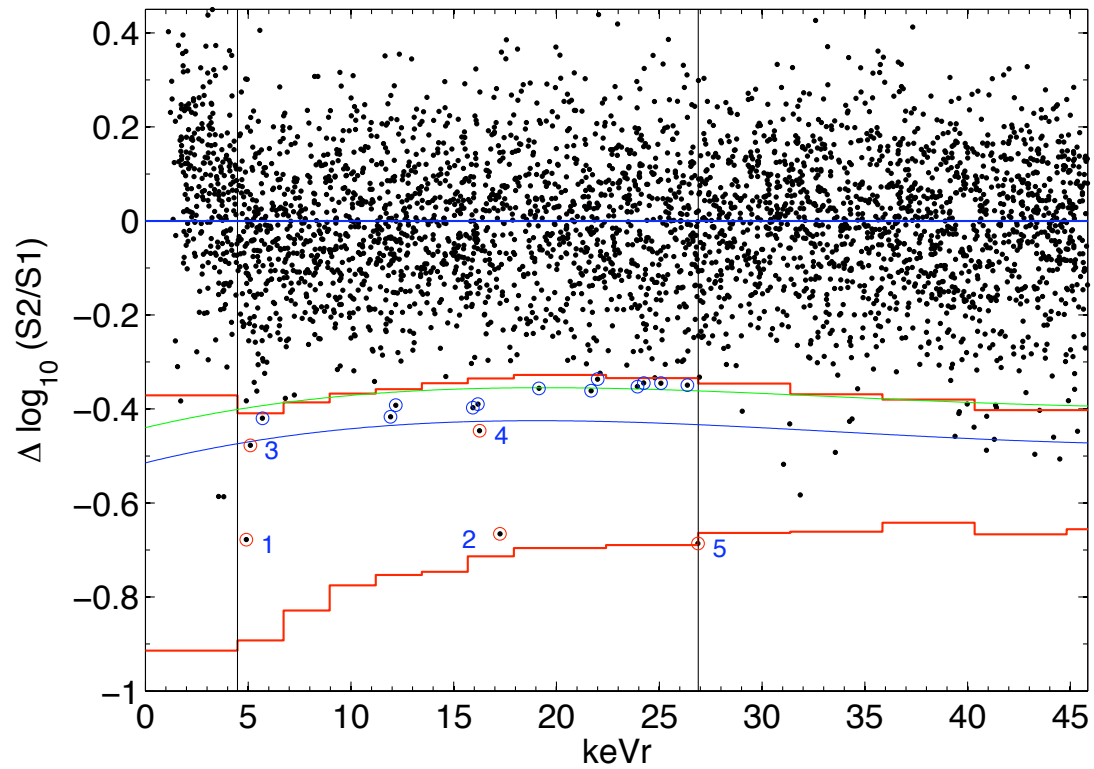
Figure 6.55: Plot of $\Delta \log_{10}(S2/S1)$ versus energy of 58.6 live days of WIMP search data in the MATLAB analysis. $\Delta \log_{10}(S2/S1)$ is $\log_{10}(S2/S1)$ centered on the electron recoil band. The WIMP acceptance window is defined by the two red lines. The green and blue lines indicate the 99.5% and 99.9% contours, respectively. The events with blue circles are those consistent with the Gaussian tail. Events 3 and 4 are may also be consistent with Gaussian leakage as they sit near the 99.9% contour. Events 1, 2 and 5 are very unlikely to be members of the tail. The two vertical lines represent the 4.5 and 26.9 keVr energy bounds.
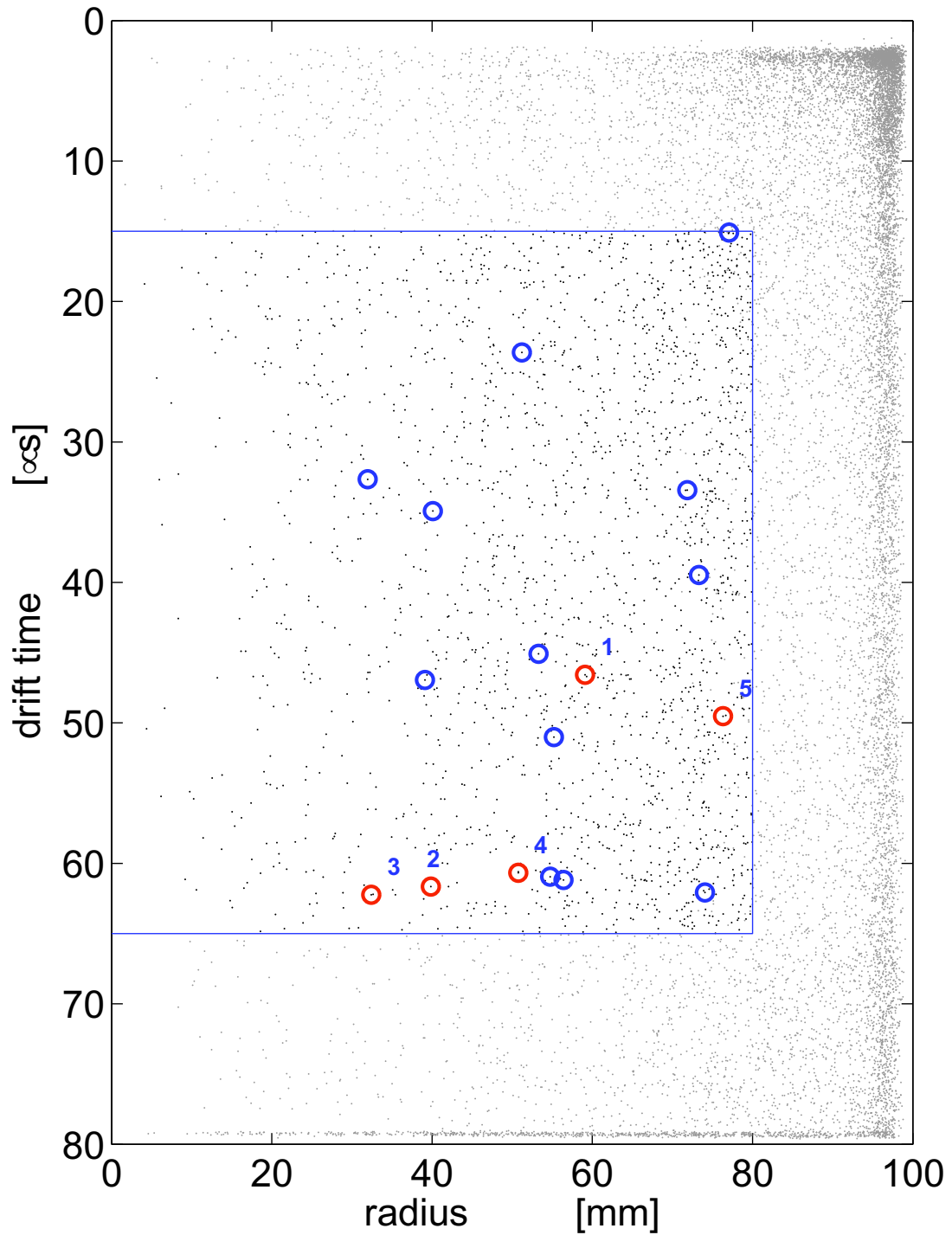
Figure 6.56: Position of events in the 4.5–26.9 keV nuclear recoil energy window from the MATLAB analysis. The blue circles indicate the WIMP candidates (also circled blue in Figure 6.55). The events with red circles are those below the 99.9% contour and are unlikely to be members of the Gaussian tail. The blue lines represent the boundaries of the fiducial volume.

search data after the application of all cuts. After applying the cuts, 1716 events remain between 4.5 and 26.9 keVr, 17 of which are in the nuclear recoil window. Twelve of the events which are near the 99.5% contour are consistent with that expected from Gaussian leakage. Events 3 and 4 may be consistent with the Gaussian tail as they are near the 99.9% contour. Events 1, 2, and 5 are highly unlikely to be members of the tail. Events 1, 2, and 4 are events that the reverse-field-region cut would have removed if the cut had slightly tighter bounds (and consequently a slightly lower nuclear recoil acceptance). Event 1 was removed in the ROOT analysis by a S1 hit pattern cut in QC2. Event 2 is also present as a WIMP candidate in the ROOT analysis (also as event #2) and, as previously stated, likely to be a reverse-field-region event as its reconstructed position is near the bottom of the fiducial volume. Event 4 was cut by QC2 of the ROOT analysis. Event 3 was removed by the QC0 of the ROOT analysis. In this event, the S1 occurred just before the S2 and, as a result, the two pulses was interpreted as a single pulse. The fake S1 pulse was an large pickup of coherent noise that should have been spotted as it consisted of 5 photoelectrons spread out among 18 PMTs, which is roughly 0.3 pe/PMT – the chances of an actual S1 giving such a pattern is small. Event 5 was admitted because its position ($r = 78$ mm) was reconstructed incorrectly due to its location near the dead PMT. The neural network algorithm of the ROOT analysis placed this event at > 85 mm, well outside the fiducial volume. There are more Gaussian leakage events in the MATLAB analysis because a position correction for the $S2$ was not included before the unblinding. This occurred because of the discrepancy between the 40 keV and 164 keV maps which lead to an uncertainty as to which would work best and, in the end, we decided to not use a correction and devote our efforts towards the removal of anamolous events. The expected number of leakage events with and without the $S2$ correction are $7.4^{+1.8}_{-1.5}$ and $12.1^{+1.9}_{-1.6}$, respectively [54]. After correcting the $S2$, only 6 Gaussain leakage events remained which is consistent with expectations.
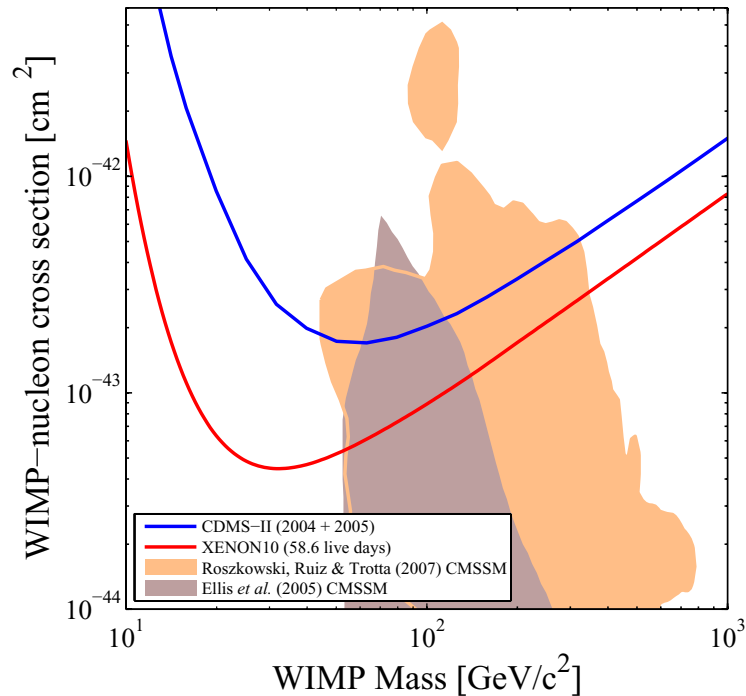
Figure 6.57: The 90% confidence level upper limit spin-independent WIMP-nucleon cross section as a function of WIMP mass as determined by the 58.6 live day WIMP search data of XENON10. This result exceeded the previous best limit.

6.8.3 Calculation of WIMP cross section upper limit

As explained in the previous section, all 10 leakage events of the ROOT analysis could be explained without invoking the existence of WIMPs but to be conservative in the calculation of the cross section upper limit, we assumed all those events to be WIMP scatters. The upper limit was calculated using the "maximum-gap" method [315] with standard assumptions on the galactic halo (see Section 2.3.1 or [170]). The statistical methods of Feldman and Cousins were not used as the background was not measured well enough for a statistically meaningful subtraction. The maximum gap method is useful for small signal experiments containing an unknown background. It provides a way of including energy regions that are likely to be least affected by the background. Here, we give a brief explanation on the application of this method. Let the energy of the i-th leakage event be E_i ordered from lowest to highest energy. The i-th gap is defined as the expected number of events of the

energy gap $E_i - E_{i+1}$:

$$x_i = \int_{E_{i+1}}^{E_{i+1}} \frac{dN}{dE} dE, \tag{6.5}$$

where $\frac{dN}{dE}$ is the recoil count spectrum scaled by a particular cross section, σ. The maximum gap, x, is the largest x_i. A particular σ is rejected if it gives a maximum gap that is highly unlikely. In this paper, Yellin derives the probability of a maximum gap being smaller than an observed x for a total expected number of events μ as

$$C_0(x, \mu) = \sum_{k=0}^{m} \frac{(kx - \mu)^k e^{-kx}}{k!} \left(1 + \frac{k}{\mu - kx}\right) \tag{6.6}$$

where m is the greatest integer $\leq \mu/k$. The 90% confidence upper limit for an observed x is the μ (σ) that gives $C_0 = 0.9$. For the XENON10, WIMP search data, the energy bounds of the maximum-gap is 4.5 and 15.5 keVr, of events 1 and 2, respectively (as seen in Figure 6.53). Recall that WIMP-nucleon coupling is characterized by two terms: spin-independent (scalar) and spin-dependent (axial vector) (see Section 2.3.1). Figure 6.57 shows the spin-independent WIMP-nucleon cross section limit as a function of WIMP mass. Also shown is the CDMS result of 2005 which was the previous best at the time [316]. CDMS has since exceeded the results of XENON10 [14].

Figure 6.58 shows the WIMP-nucleon cross section upper limits for pure-neutron ($a_p = 0$) and pure-proton ($a_n = 0$) couplings. Both ^{129}Xe (spin-1/2) and ^{131}Xe (spin-3/2) contain unpaired neutrons and thus XENON10 is most sensitive to neutron spin-dependent couplings. The 58.6 live data sets new limits across all WIMP mass. The WIMP-neutron limit has a minimum of $\sim 6 \times 10^{-39}$ cm^2 at ~ 30 GeV c^{-2}. The largest systematic uncertainty is attributed to $\mathcal{L}_{eff}$ and could raise the limit at 30 GeV c^{-2} (100 GeV c^{-2}) by $\sim 15\%$ ($\sim 18\%$). Without unpaired protons, XENON10 is unable to set a new WIMP-proton limit. It exceeds the sensitivity of CDMS and ZEPLIN-II and approaches that of NAIAD, PICASSO, KIMS, and COUPP.

The data places a constraint on a_p–a_n space at a certain mass. The expected number of events is a function of a_p and a_n:

$$N = Aa_p^2 + Ba_pa_n + Ca_n^2, \tag{6.7}$$
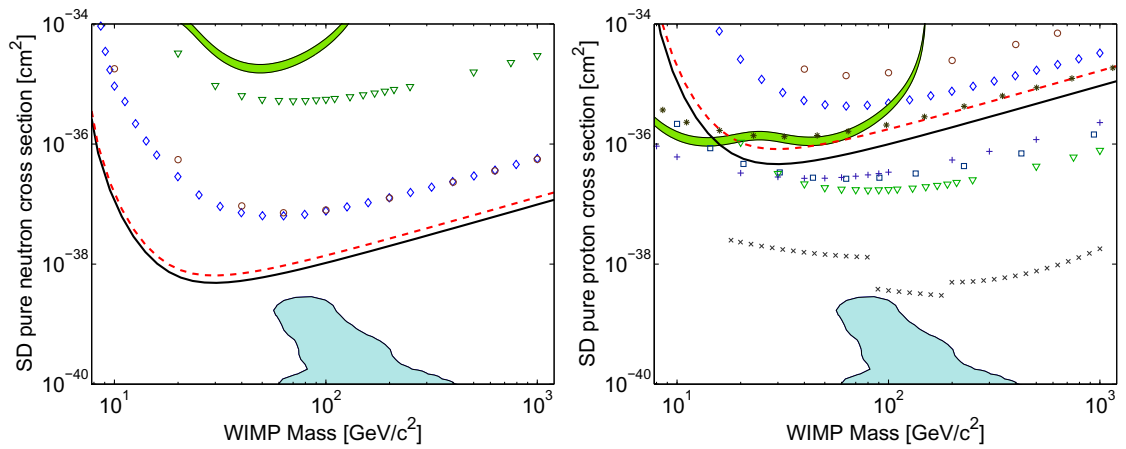
Figure 6.58: Upper limit 90% confidence level WIMP-neutron (left) and WIMP-proton (right) cross sections as a function of WIMP mass based on the 58.6 live day WIMP search data of XENON10. The black line and dashed red line represents the limit with the Bonn A and Nijmegan II potentials, respectively. Also shown are the results from the CDMS experiment [61] (diamonds), ZEPLIN-II [62] (circles), KIMS [63] (triangles), NAIAD [64] (squares), PICASSO [65] (stars), COUPP [66] (pluses), SuperK [67] (crosses), as well as the DAMA evidence region under the assumption of standard WIMP nuclear recoils and dark halo parameters (green filled region) [68]. The theoretical regions (blue filled) for the neutralino (in the constrained minimal supersymmetric model) are from [69]. These plots are from [70]

where A, B and C are constants determined by integrating dR/dE in the WIMP energy range (4.5–26.9 keVr). Figure 6.59 shows the allowed regions (inside ellipses) of a_p–a_n space at 90% confidence level for 50 GeV c^{-2} including results of CDMS, ZEPLIN-II, KIMS, and DAMA.
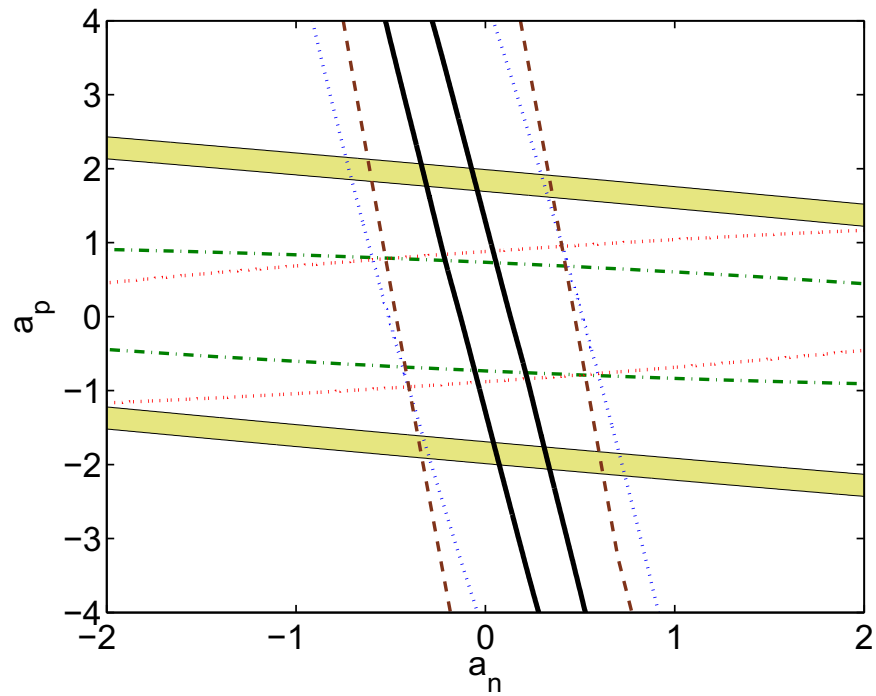
Figure 6.59: Regions in a_p–a_n space allowed at 90% confidence level by XENON10 at 50 50 GeV c^{-2} (black line). Also shown are the constraints by KIMS [63] (green, dot-dashed), COUPP [66] (red, dotted) and CDMS [61] (blue, dotted), ZEPLIN-II [62] (dashed) and the DAMA evidence region [68] (light filled region). This plot is from [70].

References

[1] Massimo Persic, Paolo Salucci, and Fulvio Stel. The Universal rotation curve of spiral galaxies: 1. The Dark matter connection. *Mon. Not. Roy. Astron. Soc.*, 281:27, 1996.

[2] M. R. Nolta et al. Five-Year Wilkinson Microwave Anisotropy Probe (WMAP) Observations: Angular Power Spectra. *Astrophys. J. Suppl.*, 180:296–305, 2009.

[3] C. Amsler et al. Review of particle physics. *Phys. Lett.*, B667:1, 2008.

[4] III Gott, J. Richard et al. A Map of the Universe. *Astrophys. J.*, 624:463, 2005.

[5] Gerard Jungman, Marc Kamionkowski, and Kim Griest. Supersymmetric dark matter. *Phys. Rept.*, 267:195–373, 1996.

[6] L. Latronico. The GLAST Gamma-Ray Observatory. Presented at 8th International Conference on Advanced Technology and Particle Physics (ICATPP 2003): Astroparticle, Particle, Space Physics, Detectors and Medical Physics Applications, Como, Italy, 6-10 Oct 2003.

[7] Paolo Gondolo and Joseph Silk. Dark matter annihilation at the galactic center. *Phys. Rev. Lett.*, 83:1719–1722, 1999.

[8] Lars Bergstrom, Joakim Edsjo, and Piero Ullio. Cosmic antiprotons as a probe for supersymmetric dark matter? *Astrophys. J.*, 526:215–235, 1999.

[9] Marc Kamionkowski and Michael S. Turner. A distinctive positron feature from heavy wimp annihilations in the galactic halo. *Phys. Rev.*, D43:1774–1780, 1991.

[10] Oscar Adriani et al. Observation of an anomalous positron abundance in the cosmic radiation. 2008.

[11] R. Bernabei et al. First results from DAMA/LIBRA and the combined results with DAMA/NaI. *Eur. Phys. J.*, C56:333–355, 2008.

[12] G. J. Alner et al. First limits on nuclear recoil events from the zeplin i galactic dark matter detector. *Astropart. Phys.*, 23:444–462, 2005.

[13] J. Angle et al. First results from the xenon10 dark matter experiment at the gran sasso national laboratory. *Phys. Rev. Lett.*, 100:021303, 2008.

[14] Z. Ahmed et al. A Search for WIMPs with the First Five-Tower Data from CDMS. 2008.

[15] V. N. Lebedenko et al. Result from the First Science Run of the ZEPLIN-III Dark Matter Search Experiment. 2008.

[16] V. N. Lebedenko et al. Limits on the spin-dependent WIMP-nucleon cross-sections from the first science run of the ZEPLIN-III experiment. 2009.

[17] D. R. Tovey, R. J. Gaitskell, P. Gondolo, Y. Ramachers, and L. Roszkowski. A new model-independent method for extracting spin- dependent cross section limits from dark matter searches. *Phys. Lett.*, B488:17–26, 2000.

[18] M. J. Berger, J. S. Coursey, M. A. Zucker, and J. Chang.

[19] E. Aprile et al. Simultaneous measurement of ionization and scintillation from nuclear recoils in liquid xenon as target for a dark matter experiment. *Phys. Rev. Lett.*, 97:081302, 2006.

[20] The stopping and ranges of ions in matter. A collection of tools for calculating the transport of ions in matter.

[21] A. Hitachi. Properties of liquid xenon scintillation for dark matter searches. *Astropart. Phys.*, 24:247–256, 2005.

[22] Akira Hitachi, Tan Takahashi, Nobutaka Funayama, Kimiaki Masuda, Jun Kikuchi, and Tadayoshi Doke. Effect of ionization density on the time dependence of luminescence from liquid argon and xenon. *Phys. Rev. B*, 27(9):5279–5285, May 1983.

[23] S. Kubota, M. Hishida, M. Suzuki, and J.-Z. Ruan. Dynamical behavior of free electrons in the recombination process in liquid argon, krypton, and xenon. *Phys. Rev. B*, 20:3486–3496, October 1979.

[24] E. Aprile et al. New Measurement of the Relative Scintillation Efficiency of Xenon Nuclear Recoils Below 10 keV. 2008.

[25] E. Aprile et al. Scintillation response of liquid xenon to low energy nuclear recoils. *Phys. Rev.*, D72:072006, 2005.

[26] V. Chepel et al. Scintillation efficiency of liquid xenon for nuclear recoils with the energy down to 5-keV. *Astropart. Phys.*, 26:58–63, 2006.

[27] D. Akimov et al. Measurements of scintillation efficiency and pulse-shape for low energy recoils in liquid xenon. *Phys. Lett.*, B524:245–251, 2002.

[28] R. Bernabei et al. Light response of a pure liquid xenon scintillator irradiated with 2.5-MeV neutrons. *Eur. Phys. J. direct*, C3:11, 2001.

[29] F. Arneodo et al. Scintillation efficiency of nuclear recoil in liquid xenon. *Nucl. Instrum. Meth.*, A449:147–157, 2000.

[30] P. Sorensen et al. Determination of the scintillation and ionization yield of liquid Xe from the XENON10 experiment. 2008.

[31] L. S. Miller, S. Howe, and W. E. Spear. Charge transport in solid and liquid ar, kr, and xe. *Phys. Rev.*, 166(3):871–878, Feb 1968.

[32] V.M. Atrazhev, A.V. Berezhnov, D.O. Dunikov, I.V. Chernysheva, V.V. Dmitrenko, and G. Kapralova. Electron transport coefficients in liquid xenon. *Dielectric Liquids,*

2005. ICDL 2005. 2005 IEEE International Conference on, pages 329–332, 26 June-1 July 2005.

[33] Manfred A. Biondi and Lorne M. Chanin. Mobilities of atomic and molecular ions in the noble gases. *Phys. Rev.*, 94(4):910–916, May 1954.

[34] T. Doke. RECENT DEVELOPMENT OF LIQUID XENON DETECTORS. (TALK). *Nucl. Instrum. Meth.*, 196:87–96, 1982.

[35] S. E. Derenzo. Lawrence berkeley laboratory, group a physics note no. 786. 1976.

[36] G. Bakale, U. Sowada, and W. F. Schmidt. Effect of an electric field on electron attachment in sf_6 , n_2o, o_2 in liquid argon and xenon. *J. Phys. Chem.*, 80:2556–9, 1976.

[37] A. I. Bolozdynya. Two-phase emission detectors and their applications. *Nucl. Instrum. Meth.*, A422:314–320, 1999.

[38] E. M. Guschin, A. A. Kruglov, and I. M. Obodovsky. Hot electron emission from liquid and solid ar and xe. *Journal of Exper. and Theor. Phys. (Russian)*, 82(5):1485–1490, 1982.

[39] A. Baldini et al. Absorption of scintillation light in a 100-l liquid xenon gamma ray detector and expected detector performance. *Nucl. Instrum. Meth.*, A545:753–764, 2005.

[40] L. M. Barkov, A. A. Grebenyuk, N. M. Ryskulov, P. Yu. Stepanov, and S. G. Zverev. Measurement of the refractive index of liquid xenon for intrinsic scintillation light. *Nucl. Instrum. Meth.*, A379:482–483, 1996.

[41] A. C. Sinnock and B. L. Smith. Refractive Indices of the Condensed Inert Gases. *Phys. Rev.*, 181:1297–1307, 1969.

[42] V. N. Solovov, V. Chepel, M. I. Lopes, and A. Hitachi. Measurement of the refractive index and attenuation length of liquid xenon for its scintillation light. *Nucl. Instrum. Meth.*, A516:462–474, 2004.

[43] P. Kadkhoda, D. Ristau, and F. von Alvensleben. Total scatter measurements in the DUV/VUV. In G. J. Exarhos, A. H. Guenther, M. R. Kozlowski, K. L. Lewis, and M. J. Soileau, editors, *Proc. SPIE Vol. 3578, p. 544-554, Laser-Induced Damage in Optical Materials: 1998, Gregory J. Exarhos; Arthur H. Guenther; Mark R. Kozlowski; Keith L. Lewis; M. J. Soileau; Eds.*, volume 3578 of *Presented at the Society of Photo-Optical Instrumentation Engineers (SPIE) Conference*, pages 544–554, April 1999.

[44] A. B. Smith, P. R. Fields, and J. H. Roberts. Spontaneous fission neutron spectrum of cf^{252}. *Phys. Rev.*, 108(2):411–413, Oct 1957.

[45] W. Moller, K-P Nikolaus, and A. Hope. Degradation of the diffuse reflectance of spectralon under low-level irradiation. *Metrologia*, 40(1):S212–S215, 2003.

[46] A guide to reflectance coatings and materials.

[47] I. B. Berlman. *Handbook of Fluoresecence Spectra of Aromatic Molecules.* Academic Press, 1965.

[48] Archana Sharma. Gaseous micropattern detectors: High energy physics and beyond. *ICFA Instrum. Bull.*, 22:01, 2001.

[49] A. Bondar et al. Two-phase argon and xenon avalanche detectors based on Gas Electron Multipliers. *Nucl. Instrum. Meth.*, A556:273–280, 2006.

[50] T. Meinschad, L. Ropelewski, and F. Sauli. Detection of primary and field-enhanced scintillation in xenon with a CsI-coated GEM detector. *Nucl. Instrum. Meth.*, A547:342–345, 2005.

[51] A. Bondar et al. First results of the two-phase argon avalanche detector performance with CsI photocathode. *Nucl. Instrum. Meth.*, A581:241–245, 2007.

[52] A. von Engle. *Ionization in gases by electrons in electric fields*, volume 21. Springer, Berlin Heidelberg, 1956.

[53] M. Matoba, T. Hirose, H. Ijiri, H. Kametani, T. Sakae, and T. Shintake. Three dimensional monte carlo simulation of the electron avalanche around an anode wire of a proportional counter. *IEEE Trans. Nucl. Sci. NS-32*, 541:541–544, 1985.

[54] P. Sorensen. *A Position-Sensitive Liquid Xenon Time-Projection Chamber for Direct Detection of Dark Matter: The XENON10 Experiment.* PhD thesis, Brown University, July 2008.

[55] G. Heusser. Low-radioactivity background techniques. *Ann. Rev. Nucl. Part. Sci.*, 45:543–590, 1995.

[56] Dongming Mei and A. Hime. Muon-induced background study for underground laboratories. *Phys. Rev.*, D73:053004, 2006.

[57] H. Wulandaria et al. Neutron flux at the gran sasso underground laboratory revisited. *Astropart. Phys.*, 22:313–322, 2004.

[58] K. Ni, U. Oberlack, G. Plante, P. Shagin, and R. Toner. Light collection simulation and xy position reconstruction for xenon10. July 2006.

[59] A. D. Ferella. *Study of the Electron Lifetime in a dual-phase Xenon Time Projection Chamber for Dark Matter Research.* PhD thesis, University of L'Aquila, November 2006.

[60] C. E. Dahl. PhD thesis, Princeton University, 2009.

[61] D. S. Akerib et al. Limits on spin-dependent wimp nucleon interactions from the cryogenic dark matter search. *Phys. Rev.*, D73:011102, 2006.

[62] G. J. Alner et al. Limits on spin-dependent WIMP-nucleon cross-sections from the first ZEPLIN-II data. *Phys. Lett.*, B653:161–166, 2007.

[63] H. S. Lee, H. C. Bhang, J. H. Choi, H. Dao, I. S. Hahn, M. J. Hwang, S. W. Jung, W. G. Kang, D. W. Kim, H. J. Kim, S. C. Kim, S. K. Kim, Y. D. Kim, J. W. Kwak, Y. J. Kwon, J. Lee, J. H. Lee, J. I. Lee, M. J. Lee, S. J. Lee, J. Li, X. Li, Y. J. Li, S. S. Myung, S. Ryu, J. H. So, Q. Yue, and J. J. Zhu KIMS Collaboration. Limits on interactions between weakly interacting massive particles and nucleons obtained with csi(tl) crystal detectors. *Physical Review Letters*, 99(9):091301, 2007.

[64] G. J. Alner et al. Limits on WIMP cross-sections from the NAIAD experiment at the Boulby Underground Laboratory. *Phys. Lett.*, B616:17–24, 2005.

[65] M. Barnabe-Heider et al. Improved spin dependent limits from the PICASSO dark matter search experiment. *Phys. Lett.*, B624:186–194, 2005.

[66] E. Behnke et al. Improved Spin-Dependent WIMP Limits from a Bubble Chamber. *Science*, 319:933–936, 2008.

[67] S. Desai et al. Search for dark matter wimps using upward through-going muons in super-kamiokande. *Phys. Rev.*, D70:083523, 2004.

[68] Christopher Savage, Paolo Gondolo, and Katherine Freese. Can WIMP spin dependent couplings explain DAMA data, in light of null results from other experiments? *Phys. Rev.*, D70:123513, 2004.

[69] S. Eidelman et al. Review of particle physics. *Phys. Lett.*, B592:1, 2004.

[70] J. Angle et al. Limits on spin-dependent WIMP-nucleon cross-sections from the XENON10 experiment. *Phys. Rev. Lett.*, 101:091301, 2008.

[71] S. Kubota, M. Hishida, and J.-Z. Ruan. Evidence for a triplet state of the self-trapped exciton states in liquid argon, krypton and xenon. *J. Phys. C: Solid State Phys.*, 11:2645–2651, June 1978.

[72] James A. Nikkel, R. Hasty, W. H. Lippincott, and D. N. McKinsey. Scintillation of liquid neon from electronic and nuclear recoils. *Astropart. Phys.*, 29:161–166, 2008.

[73] R. C. Dorf. *CRC Handbook of Engineering Tables*. CRC, 2003.

[74] Jeff Bigham. Table of emissivity values. `http://ib.cnea.gov.ar/ experim2/Cosas/omega/emisiv`

[75] M. Fragopoulou, M. Manolopoulou, S. Stoulos, R. Brandt, W. Westmeier, M. Krivo-pustov, A. Sosnin, S. Golovatyuk, and M. Zamani. Shielding around spallation neutron sources. *Journal of Physics: Conference Series*, 41:514–518, 2006.

[76] Michael Loewenstein and III White, Raymond E. Prevalence and Properties of Dark Matter in Elliptical Galaxies. *Astrophys. J.*, 518:50–63, 1999.

[77] F. Zwicky. Spectral displacement of extra galactic nebulae. *Helv. Phys. Acta*, 6:110–127, 1933.

[78] M. Girardi, Giuliano Giuricin, Fabio Mardirossian, Marino Mezzetti, and Walter Boschin. Optical mass estimates of galaxy clusters. *Astrophys. J.*, 505:74, 1998.

[79] Neta A. Bahcall, Lori M. Lubin, and Victoria Dorman. Where is the dark matter? *Astrophys. J.*, 447:L81, 1995.

[80] D. A. White, C. Jones, and W. Forman. An investigation of cooling flows and general cluster properties from an X-ray image deprojection analysis of 207 clusters of galaxies. *Mon. Not. Roy. Astron. Soc.*, 292:419, 1997.

[81] Matthias Bartelmann and Peter Schneider. Weak Gravitational Lensing. *Phys. Rept.*, 340:291–472, 2001.

[82] Alexandre Refregier. Weak Gravitational Lensing by Large-Scale Structure. *Ann. Rev. Astron. Astrophys.*, 41:645–668, 2003.

[83] Henk Hoekstra and Bhuvnesh Jain. Weak Gravitational Lensing and its Cosmological Applications. 2008.

[84] Francisco Prada et al. Observing the dark matter density profile of isolated galaxies. *Astrophys. J.*, 598:260–271, 2003.

[85] Arno A. Penzias and Robert Woodrow Wilson. A Measurement of excess antenna temperature at 4080- Mc/s. *Astrophys. J.*, 142:419–421, 1965.

[86] Wayne Hu and Scott Dodelson. Cosmic Microwave Background Anisotropies. *Ann. Rev. Astron. Astrophys.*, 40:171–216, 2002.

[87] John C. Mather et al. Measurement of the Cosmic Microwave Background spectrum by the COBE FIRAS instrument. *Astrophys. J.*, 420:439–444, 1994.

[88] William C. Jones et al. A Measurement of the Angular Power Spectrum of the CMB Temperature Anisotropy from the 2003 Flight of Boomerang. *Astrophys. J.*, 647:823, 2006.

[89] B. Rabii et al. MAXIMA: A Balloon-Borne Cosmic Microwave Background Anisotropy Experiment. *Rev. Sci. Instrum.*, 77:071101, 2006.

[90] C. L. Reichardt et al. High resolution CMB power spectrum from the complete ACBAR data set. 2008.

[91] Erik M. Leitch et al. DASI Three-Year Cosmic Microwave Background Polarization Results. *Astrophys. J.*, 624:10–20, 2005.

[92] Fabrizio Villa et al. The Planck Telescope. *AIP Conf. Proc.*, 616:224, 2002.

[93] J. Dunkley et al. Five-Year Wilkinson Microwave Anisotropy Probe (WMAP) Observations: Likelihoods and Parameters from the WMAP data. *Astrophys. J. Suppl.*, 180:306–329, 2009.

[94] R. A. Alpher, H. Bethe, and G. Gamow. The origin of chemical elements. *Phys. Rev.*, 73:803–804, 1948.

[95] Y. I. Izotov et al. Helium abundance in the most metal-deficient blue compact galaxies: I Zw 18 and SBS 0335-052. 1999.

[96] Neil H. M. Crighton, J. K. Webb, A. Ortiz-Gill, and A. Fernandez-Soto. D/H in a new Lyman limit quasar absorption system at z=3.256 towards PKS1937-1009. *Mon. Not. Roy. Astron. Soc.*, 355:1042, 2004.

[97] John M. O'Meara et al. The Deuterium to Hydrogen Abundance Ratio Towards the QSO SDSS1558-0031. *Astrophys. J.*, 649:L61–L66, 2006.

[98] Keith A. Olive, David N. Schramm, Sean T. Scully, and James W. Truran. Low Mass Stars and the He3 Problem. *Astrophys. J.*, 479:752, 1997.

[99] Corinne Charbonnel and F. Primas. The Lithium Content of the Galactic Halo Stars. 2005.

[100] Margaret J. Geller and John P. Huchra. Mapping the universe. *Science*, 246:897–903, 1989.

[101] E. W. Kolb and M. S. Turner. *The Early Universe*. Perseus Books Group, 1993.

[102] George R. Blumenthal, S. M. Faber, Joel R. Primack, and Martin J. Rees. Formation of galaxies and large-scale structure with cold dark matter. *Nature*, 311:517–525, 1984.

[103] Matthew Colless. Cosmological results from the 2dF galaxy redshift survey. 2003.

[104] Adrian C. Pope et al. Cosmological Parameters from Eigenmode Analysis of Sloan Digital Sky Survey Galaxy Redshifts. *Astrophys. J.*, 607:655–660, 2004.

[105] Max Tegmark et al. Cosmological parameters from sdss and wmap. *Phys. Rev.*, D69:103501, 2004.

[106] Ariel G. Sanchez et al. Cosmological parameters from CMB measurements and the final 2dFGRS power spectrum. *Mon. Not. Roy. Astron. Soc.*, 366:189–207, 2006.

[107] E. Komatsu et al. Five-Year Wilkinson Microwave Anisotropy Probe (WMAP) Observations: Cosmological Interpretation. *Astrophys. J. Suppl.*, 180:330–376, 2009.

[108] David H. Weinberg, Jordi Miralda-Escude, Lars Hernquist, and Neal Katz. A Lower Bound on the Cosmic Baryon Density. 1997.

[109] C. Alcock et al. The macho project: Microlensing results from 5.7 years of lmc observations. *Astrophys. J.*, 542:281–307, 2000.

[110] P. Tisserand et al. Limits on the macho content of the galactic halo from the eros-2 survey of the magellanic clouds. 2006.

[111] Y. Fukuda et al. Evidence for oscillation of atmospheric neutrinos. *Phys. Rev. Lett.*, 81:1562–1567, 1998.

[112] Q. R. Ahmad et al. Direct evidence for neutrino flavor transformation from neutral-current interactions in the sudbury neutrino observatory. *Phys. Rev. Lett.*, 89:011301, 2002.

[113] S. Tremaine and J. E. Gunn. Dynamical role of light neutral leptons in cosmology. *Phys. Rev. Lett.*, 42:407–410, 1979.

[114] R. D. Peccei and Helen R. Quinn. Cp conservation in the presence of instantons. *Phys. Rev. Lett.*, 38:1440–1443, 1977.

[115] Steven Weinberg. A new light boson? *Phys. Rev. Lett.*, 40:223–226, 1978.

[116] Frank Wilczek. Problem of strong p and t invariance in the presence of instantons. *Phys. Rev. Lett.*, 40:279–282, 1978.

[117] Wolfgang Keil et al. A fresh look at axions and sn 1987a. *Phys. Rev.*, D56:2419–2432, 1997.

[118] Michael S. Turner. Windows on the axion. *Phys. Rept.*, 197:67–97, 1990.

[119] Georg G. Raffelt. Astrophysical axion bounds. 2006.

[120] Remy Battesti et al. Axion searches in the past, at present, and in the near future. 2007.

[121] C. Hagmann et al. Results from a high-sensitivity search for cosmic axions. *Phys. Rev. Lett.*, 80:2043–2046, 1998.

[122] H. Peng et al. Cryogenic cavity detector for a large-scale cold dark- matter axion search. *Nucl. Instrum. Meth.*, A444:569–583, 2000.

[123] S. J. Asztalos et al. An improved rf cavity search for halo axions. *Phys. Rev.*, D69:011101, 2004.

[124] K. Zioutas et al. A decommissioned lhc model magnet as an axion telescope. *Nucl. Instrum. Meth.*, A425:480–489, 1999.

[125] K. Zioutas et al. First results from the cern axion solar telescope (cast). *Phys. Rev. Lett.*, 94:121301, 2005.

[126] E. Zavattini et al. Experimental observation of optical rotation generated in vacuum by a magnetic field. *Phys. Rev. Lett.*, 96:110406, 2006.

[127] E. Zavattini et al. New PVLAS results and limits on magnetically induced optical rotation and ellipticity in vacuum. *Phys. Rev.*, D77:032006, 2008.

[128] Kim Griest, Marc Kamionkowski, and Michael S. Turner. Supersymmetric dark matter above the w mass. *Phys. Rev.*, D41:3565, 1990.

[129] J. E. Gunn, B. W. Lee, I. Lerche, D. N. Schramm, and G. Steigman. Some astrophysical consequences of the existence of a heavy stable neutral lepton. *Astrophys. J.*, 223:1015–1031, 1978.

[130] G. Steigman, C. L. Sarazin, H. Quintana, and J. Faulkner. Dynamical interactions and astrophysical effects of stable heavy neutrinos. Astron. J. 83 (1978) 1050-1061. In *Srednicki, M.A. (ed.): Particle physics and cosmology* 207-218.

[131] Benjamin W. Lee and Steven Weinberg. Cosmological lower bound on heavy-neutrino masses. *Phys. Rev. Lett.*, 39:165–168, 1977.

[132] M. Milgrom. A modification of the newtonian dynamics as a possible alternative to the hidden mass hypothesis. *Astrophys. J.*, 270:365–370, 1983.

[133] Etienne Pointecouteau and Joseph Silk. New constraints on MOND from galaxy clusters. *Mon. Not. Roy. Astron. Soc.*, 364:654–658, 2005.

[134] Jacob D. Bekenstein. Relativistic gravitation theory for the mond paradigm. *Phys. Rev.*, D70:083509, 2004.

[135] Anze Slosar, Alessandro Melchiorri, and Joseph Silk. Did boomerang hit mond? *Phys. Rev.*, D72:101301, 2005.

[136] Douglas Clowe et al. A direct empirical proof of the existence of dark matter. 2006.

[137] Marusa Bradac et al. Revealing the properties of dark matter in the merging cluster MACSJ0025.4-1222. 2008.

[138] Jurg Diemand, Ben Moore, and Joachim Stadel. Convergence and scatter of cluster density profiles. *Mon. Not. Roy. Astron. Soc.*, 353:624, 2004.

[139] Lars Bergstrom, Piero Ullio, and James H. Buckley. Observability of gamma rays from dark matter neutralino annihilations in the milky way halo. *Astropart. Phys.*, 9:137–162, 1998.

[140] S. D. Hunter et al. Egret observations of the diffuse gamma-ray emission from the galactic plane. *Astrophys. J.*, 481:205–240, 1997.

[141] W. de Boer, C. Sander, V. Zhukov, A. V. Gladyshev, and D. I. Kazakov. The supersymmetric interpretation of the egret excess of diffuse galactic gamma rays. *Phys. Lett.*, B636:13–19, 2006.

[142] Wim de Boer, I. Gebauer, C. Sander, M. Weber, and V. Zhukov. Is the dark matter interpretation of the egret gamma ray excess compatible with antiproton measurements? *AIP Conf. Proc.*, 903:607–612, 2007.

[143] L. Bergstrom, J. Edsjo, Michael Gustafsson, and P. Salati. Is the dark matter interpretation of the egret gamma excess compatible with antiproton measurements? *JCAP*, 0605:006, 2006.

[144] F. W. Stecker, S. D. Hunter, and D. A. Kniffen. The likely cause of the egret gev anomaly and its implications. 2007.

[145] Jan Conrad. Searches for particle dark matter with the glast large area telescope. 2007.

[146] M. F. Cawley, D. J. Fegan, K. Harris, P. W. Kwok, A. M. Hillas, R. C. Lamb, M. J. Lang, D. A. Lewis, D. Macomb, P. T. Reynolds, D. J. Schmid, G. Vacanti, and T. C. Weekes. A high resolution imaging detector for tev gamma-ray astronomy. *Experimental Astronomy*, 1:173–193, May 1990.

[147] J. Kildea et al. The whipple observatory 10-m gamma-ray telescope, 1997- 2006. *Astropart. Phys.*, 28:182–195, 2007.

[148] Niels Gotting. Recent results from hegra: Gamma-ray observations with the hegra stereoscopic system of 5 cherenkov telescopes. *Eur. Phys. J.*, C33:s932–s934, 2004.

[149] G. MAIER et al. Veritas: Status and latest results. 2007.

[150] S. Kabuki et al. Cangaroo-iii search for gamma rays from centaurus a and the ω centauri region. 2007.

[151] D. Ferenc. The magic gamma-ray observatory. *Nucl. Instrum. Meth.*, A553:274–281, 2005.

[152] J. Albert et al. Upper limit for gamma-ray emission above 140 gev from the dwarf spheroidal galaxy draco. 2007.

[153] F. Aharonian. Observations of the sagittarius dwarf galaxy by the h.e.s.s. experiment and search for a dark matter signal. 2007.

[154] J. Lavalle et al. Indirect search for dark matter in m31 with the celeste experiment. *Astron. Astrophys.*, 450:1–8, 2006.

[155] Douglas M. Gingrich et al. The stacee ground-based gamma-ray detector. *IEEE Trans. Nucl. Sci.*, 52:2977–2985, 2005.

[156] D. D. Driscoll et al. Search for dark matter annihilation in draco with stacee. 2007.

[157] Robert W. Atkins et al. Search for very high energy gamma rays from wimp annihilations near the sun with the milagro detector. *Phys. Rev.*, D70:083516, 2004.

[158] M. M. Boliev et al. Search for supersymmetric dark matter with baksan underground telescope. *Nucl. Phys. Proc. Suppl.*, 48:83–86, 1996.

[159] Ivan De Mitri. Results of dark matter searches with the macro experiment. 2002.

[160] Andreas Gross. Recent results from the amanda-ii neutrino telescope. 2005.

[161] Gordon Lim. Indirect search for dark matter with the antares neutrino telescope. 2007.

[162] Hagar Landsman. Icecube, the world's largest dark matter detector. 2006.

[163] Piero Ullio, HongSheng Zhao, and Marc Kamionkowski. A Dark-Matter Spike at the Galactic Center? *Phys. Rev.*, D64:043504, 2001.

[164] F. W. Stecker, S. Rudaz, and T. F. Walsh. Galactic anti-protons from photinos. *Phys. Rev. Lett.*, 55:2622–2625, 1985.

[165] S. Rudaz and F. W. Stecker. Cosmic ray anti-protons, positrons and gamma-rays from halo dark matter annihilation. *Astrophys. J.*, 325:16, 1988.

[166] M. Boezio et al. The PAMELA space experiment: First year of operation. *J. Phys. Conf. Ser.*, 110:062002, 2008.

[167] A. M. Atoian, F. A. Aharonian, and H. J. Volk. Electrons and positrons in the galactic cosmic rays. *Phys. Rev.*, D52:3265–3275, 1995.

[168] R. Bernabei et al. Search for wimp annual modulation signature: Results from dama / nai-3 and dama / nai-4 and the global combined analysis. *Phys. Lett.*, B480:23–31, 2000.

[169] R. J. Gaitskell. Direct detection of dark matter. *Ann. Rev. Nucl. Part. Sci.*, 54:315–359, 2004.

[170] J. D. Lewin and P. F. Smith. Review of mathematics, numerical factors, and corrections for dark matter experiments based on elastic nuclear recoil. *Astropart. Phys.*, 6:87–112, 1996.

[171] Richard H. Helm. Inelastic and Elastic Scattering of 187-Mev Electrons from Selected Even-Even Nuclei. *Phys. Rev.*, 104:1466–1475, 1956.

[172] Katherine Freese, Joshua A. Frieman, and Andrew Gould. Signal Modulation in Cold Dark Matter Detection. *Phys. Rev.*, D37:3388, 1988.

[173] David O. Caldwell et al. Searching for the cosmion by scattering in Si detectors. *Phys. Rev. Lett.*, 65:1305–1308, 1990.

[174] L. Baudis et al. New limits on dark-matter wimps from the heidelberg-moscow experiment. *Phys. Rev.*, D59:022001, 1999.

[175] A. Morales et al. Improved constraints on wimps from the international germanium experiment igex. *Phys. Lett.*, B532:8–14, 2002.

[176] H. V. Klapdor-Kleingrothaus et al. First results from the hdms experiment in the final setup. *Astropart. Phys.*, 18:525–530, 2003.

[177] A. Morales. Non-cryogenics dark matter experiments. *Nucl. Phys. Proc. Suppl.*, 138:135–144, 2005.

[178] H. V. Klapdor-Kleingrothaus, O. Chkvorez, I. V. Krivosheina, H. Strecker, and C. Tomei. Genius test-facility started operation in gran sasso: With first ten kg of

naked germanium detectors in liquid nitrogen. *Nucl. Instrum. Meth.*, A511:341–346, 2003.

[179] A. Bettini. Gerda. germanium detector array. search for neutrino-less beta beta decay of ge-76. *Nucl. Phys. Proc. Suppl.*, 168:67–69, 2007.

[180] C. E. Aalseth et al. The majorana ge-76 double-beta decay project. *Nucl. Phys. Proc. Suppl.*, 124:247–252, 2003.

[181] R. Bernabei et al. New limits on WIMP search with large-mass low- radioactivity NaI(Tl) set-up at Gran Sasso. *Phys. Lett.*, B389:757–766, 1996.

[182] K. Fushimi et al. Application of a large volume NaI scintillator to search for dark matter. *Phys. Rev.*, C47:425–428, 1993.

[183] P. F. Smith et al. Improved dark matter limits from pulse shape discrimination in a low background sodium iodide detector at the boulby mine. *Phys. Lett.*, B379:299–308, 1996.

[184] R. Bernabei et al. Searching for wimps by the annual modulation signature. *Phys. Lett.*, B424:195–201, 1998.

[185] R. Bernabei et al. The DAMA/LIBRA apparatus. *Nucl. Instrum. Meth.*, A592:297–315, 2008.

[186] Veronique Sanglard et al. Final results of the edelweiss-i dark matter search with cryogenic heat-and-ionization ge detectors. *Phys. Rev.*, D71:122002, 2005.

[187] O. Martineau et al. Calibration of the EDELWEISS cryogenic heat-and-ionisation germanium detectors for dark matter search. *Nucl. Instrum. Meth.*, A530:426–439, 2004.

[188] A. Chantelauze. Status of the edelweiss-2 dark matter search. 2007.

[189] T. Shutt et al. A solution to the dead-layer problem in ionization and phonon-based dark matter detectors. *Nucl. Instrum. Meth.*, A444:340–344, 2000.

[190] R. Abusaidi et al. Exclusion limits on the WIMP nucleon cross-section from the Cryogenic Dark Matter Search. *Phys. Rev. Lett.*, 84:5699–5703, 2000.

[191] M. S. Armel-Funkhouser et al. Exclusion limits on the WIMP nucleon cross-section from the first run of the Cryogenic Dark Matter Search in the Soudan underground lab. *Phys. Rev.*, D72:052009, 2005.

[192] D. S. Akerib et al. The SuperCDMS proposal for dark matter detection. *Nucl. Instrum. Meth.*, A559:411–413, 2006.

[193] G. Angloher et al. Limits on wimp dark matter using sapphire cryogenic detectors. *Astropart. Phys.*, 18:43–55, 2002.

[194] G. Angloher et al. Limits on wimp dark matter using scintillating cawo-4 cryogenic detectors with active background suppression. *Astropart. Phys.*, 23:325–339, 2005.

[195] R. Bernabei et al. New limits on particle dark matter search with a liquid xenon target-scintillator. *Phys. Lett.*, B436:379–388, 1998.

[196] Y. Takeuchi. Recent status of the XMASS project. Prepared for 32nd International Conference on High-Energy Physics (ICHEP 04), Beijing, China, 16-22 Aug 2004.

[197] Y. Takeuchi. Distillation purification of xenon for krypton and measurement of radon contamination in liquid xenon. Unpublished.

[198] Masayuki Nakahata. Status of XMASS experiment. In *Heidelberg 2007, DARK MATTER IN ASTROPARTICLE AND PARTICLE PHYSICS*, 2007.

[199] Ko Abe. The XMASS experiment. *J. Phys. Conf. Ser.*, 120:042022, 2008.

[200] W. H. Lippincott et al. Scintillation time dependence and pulse shape discrimination in liquid argon. 2008.

[201] J. J. Lidgard. Pulse shape discrimination studies in liquid argon for the deap-1 detector. Master's thesis, Queen's University, 2008.

[202] M Gold. Deap/clean a liquid argon/neon detector for dark matter and neutrinos. In *2nd International Workshop on the Interconnection between Particle Physics and Cosmology*, Albuquerque, New Mexico, 2008.

[203] P. Benetti et al. First results from a dark matter search with liquid argon at 87-k in the gran sasso underground laboratory. 2007.

[204] C. Galbiati and R. Purtschert. Discovery of underground argon with low level of radioactive ^{39}Ar and possible applications to WIMP dark matter detectors. 2007.

[205] Vittorio Boccone. Recent updates on the ArDM project: A Liquid Argon TPC for Dark Matter Detection. 2008.

[206] P. Otiugova. The ArDM, a ton-scale liquid argon experiment for direct dark matter detection. *J. Phys. Conf. Ser.*, 120:042023, 2008.

[207] G. J. Alner et al. First limits on WIMP nuclear recoil signals in ZEPLIN-II: A two phase xenon detector for dark matter detection. *Astropart. Phys.*, 28:287–302, 2007.

[208] D. Yu. Akimov et al. The ZEPLIN-III dark matter detector: Instrument design, manufacture and commissioning. *Astropart. Phys.*, 27:46–60, 2007.

[209] Elena Aprile, Laura Baudis, and for the XENON100 Collaboration. Status and Sensitivity Projections for the XENON100 Dark Matter Experiment. 2009.

[210] L. Kastens. The lux detector. In *2008 APS APRIL*, 2008.

[211] G. J. Alner et al. The drift-i dark matter detector at boulby: Design, installation and operation. *Nucl. Instrum. Meth.*, A535:644–655, 2004.

[212] S. Burgos et al. First results from the drift-iia dark matter detector. 2007.

[213] Donald A. Glaser. Some Effects of Ionizing Radiation on the Formation of Bubbles in Liquids. *Phys. Rev.*, 87:665–665, 1952.

[214] J. I. Collar. Superheated microdrops as cold dark matter detectors. *Phys. Rev.*, D54:1247–1251, 1996.

[215] T. A. Girard et al. Simple dark matter search results. *Phys. Lett.*, B621:233–238, 2005.

[216] U. Wichoski et al. Status and results of the PICASSO experiment. *Nucl. Phys. Proc. Suppl.*, 173:121–124, 2007.

[217] G. Bertone, David G. Cerdeno, J. I. Collar, and Brian C. Odom. Wimp identification through a combined measurement of axial and scalar couplings. *Phys. Rev. Lett.*, 99:151301, 2007.

[218] Andreas Birkedal, Konstantin Matchev, and Maxim Perelstein. Dark matter at colliders: A model-independent approach. *Phys. Rev.*, D70:077701, 2004.

[219] Edward A. Baltz, Marco Battaglia, Michael Edward Peskin, and Tommer Wizansky. Determination of dark matter properties at high-energy colliders. *Phys. Rev.*, D74:103521, 2006.

[220] James Brau, Yasuhiro Okada, and Nicholas Walker. Ilc reference design report volume 1 - executive summary. 2007.

[221] (Ed.) Behnke, Ties et al. ILC Reference Design Report Volume 4 - Detectors. 2007.

[222] A. I. Bolozdynya, E. Aprile, T. Doke, and A. E. Bolotnikov. *Noble Gas Detectors*. Wiley-VCH, 2006.

[223] M.D. Henry and D.E. Brinza. Ds1 ion propulsion emissions characterization. *Aerospace Conference, 2001, IEEE Proceedings.*, 5:2505–2513 vol.5, 2001.

[224] J. K. Lawrence, W. F. Loomis, C. A. Tobias, and F. H. Turpin. Preliminary observations of the narcotic effect of xenon with a review of values for solubilities of gases in water and oils. *J. Physiol.*, 105:197–204, 1946.

[225] S. C. Cullen and E. G. Gross. The anesthetic properties of xenon in animals and human beings with additional observations on krypton. *Science*, 133:580–2, 1951.

[226] Thomas Marx, Michael Schmidt, Uwe Schirmer, and Helmut Reinelt. Xenon anaesthesia. *Journal of the Royal Society of Medicine*, 93:513–17, 2000.

[227] J. S. Meyer, L. A. Hayman, T. Amano, S. Nakajima, T. Shaw, P. Lauzon, S. Derman, I. Karacan, and Y. Harati. Mapping local blood flow of human brain by ct scanning during stable xenon inhalation. *Stroke*, 12:426–36, 1981.

[228] A. Oros and N. J. Shah. Hyperpolarized xenon in nmr and mri. *Phys. Med. Biol.*, 49:R105–R153, 2004.

[229] B. Chann, I. A. Nelson, L. W. Anderson, B. Driehuys, and T. G. Walker. $^{129}xe - xe$ molecular spin relaxation. *Phys. Rev. Lett.*, 88(11):113201, Feb 2002.

[230] J Wolber, A. Cherubini, M. O. Leach, and A. Bifone. On the oxygenation-dependent ^{1}29xe t_1 in blood. *NMR in Biomedicine*, 13(4):234–7, 2000.

[231] T. Doke, J. Kikuchi, and F. Nishikido. Time-of-flight positron emission tomography using liquid xenon scintillation. *Nucl. Inst. and Meth. A*, 569(3):863–871, 2006.

[232] K. Giboni, E. Aprile, T. Doke, S. Suzuki, L. M. P. Fernandes, J. A. M. Lopes, and J M F dos Santos. Compton positron emission tomography with a liquid xenon time projection chamber. *Journal of Instrumentation*, 2(10):P10001, 2007.

[233] D. Akimov et al. EXO: An advanced Enriched Xenon double-beta decay Observatory. *Nucl. Phys. Proc. Suppl.*, 138:224–226, 2005.

[234] R. F. Mould. *Chernobyl Record: The Definitive History of the Chernobyl Catastrophe.* Taylor and Francis, first edition, 2000.

[235] A. I. Bolozdynya, P. P. Brusov, T. Shutt, C. E. Dahl, and J. Kwong. A chromatographic system for removal of radioactive Kr-85 from xenon. *Nucl. Instrum. Meth.*, A579:50–53, 2007.

[236] K. Ni et al. Preparation of Neutron-activated Xenon for Liquid Xenon Detector Calibration. *Nucl. Instrum. Meth.*, A582:569–574, 2007.

[237] M. Suzuki, J. Ruan(Gen), and S. Kubota. Time dependence of the recombination luminescence from high-pressure argon, krypton and xenon excited by alpha particles. *Nucl. Instrum. Meth.*, 192:565–574, 1982.

[238] A Wambersie et al. Stopping of ions heavier than helium. *J. of the ICRU*, 5(1), 2005.

[239] Francesc Salvat, Jose M. Fernandez-Varea, and Josep Sempau. *PENELOPE - A Code System for Monte Carlo Simulation of Electron and Photon Transport*. Nuclear Energy Agency, Organisation for Economic Co-operation and Development, 2003.

[240] Shinzou Kubota, Masayo Suzuki, and Jian-zhi Ruan(Gen). Specific-ionization-density effect on the time dependence of luminescence in liquid xenon. *Phys. Rev. B*, 21(6):2632–2634, Mar 1980.

[241] D. C. Lorents. The physics of electron beam excited rare gases at high densities. *Physica C*, 82:19–26, 1976.

[242] J. Lindhard et al. Integral equations governing radiation effects. *Mat. Fys. Medd. Dan. Vid. Selsk.*, 33(10), 1963.

[243] T. Doke. Fundamental properties of liquid argon, krypton and xenon as radiation detector media. *Portugal Phys.*, 12:9–48, 1981.

[244] P. Benetti et al. A simple and effective purifier for liquid xenon. *Nucl. Instrum. Meth.*, A329:361–364, 1993.

[245] A. Bolotnikov and B. Ramsey. Development of high-pressure xe ionization detectors for hard x-ray and low energy gamma-ray astronomy. *Nuclear Science Symposium and Medical Imaging Conference Record, 1995., 1995 IEEE*, 1:258–262 vol.1, 21-28 Oct 1995.

[246] S. G. Pokachalov, M. A. Kirsanov, A. A. Kruglov, and I. M. Obodovski. Spark discharge method of liquid rare-gas purification. *Nucl. Instrum. Meth. A*, 327:159–162, 1993.

[247] V. V. Dmitrenko, S. I. Gratchev, S. E. Ulin, Z. M. Uteshev, and K. F. Vlasik. High pressure xenon gamma-spectrometers with high energy resolution. *Appl. Rad. Isot.*, 52:739–743, 2000.

[248] K. Watanabe and M. Zelikoff. Absorption coefficients of water vapor in the vacuum ultraviolet. *J. Opt. Soc. Am.*, 43:753–754, 1953.

[249] K. Watanabe, Edward C. Y. Inn, and M. Zelikoff. Absorption coefficients of oxygen in the vacuum ultraviolet. *J. Chem. Phys.*, 21:1026, 1953.

[250] L.D. Landau and E.M. Lifshitz. *Electrodynamics of Continuous Media*. Butterworth-Heinemann, Oxford, second edition, 1984.

[251] G. M. Seidel, R. E. Lanou, and W. Yao. Rayleigh scattering in rare-gas liquids. *Nucl. Instrum. Meth.*, A489:189–194, 2002.

[252] N. Ishida et al. Attenuation length measurements of scintillation light in liquid rare gases and their mixtures using an improved reflection suppresser. *Nucl. Instrum. Meth.*, A384:380–386, 1997.

[253] M. Yamashita, T. Doke, K. Kawasaki, J. Kikuchi, and S. Suzuki. Scintillation response of liquid xe surrounded by ptfe reflector for gamma rays. *Nucl. Instrum. Meth.*, A535:692–698, 2004.

[254] V. R. Weidner and J. J. Hsia. Reflection properties of pressed polytetrafluoroethylene powder. *J. Opt. Soc. Am*, 71:856–861, 1981.

[255] K. Bunzl and W. Kracke. Natural radioactive contaminants in solder. *Nucl. Instrum. Meth.*, A238:191–192, 1985.

[256] *Universal Transducer Interface*, 2003.

[257] P. Benetti et al. Detection of energy deposition down to the kev region using liquid xenon scintillation. *Nucl. Instrum. Meth.*, A327:203–206, 1993.

[258] M. Yamashita, T. Doke, J. Kikuchi, and S. Suzuki. Double phase (liquid / gas) xenon scintillation detector for wimps direct search. *Astropart. Phys.*, 20:79–84, 2003.

[259] R. Martin, J. Knauer, and P. Balo. Production, distribution and applications of californium-252 neutron sources. *Applied Radiation and Isotopes*, 53(4-5):785–92, 2000.

[260] Carl E. Dahl, J. Kwong, A. Bolozdynya, A. Bradley, P. Brusov, and T. Shutt. Measurements and models of fundamental processes governing resolution and discrimination in dual-phase xenon time projection chambers, as used to detect wimp dark matter. 2009 (to be published).

[261] C. J. Martoff and P. F. Smith. A proposed dark matter detector based on scintillation pulse shape differences in high pressure Xe gas. *Nucl. Phys. Proc. Suppl.*, 173:148–151, 2007.

[262] M. G. Boulay, A. Hime, and J. Lidgard. Design constraints for a wimp dark matter and p p solar neutrino liquid neon scintillation detector. 2004.

[263] Mark G. Boulay and A. Hime. Direct wimp detection using scintillation time discrimination in liquid argon. 2004.

[264] A. Hime. Cryogenic Low Energy Astrophysics with Neon. *Nuclear Physics B Proceedings Supplements*, 138:106–107, January 2005.

[265] Andre Rubbia. Ardm: A ton-scale liquid argon experiment for direct detection of dark matter in the universe. 2005.

[266] D. Yu. Akimov et al. Scintillating LXe/LKr electromagnetic calorimeter. *IEEE Trans. Nucl. Sci.*, 42:2244–2249, 1995.

[267] Carl E. Dahl, J. Kwong, A. Bolozdynya, A. Bradley, P. Brusov, and T. Shutt. Performance and fundamental processes at low energy in a two-phase liquid xenon dark matter detector. 2008 (to be published).

[268] S. Duncan, M. Kuss, R. van der Meer, and B. Wojtsekhowski. Effect of p-tp coating to the quantum efficiency of burle 8854 photomultiplier tubes. *Jefferson Lab Technical Note.* JLAB-TN-98-006.

[269] C. H. Lally, G. J. Davies, W. G. Jones, and N. J. T. Smith. Uv quantum efficiencies of organic fluors. *Nucl. Phys.*, B117:421–427, 1996.

[270] D. N. McKinsey, C. R. Brome, J. S. Butterworth, P. R. Huffman, J. M. Doyle, R. Golub, K. Habicht, and S. K. Lamoreaux. Fluorescence efficiencies of thin scintillating films in the extreme ultraviolet spectral region. *Nuclear Instruments and Methods in Physics Research B*, 132:351–358, November 1997.

[271] A. Bolozdynya et al. A high pressure xenon self-triggered scintillation drift chamber with 3-D sensitivity in the range of 20–140 keV deposited energy. *Nucl. Instrum. Meth.*, A385:225–238, 1997.

[272] J. Wilkerson, T. K. Edberg, J. Hamm, B. Sadoulet, P. Shestople, and G. Smith. Study of high-pressure xenon gas scintillation drift chambers with wave-shifting fiber and CsI photocathode readouts. In B. D. Ramsey and T. A. Parnell, editors, *Society of Photo-Optical Instrumentation Engineers (SPIE) Conference Series*, volume 2806 of *Presented at the Society of Photo-Optical Instrumentation Engineers (SPIE) Conference*, pages 361–371, October 1996.

[273] V. Boccone et al. Development of wavelength shifter coated reflectors for the ArDM argon dark matter detector. 2009.

[274] V. Kumar and A. K. Datta. Vacuum ultraviolet scintillators: sodium salicylate and p-terphenyl. *Appl. Opt.*, 18(9):1414–1417, 1979.

[275] T. Shutt, A. Bolozdynya, P. Brusov, C. E. Dahl, and J. Kwong. Performance and fundamental processes at low energy in a two-phase liquid xenon dark matter detector. *Nucl. Phys. Proc. Suppl.*, 173:160–163, 2007.

[276] W. L. Wolfe and G. J. Zissis. *The Infrared Handbook*. Environmental Research Institute of Michigan, Ann Arbor, Ann Arbor, MI, 1993.

[277] R. Tousey and I. Limansky. Extreme ultraviolet images televised in-flight with a rocket-borne sec vidicon system. *Appl. Opt.*, 11:1025–1031, 1972.

[278] T. Mori. Effect of magnetic field on growth of functional organic thin films. *Thin Solid Films*, 338:300–303, January 1999.

[279] F. Balzer, L. Kankate, H. Niehus, and H.-G. Rubahn. Nanoaggregates from oligothiophenes and oligophenylenes: a systematic growth survey. In J. G. Grote, T. Kaino, and F. Kajzar, editors, *Society of Photo-Optical Instrumentation Engineers (SPIE) Conference Series*, volume 5724 of *Presented at the Society of Photo-Optical Instrumentation Engineers (SPIE) Conference*, pages 285–294, April 2005.

[280] W.S. Hu, Y.-F. Lin, Y.-T. Tao, Y.-J. Hsu, and D.-H. Wei. Highly oriented growth of p-sexiphenyl molecular nanocrystals on rubbed polymethylene surface. *Macromolecules*, 38(23):9617–9624, 2005.

[281] Stephen E. Derenzo, Terry S. Mast, Haim Zaklad, and Richard A. Muller. Electron avalanche in liquid xenon. *Phys. Rev. A*, 9(6):2582–2591, Jun 1974.

[282] A. P. L. Policarpo et al. Observation of electron multiplication in liquid xenon with a microstrip plate. *Nucl. Instrum. Meth. A*, 365:568–571, 1995.

[283] V. Solovov, F. Balaua, F. Nevesa, V. Chepela, A. Pereiraa, and M. I. Lopesa. Operation of gas electron multipliers in pure xenon at low temperatures. *Nucl. Instrum. Meth. A*, A580:331–334, 2007.

[284] P. K. Lightfoot, R. Hollingworth, N. J. C. Spooner, and D. Tovey. Development of a double-phase Xenon cell using micromegas charge readout for applications in dark matter physics. *Nucl. Instrum. Meth.*, A554:266285, 2005.

[285] E. Aprile et al. Performance of dual phase xetpc with csi photocathode and pmts readout for the scintillation light. In *IEEE International Conference on Dielectric Liquids, 2005.*, pages 345–348, 2005.

[286] W. Blum and Gigi Rolandi. *Particle detection with drift chambers.* Springer, 1st edition, 1994. ISBN-13-9783540564256.

[287] K. T. McDonald. Notes on electrostatic wire grids. Internal note, 2003.

[288] B.H. Crichton. Gas discharge physics. *HV Technology (Digest No. 1996/173), IEE Colloquium on Advances in*, pages 3/1–3/5, 4 Oct 1996.

[289] Z. He. Review of the Shockley-Ramo theorem and its application in semiconductor gamma-ray detectors. *Nuclear Instruments and Methods in Physics Research A*, 463:250–267, May 2001.

[290] H. Sakurai and B. D. Ramsey. Dependence of energy resolution on anode diameter in xenon proportional counters. *Nucl. Instrum. Meth.*, A313:155–160, 1992.

[291] G. D. Alkhazov. Statistics of electron avalanches and ultimate resolution of proportional counters. *Nucl. Instrum. Meth.*, 89:155–165, 1970.

[292] H. Sipila. Energy resolution of the proportional counter. *Nucl. Instrum. Meth.*, 133:251–252, 1976.

[293] G. F. Knoll. *RADIATION DETECTION AND MEASUREMENT.* John Wiley & Sons, third edition, 2000. New York, USA: John Wiley & Sons (2000) 816 p.

[294] P. J. B. M. Rachinhas, T. H. V. T. Dias, F. P. Santos, A. D. Stauffer, and C. A. N. Conde. Monte carlo simulation of xenon filled cylindrical proportional counters. *IEEE Trans. Nucl. Sci.*, 41:984–988, 1994.

[295] T. Takahashi et al. Average energy expended per ion pair in liquid xenon. *Phys. Rev.*, A12:1771–1775, 1975.

[296] T. Doke, A. Hitachi, S. Kubota, A. Nakamoto, and T. Takahashi. Estimation of fano factors in liquid argon, krypton, xenon and xenon-doped liquid argon. *Nucl. Instrum. Methods*, 134:353, 1976.

[297] J. Seguinot, T. Ypsilantis, and J. Tischhauser. Liquid xenon scintillation: Photon yield and fano factor measurements. *Nucl. Instrum. Meth.*, A354:280–287, 1995.

[298] D. Yvon et al. Low noise voltage and charge preamplifiers for phonon and ionization detectors at very low temperature. *Nucl. Instrum. Meth.*, A368:778, 1996.

[299] V. Radeka. LOW NOISE TECHNIQUES IN DETECTORS. *Ann. Rev. Nucl. Part. Sci.*, 38:217–277, 1988.

[300] U. Fano. Ionization Yield of Radiations. 2. The Fluctuations of the Number of Ions. *Phys. Rev.*, 72:26–29, 1947.

[301] Hans R. Bilger. Fano factor in germanium at 77 k. *Phys. Rev.*, 163(2):238–253, Nov 1967.

[302] E. Conti et al. Correlated fluctuations between luminescence and ionization in liquid xenon. *Pys. Rev.*, B68:054201–054205, 2003.

[303] J. Thomas, D.A. Imel, and S. Bimmer. Statistic of charge collection in liquid argon and liquid xenon. *Phys. Rev. A*, A38:5793–5800, 1988.

[304] J. Thomas and D. A. Imel. Recombination of electron-ion pairs in liquid argon and liquid xenon. *Phys. Rev.*, A36:614–616, 1987.

[305] J. Angle et al. 3D position sensitive XeTPC for dark matter search. *Nucl. Phys. Proc. Suppl.*, 173:117–120, 2007.

[306] David R. Lide. *CRC Handbook of Chemistry and Physics, 88th Edition (Crc Handbook of Chemistry and Physics)*. CRC, June 2007.

[307] R. Bernabei et al. The liquid xenon set-up of the DAMA experiment. *Nucl. Instrum. Meth.*, A482:728–743, 2002.

[308] L. de Viveiros. PhD thesis, Brown University, 2009.

[309] M. J. Carson et al. Simulations of neutron background in a time projection chamber relevant to dark matter searches. *Nucl. Instrum. Meth.*, A546:509–522, 2005.

[310] S. Oikawa, N. Kanno, T. Sanada, N. Ohashi, M. Uesugi, K. Sato, J. Abukawa, and H. Higuchi. A nationwide survey of outdoor radon concentration in japan. *Journal of Environmental Radioactivity*, 65:203–213, 2003.

[311] R. de Boeck, F. Adams, and J. Hoste. Determination of ^{210}po in lead. *Radioanal. Chem.*, 1:397–412, 1968.

[312] A. Alessandrello et al. Measurements of internal radioactive contamination in samples of roman lead to be used in experiments on rare events. *Nucl. Instrum. Meth.*, B142:163–172, 1998.

[313] M. Ambrosio et al. Measurement of the residual energy of muons in the Gran Sasso underground laboratories. *Astropart. Phys.*, 19:313–328, 2003.

[314] H. M. Araujo et al. Low-temperature study of 35 photomultiplier tubes for the ZEPLIN III experiment. *Nucl. Instrum. Meth.*, A521:407–415, 2004.

[315] S. Yellin. Finding an upper limit in the presence of unknown background. *Phys. Rev.*, D66:032005, 2002.

[316] D. S. Akerib et al. Limits on spin-independent wimp nucleon interactions from the two-tower run of the cryogenic dark matter search. *Phys. Rev. Lett.*, 96:011302, 2006.

[317] K. Abe et al. Distillation of liquid xenon to remove krypton. 2008.

[318] R. Acciarri et al. Effects of Nitrogen contamination in liquid Argon. 2008.

[319] R. Acciarri et al. Oxygen contamination in liquid Argon: combined effects on ionization electron charge and scintillation light. 2008.

[320] A. Achterberg et al. Limits on the muon flux from neutralino annihilations at the center of the earth with amanda. *Astropart. Phys.*, 26:129–139, 2006.

[321] V.N. Afanasiev et al. Observation of primary and secondary (proportional) scintillation in two-phase xenon detector. *Phys. Atomic Nuclei*, 66(500-502), 2003.

[322] S. P. Ahlen. Theoretical and experimental aspects of the energy loss of relativistic heavily ionizing particles. *Rev. Mod. Phys.*, 52:121–173, 1980.

[323] D. S. Akerib et al. Limits on spin-independent wimp nucleon interactions from the two-tower run of the cryogenic dark matter search. 2005.

[324] S. W. Allen, R. W. Schmidt, and A. C. Fabian. Cosmological constraints from the x-ray gas mass fraction in relaxed lensing clusters observed with chandra. *Mon. Not. Roy. Astron. Soc.*, 334:L11, 2002.

[325] G. J. Alner et al. Status of the zeplin ii experiment. *New Astron. Rev.*, 49:259–263, 2005.

[326] J. Amare et al. Dark matter searches with nai scintillators in the canfranc underground laboratory: Anais experiment. *J. Phys. Conf. Ser.*, 39:123–125, 2006.

[327] F. D. Amaro et al. Operation of a single-gem in noble gases at high pressures. *Nucl. Instrum. Meth.*, A579:62–66, 2007.

[328] S. Amerio et al. Design, construction and tests of the ICARUS T600 detector. *Nucl. Instrum. Meth.*, A527:329–410, 2004.

[329] E. Aprile et al. Xenon: A 1-tonne liquid xenon experiment for a sensitive dark matter search. 2002.

[330] E. Aprile et al. Proportional light in a dual-phase xenon chamber. *IEEE Trans. Nucl. Sci.*, 51:1986–1990, 2004.

[331] E. Aprile et al. The xenon dark matter search experiment. *Nucl. Phys. Proc. Suppl.*, 138:156–159, 2005.

[332] Elena Aprile. The xenon dark matter experiment. 2005.

[333] E. Aprile et al. Scintillation spectroscopy with photomultipliers in liquid xenon. *submitted to Nucl. Inst. and Meth. A*, 2005.

[334] E. Aprile et al. Not yet published.

[335] E. Aprile et al. The xenon dark matter search: Status of xenon10. *J. Phys. Conf. Ser.*, 39:107–110, 2006.

[336] E. Aprile, K. L. Giboni, P. Majewski, K. Ni, and M. Yamashita. Observation of anti-correlation between scintillation and ionization for mev gamma-rays in liquid xenon. *Phys. Rev.*, B76:014115, 2007.

[337] Y. Asaoka et al. Measurements of cosmic-ray low-energy antiproton and proton spectra in a transient period of the solar field reversal. *Phys. Rev. Lett.*, 88:051101, 2002.

[338] J. Astrom et al. Fracture processes oberved with a cryogenic detector. *Phys. Lett.*, A356:262–266, 2006.

[339] M. Atac et al. Zeplin iv: A future large-scale liquid xenon dark matter detector. *New Astron. Rev.*, 49:283–287, 2005.

[340] Edward A. Baltz, Joakim Edsjo, Katherine Freese, and Paolo Gondolo. The cosmic ray positron excess and neutralino dark matter. *Phys. Rev.*, D65:063511, 2002.

[341] Marco Battaglia, Ian Hinchliffe, and Daniel Tovey. Cold dark matter and the LHC. *J. Phys.*, G30:R217–R244, 2004.

[342] Laura Baudis. The xenon10 wimp search experiment at the gran sasso underground laboratory. 2007.

[343] W. Baum, S. Gotz, H. Heckwolf, P. Heeg, M. Mutterer, and J.P. Theobald. Condensed xenon scintillators. *Nuclear Science, IEEE Transactions on*, 35(1):102–104, Feb 1988.

[344] Y. Becherini et al. Time correlations of high energy muons in an underground detector. *Astropart. Phys.*, 23:341–348, 2005.

[345] Jacob D. Bekenstein. Modified gravity vs dark matter: Relativistic theory for mond. *PoS*, JHW2004:012, 2005.

[346] G. Belanger, F. Boudjema, A. Cottrant, A. Pukhov, and S. Rosier-Lees. Lower limit on the neutralino mass in the general mssm. ((v). *JHEP*, 03:012, 2004.

[347] C. L. Bennett et al. First year wilkinson microwave anisotropy probe (wmap) observations: Preliminary maps and basic results. *Astrophys. J. Suppl.*, 148:1, 2003.

[348] Patrick Berghaus and for the IceCube Collaboration. Status and results from amanda/icecube. 2007.

[349] R. Bernabei et al. Dark matter search. *Riv. Nuovo Cim.*, 26N1:1–73, 2003.

[350] R. Bernabei et al. Prospects for dama/libra and beyond. *Nucl. Phys. Proc. Suppl.*, 138:48–51, 2005.

[351] Jeremy Bernstein, Lowell S. Brown, and Gerald Feinberg. The cosmological heavy neutrino problem revisited. *Phys. Rev.*, D32:3261, 1985.

[352] Gianfranco Bertone, Dan Hooper, and Joseph Silk. Particle dark matter: Evidence, candidates and constraints. *Phys. Rept.*, 405:279–390, 2005.

[353] M. Boezio and M. Pearce. Imaging dark matter with the pamela experiment. *Nucl. Instrum. Meth.*, A471:184–187, 2000.

[354] A. I. Bolozdynya. Two-phase emission detectors and their applications. *Nucl. Instrum. Meth.*, A422:314–320, 1999.

[355] W. J. Bolte et al. Development of bubble chambers with enhanced stability and sensitivity to low-energy nuclear recoils. *Nucl. Instrum. Meth.*, A577:569, 2007.

[356] A. Bondar, A. Buzulutskov, L. Shekhtman, R. Snopkov, and Y. Tikhonov. Cryogenic avalanche detectors based on gas electron multipliers. *Nucl. Instrum. Meth.*, A524:130–141, 2004.

[357] A. Bondar, A. Buzulutskov, D. Pavlyuchenko, R. Snopkov, and Yu. Tikhonov. Further studies of two-phase krypton detectors based on Gas Electron Multipliers. *Nucl. Instrum. Meth.*, A548:439–445, 2005.

[358] R. Brunetti et al. Warp: A wimp double phase argon detector. 2004.

[359] S. Cebrian et al. Status of the non-cryogenic dark matter searches at the canfranc underground laboratory. *Nucl. Phys. Proc. Suppl.*, 138:147–149, 2005.

[360] J. Chang et al. An excess of cosmic ray electrons at energies of 300.800 GeV. *Nature*, 456:362–365, 2008.

[361] V. Chepel, Solovov. V., F. Neves, A. Pereira, P. J. Mendes, C. P. Silva, A. Lindote, J. Pinto da Cunha, M. I. Lopes, and S. Kossionides. Scintillation efficiency of liquid xenon for nuclear recoils with the energy down to 5 kev. 2005.

[362] Alain Coc, Elisabeth Vangioni-Flam, Pierre Descouvemont, Abderrahim Adahchour, and Carmen Angulo. Updated Big Bang Nucleosynthesis confronted to WMAP observations and to the Abundance of Light Elements. *Astrophys. J.*, 600:544–552, 2004.

[363] J. I. Collar et al. First dark matter limits from a large-mass, low-background superheated droplet detector. *Phys. Rev. Lett.*, 85:3083–3086, 2000.

[364] Stephane Coutu et al. Cosmic-ray positrons: Are there primary sources? *Astropart. Phys.*, 11:429–435, 1999.

[365] Craig J. Copi, David N. Schramm, and Michael S. Turner. Big bang nucleosynthesis and the baryon density of the universe. *Science*, 267:192–199, 1995.

[366] Duane A. Dicus, Edward W. Kolb, Vigdor L. Teplitz, and Robert V. Wagoner. Astrophysical bounds on the masses of axions and higgs particles. *Phys. Rev.*, D18:1829, 1978.

[367] V.V. Dmitrenko, V.M. Gratchev, O.N. Kondakova, S.V. Krivov, A.S. Romanyuk, S.I. Sutchkov, S.E. Ulin, Z.M. Uteshev, K.F. Vlasik, and Yu.T. Yurkin. High pressure xenon gamma-spectrometers with high energy resolution. *Nuclear Science Symposium, 1996. Conference Record., 1996 IEEE*, 1:393–397, 1996.

[368] T. Doke. FUNDAMENTAL PROPERTIES OF LIQUID ARGON, KRYPTON AND XENON AS RADIATION DETECTOR MEDIA. IN *FERBEL, T.: EXPERIMENTAL TECHNIQUES IN HIGH ENERGY PHYSICS*, 537-577. (PORTUGAL PHYS. 12 (1981) 9).

[369] T. Doke et al. Absolute scintillation yields in liquid argon and xenon for various particles. *Jpn. J. Appl. Phys.*, 42:1528–1545, 2002.

[370] V.V. Egorov et al. Electroluminescence emission gamma-camera. *Nucl. Instrum. Methods*, 205:373–374, 1983.

[371] John R. Ellis and R. A. Flores. REALISTIC PREDICTIONS FOR THE DETECTION OF SUPERSYMMETRIC DARK MATTER. *Nucl. Phys.*, B307:883, 1988.

[372] Evaluated nuclear data file (endf) retrieval and plotting.

[373] E. J. M. Filipe, L. M. B. Dias, J. C. G. Calado, McCabe C., and G. Jackson. Is xenon an "ennobled" alkane? *Phys. Chem. Chem. Phys.*, 4:1618–1621, 2002.

[374] B. Fuchs. The amount of dark matter in spiral galaxies. 2000.

[375] I. Garcia Ferreira, J. Garcia Herrera, and L. Villasenor. The drift chambers handbook, introductory laboratory course (based on, and adapted from, A H Walenta's course notes). *J. Phys. Conf. Ser.*, 18:346–361, 2005.

[376] G. Giacomelli and A. Margiotta. The macro experiment at gran sasso. 2007.

[377] M. Girardi, S. Borgani, G. Giuricin, F. Mardirossian, and M. Mezzetti. Optical Luminosities and Mass–to–Light Ratios of Nearby Galaxy Clusters. *Astrophys. J.*, 530:62, 2000.

[378] F. Giuliani, T. Morlat, and T. A. Girard. Heavy superheated droplet detectors as a probe of spin- independent wimp dark matter existence. *Phys. Rev.*, D75:063503, 2007.

[379] Paolo Gondolo. Either neutralino dark matter or cuspy dark halos. *Phys. Lett.*, B494:181–186, 2000.

[380] Takahisa Goto, Hayato Saito, Masahiro Shinkai, Yoshinori Nakata, Fumito Ichinose, and Shigeho Morita. Xenon provides faster emergence from anesthesia than does nitrous oxide-sevoflurane or nitrous oxide-isoflurane. *Anesthesiology*, 86:1273–1278, 1997.

[381] Alister W. Graham, David Merritt, Ben Moore, Juerg Diemand, and Balsa Terzic. Empirical models for Dark Matter Halos. I. Nonparametric Construction of Density Profiles and Comparison with Parametric Models. *Astron. J.*, 132:2685, 2006.

[382] A. Heister et al. Absolute mass lower limit for the lightest neutralino of the mssm from e+ e- data at s**(1/2) up to 209-gev. *Phys. Lett.*, B583:247–263, 2004.

[383] Andreas Heithausen. Molecular hydrogen as baryonic dark matter. *Astrophys. J.*, 606:L13–L16, 2004.

[384] G. Hinshaw et al. Five-Year Wilkinson Microwave Anisotropy Probe (WMAP) Observations:Data Processing, Sky Maps, & Basic Results. *Astrophys. J. Suppl.*, 180:225–245, 2009.

[385] A. Hitachi, T. Doke, and A. Mozumder. Luminescence quenching in liquid argon under charged-particle impact: Relative scintillation yield at different linear energy transfers. *Phys. Rev.*, B46:11463–11470, 1992.

[386] Dan Hooper and Joseph Silk. Searching for dark matter with neutrino telescopes. *New. J. Phys.*, 6:23, 2004.

[387] G. W. Hutchinson. Ionization in liquid and solid argon. *Nature*, 162:610–611, 1948.

[388] J. Jortner et al. *J. Chem. Phys.*, 42:4250, 1965.

[389] J. G. Kim et al. Studies of electron avalanche behavior in liquid argon. *IEEE Trans. Nucl. Sci.*, 49:1851–1856, 2002.

[390] Robert A. Knop et al. New constraints on ω_m, ω_λ, and w from an independent set of eleven high-redshift supernovae observed with hst. *Astrophys. J.*, 598:102, 2003.

[391] Andrey Kravtsov and Anatoly Klypin. Formation of the large-scale structure in the universe: filaments.

[392] I. V. Krivosheina. Search for cold dark matter and solar neutrinos with genius and genius-tf. *Prog. Part. Nucl. Phys.*, 48:283–286, 2002.

[393] V. A. Kudryavtsev. Dark matter experiments at boulby mine. *Nucl. Phys. Proc. Suppl.*, 118:526, 2003.

[394] H. W. Lewis. Multiple scattering in an infinite medium. *Phys. Rev.*, 78(5):526–529, Jun 1950.

[395] Matthew J. Lewis and Katherine Freese. The phase of the annual modulation as a tool for determining the wimp mass. *Phys. Rev.*, D70:043501, 2004.

[396] T. M. Maddern and L. W. Mitchell. Ion transport in xenon gas: Applications to double beta decay. *Nucl. Instrum. Meth.*, A359:506–510, 1995.

[397] L. Maiani, R. Petronzio, and E. Zavattini. Effects of nearly massless, spin zero particles on light propagation in a magnetic field. *Phys. Lett.*, B175:359, 1986.

[398] A. Manzur. PhD thesis, Yale University, 2009.

[399] D. B. Marshall, F. Strohbusch, and E. M. Eyring. Solubility of organic substances in liquid xenon. *J. Chem. Eng. Data*, 26:333–334, 1981.

[400] R. A. Michniak, R. Alleaume, D. N. McKinsey, and J. M. Doyle. Alpha and beta particle induced scintillations in liquid and solid neon. *Nucl. Instrum. Meth.*, A482:387–394, 2002.

[401] M. Miyajima and S. Shibamura. Absolute number of photons produced by alpha-particles in liquid and gaseous xenon. *Nucl. Instrum. Meth.*, B63:297–308, 1992.

[402] R. N. Mohapatra and Salah Nasri. Reconciling the cast and pvlas results. *Phys. Rev. Lett.*, 98:050402, 2007.

[403] S. Moriyama. Sudbury, Canada, 2004. Low Radioactivity Techniques.

[404] T. Morlat et al. First results from a prototype cf$_3$i simple dark matter search detector. 2007.

[405] Julio F. Navarro, Carlos S. Frenk, and Simon D. M. White. The Structure of Cold Dark Matter Halos. *Astrophys. J.*, 462:563–575, 1996.

[406] K. Ni. *Development of a Liquid Xenon Time Projection Chamber for the XENON Dark Matter Search*. PhD thesis, Columbia University, 2006.

[407] NIST. Cryogenics material properties.

[408] J. P. Ostriker, P. J. E. Peebles, and A. Yahil. The size and mass of galaxies, and the mass of the universe. *Astrophys. J.*, 193:L1–L4, 1974.

[409]

[410] Daniel Pfenniger, Francoise Combes, and Louis Martinet. Is dark matter in spiral galaxies cold gas? 1. observational constraints and dynamical clues about galaxy evolution. *Astron. Astrophys.*, 285:79–83, 1994.

[411] P. Picozza et al. Pamela: A payload for antimatter matter exploration and light-nuclei astrophysics. *Astropart. Phys.*, 27:296–315, 2007.

[412] A. J. P. L. Policarpo, V. Chepel, M. I. Lopes, and R. Ferreira Marques. Electron multiplication and secondary scintillation in liquid xenon: New prospects. *ICFA Instrum. Bull.*, 15:4, 1997.

[413] P. M. Rentzepis and D. C. Douyglass. Xenon as a solvent. *Nature*, 293:165–166, 1981.

[414] J. H. Reynolds. Determination of the age of the elements. *Phys. Rev. Lett.*, 4(1):8, Jan 1960.

[415] V. C. Rubin, W. K. Ford, and J. S. Rubin. xxxx. *Astrophys. J. Lett.*, 183:111, 1973.

[416] Kiwamu Saito, Shinichi Sasaki, Hiroko Tawara, Toshiya Sanami, and Eido Shibamura. Study of scintillation in helium mixed with xenon to develop thermal neutron detectors. *Nuclear Instruments and Methods in Physics Research Section A: Accelerators, Spectrometers, Detectors and Associated Equipment*, 581(1-2):119 – 122, 2007. VCI 2007 - Proceedings of the 11th International Vienna Conference on Instrumentation.

[417] M. Salete, S. C. P. Leite, M. A. F. Alves, and A. J. P. L. Policarpo. ENERGY TRANSFER AND THE CHOICE OF GAS FILLINGS FOR THE PHOTOIONIZATION PROPORTIONAL SCINTILLATION CHAMBER. *IEEE Trans. Nucl. Sci.*, 29:319–322, 1982.

[418] F. Sauli. Principles of Operation of Multiwire Proportional and Drift Chambers. CERN-77-09.

[419] Richard A. Scalzo et al. High-energy gamma-ray observations of w comae with stacee. *Astrophys. J.*, 607:778–787, 2004.

[420] Robert J. Scherrer and Michael S. Turner. On the relic, cosmic abundance of stable weakly interacting massive particles. *Phys. Rev.*, D33:1585, 1986.

[421] W. F. Schmidt and E. Illenberger. Low energy electrons in non-polar liquids. *NUK-LEONIKA*, 48:75–82, 2003.

[422] J. Seguinot, T. Ypsilantis, G. Passardi, and J. Tischhauser. Liquid xenon ionization and scintillation: Studies for a totally active vector electromagnetic calorimeter. *Nucl. Instrum. Meth.*, A323:583–600, 1992.

[423] T. Shutt et al. To be published.

[424] T. Shutt et al. To be published.

[425] P. Sikivie. Experimental tests of the *invisible* axion. *Phys. Rev. Lett.*, 51:1415, 1983.

[426] N. J. T. Smith et al. page 302. 4th Int. Workshop Identification of Dark Matter, World Sci., 2003.

[427] Yoshiaki Sofue and Vera Rubin. Rotation Curves of Spiral Galaxies. *Ann. Rev. Astron. Astrophys.*, 39:137–174, 2001.

[428] D. N. Spergel et al. First year wilkinson microwave anisotropy probe (wmap) observations: Determination of cosmological parameters. *Astrophys. J. Suppl.*, 148:175, 2003.

[429] S. Torii et al. High-energy electron observations by PPB-BETS flight in Antarctica. 2008.

[430] S. B. Treiman and Frank Wilczek. Axion emission in decay of excited nuclear states. *Phys. Lett.*, B74:381, 1978.

[431] David Tytler, John M. O'Meara, Nao Suzuki, and Dan Lubin. Review of big bang nucleosynthesis and primordial abundances. *Phys. Scripta*, T85:12, 2000.

[432] Robert N. Varney. Drift velocities of ions in krypton and xenon. *Phys. Rev.*, 88(2):362–364, Oct 1952.

[433] M. Wood et al. A search for dark matter annihilation with the whipple 10m telescope. 2008.

[434] M. Yamashita et al. Xmass experiment ii. Prepared for International Workshop on Technique and Application of Xenon Detectors, Kashiwa, Japan, 3-4 Dec 2001.

[435] K. Yoshino, U. Sowada, and W. F. Schmidt. Effect of molecular solutes on the electron drift velocity in liquid ar, kr, and xe. *Phys. Rev. A*, 14(1):438–444, Jul 1976.

[436] J. F. Ziegler, J. P. Biersack, and U. Littmark. *The stopping and range of ions in solids*, volume 1. Pergamon Press, 1985.

[437] I. M. Missing, A. Citation, et al. Complete citation here. 2525.